



Wrocław University
of Science and Technology

Injury biomechanics of bicycle-transported children during
traffic accidents and the application of cork material to protect
the child's head

Doctoral dissertation

Johannes Wilhelm

Supervisor
dr hab inż. Mariusz Ptak

Keywords: bicycle baby carrier, kinematics, vulnerable road user, injury biomechanics, finite
element head and brain model, agglomerated cork, passive safety device

Wrocław 2020

Abstract

The bicycle has been promoted as a clean, cheap and healthy mean of transport in urban areas, outdoing even the public transport by an increased flexibility in travel path and time. And this is to be welcomed. This flexibility and freedom with health-oriented side effects is promoted mainly toward the direct user, the bicyclist. In contrary to this popular image, in the case of an impact of bicyclists against other vehicles, particularly the vulnerability of this group gets visible due to their missing cage. Related kinematics and injury biomechanics are well described for pedestrians and bicyclists as familiar representatives as Vulnerable Road Users. But a slightly overseen group of vulnerable road users is also included in this movement: children, who are transported in dedicated bicycle baby carriers. This work presents an original description of post-impact kinematics of these children transported in a bicycle baby carrier and closes the current gap in the literature. A focus is given also on the influence out of the vehicle's impacting velocity and particularly its front-end design to the post-impact kinematics of the child. Thereby, the vehicle impact scenario can lead for the transported child to a consecutive head impact to the ground. Additional experiments with an Anthropomorphic Test Dummy helped to identify thereby the comparability of both head impacts, first to the vehicle's front-end and finally by the side fall to the ground. Moreover, the experiments pointed on the discrepancy between the dummy's rigid head form and the deformable and highly non-linear characterized real head and brain. An aspect, which limits research and experiments toward the ability to identify and explain the nature of common, but tendentially severe head and brain injuries out of bicycle fall and impact situations.

To overcome this restriction in appropriately reflecting the biomechanical response of the brain to an impact, the advanced Finite Element Head and Brain Model of a two-year-old is introduced. It comes with an advanced structure and material characterisation compared to models, which are currently found in the literature. The approach allows to assess the impact scenario in-detail after the calculation. Furthermore, the direct benefit of the application of passive safety devices to the behaviour of the skull and brain structure can be observed.

The bicycle baby carrier proved during the simulations of crashes a low crashworthiness and underlined in first line its constructional background as an additional seat for a child on a bicycle only. Nonetheless, the results revealed the higher possibility of multiple occurring head impacts over the full crash and impact situation. Hence, the additional

passive safety device *U-band* was proposed, which is intended to be attached to the baby carrier. It includes the material of agglomerated cork as a shock absorption layer. Own experiments under extremely high and low temperatures for high-impact energies concentrate on this sustainable, tailorable in its mechanical properties and natural cellular material. In a result, cork is able to withstand several impacts and stands out in being promising to substitute the synthetic material of Expanded Polystyrene in these applications. The combination of the head and brain's in-detail motion assessment and the simulative application of the proposed U-band help to protect the child's head in impact situations.

The work names the inevitability of seeing in bicycle baby carrier transported children as a separate, third group of Vulnerable Road Users beside the established groups of pedestrians and bicyclists in order to respect the needs of this youngest group of traffic participants.

Keywords: bicycle baby carrier, kinematics, vulnerable road user, injury biomechanics, finite element head and brain model, agglomerated cork, passive safety device

Streszczenie

Rower jest promowany jako ekologiczny, tani i zdrowy środek transportu na obszarach miejskich, wyprzedzając nawet transport publiczny dzięki większej elastyczności. Ta elastyczność i wolność są promowana głównie w stosunku do bezpośredniego użytkownika tj. rowerzysty. Niemniej jednak w przypadku zderzenia pojazdu z rowerzystą, podatność na urazy tej grupy uczestników ruchu drogowego staje się szczególnie charakterystyczna. Kinematyka i biomechanika urazów są dobrze opisana w literaturze dla pieszych i rowerzystów – czyli przedstawicieli niechronionych użytkowników ruchu drogowego. Do niechronionych użytkowników dróg należą również dzieci, które są przewożone w dedykowanych fotelikach rowerowych. W pracy przedstawiono autorski opis kinematyki dzieci przewożonych na foteliku rowerowym podczas wypadku i tym samym uzupełniono obecną lukę badawczą. W pracy nacisk położony został również na wpływ prędkości uderzenia pojazdu oraz geometrii jego przedniej części, na kinematykę dziecka po zderzeniu. W ten sposób uderzenie pojazdu może doprowadzić do kolejnego wtórnego uderzenia głowy dziecka w podłoże. Dodatkowe symulacje z antropomorficznym manekinem testowym pomogły opisać zjawisko uderzenia głowy dziecka najpierw w przód pojazdu, a następnie upadek na ziemię. Ponadto eksperymenty wykazały rozbieżność między sztywną postacią głowy manekina a odkształcalnym i wysoce nieliniowym opracowanym modelem głowy małego dziecka. Jest to aspekt, który ograniczał możliwości zidentyfikowania i wyjaśnienia natury typowych, ale poważnych urazów głowy i mózgu małych dzieci.

W celu rozwiązania tego problemu autor zaproponował zaawansowany model głowy i mózgu, oparty m.in na metodzie elementów skończonych i metodach bezsiatkowych, dwuletniego dziecka. Opracowany model ma zaawansowaną strukturę i charakterystykę materiałową w porównaniu do modeli, które obecnie znajdują się w literaturze. Podejście to pozwala szczegółowo ocenić ryzyko obrażeń dla różnych konfiguracji zderzeniowych. Ponadto można zaobserwować bezpośrednią korzyść z zastosowania urządzeń bezpieczeństwa biernego w celu redukcji urazów struktury czaszki i mózgu.

Foteliki rowerowe podczas symulacji wypadków wykazały niski poziom redukcji obrażeń u dzieci. Podkreśla się, że nie należy fotelików rowerowych traktować jako urządzeń bezpieczeństwa biernego. Wyniki analiz numerycznych ujawniły wyższą możliwość wielokrotnych uderzeń głową w czasie zderzenia. W związku z tym zaproponowano dodatkowe pasywne urządzenie nazwane U-band, które może być

przymocowane do fotelika. Urządzenie wykorzystuje materiał korkowy jako warstwę pochłaniającą energię zderzenia. Przeprowadzone eksperymenty w ekstremalnie wysokich i niskich temperaturach dla różnych energii kinetycznych wykazały, pożądane ze względu na absorpcję energii, właściwości aglomerowanego korka. W rezultacie materiał korkowy jest w stanie przenieść obciążenia wynikające z kilku uderzeń - może on zatem z powodzeniem zastąpić bardzo powszechnie stosowany w urządzeniach ochrony osobistej spieniony polistyren. Połączenie szczegółowej oceny ruchu głowy i mózgu oraz symulacyjnego zastosowania proponowanego U-band pomaga chronić głowę dziecka podczas uderzenia.

Niniejsza praca ma celu wyodrębnienie i opisanie w kontekście kinematycznym i biomechanicznym kolejnej grupy niechronionych użytkowników ruchu drogowego spośród już opisanych w literaturze: pieszych, rowerzystów i motocyklistów.

Słowa kluczowe: fotelik rowerowy, kinematyka, niechroniony użytkownik ruchu drogowego, biomechanika urazów, urazy głowy, model numeryczny, metoda elementów skończonych, materiał korkowy, urządzenia bezpieczeństwa biernego, bezpieczeństwo dzieci

Table of contents

Abstract	I
Streszczenie	III
Table of contents	V
Abbreviations directory	VII
Note of thanks	IX
1 State of the art – literature review	10
1.1 Vulnerable Road Users in vehicle collisions.....	10
1.2 Children on bicycles in baby carriers.....	15
1.3 Head and neck injury criteria	18
1.4 Finite Element Head and Brain models with a focus on child models	22
2 Objectives of the thesis	26
3 Original description of kinematics of children transported in bicycle-mounted baby carriers during impact situations	28
3.1 Methodology.....	28
3.2 Representing the impacting vehicle as a FE-model.....	29
3.3 Establishing a generic model of the baby carrier.....	31
3.3.1 3D-scanning of the geometry	31
3.3.2 Material characterization.....	32
3.3.3 Modelling the harness of the baby carrier.....	33
3.4 Representing the bicycle as a multibody model in MADYMO	34
3.5 Simulation of FE-code in LS-DYNA coupled with MADYMO multibodies and dummies.....	35
3.6 Definition of impact situations as simulation configurations.....	36
3.7 Discussion of the obtained results	38
3.8 Chapter conclusions	53
4 Investigating the influence of the vehicle front-end geometry to the transported babies after-crash kinematics	55
4.1 Choice of vehicle models and definition of configurations	56
4.2 Implementation of MADYMO models of the dummies and a bicycle with baby carrier.....	59
4.3 Discussion of the results.....	61
4.4 Chapter conclusions	70
5 Experimental tests of a fall situation to the side	72

Injury biomechanics of bicycle-transported children during traffic accidents and the application of cork material to protect the child's head	VI
5.1 Intention for performing a full-scale side fall test	72
5.2 Experiment setup	73
5.3 Discussion of the results.....	76
5.4 Chapter conclusions	84
6 Creation of a Finite Element Head and Brain Model of a 2-year-old	86
6.1 Introduction	86
6.2 Choice of patient data	87
6.3 Scope of the two-year-old FEHM.....	88
6.4 Anatomical specialties of a child's head and brain.....	90
6.5 DICOM handling for the creation of a geometrical (CAD) model	93
6.6 Original method to extract the skull geometry out of a MRI data set.....	99
6.7 Translation of the CAD-data into a discrete (CAE) model.....	103
6.8 Re-calculating the side fall experiment by the use of the original FEHM child model	110
6.9 Chapter conclusions	124
7 Challenging the vulnerability of the child's head during impacts by implementing an additional passive safety device to the baby carrier.....	126
7.1 Introduction	126
7.2 Agglomerated cork as a sustainable substitution for EPS.....	128
7.3 Experimental tests.....	133
7.4 Material modelling.....	141
7.5 Numerical simulation: considering the U-band as a passive safety device.....	146
7.6 Chapter conclusions	153
8 Final conclusions and future related work.....	155
8.1 Final conclusions	155
8.2 Future research	159
Bibliography.....	160
Statement of authorship	173

Abbreviations directory

1D	One Dimensional
2D	Two Dimensional
3D	Three Dimensional
AC	Agglomerated Cork
ADAC	Allgemeiner Deutscher Automobilclub
aHEAD	advances Head models for safety Enhancement And medical Development
ALE	Arbitrary Lagrangian-Eulerian formulation
AIS	Abbreviated Injury Scale
ATD	Anthropomorphic Test Dummy
BAST	Bundesanstalt für Straßenwesen (German Federal Highway Research Institute)
BLE	Bonnet Leading Edge
BV	Bridging Vein
CAD	Computer-Aided Design
CAE	Computer-Aided Engineering
CC	Corpus Callosum
CoG	Center of Gravity
CSF	Cerebrospinal Fluid
CT	Computed Tomography
CTA	Computed Tomographic Angiography
DAI	Diffuse Axonal Injury
DICOM	Digital Imaging and COmmunications in Medicine
DIN	Deutsches Institut für Normung
EC	Expanded Cork
EN	European Standard/European Norm
EOS	Equation of State
EU	European Union
EPP	Expanded Polypropylene
EPS	Expanded Polystyrene
FE	Finite Element

FEA	Finite Element Analysis
FEHM	Finite Element Head and Brain Model
FEM	Finite Element Method
FMVSS	Federal Motor Vehicle Safety Standard
FSI	Fluid-Structure Interaction
GHBMC	Global Human Body Models Consortium
HIC	Head Injury Criterion
LBRL	Lower Bumper Reference Line
LM	Liliequist Membrane
MB	Multi Body
MRI	Magnetic Resonance Imaging
MTB	Mountain Bike
NCS	National Cycling Strategy
NIC	Neck Injury Criteria
PP	Polypropylene
PSD	Passive Safety Device
PU	Polyurethane
SDH	Subdural Haematoma
SPH	Smoothed Particle Hydrodynamics
SSS	Superior Sagittal Sinus
STL	Stereolithography model
SUV	Sport Utility Vehicle
TBI	Traumatic Brain Injury
TE	Time to Echo
THUMS	Total Human Model for Safety
TR	Repetition Time
VRU	Vulnerable Road User
WAD	Wrap Around Distance
WFD	Waveform Digitizing

Note of thanks

A crucial part behind the written work is always the support, which lacks of direct visibility. But without all the heart-warming help, fruitful discussions, vague and ambitious ideas, which enabled to grow beyond own expectations, well, and thousands of small stories that could be told, it would not have been these four adventurous years in Poland with this doctoral dissertation in the result.

I want to send my honest and sincere thanks

To dr hab inż. Mariusz Ptak for being an outstanding mentor with his visions and ambition, the scientific but also personal guidance of myself during this culturally changed lifetime in Poland but particularly for being a good friend in all moments.

To the entire Katedra Konstrukcji Badań Maszyn i Pojazdów for welcoming and treating me as a part of their amazing team and matey environment.

To my family for supporting me in striving my ambitious goals, giving me the strength to go this path by providing me moments of fun, joy, shelter and never-ending streams of good food and smiles. Thank you, my mother Renate Wilhelm, my sister Dr. rer. nat. Franziska Wilhelm and family, my brother Benjamin Wilhelm and Cellina, my beloved Yudith Mariaran Tresnowati and kids.

1 State of the art – literature review

“It would appear that pedestrians and vehicles are just not compatible.”

Fisher & Hall, 1972 [1]

Nowadays urban traffic is diverse. What started in a behavior of being susceptible for “green tendencies”, saving resources and lowering one’s own footprint on Earth, developed to a new understanding of living in urban areas. This includes particularly the types of movement and transport, which have to be understood nowadays also in terms of sports and recreational activities and find extreme examples also on long-distance runs and rides to work. Particularly the bicycle gained importance as a more and more popular mean of transport for commuting to work. The phenomenon may base in this concern also on two arguments. Choosing a greener mean of transport may contribute to improve the air conditions regionally. In the same time, a more muscle-based form of commuting can be supportive for both a mental and physical health status, which occurred to be even before the COVID-19 pandemic an aspect of wider social acceptance and priority. These ideals went consequently as well into parenting, where the introduction of children into the world of muscle-based movement as part of familiarly activities could be seen also as a kind of ethical and motorial education.

1.1 Vulnerable Road Users in vehicle collisions

However, combining all the so far mentioned forms and intentions of movement, it hosts them all with their different forms of motion, velocities, infrastructural needs and habits in the same urban space. In an example, pavements might be shared by bicyclists of different ages, regular pedestrians as well as by runners. It is not surprising, that consequently also a large number of injuries and accidents – generally spoken: impacts – will be reported year by year, in an example for cyclists [2]. Riding a bicycle makes it thereby mandatory to have appropriate motor skills developed. Regarding the youngest bicyclists, this might point on the necessity of a proper age to take part actively in the traffic. To overcome this restriction, young children are likely transported in dedicated

baby carriers on bicycles. Beside these bicycle-mounted additional seats, also forms of trailers, specific places in cargo bikes or bike-a-like-trailers can be recognized for child transport. Especially the dedicated baby carrier mounted to the bicycle stands out with its popularity [3]. As already mentioned, the increasing complexity of traffic contenders on still limited space within the urban areas leads to conflict potential, which might end in a collision. Connected to this might be the loss of physical integrity with specific risks for every sub-group [4]. The types of contenders are thereby united by the term of being a Vulnerable Road User (VRU). In the summary of the regulation (EC) No 78/2009, the European Commission presented a definition of the key term VRU. Thereby, VRUs are seen as *"non-motorized road users, such as pedestrians and cyclists as well as motorcyclists and persons with disabilities or reduced mobility and orientation"* [5,6]. Interestingly, beside the lack of an external "cage-like" protection also a focus is set on persons with reduced mobility and persons without orientation, which overall includes passengers [7]. Taking also children in these aspects of safety assessment into consideration is thereby an established topic for several decades already. Since the late 1970s, the bicycle-based transport of children is known and popular in America [8]. Within the Australian National Cycling Strategy 2011–2016 (NCS), cycling was even described as safe, viable and enjoyable, considering it as a mode of transport and promoting its recreational benefits [9,10]. Seeing on the other hand the conflict potential in the diversity of nowadays traffic contenders and raising injury cases on the shared but limited inner-city space, the statement might be overthought critically. Particularly, as only limited effort was done so far to the topic of children in bicycle baby carriers [11–13].

In opposite to this special group of young VRUs, the higher percentage of occurrence of vehicle impacts and collisions involving regular, adult pedestrians and cyclists led to their high amount of related and available research [14,15]. Especially the impact to the VRUs side – for example likely to occur while crossing the street – is in these works named as the most common impact configuration overall [16]. It is beside the general question, if this conflict potential, which is ending in a collision, arisen from a lack of communication. Fisher and Hall stated in 1972 suiting: "It would appear that pedestrians and vehicles are just not compatible." [1]. The try to answer the background of this complex can be found in several approaches, but especially by collecting accident data and consecutively in the reconstruction of fatal traffic accidents [17,18] or by human cadaver tests [19,20]. These contributed thereby especially regarding the validation of the reconstructions and used

models. Moreover, they revealed a deeper insight in the complex event, which helps to overcome the lack of normally available real-world experimental data. When it comes to human-related experimental data, the topic is out of its nature always very sensitive and connected to ethical questions, too. As a supportive and partially substitutional element, the evolution of Anthropomorphic Test Dummies (ATD) is recognized. Consequently, also the application of ATDs in the majority of the research is given, in physical as well as in virtual form. A focus in vehicle collisions is thereby set primarily on two aspects: the post-impact VRU kinematics and the influencing vehicle front-end geometry. Regarding the latter, especially the nowadays more and more preferably driven Sport Utility Vehicles (SUV) enriched the diversity of shapes in traffic [21]. Unfortunately, their involvement in VRU impacts increased as well potentially the severity of injuries [14,22,23]. Moreover, it was stated, that after VRU impacts to higher vehicles like SUVs, a secondary head impact to the ground was still and likely possible [24]. Generally, and what seems to be stated over all the research, the VRUs motion during the impact is a descriptive element for the consequently and mainly injured body regions after the vehicle impact [14]. This implies as well, that the understanding of these kinematics can be helpful to design safer vehicle front-ends [25,26]. It might sound at first problem enforcing, that the post-impact patterns of pedestrians and bicyclists are showing similar motion patterns [14]. Nonetheless, already the presence of pre-impact motion, posture and impact avoidance motion (see Fig. 1) can increase the variables significantly [27]. As examples, which are influencing the kinematics and hence also the measured outcome, it can be named the different height ratio of VRU to vehicle front-end, changes in the stiffness over the impacting vehicle front-end, the presence of muscle contraction, the uncertainty about an impact angle, boundary conditions and many more. When considering this information out of witness data, it gets inevitable to have recourse on empirical data for an iterative reconstruction. This might consequently include also a wider simulation set for distinguishing the influence of these rather unknown or widely specified variables [14].

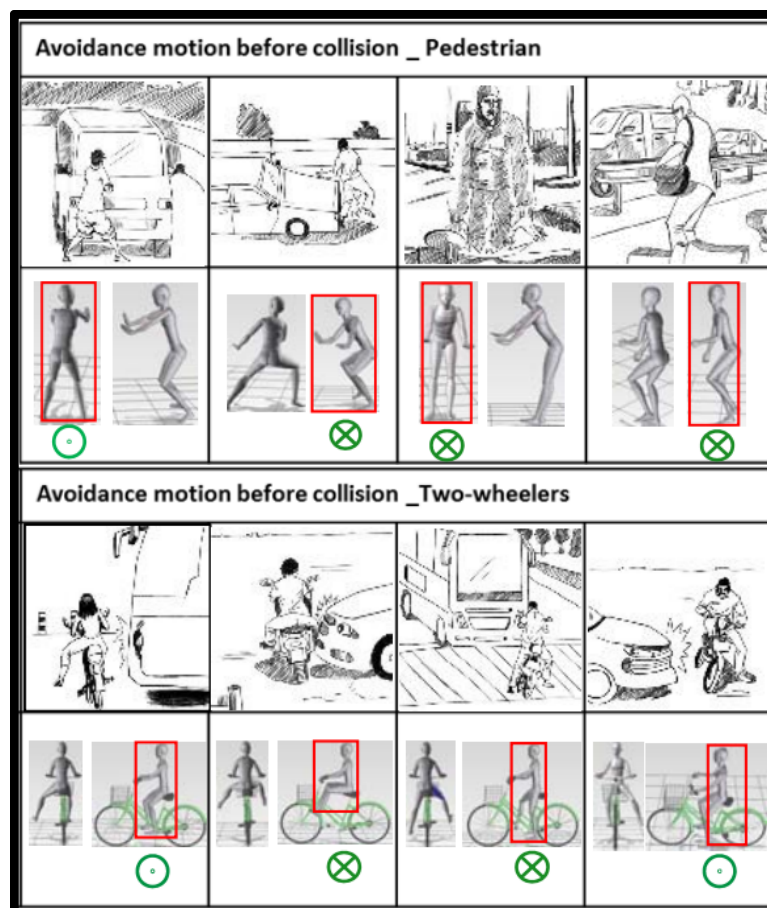


Fig. 1 Avoidance motion and posture of VRU (circle with point: view toward the impacting vehicles; circle with cross: view in driving direction of the vehicle) [27]

Regarding the VRUs motion pattern after the impact, a higher importance is given to the height ratio between center of gravity (CoG) of the VRU and the front-end geometry of the impacting vehicle [14]. Base for the majority of kinematic research is the assumption of a vehicle impact to the side of an upright standing VRU, while there is no major movement of the VRU considered. Depending on the vehicle height, post-impact VRU kinematics cover thereby the common forms of 1) somersault over the vehicle into 2) dragging, also underneath the vehicle, up to 3) a clear projection in the vehicles' direction of driving [22]. Common vehicle measurements for these assessments are thereby the vehicles' front-end geometry describing parameters of Bonnet Leading Edge (BLE) and Lower Bumper Reference Line (LBRL) as well as the finally recognized Wrap Around Distance (WAD) of the VRU [28]. The WAD is the measured length from the ground over the vehicle's front up to the head impact location [14] and was stated to be similar for pedestrians and bicyclists, while the latter seems to have a more rearward located head impact position, initially seen to be more severe in the injury outcome [29]. It was assumed to be connected to both, to the higher seating position and hence a higher located

center of mass, but also independent to this center to higher impact velocities [30]. Fanta et al. connected the phenomenon to different bicycle types and the corresponding seating position or posture, which changed the riders' center of gravity [16]. A change or renewal to these statements can be recognized, as a relation is now seen as well to the pelvis height and pelvis injury outcome. Compared to the average pedestrian, the bicyclist shows based on the difference in pelvis height – dependent on the presence of a bonnet type of vehicle, an increased sliding over the vehicle's bonnet [14,26], which is potentially able to lead to higher occurring WAD values. The discussion was led mainly regarding the impact area on the vehicle, which might be preferably less stiff or relatively compliant leading to a less severe injury pattern, while for example the area around the rearward bonnet edge might show the opposite. Beside the general statement, that a collision scenario between a VRU and a vehicle is commonly affecting the VRUs integrity significantly, but it remained: an inappropriate frontal vehicle design – with in a way “aggressive properties” – is able to increase the VRUs injury severity. And especially this inappropriate ratio or frontal aggressiveness in the constellation pedestrian–SUV seems to entail a higher risk for the presence of a fatal collisions than for sedan or compact vehicles [31]. Even though this tendency was supported throughout the literature, the addendum was done, that this effect or this phenomenon is mainly occurring for velocities under 30 km/h [32]. This intensifies the complexity for urban accidents, as pedestrian and bicyclist impact scenarios are reported mostly for inner-city velocities, but covering also the range up to 50 km/h [33].

The presented literature seems to enlighten the topic of VRU-vehicle impacts entirely by considering their post-impact kinematics, including frontal vehicle-shapes, impact avoidance motion and many more. Nonetheless, it needs to be noted, that the consideration in the presented research was commonly an *active*, so self-walking pedestrian or self-riding bicyclist. It included thereby the specific center of gravity or the pelvis height. The introduction of the significant increasing height of the BLE showed to be able to shift the observations, to make the kinematics and injury outcome comparable for the constellations “SUV-vs-tall pedestrian” and “sedan vehicle-vs-small pedestrian”. However, in an extreme example, the current research was so far not able to answer the same questions for a child, which is simply seated and fixed to a bicycle. It might be even more complex, as this passive VRU shows a significant differing center of gravity and pelvis height to any of the connected VRU groups.

1.2 Children on bicycles in baby carriers

A special form and particularly differing to the beforehand presented VRUs is a child, which is transported in a bicycle baby carrier. The popularity of the rear-mounted baby carrier for bicycles is also recognizable in the European Union due to its simplicity and brilliant cost-benefit-ratio regarding child transport [34,35]. It enables people to commute in urban areas even with younger children, which might lack still the motor skills for riding a bicycle alone or take part actively in the traffic [3]. Typically, the baby carriers are fitting to common bicycles with a specifically demanded seat post tube diameter, where a mounting bracket has to be installed. It connects the bicycle frame by a vertical strut with the horizontal seat platform of the baby carrier. The seat platform is seamless connected with the structures of arm and backrest. It shall be noted, that beside rear-mounted versions also front-mounted baby carrier versions for increased interaction with the child are existent on the market (see Fig. 2). As features, spoke and feet guards, a harness acting similar to a seat belt and reflectors are commonly present.



Fig. 2 Common bicycle baby carrier types: mounted to rear-rack (left), rear-frame (middle), front (right) [4]

It is not entirely clear or defined, if the features may or have to be named precisely as safety features, but some baby carrier models are showing additionally a grab bar, which potentially could act as a front restraint [36].

Beside the general positive aspects of bicycle baby carriers, the use may include also negative sides, as for example the overall uncaged situation allows dropping items, in worst case also into the rear wheel spokes. Moreover, child and adult are closely located to each other, which might be leading to contact situations while moving on the bicycle or even while pedaling, once for example the child's feet are not fixed by the foot straps. Other aspects of difficulties have to be seen in the circumstance, that safely seating the child depends mainly on the child's willingness to cooperate.

Technically, bicycle baby carriers are mainly designed to carry a child with a mass of up to 22 kg. Thereby, they have to match the constructive demands out of DIN EN 14344

for the European market [37]. The norm sees several technical functionalities as necessarily to prove in action, as for example to keep the carried child's feet away from the wheel spokes and serve with a sufficient shock and temperature resistance. Overall, a major constructional focus within the norm seems to be set toward the lower geometry of the seat including the bracket, the used material for the carrier and its general strength. An exception has to be seen in the assessment of the harness performance within a roll-over test. By this, the norm concentrates on securing the child in its intended position. This gains importance, as especially upper body and head are reported to be among others the most affected body regions due to accidents and impacts [10,38]. Even though it is not directly mentioned, the norm with its guidelines for construction and usage are pointing on the top priority to reduce the severity of injuries in these regions, as they may arise out of the accidental-afflicted usage of bicycle baby carriers. However, the information about child occupant safety on bicycles is limited [39]. Often, necessary background information is missing. The involved type of baby carrier, backrest length, helmet usage and wearing situation are only a few examples. Hence, little is known about the direct connected injury outcome of a child after a fall while sitting in the baby carrier [13]. A source of information, which delivers crucial data for the related research, is found in data about in total occurred injury, which was treated in emergency departments or by hospital admissions (see Fig. 3) [10].

Body region	Emergency department presentations			Hospital admissions		
	0–3 Years	4–6 Years	7–10 Years	0–3 Years	4–6 Years	7–10 Years
Head	1,459 (58.6%)	2,475 (49.6%)	2,303 (22.2%)	299 (58.1%)	652 (47.1%)	797 (27.5%)
Neck	5 (0.2%)	38 (0.8%)	77 (0.7%)	0 (0%)	14 (1%)	30 (1%)
Thorax	0 (0%)	0 (0%)	131 (1.3%)	0 (0%)	5 (0.4%)	17 (0.6%)
Abdomen, lower back, lumbar spine, and pelvis	35 (1.4%)	163 (3.3%)	395 (3.8%)	12 (2.3%)	74 (5.3%)	267 (9.2%)
Shoulder and upper arm	53 (2.1%)	159 (3.2%)	473 (4.6%)	52 (10.1%)	147 (10.6%)	236 (8.2%)
Elbow and forearm	274 (11%)	568 (11.4%)	1,774 (17.1%)	93 (18.1%)	243 (17.6%)	942 (32.5%)
Wrist and hand	245 (9.8%)	508 (10.2%)	2,162 (20.8%)	18 (3.5%)	65 (4.7%)	171 (5.9%)
Hip and thigh	8 (0.3%)	59 (1.2%)	299 (2.9%)	13 (2.5%)	42 (3%)	113 (3.9%)
Knee and lower leg	85 (3.4%)	294 (5.9%)	1,218 (11.7%)	18 (3.5%)	97 (7%)	241 (8.3%)
Ankle and foot	230 (9.2%)	427 (8.6%)	890 (8.6%)	7 (1.4%)	37 (2.7%)	67 (2.3%)
Other	97 (3.9%)	297 (6%)	658 (6.3%)	3 (0.6%)	8 (0.6%)	14 (0.5%)
Total	2,491	4,988	10,380	515	1,384	2,895

Fig. 3 Registered injuries regarding body region and age group for baby carrier impact cases [10]

Commonly affected after a fall or impact are head, elbow and forearm, but also wrist, hand and foot with ankle. As the head is in a majority of cases the main treated body region, the data correlates with the research of Miyamoto and Inoue [39], as well as Kishibe et al. [40]. Oxley et al. also stated, that it was not clearly reported for the age group of 0-3 years, if the patient was riding alone or transported by a carrier [10]. The higher presence of hand and wrist injuries indicates furthermore the potential presence of an impact avoidance motion, which potentially failed or was insufficient to protect the

head from the severe impact. Nonetheless, most of the occurring injuries were reported after impacts in regions of lower, inner-city velocities [41]. This supports also the urban areas as main region of usage for bicycle baby carriers. Unfortunately, case specific, reliable data is often difficult or impossible to be provided by the police, as in many scenes more specific data was partially not collected or the case was not reported at all to the police [10,42]. The high percentage of treated injuries on the head may point on this circumstance as well, that *simpler* or less severe injuries might be handled at home without involving an institution at all. However, as the head is the mainly affected body region and top priority to protect against injuries, a common advice or result of the connected research is to favor wearing a helmet. It is widely accepted, that when it comes to a direct cranial impact, helmets are able to reduce the severity of the head injury. This advice refers as well to adult bicyclists. Seeing the helmet as a passive safety device, it has to be in line with the demands and test protocols out of EN 1078 for general bicycle helmets. The demanded drop tower tests involve a corresponding head form and allow a maximum of 250 g acting acceleration in order to achieve certification of the helmet as safety gear. Nonetheless, there is exemplarily in Germany for bicyclists still no direct demand or law to wear a helmet. It has to be seen rather as a social phenomenon, that the acceptance to wear a helmet – or passive safety gear generally – increased [12]. It is still not clear, if it appeared as a matter of style and lifestyle, a statement toward healthy lifestyle or dedication to a specific sport or brand. For children, this last statement is only partially true. In 2014 in Germany it was more than 2/3 of children with an age from 6 to 10 years, which were wearing a helmet during their bicycle ride. For the age group of at least 17 years old children and young adults, the helmet wearing rate dropped to 7 to 16 % only [43].

Nonetheless, it is widely accepted, that a suiting safety helmet can reduce the risk of head injuries in terms of severity, when it comes to a head impact [20,44,45].

With the youngest bicyclists having a higher helmet wearing rate, also the choice and wearing conditions of passive safety gear might be different from other age groups, as the supervision for young children is on the parents. Nonetheless, the hazard of improper safety devices or the improper use of them would remain in this assumption [46]. Particularly for the transported children on bicycles, this discussion is extended moreover by a proper ride preparation, which includes the correct fastening of the child by the harness [47]. In contrary to this, Miyamoto and Inoue added their finding, that the usage of a seat belt could even increase head impacts in their severity, as long as the bicycle

was stationary flipping and a low-back seat was used. Nonetheless, finally they recommended the use of both a high backrest and a helmet [39].

1.3 Head and neck injury criteria

It was shown, that a significant amount of data concerning head injuries is gathered from emergency departments, thus once a head injury occurred at a patient. By considering the connected witness data, especially this combined empirical data helped to estimate the severity of impacts and understand the injury mechanism behind. Thus, the connection of an impact to a direct acting acceleration on the head is seen. This followed among others the motivation to develop injury criteria that may associate particularly accelerations to commonly observable injury patterns and intensities, which gained a priority in this field of research. Bandak described 1997, that translational acceleration was able to create intracranial pressure gradients, while the rotational acceleration followed a relative motion between skull and brain [48]. It will be shown, that this assumption is still in charge and finds usage in the frequently used Head Injury Criterion (HIC). HIC is basing on the resultant linear acceleration (a) in time domain (t) – commonly calculated for a maximum time range of 15 or 36 ms – and is formulated by the equation 1:

$$HIC = \left(\left[\frac{1}{t_2 - t_1} \int_{t_1}^{t_2} a(t) dt \right]^{2.5} (t_2 - t_1) \right)_{max} \quad (1)$$

The rotational acceleration is not considered within HIC, even though it is stated to occur naturally as well [38,49]. In its assessment for the certification of passive safety devices, the calculated HIC value as well as the general recognized peak of translational acceleration have to be below a threshold. An example shall be given in the ECE Regulation 22.05, where the HIC(36) value and linear peak acceleration have to be below 2400 respectively below 275 g [50]. To present a comparison: The HIC(36) value of 1000 is widely accepted to represent a threshold for the 50% probability of severe but not life-threatening head injury [51], [52]. Including these thresholds in the assessment of passive safety devices has the intention to limit or avoid Traumatic Brain Injuries (TBI). A focus has to be seen as well in the possibility of skull fracture, which relies – for example after an impact to the ground – as well rather on the linear acceleration and hence on the deformation of the skull [53]. Regarding the HIC, the so-called 3 ms-

threshold was introduced and proposed with 80 g as a maximum acceleration sustained for at least the named 3 ms, which would presumably cause skull fracture [14].

Even though a recognizable amount of research reports the translational acceleration as base for the assessment, Diffuse Axonal Injury (DAI) and Subdural Hematoma (SDH) are two common injury types, which are recognized after bicycle accidents, but not only connected to translational acceleration situations. Both injuries arise mainly due to relative motion and depend thereby also on the rotational acceleration. The DAI shows shear affected neuronal axons in the transition zone of white and grey matter, which get swollen and tend to be ruptured in a consecutive step as a secondary injury. For SDH, the relative motion causes a tearing of the bridging veins of the subdural space, which are exposed secondarily to failure and lead to bleeding and increased pressure in the affected area. [52,54]

What can be recognized in the connected research: for example HIC(36) thresholds are giving the 50% probability of the presence of an injury. The given examples of recognized cases of long-term disability or vegetative states point clearly out [45,52,55], that skull fracture, brain concussion, DAI, SDH and other head and brain injuries can be found also below the thresholds [56–58]. In this context, it needs also to be highlighted, that in some literature a correlation of the magnitude of angular acceleration with the magnitude of linear acceleration is seen [59]. Overall, the try to correlate accelerations with any form of these injuries is up to today likely centre of various research projects. Hence, also numerous injury criteria were proposed, which are either 1) basing on translational or rotational accelerations or 2) on the combination of both [60]. Beside this empirical based data and physical experimental related approaches, with the increasing evolution and application of numerical systems and models, the focus on stress and strain gained more importance. Even though calculated stress on the brain instances might show a better sensitivity for the high energy and short time impact scenario, it was also criticized, that it was not able to show for example haemorrhages although overcoming defined thresholds. Fernandes et al. gave in this concern a wider review of related injury criteria and the stated thresholds. [60,61]

Nonetheless, most of the established criteria and connected Finite Element Head Models are concentrating on adult values and representations. The demand of criteria tailored to young children have arisen naturally. Literature shows not a clear answer, if values simply have to be scaled or adjusted, since real-world data is rare or nearly impossible to gather.

Nonetheless, scaling adult values based on tests with numerical models within real-world accident reconstructions was presented as a promising approach [62]. Nonetheless, the try to establish general accepted values for children is still seen sceptical through the literature, but partially supported [63]. This has to be seen in the context of the anatomical specialties, for example the different body proportion of head-to-torso for young children compared to adults [64]. As rotational accelerations and hence the so far established injury thresholds are strongly connected to the mass of the brain [65], but the mass of the child's brains differ to adult brains and even in their own age group significantly, a bigger discrepancy needs to be taken [66]. Moreover, the search for common values gets complicated for example also by the continuous change of mechanical properties like the skull's Young's modulus over the first years of a human's life [67] – which again does not happen in the same time and amount for all humans. Hence, presented threshold values out of the literature need to be taken carefully in terms of their patients or models age and the possible correlation with a regional average of the corresponding age group.

As initially remarked, head injuries can be a result of a direct cranial impact. Another scenario causing a head injury can be described by an indirectly acting force on head and neck, for example due to an abrupt acceleration-deceleration of body and torso. This can be found in rear-end vehicle crashes, simulated by sled-tests. It shows thereby the so-called whiplash effect and results in an excessive movement of both head and neck, allowed as well by insufficient muscular tension. Finally, this can lead to neck distortion or even the fracture of cervical vertebrae [68]. Regardless of the possibility of highly complex post-impact motion of bicycles, seeing a seated child in the bicycle baby carrier could include the basic kinematics of these types of injuries in bicycle crashes. Injuries out of excessive neck motion are often connected and assessed by the Neck Injury Criterion (NIC). It was introduced and described in 1996 by Boström [69]. Base for the calculated value is the head's movement relative to its base in T1 vertebrae and the connected damage in the cervical spinal ganglia [69]. The phenomenon was tested surprisingly firstly on pigs (see Fig. 4) and relates specifically to the neck's motion of flexion and extension.

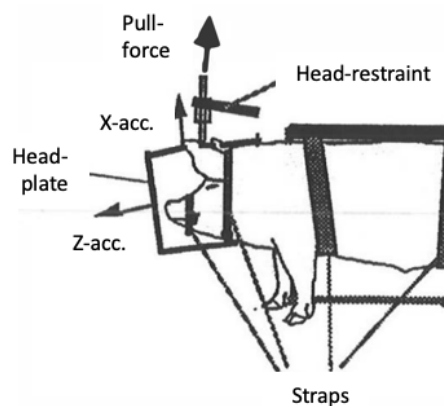


Fig. 4 The test setup for the proposed NIC [69]

This damage is reported to arise out of transient pressure changes within the spinal canal [70] and is assumed as an explanation for typical symptoms of patients after rear-end crashes with AIS 1-neck injuries [69].

AIS stands thereby for Abbreviated Injury Scale (AIS) and is not only connected to neck respectively head injuries. It is used universally as an anatomically-based scoring tool for injury classification. Haasper et al. concentrated on the potential but also on problems of AIS application in practice and showed, that AIS relates in its classification to the relative importance of a body region [71]. Generally, a significant amount of the AIS 2+ cases found in the literature showed fractures in the upper extremities, torso and lower extremities, when road users were not protected by a cage-like structure, which could be found for example in a car. In this scale, brain injuries ranked with around 10% of all AIS 2+ injuries close to the fractures and project the risk of suffering from these due to bicycle impacts, the fall out of a carrier, single falls or even a flip-over [42], [46].

A standard, which is considering as well the neck movement, but adds another tolerance level, is the Federal Motor Vehicle Safety Standard (FMVSS) No. 208 [72]. The standard presented tolerance levels or limits individually for compression, tension, shear, flexion moment and extension moment of the neck. With a focus on rear-end crashes and sled tests the limitation had to be seen in the absence of angular acceleration around the human z-axis and lateral bending [68]. It should be seen with skepticism to apply directly the tolerance limits out of NIC and FMVSS No. 208 in respect of the potentially more complex torso, head and neck movement in bicycle crashes. Especially the excessive rotation of the head and neck around the human z-axis might occur, where cadaver tests revealed 114° as a critical value, able to produce atlantoaxial dislocation [73]. Yoganandan et al. saw furthermore the torsional tolerance of approximately 28 Nm for

this case and added, that the atlantoaxial joint seems to be weaker than the lower cervical spine in torsion. In which concern the beforehand presented criteria would be effected quantitatively by torsion or general rotation around the humans' z-axis is not stated.

1.4 Finite Element Head and Brain models with a focus on child models

The complexity of the described body motion and interaction during traffic impact situations creates problems in predicting injuries. First of all, as a variety of input parameters to reconstruct a specific event might be unclear. Moreover, due to the complexity of motion, particularly with a focus on the head and neck structure during these events, several of the real-world injury based injury criteria might be only reduced applicable, as the base motion in the case needs to be in line with the criterions assumption. Moreover, as experiments regarding injuries on humans cannot be carried out without ethical barriers as it would be possible on objects, hence a possibility to correlate own results is widely missing. To overcome the lack of real-world experimental data and consequently the clear insight in the injury biomechanics, numerical models were increasingly applied to fill this gap [38], [51].

A representative of the state-of-the-art models is in this concern the Finite Element Head and Brain Model (FEHM) of the Global Human Body Models Consortium (GHMBC). As it is shown in Fig. 5, it includes over 22 sub-components with 52 individual neck muscles as 1D and 3D elements, 2D and 3D deformable neck vertebrae with 3D cartilage, 1D ligaments and 2D/3D intervertebral discs. Mainly 3D elements were used to model the skull and brain. Only a minor amount of instances was modelled by 2D elements, for example the falx cerebri and tentorium [74].

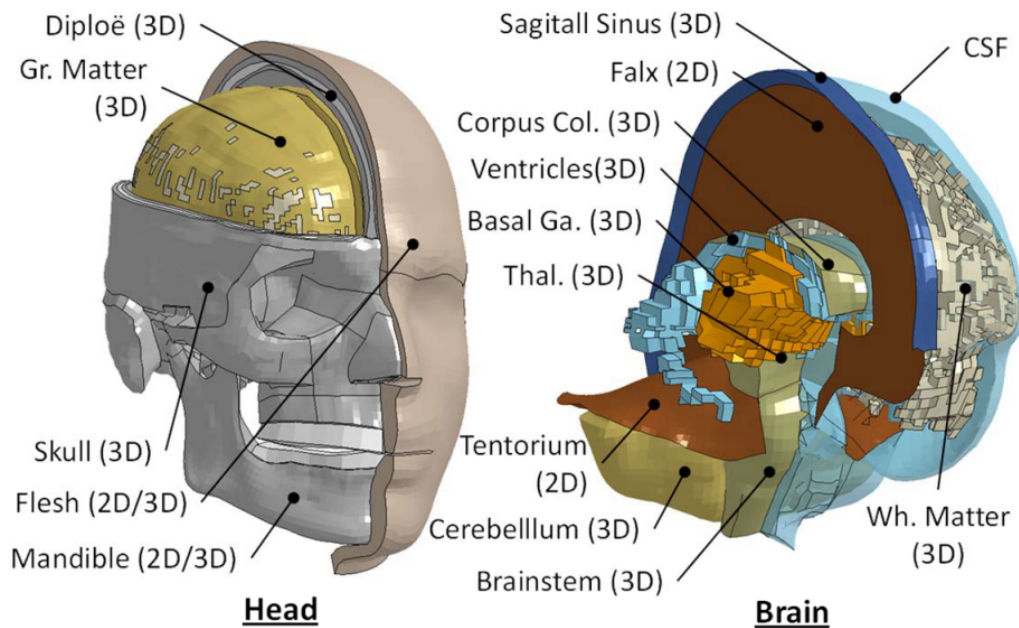


Fig. 5 Description of the GHMBC model [74]

Showing this high informational density, the GHMBC model is one of the most advanced full body and head models used in the related research. The partially simplified geometry leads to missing details such as the path of the superficial temporal artery and its branches, which could be recognized naturally as well on the inside of the skull. Nonetheless, GHMBC represents a state-of-the-art model and is able to overcome the difficultness in modelling and representing the human body as a biomechanical system. Respecting beside the complex geometry also the highly non-linear material behaviour is in the creation of these models one of the main challenges. Particularly for child models, as not only their head and body morphes in proportions significantly in their first years of life, but also the material properties of all the involved soft and hard tissues. Gathering crucial information about these aspects gets additionally more difficult, as the availability of post-mortem specimen or reliable data out of accidents is rare and – if theoretically available – always connected to ethical questions [75]. In a result, FEHM of especially young children are – compared in their amount to adult models – rare and follow even different approaches in their creation.

Beginning with the late 1990s, first published models of young children appeared in the literature, whereas Prange, Kiralyfalvi and Margulies presented in 1999 a quasi-3D model of a 2 week old child [76]. It included an Ogden material model for the brain and showed a rigid skull and falx cerebri. One year later, Margulies and Thibault presented a more detailed model of a slightly older child with approx. 1 month. There they introduced the

viscoelastic material behavior of the brain and the linear elastic material behavior of the skull and modelled beside bone also the sutures [77]. Later in 2007, Coats, Margulies and Ji published in their work the model of a 1.5-month old child, which was calculated in Abaqus explicit code. It was based on CT and MRI, showing idealized sutures as well the scalp [78]. In opposite to the beforehand presented models, in an aspect it included a form of validation, which was based on skull fractures related to the location and a prediction via ultimate stress. Within the last two decades increasingly complex models and older child models appeared, where especially the works of Desantis Klinich, Hulbert and Schneider in 2002 [79] and Roth et al. in 2007 and 2009 [80,81] have to be named, representing now child models with the age of 6 month and 3 years. Basing now predominantly on medical imaging data in their creation, having recourse on scaled adult anthropomorphic was eliminated, but the problem of validation was still not possible to be solved. Meyer et al. pointed in their work of developing a 3-year-old child head–neck finite element model and the try to derive a novel head injury criterion, that the continuing changes in the material properties may generate partially unknown initial data [67]. It underlines, that substitutional data needs to be gathered and the correlation with real-world cases might be a preliminary solution to state about a models capabilities to mimik nature.

A special form of models, which were able to be succesfully compared against real-world accident data are particularly full-body models. Untaroiu et al. presented a 6-year-old full-body model, which was based in its FE mesh on the GHBM 5th percentile female pedestrian model [82]. Even though it bases on the high detail level of the source models, it remains a scaled and manually morphed model, which might be not able to resemble the anthropomorphic specialties of children in detail.

Ito et al. showed with the THUMS Version 4 models CT-based full-body FE models for 3-, 6- and 10-years-old children [83]. In the implemented head and neck model (see Fig. 6) the instances of the cerebrum, cerebellum, brainstem, ventricles, corpus callosum, dura mater, subarachnoid, pia mater, scalp and skull were modelled. Moreover, also the CSF was included by filling the gap between brain and skull with solid elements.

Nonetheless, the overall complexity of full-body models and their prior usage as a virtual form of ATDs inherits several simplifications. This has to be seen mainly in the demand of calculability of the FE model, which means the balance of computational effort versus meaningfulnes of the results.

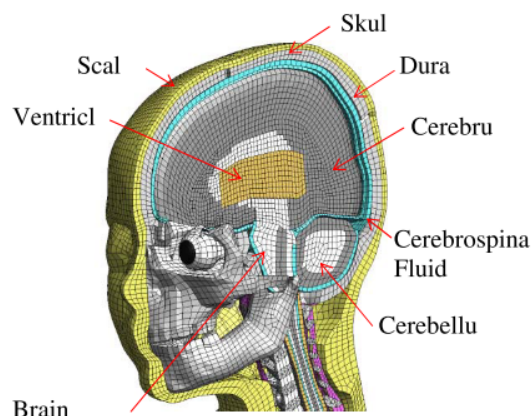


Fig. 6 THUMS Version 4 3YO head and neck model [83]

With their increased element size and a strong focus to the FE element quality, several details are naturally missed or oversimplified. An example in this concern is the complex structure of gyri and sulci of the cerebrum. In most of the models, the cerebrum is simply represented as a flattened ellipsoid. In the case of adult Finite Element Head Models, this significant motion-influencing detail was addressed by Fernandes in 2017, who consequently included gyri and sulci in the FEHB model called YEAHM [52].

An advanced approach of modelling the young head and brain can be seen in the PIPER model and the work of Giordano and Kleiven [84], [85]. The head model stands out with the aim to be scalable for the ages between 1.5 and 6 years. The authors state thereby in their work the validation against post-mortem drop and compression tests out of Loyd's collection of experiments. Generally, the lack of regional fitting, age-dependent and reliable data is one of the major contra arguments for a robust validation of child models [75,82], which might be only valid against the specific patient or post-mortem data. As already a gap in age and geometry exists, the common approach of validating a model against the post-mortem tests of Nahum [86] and Hardy [87] can be in best case only of supportive, descriptive nature. The lack of clear impact biomechanics data for children throughout the population makes it hence very difficult to define the accuracy or meaningfulness of these models regarding the material parameters, kinematics or the injury response itself [75]. The same authors proposed to concentrate with a comparison of simulative results on a huge number of real-world cases. In an important statement they motivated, that even non-validated models would be helpful to understand impact response by a correctly performed interpretation of the results [75].

2 Objectives of the thesis

Seeing the gap in the research and literature regarding bicycle-transported children, the scope and goal of the work within this doctoral dissertation are described.

The literature review gave an insight into the topic of children as passive traffic participants and the injury assessment, when it comes to related impacts. Thereby, it is beside the extremities particularly the head, which is in most cases affected in its integrity, potentially leading to TBI. It figured out, that related data is commonly available from emergency departments or hospital admissions, while the basing kinematics during and shortly after the impact, as well as injury mechanisms and biomechanics are partially undescribed. This is particularly the case for children seated in bicycle baby carriers. Thus, the topic remained in a sense as the recognition of the youngest group of traffic participants in this complex environment only.

Consequently, this doctoral dissertation is aiming at the following points:

1. An original description of the post-vehicle-impact kinematics of a child, which is seated in a bicycle baby carrier. The influence of the impacting vehicle's front-end design to the child's and bicycle's post-impact motion is furthermore an important aspect to be highlighted.
For this sake, numerical models have to be established accordingly.
2. In order to compare the numerical results to real-world data, experimental tests shall be carried out by using an ATD in a bicycle baby carrier.
3. As paediatric anthropomorphic cannot be feasibly gathered out of scaled adult numerical models, a paediatric Finite Element Head and Brain Model of a two-year-old will be established and presented.
4. The vulnerability of the child's head during impacts is stated. By proposing the implementation of an additional passive safety device to the baby carrier, particularly this issue shall be addressed. It is thereby envisaged, to overcome the

restriction to handle one major impact only, which is given to passive safety devices made out of EPS.

Hence, this doctoral dissertation is dedicated to a complex, which is formed out of the three parts of

- 1) Original description of the seated child kinematics and biomechanics during impacts,
- 2) Building a possibility to depict the biomechanics and mechanisms behind a head and brain injury and
- 3) Evaluating the possibility of seeing bicycle baby carriers as a passive safety device (PSD) or to extend them by an additional PSD.

These three parts are wrapping in their centre the hypothesis:

“The post-impact kinematics of a child model, which is seated in a bicycle baby carrier, is neither represented by pedestrian’s nor bicyclist’s kinematics.”

3 Original description of kinematics of children transported in bicycle-mounted baby carriers during impact situations

“The use of bicycle-mounted child seats allows young children and even toddlers to accompany adults on bicycle rides. [Miyamoto] has treated more than 100 children taken to emergency rooms in a hospital in Tokyo each year because of injuries related to bicycle-mounted child seats. Some young children presented with a comatose state because of acute epidural hematoma that required emergency operations.” [39]

The central point of interest in this chapter is the description of the baby carrier-seated children’s kinematics during impact situation, hence also in the assessment of its general situation within this period, which includes also the general safety situation. A first step is in this context the decomposition of the problem itself.

3.1 Methodology

The decision felt toward a 2-way approach, which consists on the first path out of the child seat modelling and its verification, while the second path rounds out with the complexity of bike modelling and consecutively with the appropriate set-up with the dummies, the coupling with the first paths’ child seat and the finally impacting vehicle. Fig. 7 illustrates this 2-way approach in a graphical abstract and describes all the single steps shortly.

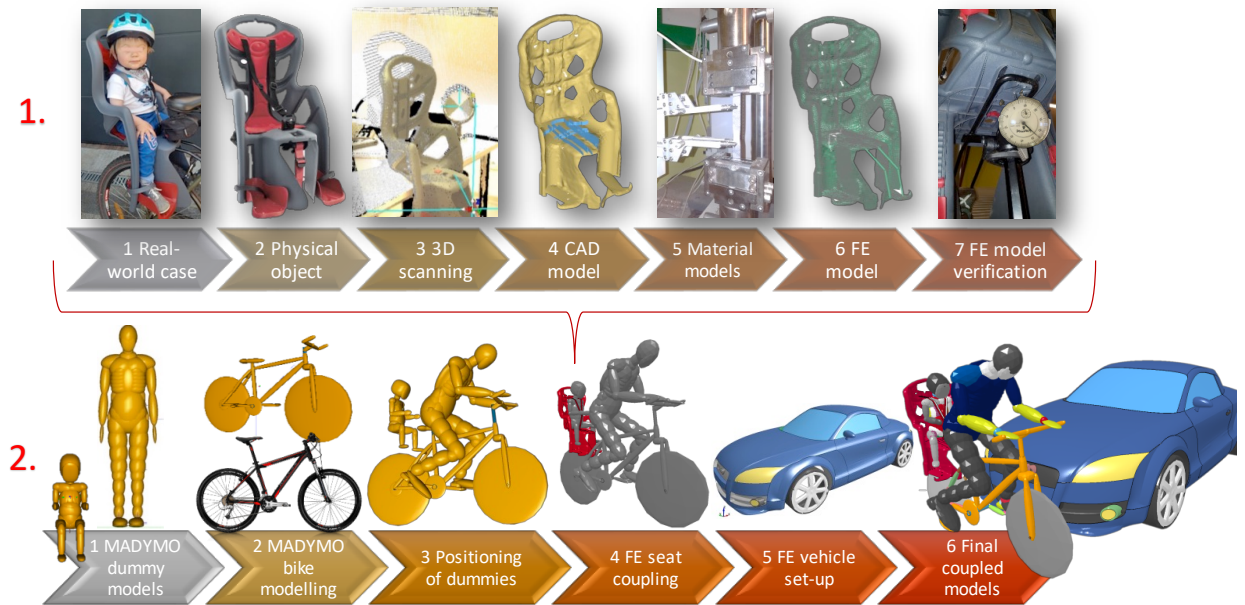


Fig. 7 A novel 2-way approach consisting of baby carrier modelling and verification (top row) as well as bicycle modelling, dummy and carrier positioning and vehicle setup (bottom row) in order to perform a bicycle-dummy-vehicle-coupling

Each step in Fig. 7 is described below.

- | | |
|---|---|
| 1.1 Considering a real-world case | 2.1 Choosing MADYMO dummy models |
| 1.2 The baby carrier as physical object | 2.2 MADYMO multibody (MB) bicycle modelling |
| 1.3 3D scan of the baby carrier | 2.3 Adjusting and positioning the dummies |
| 1.4 Creating a geometrical (CAD) model | 2.4 Coupling of FE baby carrier with MB bicycle and dummy models (inclusion of steps 1.1-1.7) |
| 1.5 Establishing a material model | 2.5 FE vehicle set-up |
| 1.6 Finite Element (FE) model | 2.6 Final coupling of bicycle and vehicle |
| 1.7 Experimental verification of the FE model | |

A deeper explanation for each of the points will be given within this chapter. A combination of single points was done in order to increase readability and consecutively understandability of a thematically complex, thus the above shown points have not to be in the same order or separated as shown in Fig. 7.

3.2 Representing the impacting vehicle as a FE-model

As exemplarily in [14,88] stated, the vehicle's front-end shape influences in a significant way the post-impact kinematics of an impacted pedestrian. Consequently, the shown approach should base on an average front-shape of a vehicle and present an according definition for the further research. On the other hand, since several years an increasing

number of Sport Utility Vehicles (SUV) or so-called cross-over cars can be recognized in nowadays traffic. This leads as well to changing front-end shapes, while impacts generally shall be registered more likely for older cars [16,42,89,90]. The terms of *newer* and *older* cars should not be taken literally, as a straight definition is missing and may vary due to subjectivity from publication to publication. An explanation might be found in the increasing number of on-board active assistance and accident prevention systems in vehicles.

A compromise was done in using the model of an Audi TT 2007, as the model was already validated within the reconstruction of a fatal pedestrian-vehicle-impact situation [91] and is also further described in [61]. For reasons of comparability, an example – and to the honest knowledge of the author – the only published and documented full-scale test including a baby carrier on a bicycle is given by the Federal Highway Research Institute (BASt, Germany) in [92]. In their experiments, a Volkswagen Golf V was used, which shows – at first on a visual level only – a comparable front-end geometry to the Audi TT. Zander et al. [29] used in their experiment in total five different bicycles and two different rear-mounted baby carriers. The combination was impacted by an angle of 90° to its side by the vehicle with an impact velocity of 40 km/h. The bicycle was standing in this moment, but was covered completely by the front-end of the impacting vehicle. It needs to be underlined, that the research is not intended to assess the performance or behavior of a specific vehicle or even to reconstruct a particular real-world case, so the choice of the vehicle needs to be seen as the choice of a generic vehicle model. The full-scale test out of literature will be helpful to be used as a comparison for the presented simulations.

To support the model choice and prove the comparability, in a first step a comparison of both front-ends on a geometrical level was done. For the description of a front-end shape commonly used are the Bonnet Leading Edge (BLE) and Lower Bumper Reference Line (LBRL) [6,93,94]. It should be noted, that the terms might be used partially mistakably through the literature, as both are measured initially at the longitudinal center plane of a vehicle, but are used finally not as a line but expressing the height of this line above the ground. Fig. 8 shows the virtually measured BLE and LBRL for both vehicles, the Golf and the TT. These measurements were based on 3D-scanned vehicles of the same type. The determined values were thereby comparable. The BLE differed by 17 mm and the LBRL by 19 mm. But to recapitulate, especially the height of the bonnet and the to this connected value of the BLE are mentioned to be significantly influencing the VRU post impact kinematics [88]. As the value for both vehicles differs by several mm, a

discrepancy between the gathered simulative results and the experimental test results from Zander et al. is expected. The motivation to use the author-owned model of a different but comparable in size vehicle model needs to be seen in the circumstance, that the model was already validated within the accident reconstruction [91].

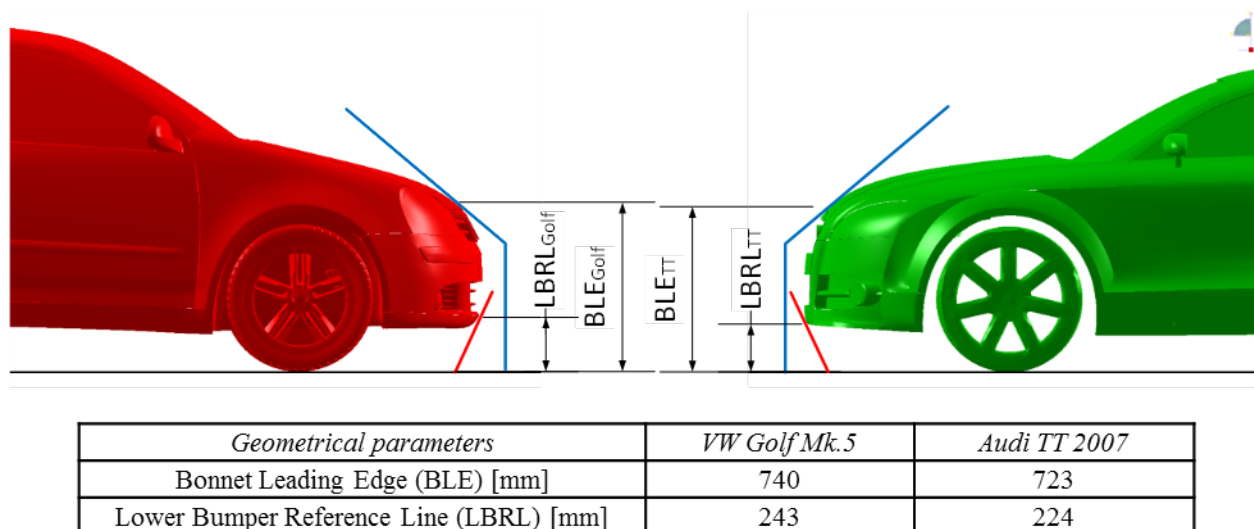


Fig. 8 Front-end main geometrical parameters of two compact vehicles: VW Golf Mk.5 – left, Audi TT 2007 – right.

3.3 Establishing a generic model of the baby carrier

Comparably to establishing a generic model of an impacting vehicle, also the baby carrier is not connected to a specific model in order to assess possible performance or quality properties of a specific, branded product. The motivation is to observe the post-impact kinematics of a child seated in a commonly used type of bicycle baby carrier. In this case, the choice fell on a rear-mounted bicycle baby carrier. It was recognized for the majority of these carriers within the European Union, that they are made out of polypropylene. The installation for this kind of carrier to the bicycle takes place by using a bracket, which embraces the seat post tube of the bicycle frame. The carrier itself includes a harness, which resembles a 3-point seat belt.

3.3.1 3D-scanning of the geometry

In a first step, the representative baby carrier was 3D-scanned by using a Leica ScanStation P20 with an 808 nm wavelength laser scanner unit. The process of scanning

is characterized of a rotating scanner head in the horizontal and vertical axis, which follows measurements in a spherical coordinate system after combining the two axis rotation results. Waveform Digitizing (WFD) realizes the interferometry by a processor, which is calculating the distance to the object for each of these measurements basing on the difference in time between the reference signal and the signal of the reflected laser. By these steps, a so-called cloud of points is created, which embodies the base for the next step, the recreation of the baby carrier's geometry for further proceedings and is shown in Fig. 9. Processing the cloud of points took place in the CATIA software, where it is possible to construct surfaces based on filtered clouds of points. At this moment, missing functional elements exemplarily such as ribs on the bottom side of the carrier – they were hidden during the process of scanning as it is an optical principle – were added to the geometrical model.

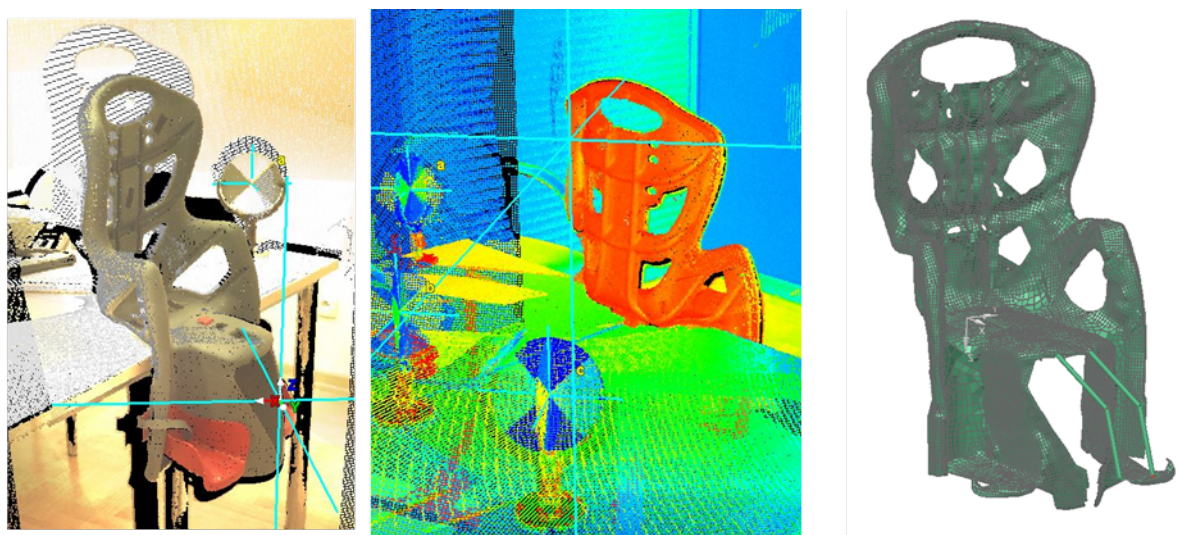


Fig. 9 Preliminary results of the 3D laser scanning process: mapping of images on the cloud of points (left), the reflectivity colour spectrum (middle) and the created mesh of the generic baby carrier model (right)

Fig. 9 shows as well the created, generic model of the bicycle baby carrier, which resulted after transferring the geometrical model to LS-DYNA and the consecutively meshing of it.

3.3.2 Material characterization

Labelled as PP05, the available baby carrier is mainly produced out of polypropylene (PP), not including an additional fibre reinforcement. Polypropylene can vary widely in

its material properties. Thus, it makes it reasonable to run own physical experiments by performing a tensile test. By this, it is possible to gain proper information about the used polypropylene used in this particular baby carrier. For this sake, numerous specimens were cut out from the leg guards, as the material in this area is straight and keeps a constant thickness.

All specimens were tested within a quasi-static tensile test with a velocity of 10 mm/min of the crosshead while the force was measured by a machine-build-in absolute force sensor and the overall displacement parallel by the travelling of the crosshead and a macro extensometer. In a result, the Young's modulus as well as maximum tensile force and maximum specimen elongation were gathered. The testing procedure and characteristically occurring necking of the specimen are shown in Fig. 10.

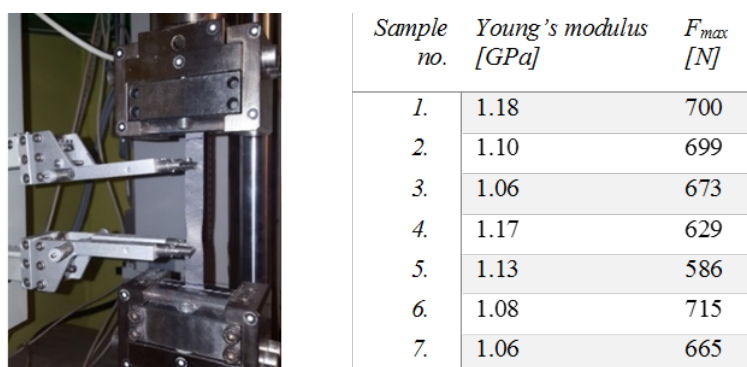


Fig. 10 Specimen while tensile test (left) with the outcome data

On average, the Young's modulus of 1.11 GPa was obtained in these experimental tests, which is covered by the range of values found in the literature, given by 0.89 – 1.55 GPa [95]. Consecutively, it was possible to fill the material keyword MAT_ELASTIC in LS-DYNA by the obtained value, as well by the Poisson's ration $\nu = 0.4$. Furthermore, the thickness for the corresponding shell elements was set to $t = 2.5$ mm to meet the measured thickness of the baby carrier material.

3.3.3 Modelling the harness of the baby carrier

Similar to the material characterization of the used PP, also gathering the harness material's force-extension curve straight from the manufacturer was not possible, so once more own experimental tensile tests were necessary and performed – including an initial technical review of the harness as a restrain device. The harness as a specimen was produced out of polyamide fibers. Comparing to a conventional seat belt system in a car, the harness used in a baby carrier is already out of the materials point of view a way

simpler representation of a restraint device and lacks technically exemplarily of belt roller and retractor as well. Also the easy weave of the polyamide fibers of the baby carrier harness itself will be able to be extended significantly by lower acting forces already, compared to a homologized seat belt for in-car usage. Consequently, the seated child may face increased harness slack in various situations, which might be also furthermore negatively affected by suboptimal clothing conditions given exemplarily by a thick and compressible winter jacket or the inappropriate sitting posture due to a situation of helmet- or head-to-backrest interaction. Hence it is necessary to bear in mind a natural slack between the harness and the torso of the seated child. A support of this statement may be seen in the DIN EN 14344 [37] describing a roll-over test, in which 30 mm spacers are applied to the shoulders of the artificial dummy during the seating process, before any of this described slack has to be eliminated by removing the spacers and tightening the harness. But in case, that repositioning of the dummy during the three times forward and backward rotation with a rotation velocity of 4 ± 0.5 RPM gets necessary – which might be caused by the harness elongation as well – a relocation of the artificial child substitution but without altering the restraint device is allowed. Beside this, it needs to be recapitulated, that the baby carrier is made of significantly deformable PP and regarding its geometry shows up only with a limited moment of inertia regarding possible acting side forces. Consequently, a focus was set in the numerical approach to reduce the initial slack to a value below 5 mm, which was measured between harness and torso. The quad SHELL elements were used within the discrete model to represent the harness by including general creation and belt routing methods from the literature [96], taking finally recourse on an elastic material model with the Young's modulus $E = 607.5$ MPa, which was revealed in the own experiments.

3.4 Representing the bicycle as a multibody model in MADYMO

Recognizing a 26-inch mountain bike (MTB) as a popularly used bicycle type for the combination with a baby carrier in the author's area, the creation of an appropriate model able to be calculated in a timely manner by achieving reasonable results at the same time was a point of interest. Moreover, a study named this bicycle as an average type for this consideration [97] and fits also the general advices for the necessary seat post tube diameter to properly mount the baby carrier as well as the rim-tyre-combination in order

to handle side forces while riding. As a significant deformation of the bicycle was not expected – see in this context [29] – the decision was done to represent the bicycle, unlike the baby carrier, in the MADYMO code. On the one hand, using multibodies (MB) as visually rigid ellipsoids simplifies the geometry but includes crucial information as inertia, mass and material properties such as the Young's modulus and characteristic contact definition [14,88], which enables finally gaining a reasonable ratio of calculation time versus feasible simulation results.

The particular effort was necessary to rebuild the chosen type of bicycle with the geometry in the MADYMO code by including also a front suspension as a common feature for the used type of bicycle as well as a representation of this real world bicycle's general moments of inertia [98]. Exemplarily for the frame, several rigid bodies computed as aluminum alloy tubes with the appropriate moments of inertia were connected by bracket joints, while the front fork and the pedals were attached by revolute joints.

3.5 Simulation of FE-code in LS-DYNA coupled with MADYMO multibodies and dummies

As described, parts of the full model setup are belonging to different numerical codes, in this case LS-DYNA for handling FE-code, respectively MADYMO for MB-code. As both codes are offering particular advantages, the combination of both codes via an interface during the simulation enables to have a recourse on benefits, which were not available in a stand-alone approach. The base idea is thereby to exchange data between the codes during the simulation as an iterated input for the primary and the secondary code respectively. The so-called coupling, here as the code linkage of LS-DYNA with MADYMO, is especially in this constellation common practice to solve simulative problems in the area of crash analyses, particularly under consideration of involved VRUs. As a main argument for using the MADYMO code the significant decrease of calculation time for a simulation is given, as geometries are represented in a noticeably reduced complexity. This term is applicable as well for the human body models, so-called dummy models or the virtual equivalent to an Anthropomorphic Test Dummy (ATD). Regardless to their visual first impression, the approach of taking recourse on MADYMO dummies for crash kinematic observation and assessment is due to the high bio-fidelity of the dummies and good correlation of numerical results to real-world measurements common practice for decades. The Hybrid III-dummy in the 50th percentile male version

is the commonly implemented MADYMO dummy in the area of automotive restraint and (passive) safety device evaluation [91] and used also for the here presented simulation. In case of the seated child the dummy of a one-and-a-half-year-old out of the MADYMO version 7.5 is implemented [96].

Consecutively, all the connections and links between the different code parts and instances were realized. This concerns the interaction between MB–instances and –parts of the bicycle and the dummies versus the FE–instances and parts of the impacting vehicle, the baby carrier and the harness, which were installed by a COUPLING and the sub-elements of CONTACTs and RESTRAINTs.

3.6 Definition of impact situations as simulation configurations

Hitting a cyclist's side by a forward driving vehicle is supposed to be the most common impact configuration between these two groups of mean of transport [42] for the case of their unintended physical confrontation. Nonetheless, there is a great diversity when it comes to the conflict situation in terms of bicyclist characteristics and possible injury mechanisms [42]. Also the great diversity of involved degrees of freedom leads to a highly complex situation [17], which demands a huge number of countermeasures or alternatively the preselection of restricted – in the experiment varied – parameters under the premise of an unaltered base setup. In this meaning, the main emphasis in the herein shown simulations and their outcome shall be on this premise, as well. It is intended to vary the bicycles offset to the longitudinal center plane of the car, their initial velocities and the initial impact angle. Beside this, also several configurations are intended to illustrate a failed passing maneuver. All simulations shall be calculated for 350 ms, as for the time range of 100 to 200 ms after the initial contact between both transport types a head impact of an adult cyclist in such an impact situation is expected generally [18]. Regardless of the presence of a head impact to the vehicle, a head impact to the ground is possible for all cases but it is not the center of interest in this approach.

Fig. 11 shows the initial setup for one of the simulated impact scenarios. Also the variables and regarded directions of movement are described in this figure, namely by the offset distance d between the bike transition plane, which is perpendicular located to the ground crossing the bicycles bottom bracket and the vehicle's longitudinal symmetry plane. Furthermore, the impact angle α is marked.

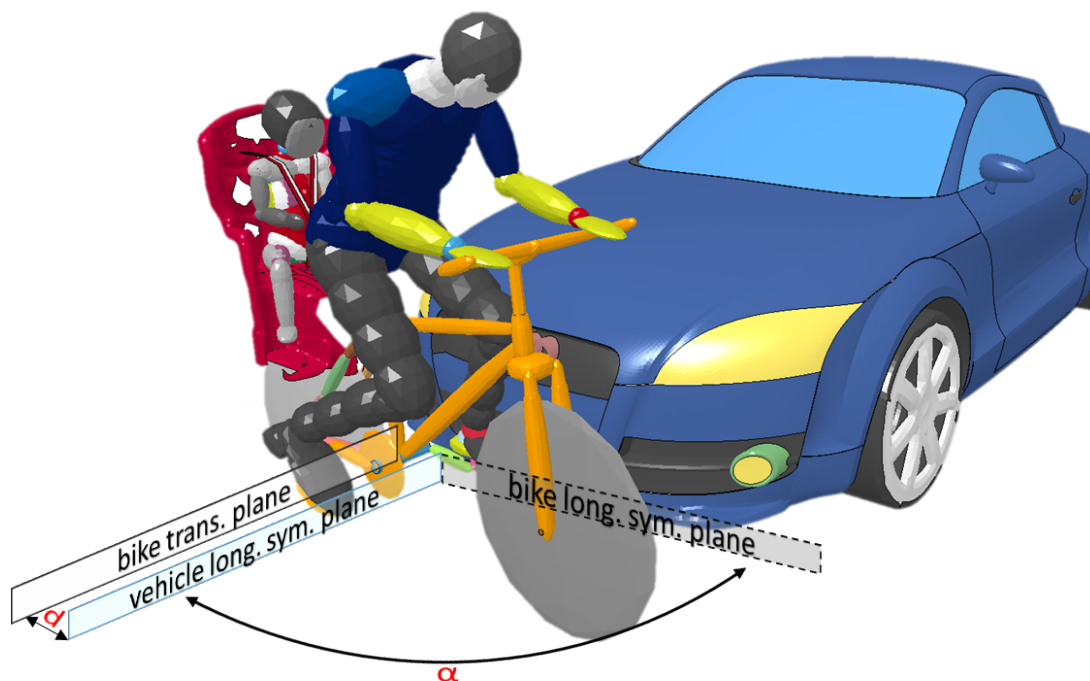


Fig. 11 Visualization of setup of impact angle α and offset distance “d”

As shown in Fig. 11, an 0° impact angle follows a rear-end-impact, which mimics a failed passing maneuver, while 90° impact angle covers the most common impact situation to the bicycle’s side by a forward driving car. By the author’s definition and as an illustrative example given in Fig. 11, a negative value for the offset distance d describes a location of the bicycle tending toward the right side of the vehicle in terms of its forward driving direction. The velocities v_0 and v_1 are defining the forward movement of the vehicle or the bicycle respectively. They are covering 0, 10 and 15 km/h for the bicycle, and 20, 30 and 40 km/h for the vehicle. The overall chosen combinations of values for the mentioned variables are listed for each configuration in Table 1 below.

Table 1 Simulation setup for each configuration

#	First impacted area of the bicycle	Impact angle α [°]	Offset distance d [mm]	Initial velocity	
				Audi TT v_0 [km·h ⁻¹]	Bicycle v_1 [km·h ⁻¹]
1	rear wheel; baby carrier	30	-275	30	15
2	rear wheel; baby carrier	90	589	30	0
3	adult, centered to car	90	-210	30	10
4	adult, centered to car	90	-210	40	0

5	adult, centered to car	90	-210	40	10
6	front wheel	90	-810	30	0
7	direct rear impact	0	0	20	0
8	taking over, urban velocity	0	-700	30	0
9	baby centered to the car	90	390	30	15
10	baby centered to the car	90	590	30	0
11	adult, centered to car	90	-221	20	0
12	direct rear impact	0	-700	40	0

3.7 Discussion of the obtained results

With a clear focus on occurring head impacts to the front structure of the vehicle, it needs to be pointed out, that in a few cases neither a head impact to the bonnet nor to the windshield occurred. Consequently, in most of the cases it is a plural of head impact for the VRU of a bicyclist in the simulated constellations, that one should be aware of. This leads as well to another point of view for the discussion of the obtained results. Under the assumption, that common passive safety devices such as bicycle helmets etc. could be involved generally, it has to be noted, that most of these devices are relying on Expanded Polystyrene (EPS) as material for the shock absorption layer. EPS is thereby considered to handle the occurring impact energy by self-destruction and is consequently subjected to a single major impact only. Thus, a helmet as a passive safety device might lose its ability to protect the user after this first major impact and increases thereby the importance of the observation and assessment of this event [49,99]. Fig. 12 shows for the simulated cases the recognized head impact position; in yellow color for the transported child, in black color for the bicycle-riding adult. The number corresponds thereby to the configuration given in Table 1. In the Fig. 12 there are the marking lines for the Wrap Around Distance (WAD) of 1300, 1800 and 2100 mm.

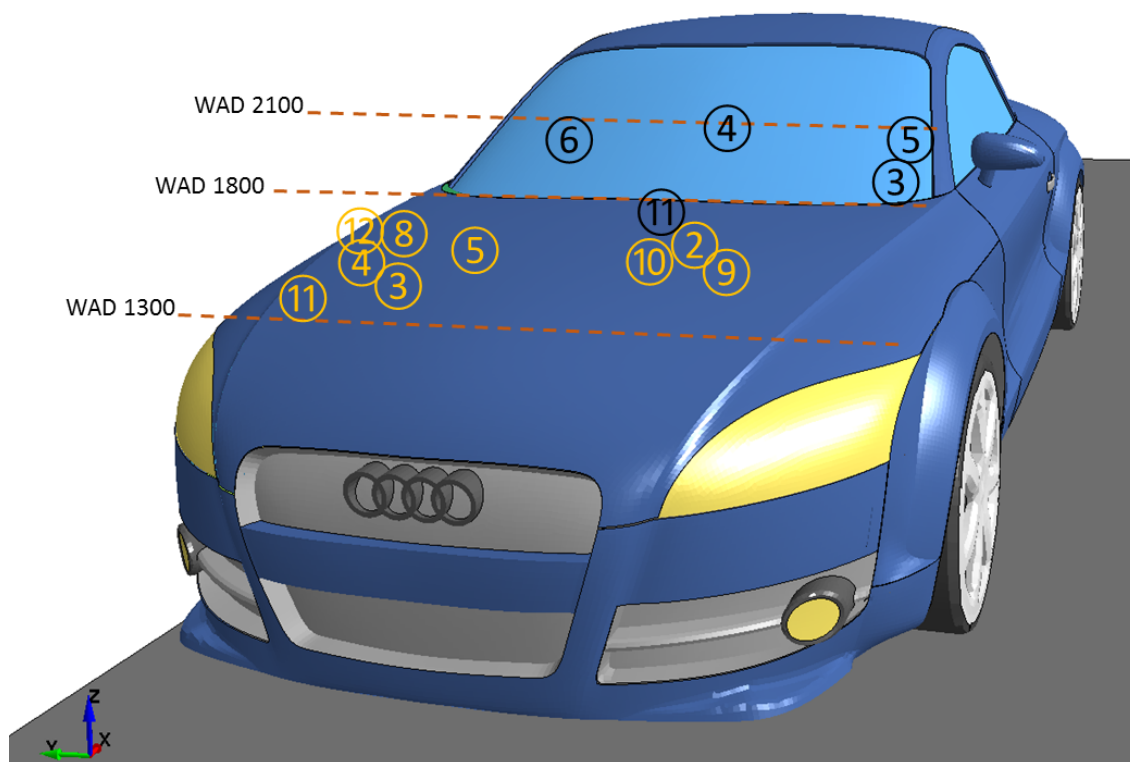


Fig. 12 The marked head impact locations for the adult (black colour) and the child (yellow colour) with the Wrap Around Distance (WAD) marking lines

A comparison of the simulative results with the full-scale test results out of the literature from Zander et al. [92] can be realized in terms of the recognized head impact position and the consecutively measured WAD. In their work they concluded, that the WAD of 2100 mm was not adequate as a rearward limitation for an adult, as they revealed higher values in their experiments. The herein shown simulations covers with configuration No. 4 a comparable setup respecting the differences in the used bicycle type and initial overall height of the adult dummy exemplarily. Thereby, a WAD of 2200 mm was revealed in the simulation and supports the statement out of the literature. Regarding the transported child, the literature concluded the sufficiency of a WAD of 1700 mm as a rearward limitation as it covered all their recognized head impacts, which were mostly valued around 1500 mm. In the numerical approach a maximum value of approx. 1600 mm was recognized for the configuration No. 2 and is in line with the findings of Zander et al. It could be firstly summarized, that in case of a direct cranial impact to the vehicle the child impacts with the head always to the bonnet, while with exception of one case, all adult head impacts were reported to the windshield, in a timely point of view always later than the child's head impacted. In this one exceptional case in configuration No. 11, the adult's head hit the rear-edge of the bonnet where regularly installations such as wipers can be

found, as well. Overall, the so far gathered kinematical results subjectively correlated with the results out of the literature, even though the used bicycle differed in terms of geometry, e.g. seat height. The difference in seat height is recognizable within the full-scale test itself, but also compared to the numerical approach [92]. But especially the different seating posture within the numerical approach led to a difference in the overall-measured height of the seated dummy on the bicycles. The full-scale test showed an averaged overall height of the adult dummy of 177.6 cm, while the value measured for the simulation was only 153.0 cm, even though in both cases the 50th percentile male dummy was the adult rider. The transported child was measured in the overall height within the experimental tests by around 134.6 cm and 130 cm in the simulation. Furthermore, it has to be pointed on the difference in the used dummies: the simulation took recourse on the Q1.5 – a dummy with a mass of 11 kg instead the 3-year-old dummy with 15 kg, which was used in the experiments [100], [101].

Referring to the general kinematics of adult and child during the impact, both behave significant different. With a specific limitation, the child is driven by bicycle and baby carrier, moves rather as a part of this combination due to the belted situation. Especially when the bicycle is lifted or even just dragged to its side by the impacting vehicle, a head impact of the child to the frontal geometry is very likely to occur.

To have a short thematic excursion, the post-impact motion and kinematics of a bicyclist are commonly compared to the kinematics of pedestrians [24,102]. Concerning the outcome, which is often seen in the measured WAD, these two groups of VRUs differ in a more rearward location for the head impact of a bicyclist [92] provoked by a higher initial body position due to being high-seated on the bicycle [103]. A restriction to this might be seen in the requirement of the absence of special bicycle equipment as click-in pedals for sport bicycles, which could prevent the bicyclist from loosening freely from the bicycle during an impact. Nonetheless, the kinematics is comparable to the pedestrian kinematics, at least for adults. In opposite to this, the height ratio of a smaller children sitting on a likewise much smaller bicycle against a regular vehicle front-end geometry is leading to deviations from this assumption. Moreover, details about child kinematic in post-crash situation is still rare in literature or partially not available [10].

The beforehand mentioned limitation of this behavior is visualized in Fig. 13 by pointing on the slipping harness during the impact.

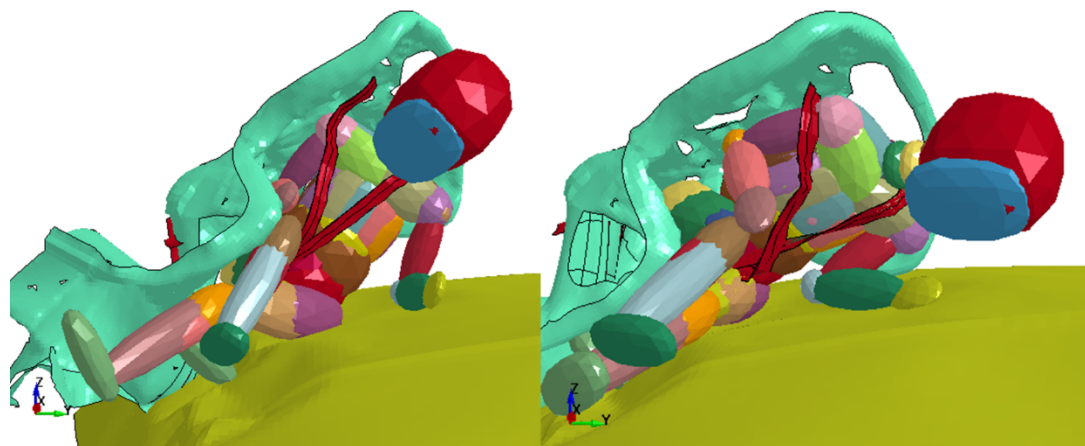


Fig. 13 Slipping of the right shoulder under the harness in the configuration #9 at 90 ms and 125 ms after the initial impact

While inertia forces the child to hang into the left side of the harness, the right shoulder slips under the harness. This underlines the initially stated raises questions about the secured seating situation regarding the slack during the impact scenario in this 3-point-version. The general advices given by manufacturer or bicycle clubs agree here to the simulative outcome. Improper clothing situations like thick, compressible winter jackets or improper seating situation with slack might influence the safety situation negatively. It may be able to induce a lower effectivity of the restraint system, in this context even higher connected injury probabilities [37]. In a result – even though a baby carrier is not defined as a passive safety device – the ability to drive and direct the child within the baby carrier geometry is limited, as torso and head of the child are able to escape the general geometry of the baby carrier, which is not constructed as a protective cage. Fig. 14 illustrates this behavior. In several simulations, it was clearly visible, that exemplarily an interaction of the babies' arms preceded the head impact at the same position and cushioned the impact. At the same time, it needs to be stated, that a muscle contraction was not considered in the numerical model. Generally, the forthcoming impact could be leading in a real-world case to an avoidance motion of the bicyclist, intended or by reflex, in order to avoid or lower the severity of the collision. As it could change the kinematical outcome [104] by changing body orientation, stiffness, and new occurring moments, none of these effects or circumstances are implemented in this setup in order to keep the changing variables low. This is also operative for the pre-impact driving behavior or even phenomena of slides, initiated turns or fidgeting child in the carrier, which is neglected at this point by a bicycle without applied initial velocity but loaded by gravity only.

In opposite to the observations regarding the child, the adult was able to loosen from the bicycle. The motion can be described thereby less driven or restricted. Nonetheless, this led not straight to a rotation which caused more occipital-directed or face-first impacts of the adult, the body simply stretched more from the impacted hip – mostly located on the front-end of the bonnet. The stretching of the body forced the adult's body rather to adapt to the front-end of the vehicle, until the head impacted the windshield. This behavior is shown as configuration 4 (compare Table 1) in Fig. 14, which corresponds the most with the full-scale experiments out of the literature.

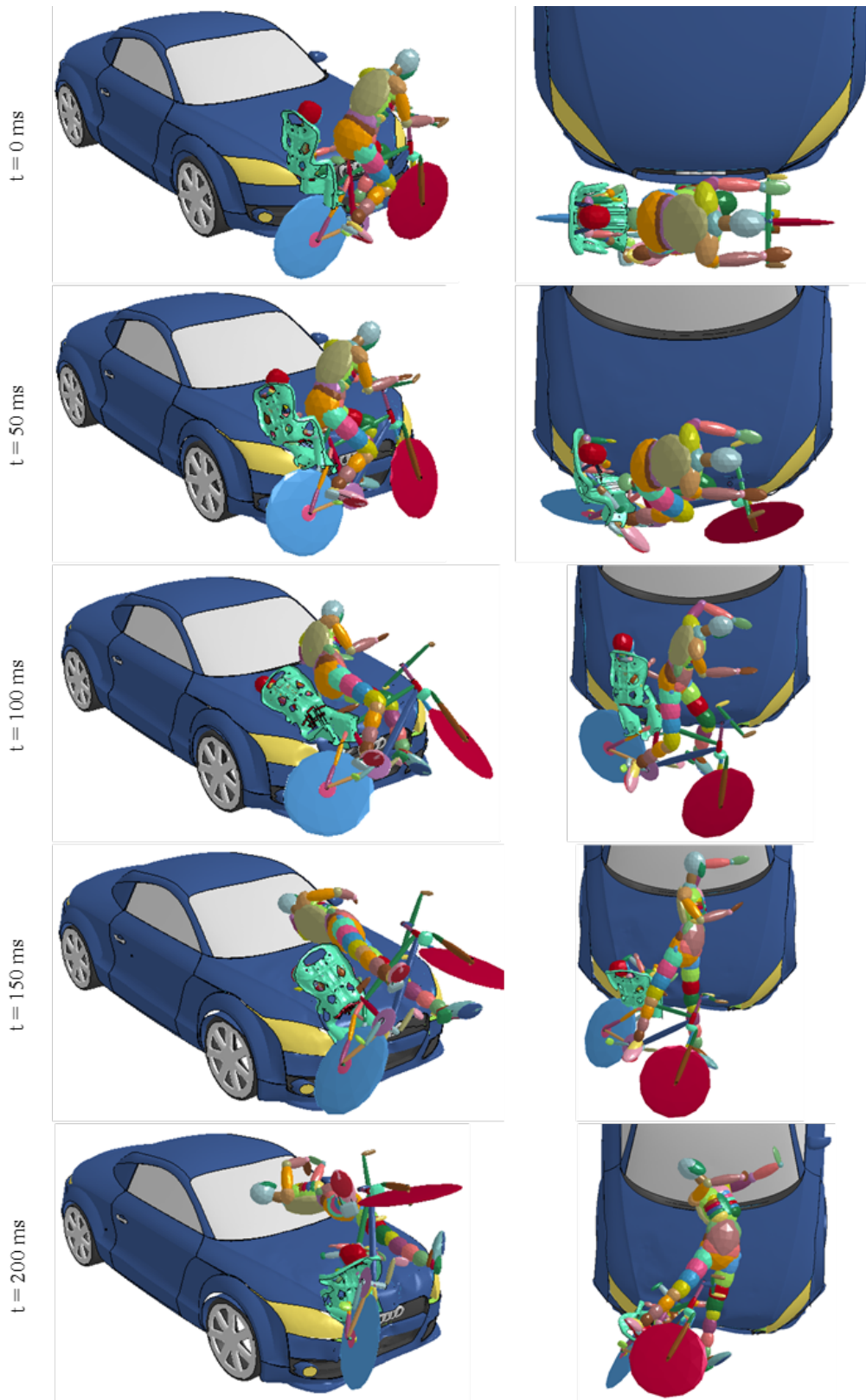


Fig. 14 Configuration No. 4 visualized in intervals of 50 ms

The adult kinematics are comparable to the bicyclist kinematics described in the literature, which is described as behaving similar to an impacted pedestrian but with higher rearward limitation in terms of the WAD [14,29]. The child behaves here different. Also after the initial impact, the child is belted to the combination of bicycle and baby carrier and forms with them a complex in terms of their post-impact motion. The latter can be described by an initial drag of the bicycle in the driving direction on the vehicle. In this moment, the whole bicycle is lifted slightly, so a contact of the tires to the ground disappears. Generally, the bicycle then rotates to its left side and supports finally by this motion the child's head impact to the bonnet. The first contact of the vehicle to the bicycle is rather low located around the height of the bicycle pedals, while the rotation center and center of mass are influenced by the presence of the child with its mass and high seating position, leading in the end to this motion. A significant and over the first milliseconds increasing deformation of the discrete representation of the baby carrier mounting will be visible over the full simulation. The overall airborne situation of the bicycle with the mounted baby carrier and the seated child makes a second major impact of the child to the ground possible.

With a special interest in the first 70 ms, the movement of the seated child shall be highlighted, as it showed in all simulated cases of a side impact where the impact angle α was measured by 90° a characteristic behavior. In this context, Fig. 14 gives by the times of $t = 0$ and $t = 50$ ms after the initial impact the crucial visualizations. The first contact of the vehicle to the bicycle leads to a shift or projection of the bicycle to its right side. Connected to this, the child rather remains due to inertia in its position and bounces with its left hip into the baby carrier. It can be recognized, that the 3-point-harness is only barely able to handle lateral forces [105]. Further, the baby carrier tilts for several degrees toward the vehicle, as it is also shown in Fig. 14 for the time of $t = 50$ ms. It might be supportive for this behavior, that the center of mass is shifted due to the new position of the child aside the bicycle's longitudinal symmetry plane and the child tends to lean toward the vehicle. The tilt of the baby carrier indicated thereby always the direction of the impacting vehicle and was as well visible and stated by Zander et al. in [29]. Following to this first hip impact and leaning of the child, another hip impact but to the opposite side of the baby carrier could be recognized, interestingly the tilt of the baby carrier remained in its direction. It was possible to lift and flip the bicycle over the bonnet for this impact constellation, which related mainly to the vehicles front-end geometry, the chosen velocities and the impacted bicycle with mounted baby carrier. As this was in the majority

of cases able to provoke a head impact of the child to the bonnet, the possibility of a second head impact to the ground remains. The bicycle does not have to remain in this situation on the bonnet. The drop from the bonnet still inherits a dropping height with a consequently given vertical impact velocity, which might be in the range of a regular bicycle fall incident. Consequently, it could lead to severe – additional – injuries as well. Although head and body impacts were observed, these have been recognized partially as arm-or leg-cushioned impacts, which changed in the intensity of involvement. The literature points for this phenomenon on different sources, beside muscle contraction – which is not considered here in this set of simulations – especially on the initial leg position and its influence to the kinematical outcome [104]. For a cyclist, the leg position might be connected to the initial position of the bicycle pedals, as well. To reduce this effect in this set of simulations, the initial posture of both dummies was kept equal. Nonetheless, it can be noted, that the full-scale test showed five different bicycles with differing frame geometry and rim diameters and two different baby carrier models [92]. In a consequence, the posture and the overall measured height of the seated dummies was not kept equal, leading as well to a differing leg and foot positioning. Within the numerical approach, only a shift of the bicycle in relation to the longitudinal symmetry plane of the vehicle was performed. The range for d as the earlier described offset distance is thereby within -850 to +850 mm – according to literature the most common impact range [29] – and intended to compare the kinematics outcome and WAD at least qualitatively; despite all slight discrepancies in the postures. Even though this shift induces also a change in the leg position, as the situation changes relatively by time due to the naturally uneven and rather curved front-end geometry of cars and their bumpers. One measurement point for the offset distance d was defined as the rotation axis of the bicycles bottom bracket, which is seen as a central point of a bicycle. Earlier in the result discussion, a focus was on the center of gravity (CoG) change aside the bicycle during the impact. The shift of the bicycle in terms of the offset distance d revealed also the child and baby carrier influence to the center of mass of the whole bicycle along its longitudinal plane [106]. In total three simulative cases there was no head impact of the child to the front-end geometry, as the bicycle was dragged to the side and rotated due to the side impact rather around a pivot closer located to the position of the baby carrier. Generally, and for all cases: it could be observed, that the rear part of the bicycle with the mounted baby carrier stayed closer to the impacting vehicle than its front side with the fork and steering bar. Consequently, even if the range of d between -850 and +850 mm might be a

common constellation for single bicyclists to interact with their head with the bonnet or windshield, the same range cannot be considered for the seated child due to its more rearward position on the bicycle and the changed center of mass. It might be rather seen as an indicator for the existence of a critical line, for which – depending on the driving direction of the bicycle – a drag of the bicycle to the vehicles side or a projection of the bicycle in driving direction of the vehicle could be assumed. Nevertheless, the child's head interacted with the frontal part of the bonnet in terms of a clear head impact each time the bicycle was projected or pushed in driving direction of the vehicle. This leads to a variation of the assumption, that the bicyclists pedal, leg and foot position influence the kinematical outcome, but also the changed moment of inertia of the bicycle due to presence of the baby carrier and child. Thus – compared to a single bicycle rider and to a pedestrian – the post-impact kinematics of a child seated in a bicycle baby carrier differs. This is clearly visible, when the adult rider loosens during the impact from the bicycle and bends over the front-end geometry of the vehicle.

In another aspect, the introduction of an initial bicycle velocity in forward driving direction reveals the influence to the head impact zone in the cases, where beforehand a head impact was recognized. This refers especially to the configurations 3,4 and 5 from Table 1 and the revealed head impact locations visualized in Fig. 12. Moderate velocity of 10 km/h applied only to the bicycle lead to a head impact of the adult significant closer to the A-pillar, while the position for the child did not change in the same amount.

Even though an initial velocity was not considered in the full-scale test in the literature, an influence to the impact position and general kinematical outcome has been proven by the numerical approach. It extends the so far described list out of initial posture or leg position and position of the baby carrier before the initial vehicle contact. Nonetheless, the observation results have to be understood qualitatively, as the dataset is too small for stating a clear quantitatively influence or revealing the critical line for the side drag vs. projection phenomenon. Therefore, additional simulation setups including a variety of differing vehicles and their detailed front-end geometries would be necessary in future.

As the last paragraph concentrated on the presence of head impacts, generally the following paragraphs concentrate on the measurements of the recognized head impacts. Table 2 shows the adult's head velocity in the moment of impact and the involved head region.

Table 2 Velocity of the adult's head before the head impact and the affected head region

Configuration	Head impact velocity (resultant) [m·s⁻¹]	Impacted head region
1	-	No head impact
2	-	No head impact
3	5.02	Temporal, parietal
4	9.35	Temporal, occipital
5	7.50	Temporal, parietal
6	2.82	Temporal, parietal
7	1.70	Frontal to handlebar
8	2.00	Temporal to steering bar
9	7.93	Temporal, parietal to tarmac
10	-	No head impact
11	3.25	Temporal, Parietal
12	3.03	Parietal to steering bar

It was necessary to forgo the calculation of the HIC(36) for the adult, as the impact was recognized mainly to the windshield. The impact to the windshield's material is in the current representation not preferable to assess the values doubtless, as the material model for this part already is not able to be validated against the real model of a laminated safety glass, which is commonly used in vehicles nowadays [107]. Oppositely to this, the child did not impact to the windshield, but to the validated front-end of the vehicle. Its calculated HIC(36) for the configurations varies and shows the diversity of head impact conditions due to the changed parameters of offset distance d , impact angle α and initial velocities v_0 and v_1 . By recapitulating the formula of HIC, the value is dependent on the resultant linear acceleration. A direct connection needs to be seen consequently in the stiffness of the contenders in the contact pairing. A HIC-lowering circumstance was observed, when exemplarily the arm of the child cushioned the impact of the head to the bonnet. The high HIC(36) values were calculated especially for the rear-impact scenarios with α less than 90° . The overall gathered head velocities for the child in the moment of the impact as well as the calculated HIC(36) for all configurations are given in Table 3.

Table 3 Calculated HIC(36) and impacted head region for Q1.5-dummy model

Configuration	Child's head velocity at bonnet impact		HIC(36) for child	Affected child's head region at impact
	Resultant [m·s ⁻¹]	Component in -Z [m·s ⁻¹]		
1	-	-	125.1	Occipital to carrier's backrest
2	7.4	5.1	146.5	Frontal, parietal to bonnet
3	12.5	3.8	369.3	Frontal to bonnet
4	15.7	5.2	1699.0	Frontal, parietal to bonnet
5	17.3	3.6	1433.7	Frontal to bonnet
6	-	-	120.8	No direct cranial impact observed
7	-	-	1808.3	Occipital to carrier's backrest and frontal to adult; <i>HIC(36)-value observed during children frontal head impact to the adult's body</i>
8	6.7	1.1	311.1	Occipital to carrier's backrest and bonnet
9	11.2	4.2	401.6	Frontal, parietal to bonnet
10	7.1	4.5	123.9	Frontal, parietal to bonnet
11	5.5	1.9	77.6	Frontal to bonnet
12	6.1	5.8	3943.9	Occipital to carrier's backrest and parietal to bonnet; <i>HIC(36)-value observed during children frontal head impact to the bicycle frame</i>

The amount of recognized head impacts shows already, that the baby carrier was not able to prevent by its geometry the child from an impact. It remains as a seat defining in a limited intensity the position of the child on the bicycle, but acts not as a passive safety device. The backrest was neither present as a side pad nor able to act as a spacer by its stiffness. Furthermore, the 3-point-harness is only rudimentary able to handle lateral forces, which would keep the seated child straight in its initial, optimal seating position. A partial slipping with one shoulder under the harness was also recognized and it increases even the child movability. For the rear-end impact cases the backrest was identified acting as a hazardous wall in terms of the child's back head. Cumulating to this, the general hazard of occurring diffuse injuries, common for whiplash- or whiplash-similar crash scenarios is necessary to be bear in mind [108].

Beside the Head Injury Criterion and similar oriented injury assessment tools, a wide variety of literature is setting a focus to possible neck injuries. Commonly, these are based on sled-tests and the results from whiplash-effects. An adequate and widely accepted criterion specialized on bicyclists or motorcyclists is missing so far. The background can be seen in the much complex motion of the bicyclists head and torso during an impact. The simulations revealed even excessive lateral bending of the neck as well as rotation of the head to torso. Hence, taking recourse on NIC is vague, as it does not consider this combination of movement in its components for calculation. Nonetheless, the occurring torques in their components and the comparison to thresholds out of literature can be an indicator for the intensity of the situation for the neck. Combining this outcome with the behavior of the baby carrier as a restraint device in the specific configurations shall enable researchers to conclude a statement about the injury probability by using a baby carrier. Table 4 helps to read the calculated values of the maximum resultant torque acting in the neck of an adult and child during the specific configurations. The information about the child's neck is extended by the value for flexion and extension.

Table 4 Maximum torque in adult's and child's neck as the resultant constraint torque [Nm] in relation to the configuration number.

Configuration	Torque [Nm]				
	Adult's neck		Child's neck		
	Lower neck, max. resultant	Upper neck, max. resultant	Max. resultant	Max. flexion	Max. extension
1	27.31	27.31	29.02	19.18	28.64
2	110.54	27.91	19.60	11.68	10.69
3	154.51	145.77	22.50	15.89	16.64
4	160.84	128.36	38.46	28.41	20.54
5	214.45	93.23	93.82	35.91	48.07
6	176.99	92.12	11.01	6.12	5.55
7	223.61	170.79	70.52	69.53	24.22
8	667.87	250.86	47.13	28.67	40.16
9	57.61	12.61	20.16	18.21	13.17
10	114.50	28.21	23.90	13.86	9.89
11	84.04	37.23	16.04	14.73	7.88
12	492.20	389.87	46.11	28.24	30.48

Generally, it is controversially discussed if adult thresholds can be transferred directly to the child thresholds. Hence, the literature gives only a range of values. Exemplarily for the pure flexion torque of a 12-month-old to 3-year-old child a low probability of serious injury might be given by 25 to 45 Nm, respectively 8 to 13 Nm for extension torque as estimated neck protection reference value [63]. It was consequently decided to calculate the torques as maximum resultant value, respectively the same for flexion and extension separately, in order to serve with an estimation only, which bases as a pure comparison in components only. The background needs to be seen in the circumstance, that the values as reference values would underlie the insufficiency of biomechanical data, and are limited in their applicability [63]. This makes the calculation of NIC or one of its modifications unreasonable.

The configuration 12, which is shown in Fig. 15, depicts another restriction, During the rear-end crash as a simulated, i.e. failed passing maneuver, the neck of the child bends at $t = 120$ ms after the initial impact over the backrest of the baby carrier.

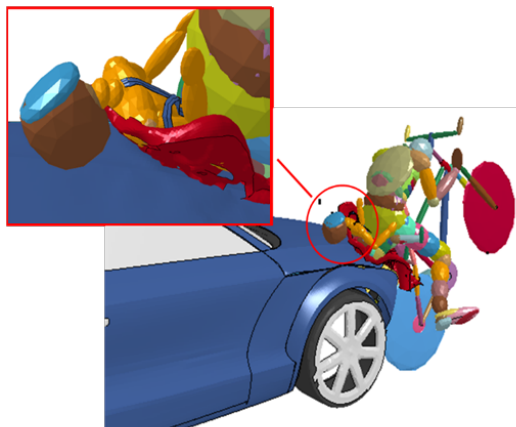


Fig. 15 Overstretching the child's neck, by the carrier device, combined with a direct cranial impact in configuration #12 at $t = 120$ ms after impact.

The situation points again on the improper belting situation of the child, which could lead to escape the baby from the carrier. In the shown case of configuration 12, the excessive bending of the neck over the backrest, after being lifted into the stretching harness, enables the child to impact directly with the head to the bonnet in the occipital and parietal head region. The extension torque on the neck was calculated as approx. 30 Nm. The value exceeds the previously given reference value for a low risk of severe neck injury. Fig. 11 illustrates the acceleration of the child's head CoG and the occurring torque pointing out flexion and extension movement. Beside this, the case presents an argument for the inevitability of a properly fitted harness. Another point of view might be the implementation of additional restricting geometries and paddings, as they are common practice in child seats and restraint devices for in-car usage.

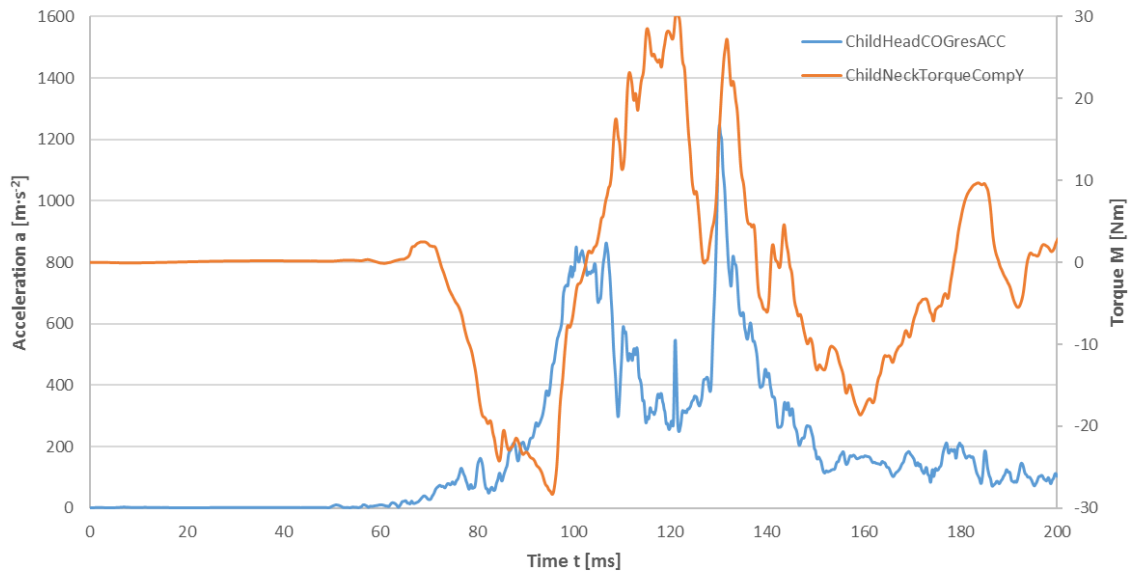


Fig. 16 Graphs of resultant acceleration a in CoG of child's head (blue graph) and torque M around child's neck Y-axis (orange graph) in configuration 12

Summarizing, the discussion is pointed again on the possibility of multi-impacts of both riders' heads during a bicycle crash, which might potentially induce diffuse injuries

The topic of the rear-end crash as a failed passing manoeuvre was also picked as a central theme by the Allgemeiner Deutscher Automobilclub (ADAC) in a full-scale test [109]. The test is considered as a customer test on the transportability of children on or by bicycles in the different available carrier types. An older vehicle was involved in the crash. Nevertheless, the full-scale test inspired the alternation of the presented simulations to a similar setup, as the information given by ADAC was rudimental. Fig. 17 illustrates two detailed views i.e. the penetration of the bumper and grill of the vehicle by the rear wheel of the bicycle and the later occurring bicycle's front wheel lifting. Furthermore, the figure depicts the outcome of the author's simulation.

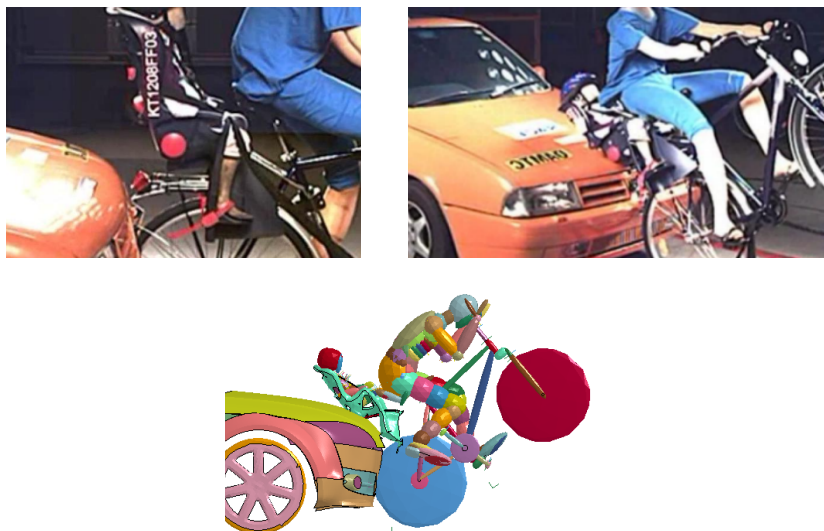


Fig. 17. Rear-end crash – top row: full-scale test performed by ADAC [109]; bottom: author's simulation for a rear-mounted child seat

Both the simulation and full-scale test were performed under the vehicle initial impact velocity of 25 km/h while the bicycle was standing in its regular position. The characteristic penetration of the vehicle front by the wheel could be reproduced. This is also true for the lifting of the front-wheel, which is supported by the child and baby carrier influenced centre of mass. Moreover, the already recognized rolling of the child in its carrier over the bonnet reoccurred in this simulation. It can be stated once more, that the properly chosen backrest length and the properly fitted harness [110], in any kind of child transportation device, are inevitable for the usage. The situation in the following milliseconds is characterized by a clear throwing of the bicycle in driving direction of the vehicle. In a consecutive step, the case-dependent increased dropping height leads to an increased vertical dropping velocity. This might lead to the rise of HIC and a generally higher injury risk. It might precede to this another impact, as the adult can potentially be hit by the child due to the child's body inertia, as it was already visible in Fig. 15.

3.8 Chapter conclusions

The motivation of this chapter was to setup an original model and approach to simulate and assess the vulnerability of children transported in a baby carrier on a bicycle. The research and findings in this field are up to today rare and partially limited to consumer-oriented product tests. The crashworthiness of these devices is often neglected as a point worth to observe despite their common visibility in nowadays traffic. In a consequence, a main point of interest was set to this regard, even though the crashworthiness needs to

be stated as low. In fact, instead of describing the carrier as a potential passive safety device in its current shape, the results pointed rather on a device, which only fulfills the demands as a seat for a child on a bicycle. Attaching a baby carrier to a bicycle and seating a child into it, influences the crash characteristics of the bicycle significantly. The commonly given advice to wear additional safety gear such as helmet, is comprehensible due to the possibility of at least one head impact during an impact scenario. The baby carrier as a seat was not significantly able to improve the situation for the child in terms of acting like a cage or a safety spacer. Especially in terms of lateral impacts, when the insufficient seat geometry or the lack of an additional head movement restriction got visible. Furthermore, the 3-point-harness was not able to secure the position of the child over the crash scenario. This lead in a few cases to situations, where diffuse injury patterns have to be considered, which points on the combination of head and neck injuries. Overall, the post-impact kinematics of baby carrier-seated children was proven to be different from the one reported to regular bicyclists. Another difference is the smaller influence of introduced initial bicycle velocity for seated children compared to the driving adult bicyclist regarding the impact zone on a vehicle. Summarizing, the observed child kinematics neither correlated with the generally used description of an impacted pedestrian nor with an impacted bicyclist, but forms a separate, third group. A shared circumstance for all the three groups remains in the vulnerability of their extremities, torso and their head in a situation of collision.

4 Investigating the influence of the vehicle front-end geometry to the transported babies after-crash kinematics

In this chapter, a focus is set on the influence of the vehicle's front-end as a main driving variable for the estimation of the WAD of an impacted child, which is seated in a bicycle baby carrier.

The previous chapter concentrated on the post-crash kinematics of children being transported in bicycle-mounted baby carriers. Each of the simulation took recourse on the same impacting vehicle but with a differing positioning or impact angle. Although the frontal geometry figured out to be corresponding to two vehicles with moderate market share, current traffic inherits a wide variety of differing vehicles and their corresponding shapes. In a consequence, the presented results are applicable to vehicle models only, which are comparable to the presented model of the Audi TT (2007) in terms of the based front-end parameters. Important parameters for the description of the frontal geometry of a vehicle are – as already previously described – the heights of the Bonnet Leading Edge (BLE) and the Lower Bumper Reference Line (LBRL). Especially the BLE and the bonnets shape are named as affecting the subsequent head kinematics. Moreover, for children, the BLE might be seen also as a line for direct head impact to the vehicle [14]. Several studies and research stated the influences of the BLE and bonnet shape [14,21,32,90,103], even though it was partially not respected, that the general shape of the front of the vehicle was significant differing. Exemplarily, [14] pointed on the inevitable categorization of vehicles, exemplarily into wedge or box-shape, but refers thereby to possibly old-fashioned terms, as o contemporary vehicle forms such as Mini-SUV or Kei-cars are appearing. It needs to be bear in mind, that the cyclist posture, bicycle geometry and many more factors influence the post-crash kinematics. In this context the question may be raised, in which way the change of the heights of LBRL and

BLE can be influencing the post-crash kinematics of children seated in bicycle baby carriers.

4.1 Choice of vehicle models and definition of configurations

In order to state about the influence of the BLE to the after-crash kinematics of the transported child, an appropriate set of simulations is envisaged using the MADYMO code. The car category shall be fixed consequently over the full set of simulations. Furthermore, the change of these frontal-geometry parameters has to match to vehicles, which are common in the region, where the simulation was carried out in order to be meaningfulness. Several manufacturers try to keep the general design of the fleet inherent. However, the design within their fleet remains similar in order to create recognition value and to offer customers even for the smallest models a specific premium subjectivity. Hence, their general design and frontal shape needs to be kept for the range of the manufacturers models. Consequently, the choice fell on two models from one manufacturer, as they are shown in the Fig. 18.

Fig. 18 Mercedes GLE and Mercedes CLA [111]

Physical measurements were done by the author at a local dealer in Dresden in order to gain the vehicles BLE and LBRL. All measured values were counterchecked by the help of manufacturer-given technical information or blue prints, available in the appropriate

user instruction for each of the vehicles. Fig. 19 gives an example of determining the height of the BLE of one of the vehicles by using the manufacturer-given blue print.

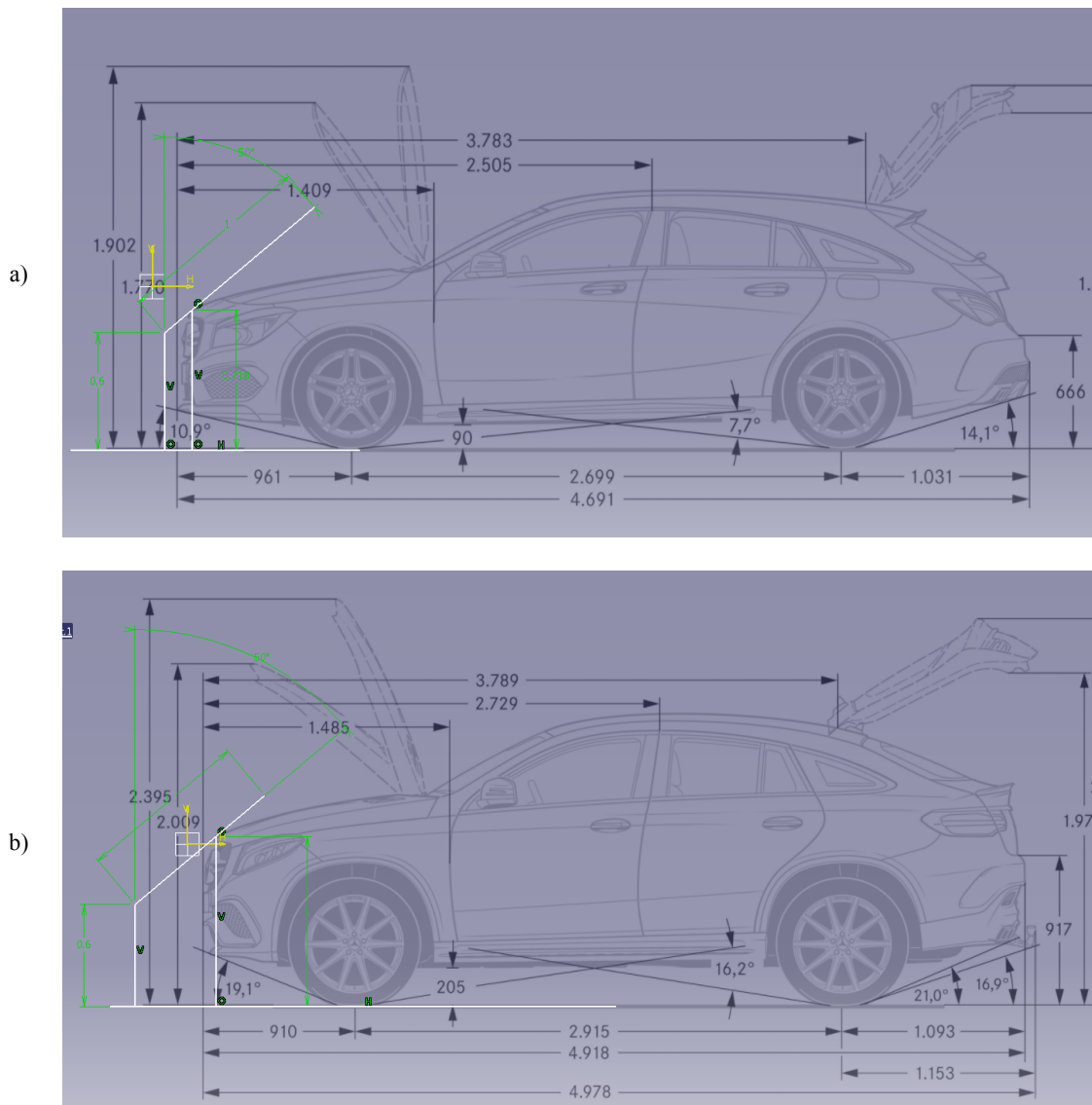


Fig. 19 Measurement of the height of BLE for a) Mercedes-Benz CLA and b) Mercedes-Benz GLE by using a blue print

These two models were used to describe an upper and lower limit of the heights for BLE and LBRL for the envisaged experiment, as they are representing for the same manufacturer the lowest and highest front-end profile by ensuring at the same time a comparable front-end shape. However, by linear inter- and extrapolation, the range was extended to in total 14 steps for the combination of both values. The heights for LBRL changed between 230 mm and 370 mm, while the BLE varied between 700 mm and 1100 mm. Table 5 below shows the full combination table of BLE and LBRL for the experiment.

Table 5 Configuration table for the used combinations of BLE and LBRL

Configuration #	BLE [mm] / LBRL [mm]
1	700 / 230
2	720 / 237
3	740 / 244
4	760 / 251
5	780 / 258
6	800 / 265
7	820 / 272
8	860 / 286
9	900 / 300
10	940 / 314
11	980 / 328
12	1020 / 342
13	1060 / 356
14	1100 / 370

It may be remarked, that the previously used model of an Audi TT would match the configuration #2, the Volkswagen Golf V out of the literature configuration #3, but angles and length of e.g. the bonnet may differ. Nonetheless, the influence of the changing BLE and connected LBRL for the one chosen frontal shape shall be investigated. In this concern, the velocities of 20, 25, 30, 35 and 40 km/h were chosen, as most of impacts are reported to be within this velocity range [31,112,113] The concentrated mass of the impacting vehicle was kept at 1430 kg equally for all configurations, in order to concentrate with the recognized effects on the change done to the vehicle front-end parameters.

The vehicle model thereby represents only the rough frontal shape and it does not consider complex grill geometry, headlights or similar. For the configurations # 2 and #12, the MADYMO models are shown below in Fig. 20.

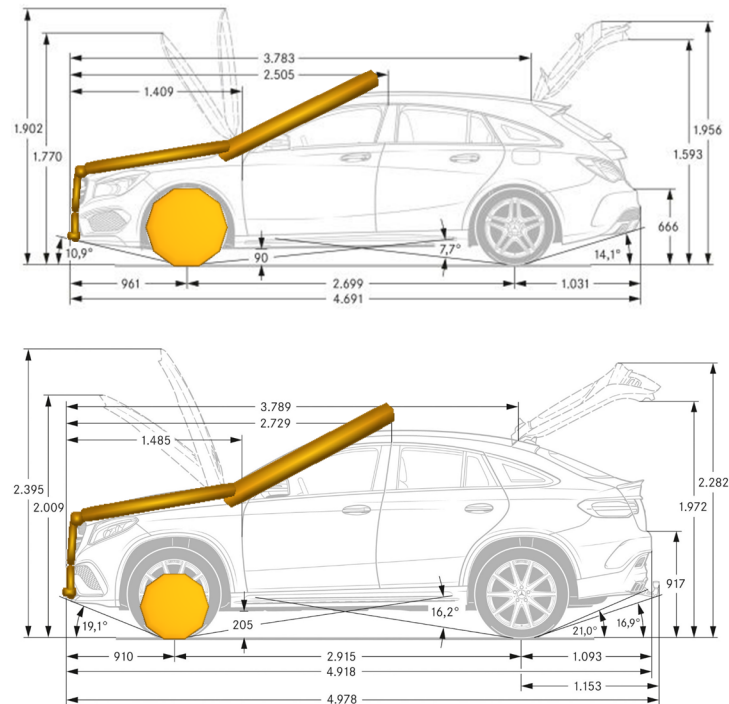


Fig. 20 Visualisation of the LBRL and BLE corresponding MADYMO vehicle-models, configuration #2 (top) and #12 (bottom)

4.2 Implementation of MADYMO models of the dummies and a bicycle with baby carrier

In a consecutive step, the bicycle with both dummies and the baby carrier need to be implemented. Generally, when it comes to VRU impacts, the number of unknown conditions is high. Hence, a significant number of simulations or demands the strict definition of the initial condition itself are demanded. There is an extensive range of possible values for a wide spectrum of possible interacting vehicle parts as well as postures of the VRU itself. Furthermore, every of these already complex events results in kinematics, that might have also a non-linear relationship regarding the initial conditions [17]. A bicycle increases the variables and degrees of freedom of the system in terms of the additionally interacting parts with their initial position – pedal position and steering position, to name exemplarily only two – mass, frame size and the corresponding posture of the bicyclist. Naturally, the ability of the bicyclist to lose from the bicycle during the accident needs to be considered. This cannot be considered for the seated and belted child.

The experiment was set up consequently and with a strictly limited number of initial conditions, that were kept equally over all configurations. Fig. 21 shows the MADYMO model of a 26-inch mountain bike with the mounted baby carrier, a driving adult and the

seated child. Both MADYMO dummies and the bicycle were kept the same as from the previously shown simulations in Chapter 3.

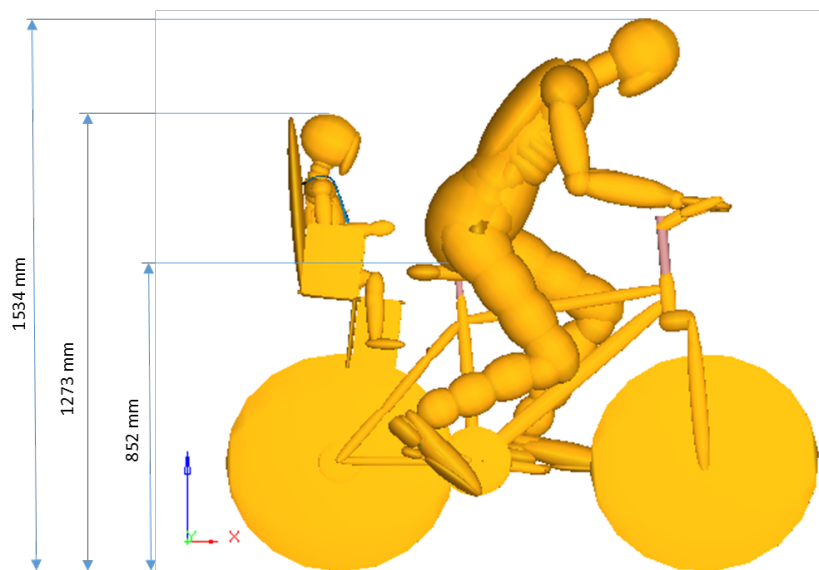


Fig. 21 The configuration for all simulations out of bicycle (MTB), adult, child and baby carrier

The bicycle setup was not changed in order to keep comparability to the earlier simulations, even though the FE baby carrier was substituted to a full MADYMO representation. Supportive to this statement, the average bicycle was characterized by Yi et al [97] as a mountain- or all-terrain-bike with 26-inch diameter wheels, according to the presented MADYMO model. In addition, the posture of both VRUs is unchanged. Only the overall sitting height of the child changed by -34 mm to now 1273 mm compared to the model in Chapter 3. The substitution of the FE parts by MADYMO code was done, as it reduces the calculation time significantly, yet it enables to reveal general kinematics in a sufficient way.

Finally, all MADYMO models with their specific BLE and LBRL were set up separately and run consequently for the various velocities. The vehicle was displaced along its driving axis (Y), so within the first 50 ms the defined contacts and gravity were stabilized. Every simulation was calculated for 500 ms in total, as head impacts occur for both VRUs within this time. Fig. 22 shows the initial setup for the MTB-configuration #3.

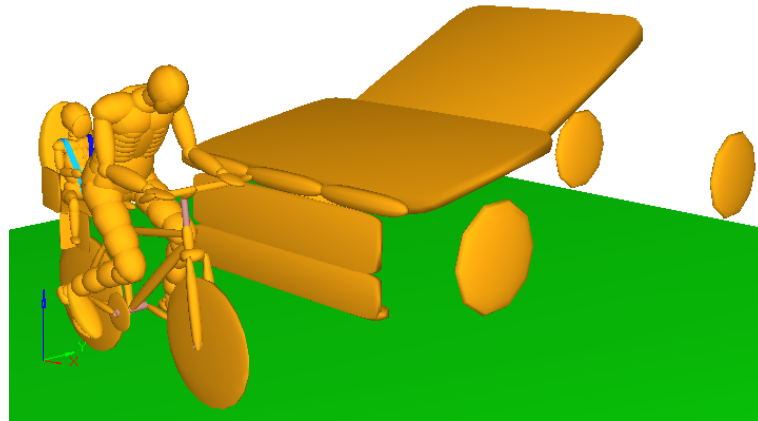


Fig. 22 Configuration #3 for the MTB set up with the vehicle model

4.3 Discussion of the results

Due to the differences in frontal shape of the vehicles, a direct validation of the presented model against the full-scale test of Zander et al. in [29] and the previously achieved simulative results is not feasible. Nonetheless, several observed phenomena out of the literature can help to adjust the MADYMO model and hence the test to a convenient behaviour. MADYMO models are not intended to show or visualize deformation, as it is common in FE models. A kind of exception from this is the relative motion of ellipsoids to each other, connected by joints. One of the corresponding phenomena in this context is the lateral tilting of the baby carrier due to the vehicle impact. Fig. 23 (left) shows on the left an image of the full-scale impact situation 148 ms after the initial vehicle impact, while Fig. 23 (right) shows the situation at the same time for the MTB-configuration #3. Clearly, a lateral tilt of the baby carrier toward the impacting vehicle is recognizable, which was realized for the MADYMO model by a revolute joint, which enables the rotation around the joints ξ -axis only.

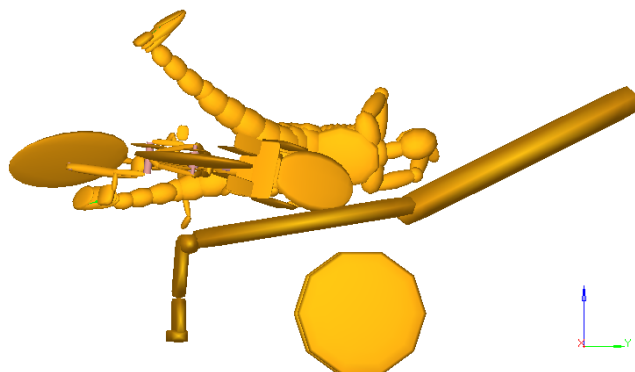


Fig. 23 Tilting phenomenon at $t=148$ ms after the first impact in the full-scale test (left) and MADYMO-configuration #3 (right)

The picture of [29] shows the state of tilt 148 ms after the initial impact. It may be asked, if the tilt is prevented or at least limited by the stiffness of the mounting and bracket. To have again a recourse: the baby carrier is connected in this way, that the baby carrier is during its installation process firstly clipped onto the mounting bars. In a second step, the seat is secured by one single bolt connection at the front to the bar structure. In total, the full assembly is connected by the use of a bracket to the bicycle frame. A significant tilt can be recognized in all forms of side crash tests, already in early moments after the first contact with the vehicle. This might be connected to at least two possible scenarios. Firstly, to the elastic and plastic behaviour of the seat material and the mounting rods material. Secondly – and this can be seen as a kind of behaviour-amplifying circumstance – the motion of the child dummy during the impact scenario. In chapter 3 the author has already described the child's bouncing immediately after the first vehicle side impact, leading to a bending posture of the child toward the impacting vehicle. Fig. 24 illustrates a sequence of images for the first 70 ms after the initial contact with the vehicle. The backrest is blanked in order to show the child dummy motion properly.

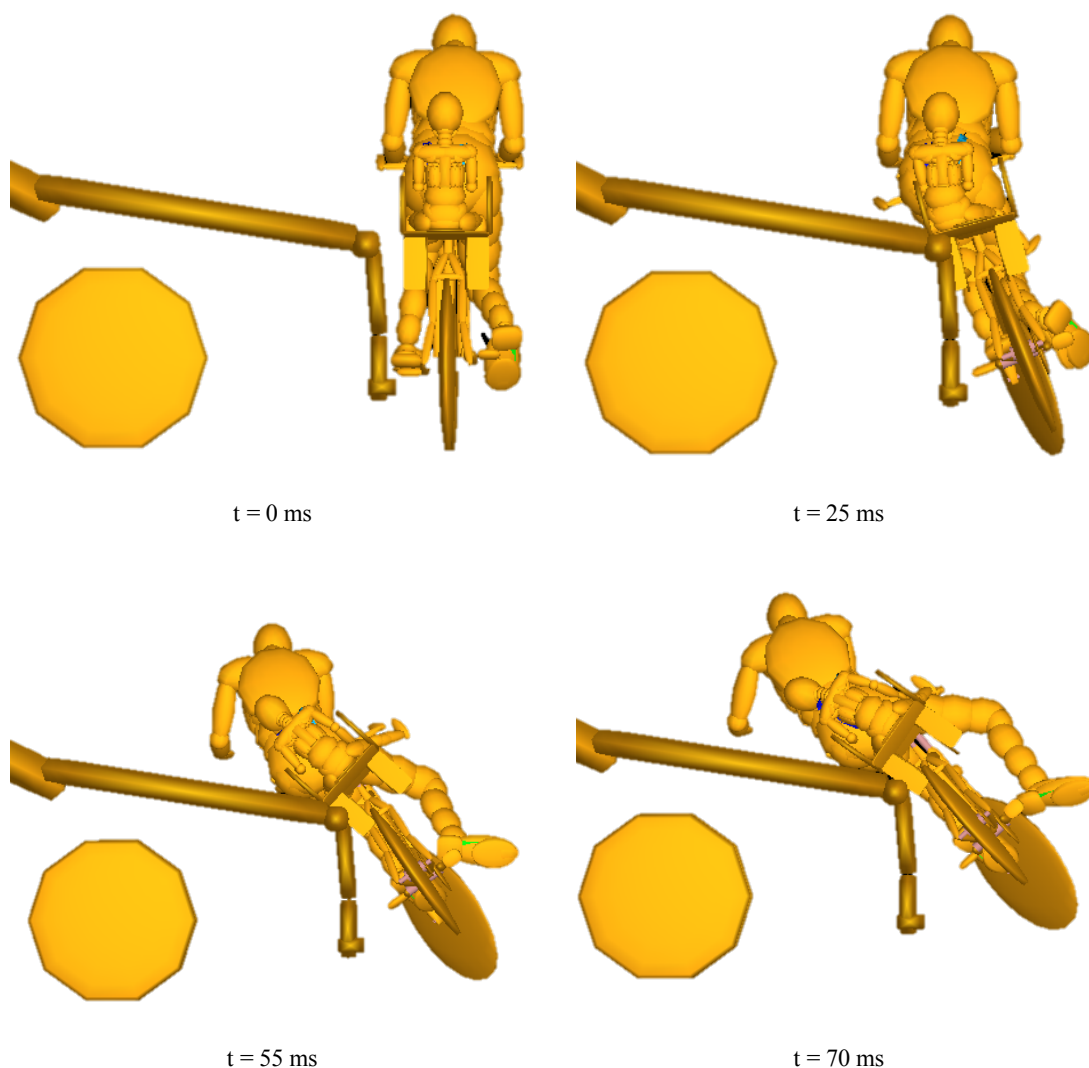


Fig. 24 Sequence of the impact for 0, 25, 55 and 70 ms after the initial vehicle impact in configuration #3

Moreover, concentrating on the initial 70 ms in the MADYMO experiments, the kinematics are close to the MADYMO-LS-DYNA coupling-results. Especially for the adult dummy, as shoulder and elbow are very present, comparable to the results of chapter 3. While the buttock is placed even beforehand on the bonnet, the outer leg goes up, and in total, a direct head impact on the bonnet toward the wind shield is awaited. In case of the child, firstly a contact of the front-end of the vehicle to the left bicycle pedal can be recognized, leading to an initial projection of the bicycle with a slight tilt toward the vehicle. Thereby, the rear wheel is lifted higher than the front wheel. Secondly, it is the initial contact of the baby carrier to the front-end of the vehicle, which leads to a relative projection of the baby carrier to the child, while the child remains in its initial position due to its inertia. Consequently, the first child dummy impact is with the hip area against

the left baby carrier armrest. In this moment ($t = 25$ ms shown in Fig. 24), the bicycle demonstrates a tilt angle against the impacting vehicle. In 55 ms, the lifting process of the bicycle with baby carrier continues, but with a change in the tilt direction of the baby carrier. The carrier is now pointing toward the impacting vehicle, while the child bounces with its right hip against the right baby carrier arm rest. Its right leg tends to be thrown in driving direction of the vehicle. The baby carrier is located from this moment on already on the bonnet of the vehicle. Combined with the described lifting of the bicycle, a somersault motion of the bicycle can be observed. This somersault motion results in a direct head impact of the child to the bonnet, as the baby carrier construction cannot serve as a restricting geometry or cage. The tilt of the baby carrier remains further on. It should be pointed in this case on the construction of the mounting rods and their moment of inertia, which is overall not intended to handle immense lateral forces. The information about the tilting phenomena is not provided by Zander et al in [29]. In any way, the tilt can be recognized already in early moments after the first impact and remains at least up to the moment of the head impact. The tilt might be limited by the interaction of the leg pads of the carrier with the rear wheel, the luggage rack respectively. The tilt is considered in this case to have a permanent nature and recognized early in all corresponding cases. As the MADYMO model can represent this behaviour, the influence of the rotational stiffness of the mounting is stepping into the background. In a result, tilting was enabled for all the MADYMO-simulations by releasing the rotational degree of freedom of the according joint around the x-axis in the local coordinate system of the bicycle. It enables mimicking the recognized and described tilting effects. Overall, the shown behaviour was comparable to the general post-impact child kinematics with the previously described simulative results and with the full-scale test from the literature. In this context, a central concentration is now the measured Wrap-Around-Distance (WAD) of both the child and the adult according to BLE and velocity of the vehicle.

Zander et al. stated, that the child impacted in four out of five cases for the impact velocity of 40 km/h below WAD 1500 mm, while the adult reached even values beyond WAD 2100 mm [29]. Fig. 25 and Fig. 26 present the graphs for the measured WAD of the child the adult respectively, seated on a MTB for the varying impact velocities in relation to BLE and LBRL. The front-end of the vehicle from the full-scale test corresponds to the configuration no.3.

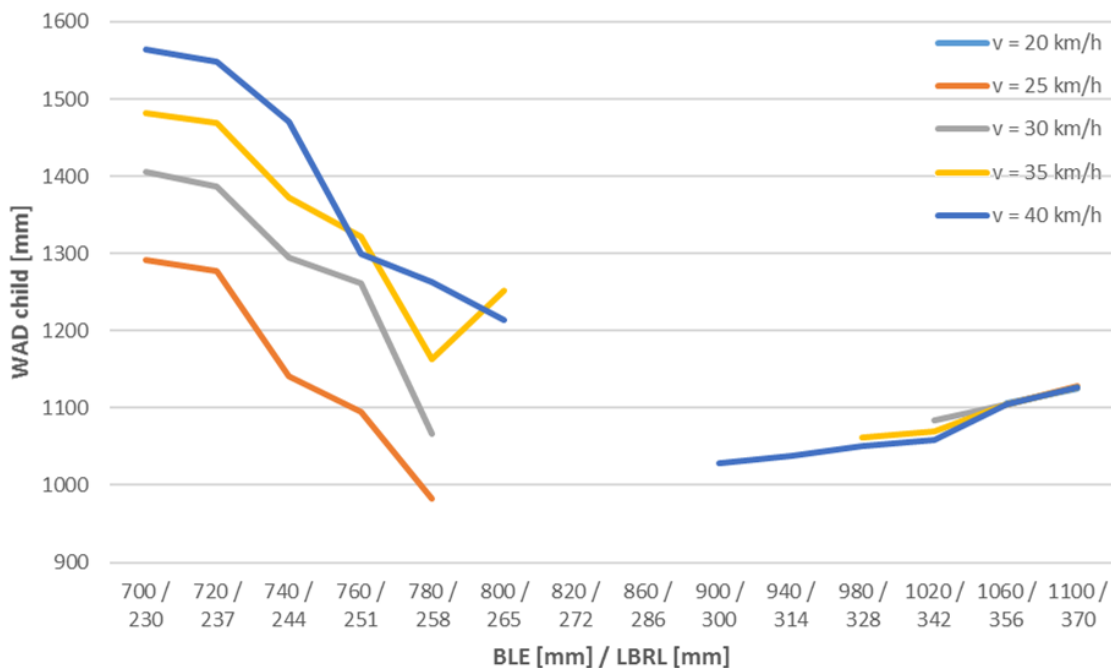


Fig. 25 Measured WAD of the child seated in a MTB-mounted baby carrier for the varying impact velocities in relation to BLE and LBRL

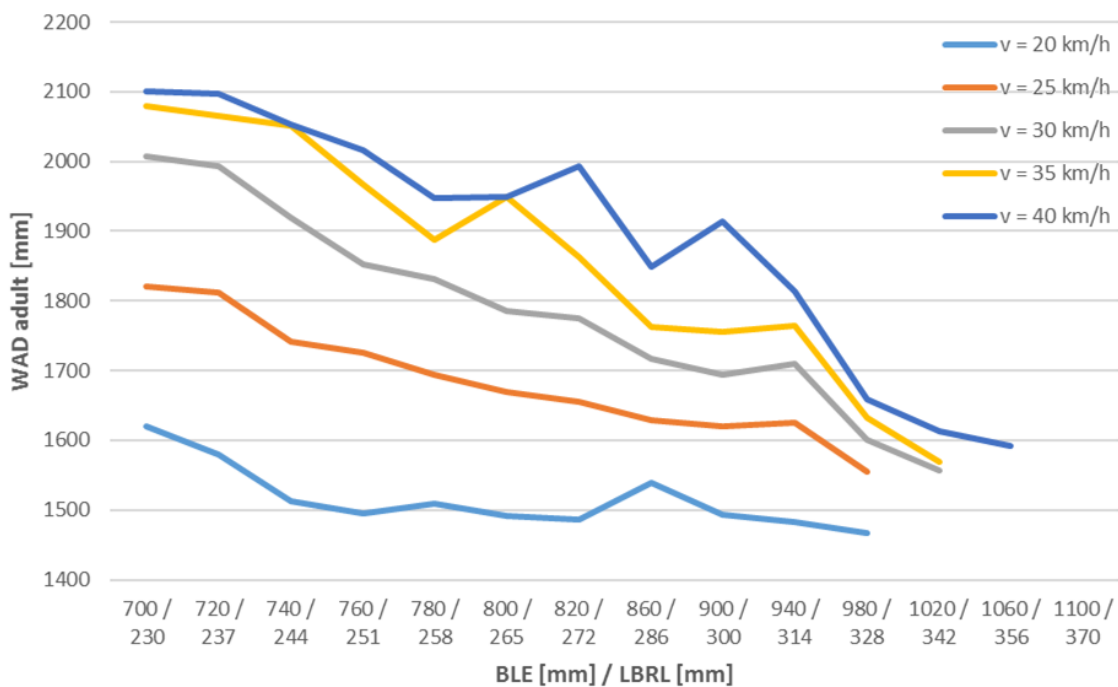


Fig. 26 Measured WAD of the adult seated on a MTB for the varying impact velocities in relation to BLE and LBRL

In a more detailed view, the following results shall be formulated. For the sake of readability, they are grouped to logical points.

Seeing Fig. 25 and Fig. 26, with an increasing BLE – and increasing LBRL, as they are connected here – WAD decreases tendentially for both VRUs on the bicycle.

Considering a constant BLE, an increasing impact velocity leads to an increasing WAD. As this corresponds for the full range of tested BLE values for the adult, this trend can be stated for the child only up to a BLE of 780 mm. At BLE = 800 mm and $v = 35$ km/h, the WAD was higher by 37 mm.

In the following configurations, an increasing of BLE/LBRL ratio switched the cartwheel or flipping of the bicycle into a projection in driving direction of the vehicle. Fig. 27 illustrates the mentioned change by showing the characteristic interaction of VRUs and vehicle for the MTB-configurations number 2, 8 and 14. It shall be pointed also on the kinematics of the adult, who is less likely to lose from the bicycle while the BLE increases and influences the bicycles motion. Nevertheless, for the BLE of 800 mm and the velocities of 35 and 40 km/h, the energy of the impacting vehicle was high enough to flip the bicycle. Combined with this, it was observed that it led to a significant bending of the child's neck toward the vehicle, which finally still enabled a direct head impact to the bonnet.

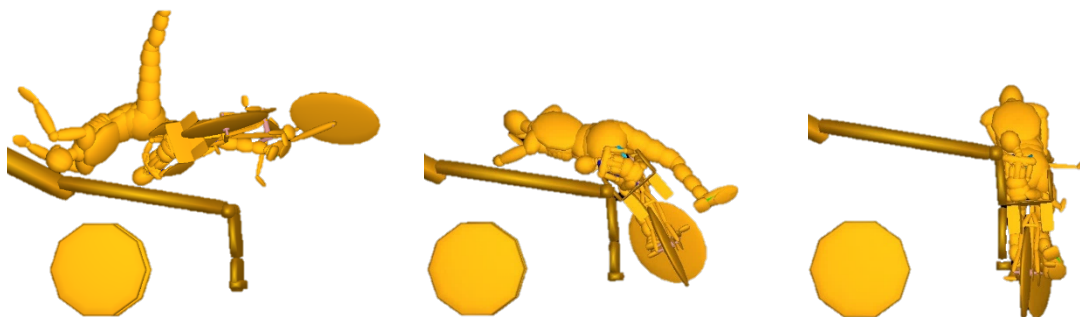


Fig. 27 The change of the bicycles kinematics for different vehicle front-end geometry at $v = 40$ km/h impact for the configurations: #2 (left) – somersault; #8 (middle) – wrap; #14 (right) forward projection

Fig. 27 (middle) reveals exemplarily for the corridor of $800 \text{ mm} < \text{BLE} < 900 \text{ mm}$, that – with exception of configuration #6 and #9 each with $v = 40$ km/h – it was not possible to recognized for any simulated impact velocity a direct head impact of the child. Again beginning at $v = 40$ km/h for configuration #9, the recognized head impact occurred practically for the same WAD for all velocities and a specific BLE. The impact location was in these cases always close to the bonnet's edge. The WAD was thereby measured by a higher value than the BLE. In this concern it needs to be explained, that the WAD is

a measured value from the ground along the geometrical outer shape of the impacting vehicle, while the BLE is treated here as a height (see Fig. 28).

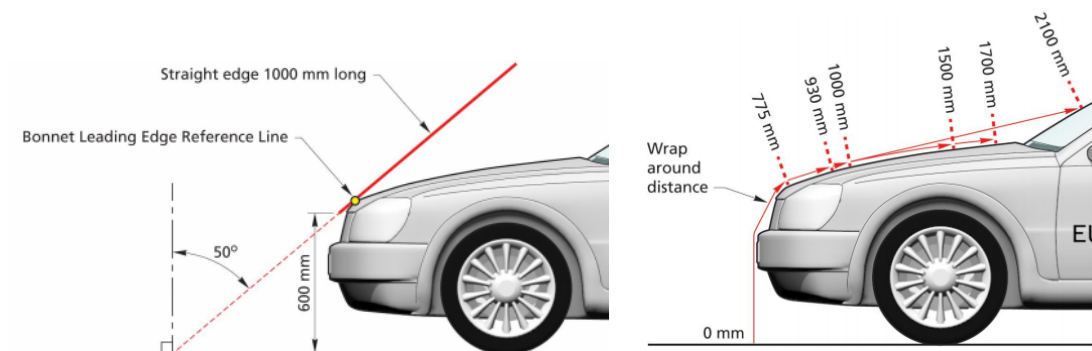


Fig. 28 Determination of BLE (left) and WAD (right) [28]

The projection of the bicycle did not mean that the bicycle with the baby carrier is instantly projected from the vehicle. It rather remains at the front-end – only the lateral bending of the child’s neck leads to the possibility of a direct head impact for the configurations with BLE > 900 mm. Thereby, the maximum value while increasing the BLE seems to be stabilizing at a value slightly below the initial overall seating height of the child. This corresponds to a reduction caused by the neck’s bending ability in relation to the distance of the bicycle carrier to the car while being projected (see Fig. 29).



Fig. 29 MTB-configuration #12 showing the projection of the bicycle and the moment of the child's head impact

Interestingly, the behaviour of the adult changes from wrapping into a projection by an increasing BLE and LBRL, which gets visible in the graph of Fig. 26 and in Fig. 29, starting characteristically with the configuration #12 corresponding to a BLE from 1020 mm. Up from this BLE, only higher velocities could provoke in a few cases a direct head impact to the bonnet or front-end. Thus, the frontal projection starts to appear, as the adult is impacted significantly above the hip i.e. above his/her centre of mass. In general,

the horizontal position of the centre of mass plays a major role for each VRU, beside the BLE, for the post-impact kinematics. By rising the BLE value over the corresponding assumed initial centre of mass, projection is occurring more clearly. The adult VRU seems to loosen from the bicycle, while it is only the bicycle with its frame and handlebar geometry, which is influencing the loosening procedure. As at least for impacts up to the adult's hip the adult was able to be shifted from the bicycle onto the bonnet, cases of projection without a direct head impact to the bonnet appeared. This happened, when the height of the BLE reference line was significantly above the adult's hip and consecutively the flexibility of torso and neck were insufficient to provoke a contact. Finally, for both VRUs the change of performing a cartwheel over the vehicle into a forward projection can be recognized for an increasing height of the BLE.

The presented results referred to the average American adult male of 1.73 m tall, sitting on an average mountain bike (MTB) bicycle [97] with an additionally attached baby carrier. Zander et al. varied the bicycle geometry in their experiment by 5 different bicycle types and two baby carriers. Nonetheless, the presented MADYMO configurations revealed very comparable WAD values for a vehicle, which is only comparable in terms of BLE to the Golf Mk.5, which was the used vehicle in the full-scale test [29]. As a remark: the overall adult height while sitting on the bicycle was only 1.53 m. Zander et al. declared, that the rearward limitation of WAD = 2100 mm for an adult might not be sufficient, which is underlined by the presented cases, where this value was already reached. Especially, by putting a focus on the stretching behaviour of the adult during the impact incident, shown in Fig. 30.

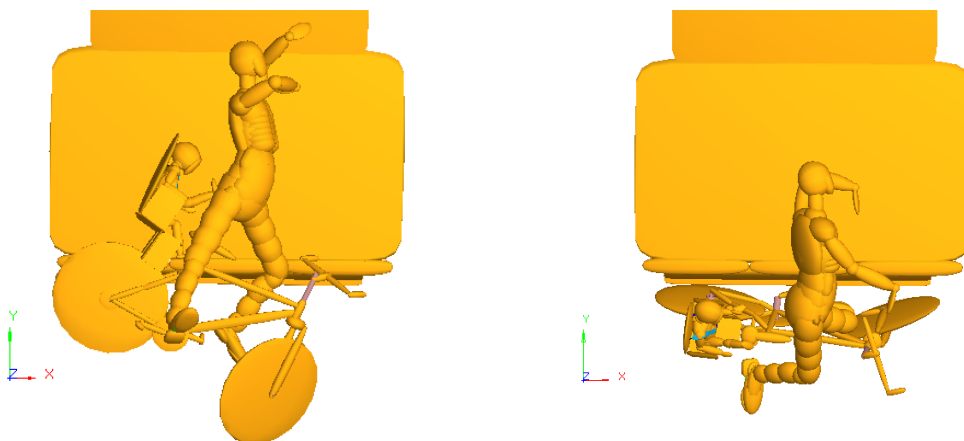


Fig. 30 The adult's wrapping behaviour during the impact in the configurations #2 / BLE= 0.72 m (left) and #12 / BLE = 1.02 m (right), impact velocity $v = 40$ km/h.

The cyclist's upper body stretches after the impact before the head impacts to the bonnet. In addition, a turn of the adult's body around his Z-axis is thereby reported for all the cases. It underlines, that the sporty riding and seating position represented by the upper body posture is not significantly influencing the WAD value. Consequently, the upper body and the resulting overall cyclist's height play a minor role, as long as the upper body or arm is not kept by the initial vehicle contact. On the other hand, the low seat height of the adult in the MADYMO test is a base for assumption, that a higher initial seat height would firstly enable then the adult to be shifted onto the bonnet. Secondly, higher WAD values are reached due to the initial pelvis height, which allowed to travel along the vehicle's frontal geometry, especially over the bonnet. Hence, up to a hit in the region of the hip, the major driving criteria for the WAD is the bicycle seat height. The riding position or posture of the adult bicyclist may gain more importance for the recognized WAD, when it comes to a collision with significantly larger or higher vehicles such as buses.

The presented MADYMO simulations focused particularly on the post-impact kinematics and related head impacts of the child to the vehicle. Consequently, a mathematical model was established to provide a fast calculability of the WAD for the child dependent on BLE and initial velocity of the impacting vehicle. The function $WAD(BLE, v_{iv})$ gives back the approximated WAD of the child in [mm], where BLE is meant as the height of the BLE reference line above the ground in [mm] and v_{iv} is the initial velocity of the impacting vehicle in [$\frac{km}{h}$].

It has the form of equation (2):

$$WAD(BLE, v_{iv}) = \begin{cases} -3.624 \cdot BLE + 17.93 \cdot v_{iv} + 3413 & \text{for } 700 \text{ mm} \leq BLE \leq 780 \text{ mm}, & 20 \frac{km}{h} \leq v_{iv} \leq 40 \frac{km}{h} \\ \text{not defined} & \text{for } 780 \text{ mm} < BLE < 900 \text{ mm} \\ 0.3155 \cdot BLE - 2.549 \cdot v_{iv} + 1091 & \text{for } 900 \text{ mm} \leq BLE \leq 1100 \text{ mm}, & 20 \frac{km}{h} \leq v_{iv} \leq 40 \frac{km}{h} \end{cases} \quad (2)$$

It has to be clearly stated, that the function bases on results from the commenced simulations and it is valid for the presented data – particularly for the used vehicle shape, height of the BLE and the range of initial impact velocity. Despite the initial velocity, for the range of $780 \text{ mm} < BLE < 900 \text{ mm}$ no head impact of the child was recognized to the vehicle front. Fig. 25 showed this range of configurations. Due to this circumstance, the overall function is divided into three ranges and visualised in its entirety in Fig. 31.

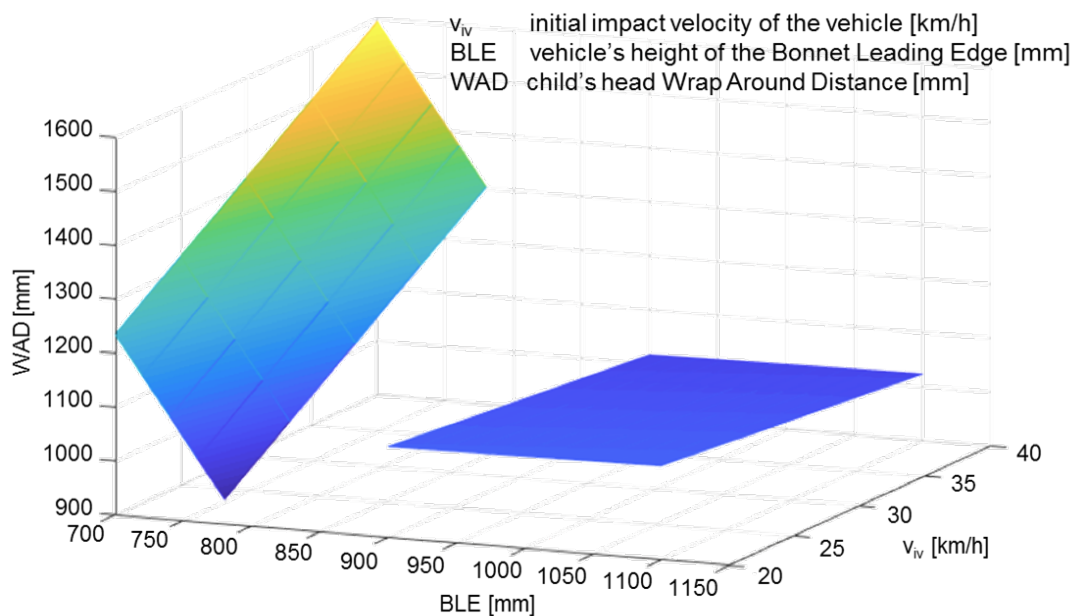


Fig. 31 The graph of the function $WAD(BLE, v_{iv})$ for the MTB-configurations

The functions were created by using MATLABs *Curve Fitting Tool* based on the unfiltered dataset shown in Fig. 25. The functions are polynomial fits *Poly11* establishing for each range a surface. The R-square value for the first range with $700 \text{ mm} \leq BLE \leq 780 \text{ mm}$ and $20 \frac{\text{km}}{\text{h}} \leq v_{iv} \leq 40 \frac{\text{km}}{\text{h}}$ is given by 0.9129, by 0.9539 for the third range with $900 \text{ mm} \leq BLE \leq 1100 \text{ mm}$ and $20 \frac{\text{km}}{\text{h}} \leq v_{iv} \leq 40 \frac{\text{km}}{\text{h}}$.

The third range represents again the stabilizing possibility of a direct head impact to the front-end of the vehicle, as the WAD is nearly unchanging for the various combinations of BLE height and velocity. It can be noted on the first interval, that especially the varying BLE gains a higher importance toward a change in the resulting WAD than the velocity. Nevertheless, the highest WAD can be achieved by this model only for the combination of the fastest impacting simulated vehicle model with the lowest front-end. The rearward limitation of WAD 1700, which was stated in the literature for a baby carrier seated child, seems to be kept [29].

4.4 Chapter conclusions

The focus in this chapter was set to the influence of the Bonnet Leading Edge (BLE) as main driving parameter to change the Wrap Around Distance (WAD) of an impacted

child, who is seated in a bicycle baby carrier. The previously described post-impact kinematics of the child was reproduced in a different approach i.e. MADYMO.

As the main conclusion, a formula to estimate the child's WAD in dependency of the vehicle's BLE and initial impact velocity was created. The calculation is three-parted, as height-gaining vehicles are provoking a switch from a bicycles' cartwheel-move over the bonnet into a clear frontal projection of the bicycle. Thus, it is possible, that even though a high impact velocity is registered, the child's head is not about to impact onto the vehicle's front-end. For vehicles with even higher BLE, a head impact to the front-end of the vehicle at a nearly constant height over the ground according to the seating position of the child can be characteristically. In a summary, the BLE inherits a higher importance to the change in the outcome of the WAD than the impact velocity itself. The absence of a child head impact to the front-end geometry of the vehicle for a specific corridor does not stand for a safer constellation or recommendation for a specific vehicle design. The hazard of a head impact to the ground remains as well as possible body injuries. The mathematical description can help to estimate accident or impact circumstances in the field of forensics sciences.

5 Experimental tests of a fall situation to the side

Real-world experiments with an HybridIII-3YO-dummy in this chapter help to validate the related numerical results. Furthermore, the potential severity of a simple bicycle side fall situation will be shown.

5.1 Intention for performing a full-scale side fall test

The previous chapters concentrated on the simulation of the vulnerability of the transported child due to a hit by a vehicle. The topic-initializing simulations resulted in the original description of the post-impact kinematics after the hit by a vehicle and proved, that a transported child's kinematics is thereby neither represented by the characteristics of a pedestrian nor these of a bicyclist. The main assumption within these experiments was the involvement of a vehicle in the crash constellation under a variety of changing input parameters such as impact angle or the initial impact velocity. Circumstances, which were in all cases neglected, could be named exemplarily by pre-crash behavior or special kinematics, which could be found already in a drift or slide of the bicycle. Particularly, beside the described absence of a vehicle, also the presence of an instability of the bicycle could lead to a fall to the ground. Regarding the results of the previous chapters, also this situation might affect the physical integrity of both adult rider and transported child. As in such an event the main influencing variable for the later injury assessment would be given by the vertical head impact velocity, it is a feasible step to reduce the experiment to a full-scale side fall of the bicycle with a seated child in the baby carrier, where the vertical head impact velocity $v_{\text{vertical,imp}}$ will reach its theoretical maximum according to $\sqrt{2 \cdot g \cdot h}$ out of the energy conservation rate, where g is the gravitational acceleration in $[\text{m/s}^2]$ and h is the drop height in $[\text{m}]$. Overall, the theoretical maximum of vertical impact velocity of approx. 5 m/s is expected with the drop height of 1.3 m equal to the overall seating height of the dummy.

Particularly, it needs to be pointed directly on one circumstance: The vertical head impact velocity by a bicycle side fall is very comparable to the vertical head impact velocities, which were recognized during the vehicle impact scenarios out of Chapter 3 *Original description of kinematics of children transported in bicycle-mounted baby carriers during impact situations*. Moreover, the results out of chapter 3 and 4 described the possibility of multiple head impacts during the impact situation, which might occur against the vehicle, but as well against the ground. In a consequence, the seated child could have to face several comparable head impacts during vehicle impact situations.

The experiment, which is presented in the following, allows to capture the event of an impact against the ground by the use of available test equipment such as a 3-year-old ATD with an additional head accelerometer, a bicycle with attached baby carrier and a high-speed camera for video capturing. Performing the side fall experiment will give the possibility to have an insight into the child's motion during the impact and the occurring resultant head impact accelerations. Moreover, a possibility is given to validate the used simulation models and approaches.

5.2 Experiment setup

The setup consists first of all of the bicycle, that was the base for the establishment of the MADYMO bicycle model. A rear-mounted baby carrier is attached to a MTB, which is characterized by its 26-inch wheel size. The baby carrier is designed for carrying a child with a mass of up to 22 kg, as most of the baby carriers on the market. A HybridIII-3YO dummy from Humanetics was then seated and belted. The 3YO-dummy differs in terms of measurements from the beforehand used virtual 1.5-YO-dummy out of the MADYMO or coupled LS-DYNA/MADYMO-simulations. In order to overcome this issue, in both virtual and physical tests, the 3YO-dummy was used from now on. By this, the overall sitting height increases by 5 cm to 55 cm and the weight by approximately 5 kg from 11 to 16 kg [114], [115]. The seated child on the bicycle is shown in Fig. 32.



Fig. 32 Seated HybridIII-3YO ATD on the MTB with baby carrier

As the main considered impact is the head impact and the general head acceleration, a focus shall be on the head and neck of the ATD. In case of the HybridIII-3YO it is a fiberglass skull, which is covered by a vinyl skin and certified to head drop and impact tests. A segmented neck structure is assembled to the skull, made of a moulded butyl rubber construction, while the partition is done by metallic plates.

The neck flexibility is given by the butyl rubber material and also by the cut rubber geometry, which is in total intended to show biofidelic flexion and extension motion. Certification to these corridors of biofidelic flexion and extension moments or rotations is according to the manufacturer given in [115].

In order to record the head acceleration during the experiment, a T356A15 piezoelectric ICP® accelerometer was installed inside the HybridIII-3YO-skull, as it is shown in Fig. 33. The measurement values were handled by using a computer with an installed Siemens LMS acquisition card with its included 24-bit analog-to-digital converter at a sample rate of 51200 Hz.

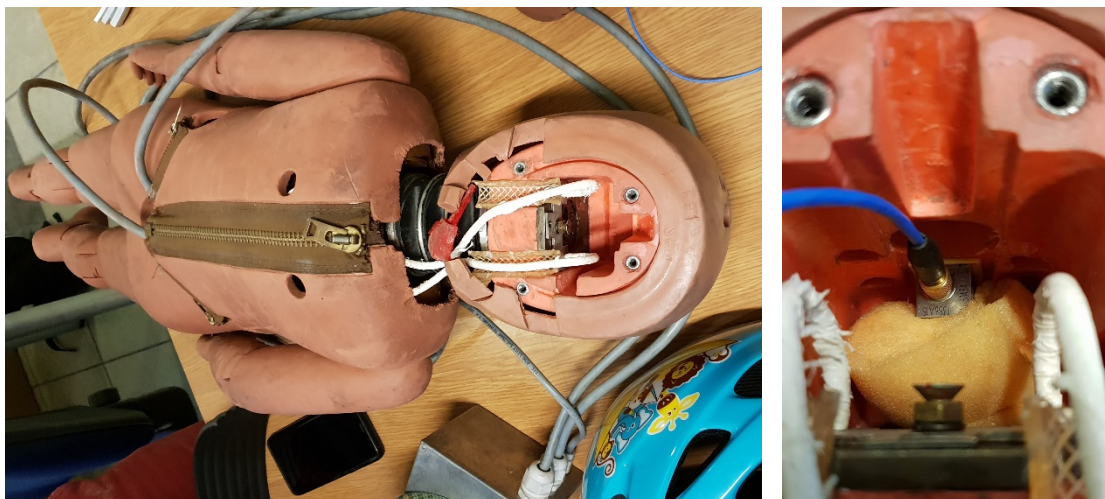


Fig. 33 Installed accelerometer in the head of the HybridIII-3YO-ATD

Furthermore, a high-speed camera Phantom V12 was set up, in order to record the fall over experiment at 10000 frames per second (fps). The video files were used in a consecutive step to be analysed in TEMA Motion as a dedicated software in order to create displacement-time data sets for high-contrast markers. These markers were attached to the dummy's head and can be recognized in Fig. 32.

By installing two more video recording smartphones and two GoPro action cams, the gathered video footage was enriched. Particularly the GoPro action cameras, which were located above the head impact area and on the top pipe of the bicycle frame, should help to reveal a more detailed and coloured view on the happening for cases of uncertainty while interpreting the gathered data.

The bicycle was set up by standing with a slight angle toward the intended side of fall, the side stand folded and finally released manually and left to under the gravity force.

5.3 Discussion of the results

The sequence of the bicycle fall over is visually presented in Fig. 34.

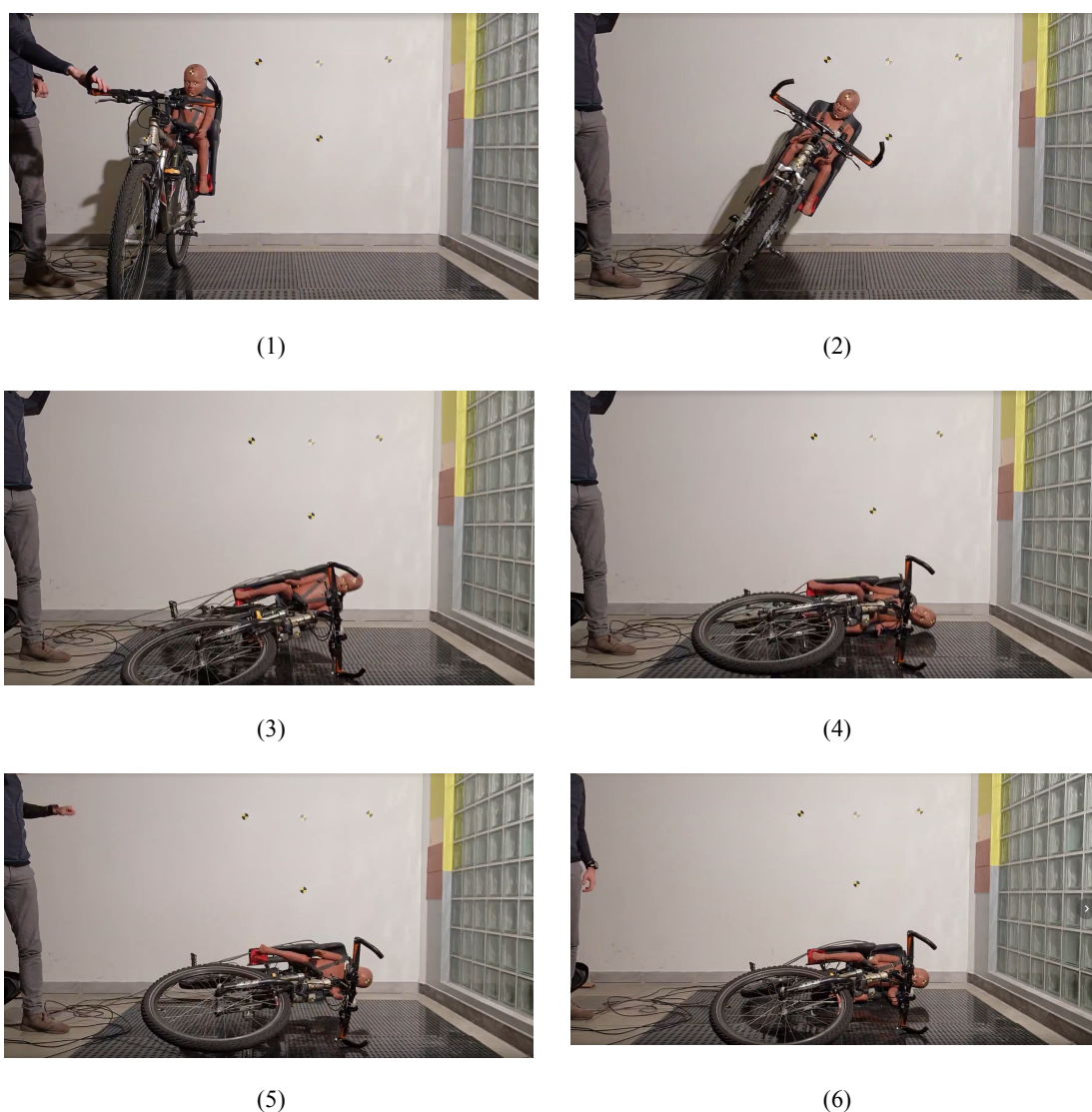


Fig. 34 Sequence of falling, recorded at 30 fps

The sequence shows at first the fall itself, leading around step 4 to the moment of the assumed head impact to the ground. Followed in step 5, the bicycle shows another lift off from the ground, particularly with the rear-end of the bicycle, before the bicycle comes with another impact to rest and remains at its position as shown in step 6. The picture in step 4 has already revealed a slight gap between head and ground, which let to consider, that no head impact at all happened during this test. Consequently, the accelerometer and high-speed camera data was observed. Fig. 35 shows the moment, where the head was located the closest to the ground. In addition, the small gap between floor and head is recognizable and supports the initial assumption of the absence of a head impact.

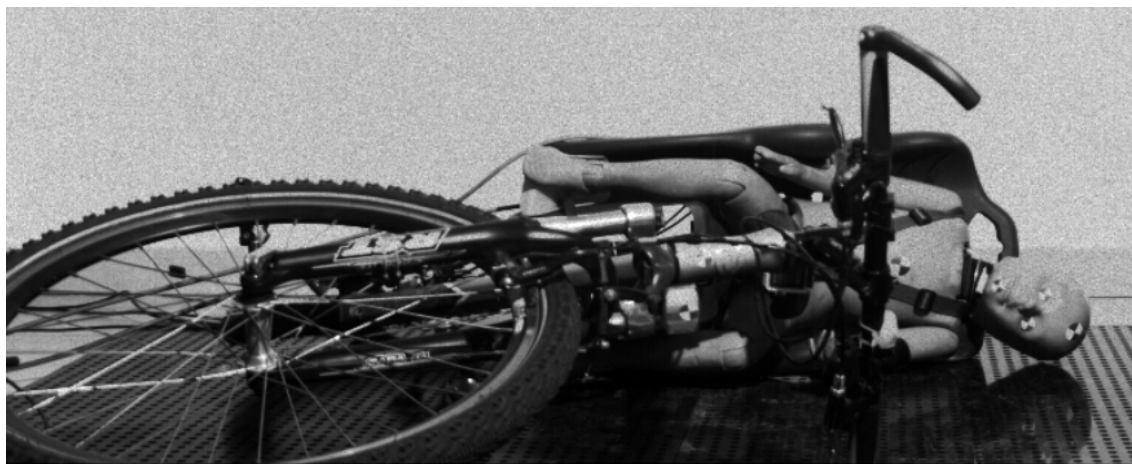


Fig. 35 Moment of the closest distance between the head and ground during the high-speed camera recording.

The corresponding acceleration curve was worked out by using the dedicated software TEMA motion and is plotted together with the acceleration curve gathered by the head accelerometer in Fig. 36.

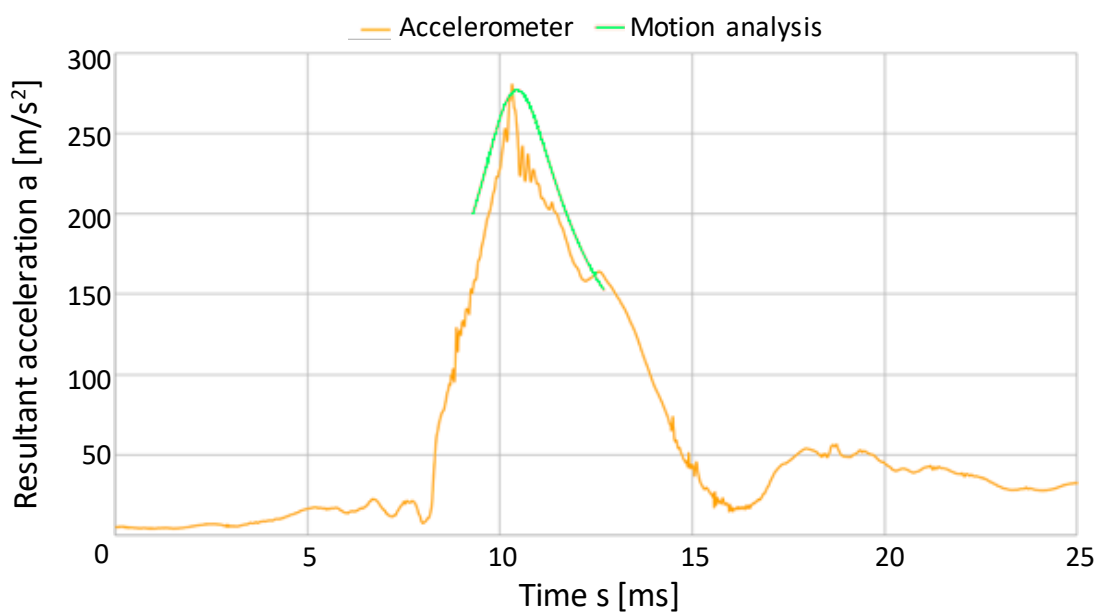


Fig. 36 The resultant acceleration measured by accelerometer in the dummy's head and by motion analysis

The resultant acceleration from the piezoelectric accelerometer shows a steep ascent with a peak at 280.5 m/s^2 , equal to 28.6 g . Initial altering of the acceleration value can be explained by contacts, that start to be established with the baby carriers foot guards, the arm rest, in case of specific initial postures even the babies shoulder etc., before the highest peak occurs. Several smaller altering and one approx. 1.5 ms long plateau around

160 m/s² can be seen at the descent of the acceleration curve. It represents the loosening of the bike from the ground. It is particularly visible due to friction effects, as not only the bike but also the shoulder of the child dummy is sliding or moving along the ground after the fall of the bicycle. This slight sideward movement can be also seen in the fall sequence shown in Fig. 34.

In opposite to this detailed and incident covering graph of the accelerometer, the range of the plotted curve gathered from the high-speed camera is very limited and covers only the moment of the before head impact. This limitation is connected to the previously described movement of the bicycle with the attached child along the ground. In order to evaluate the high-speed camera footage, the scale ratio of one pixel in a real length according to the captured frame needs to be defined – which is called scaling. The scaled video set is only usable, if all the pictures, in which a measurement takes place, are captured in the same plane and the captured item remains in the same distance to the matrix of the high-speed camera. Thus, the used Phantom V12 works in a 2D-workspace of x- and y-coordinates only. This scaling was performed for the assumed impact position of the child dummies head. However, as explained, the head undergoes significant movement in neck flexion and extension, but also out of the plane, as the bicycle is moved due to inertia after the impact. The movement can be seen in the fall sequence visualized in Fig. 34. In a consequence, the gathered data needs to be limited to the area, in which scaling or calibration took place. For this range, a maximum resultant acceleration of 276.8 m/s², equal to 28.2 g was observed. This resultant acceleration was calculated from a single-view video file for two components i.e. x and y. Nonetheless, the slope, peak and overall time range for both measurement techniques are correlating. This step of correlating both input sequences was done in the dedicated software National Instruments LabVIEW 2013.

As it was initially described in the scope of this chapter, the experiment was modelled also by using the MADYMO code. The used model remained the same in terms of the bicycle and the baby carrier. The child dummy was exchanged consequently to the real dummy equivalent, the HybridIII-3YO dummy out of the MADYMO 7.5 version. After positioning the dummy comparable to the real-world experiment, the belts were routed in accordance to the new dummy, also to keep the slack at a reasonable minimum. In order to force the bicycle to fall in a specific direction, the whole combination of bicycle, baby carrier, child dummy und harness was rotated by 2.5 degree. The model was only loaded

by gravity and calculated for 1.5 s in total. This includes the time for initialisation of gravity and contacts. The full setup is shown in Fig. 37.

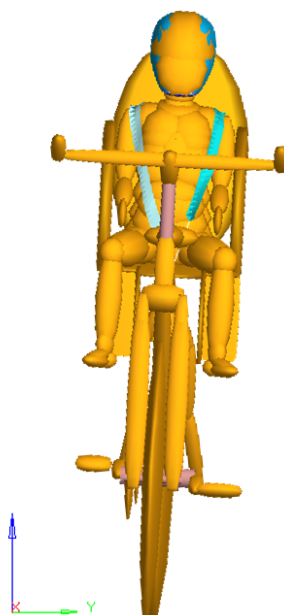


Fig. 37 MADYMO model of the side fall experiment

Also in the MADYMO simulation, the bicycle fall over and the first contact is reported for the pedals of the bicycle, which starts to move the bicycle slightly. In the following milliseconds, not only the steering bar but also the baby carrier interacts with the ground, as well as the child's left leg due to gravity, as it is not secured in its position by a strap to the foot guard. With the full contact of the baby carrier to the ground, the child blocks with its left shoulder into the baby carrier geometry and the neck bends laterally. Also in the simulation, it remains as a moment with a close distance between head and ground, as it can be seen in Fig. 38.

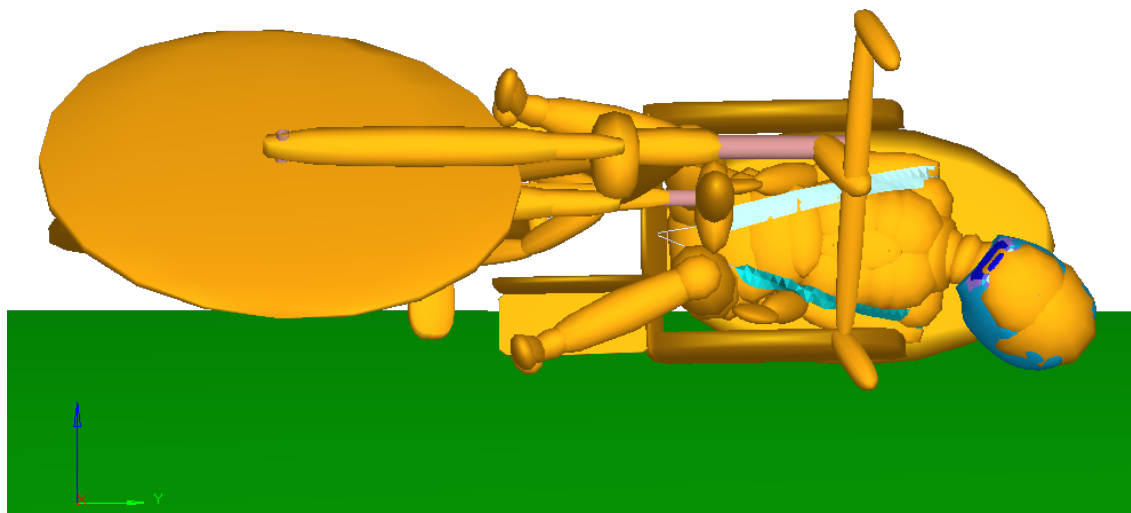


Fig. 38 Moment of the closest distance between head and ground during the MADYMO simulation (the view is slightly rotated around the y-axis to make the ground surface visible)

The maximum resultant head acceleration was calculated by 297.3 m/s^2 , which equals to 30.3 g and is 6% higher than the value measured by the accelerometer, respectively and 7.4% higher compared to the high-speed camera motion analysis.

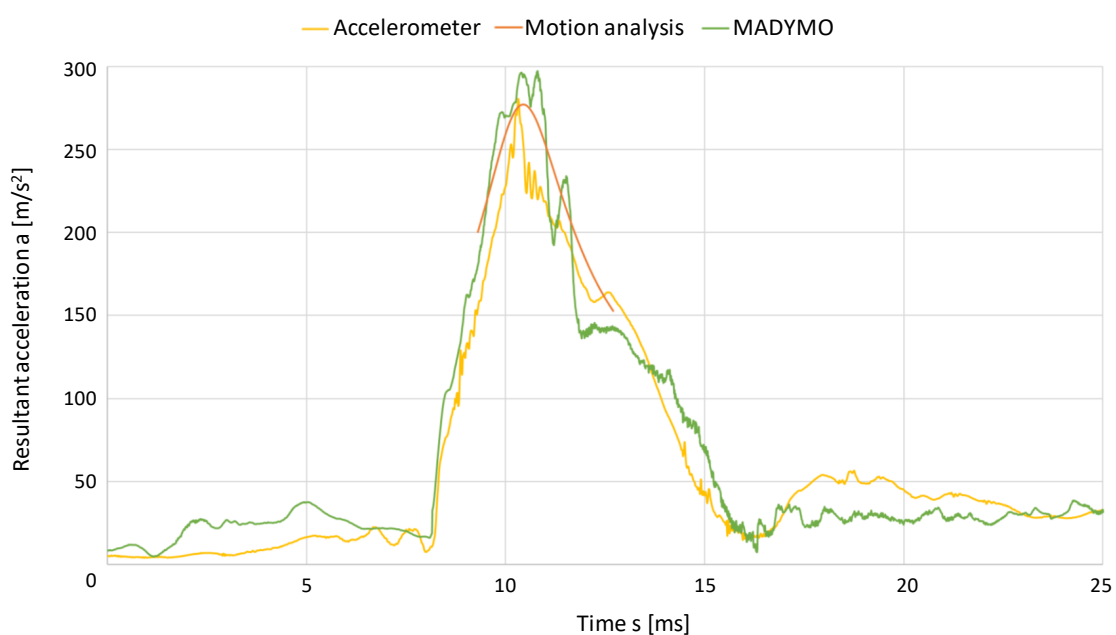


Fig. 39 Resultant head acceleration values for different measurement types

Nonetheless, the case showed just a close distance and not a direct cranial impact due to several possible aspects. Firstly, the seating situation. Both, real-world and simulative dummy were restraint by a harness and additionally by the arm rest geometry. It was noticeable, that arm and shoulder were substantially involved in order to remain a

maximum of distance of the head to the ground, which was not able to be overcome by the bending of the neck. A detail view is given in Fig. 40.



Fig. 40 Head and neck structure of the HybridIII-3YO dummy

As the neck structure is described as being able to show biofidelic flexion and extension motion, lateral bending is limited here especially by the neck's geometry. As the neck does not show any lateral notches or similar, bending can be recognized only due to the butyl rubber's ability of being compressed respectively stretched on the opposite side. In this respect, it shall be only argued, that the flexibility might be too limited compared to a real human body. It may also represent a special case, in which muscle contraction and awareness of the imminent impact could lead to the reduced flexibility. The fact is, that ATDs are initially intended for frontal impacts or sled tests. This needs to be highlighted also for the numerical dummies. It is clearly stated, that the models were not validated for side impact loading, but may give acceptable results in these conditions [96]. Unfortunately, a corridor for this description is not given. The presented side fall case turned out to be a deceleration scenario of the head only and being without a direct cranial impact. Nonetheless, the gathered acceleration graphs from the different measurement and simulation approaches correlated. The term *side impact* shall be seen as relatively here for the head.

The full-scale test was conducted once more – this time with the dummy equipped with a helmet. Fig. 41 shows this case in time-sequences.

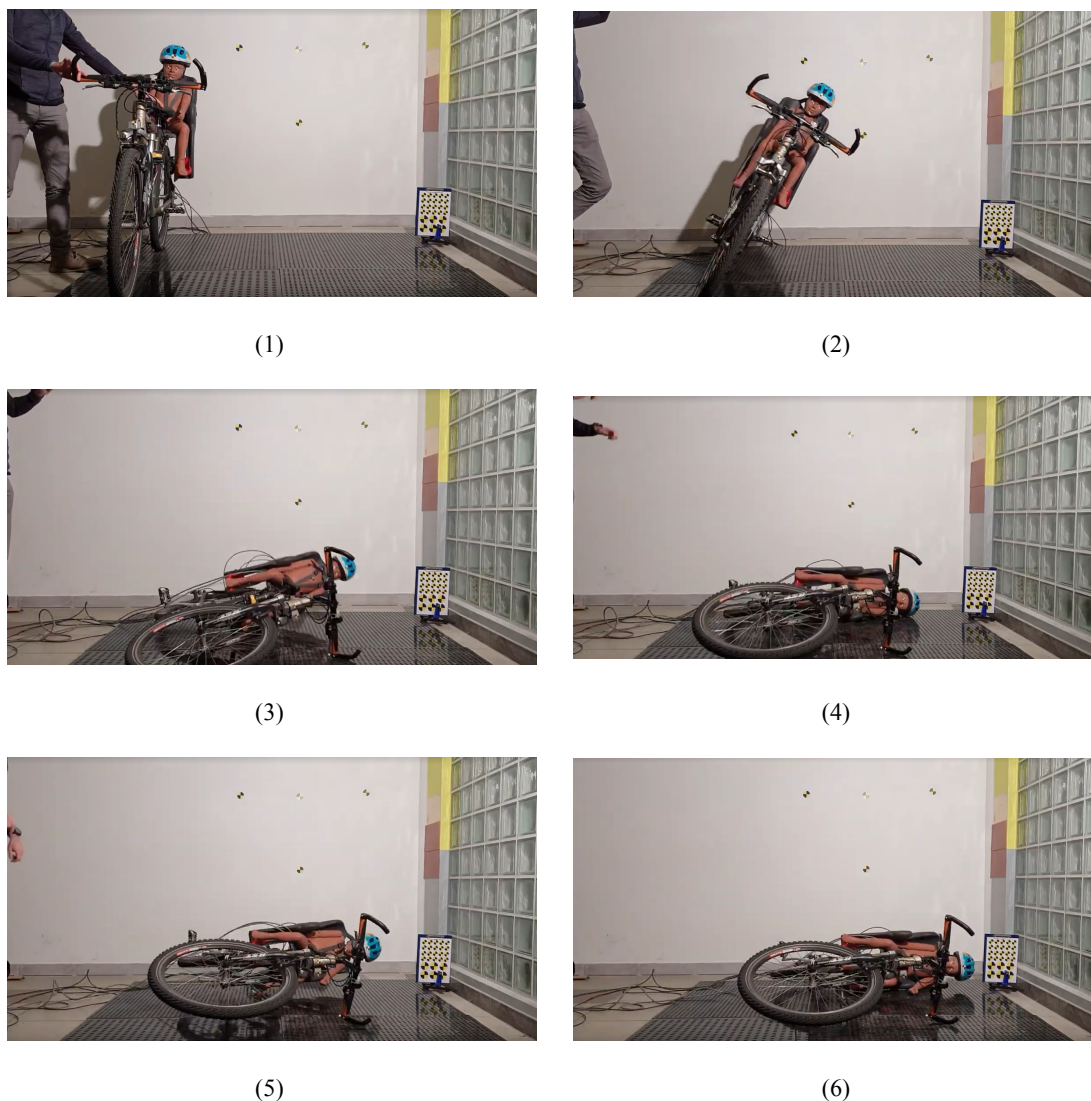


Fig. 41 Sequence of falling over after including a helmet, recorded at 30 fps

As the presence of the attached helmet literally reduced the gap between the ground and helmeted head, a direct cranial impact could be observed and measured. Fig. 42 illustrates the acceleration curve, which was measured by the use of the piezoelectric accelerometer inside the dummy's head.

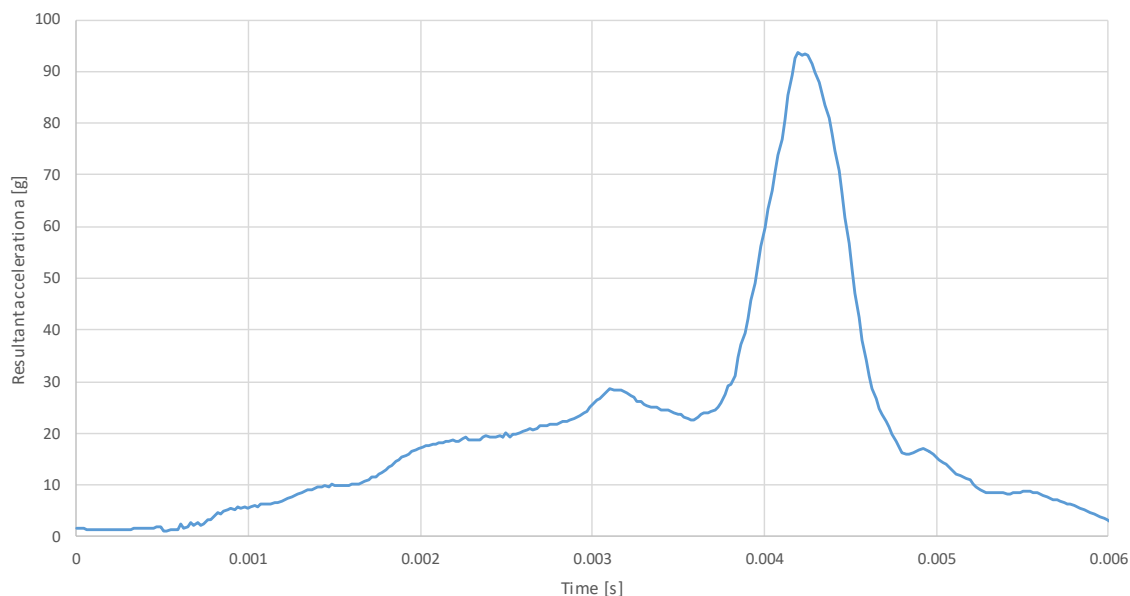


Fig. 42 Acceleration graph for the head (equipped with a helmet), measured by an accelerometer

The head's CoG acceleration curve features a narrower, comparing to non-helmeted situation, corridor of high acceleration with a peak at 93.77 g, equal to 919.9 m/s². The peak acceleration raised in this concern by the factor of 3.28 compared to the unhelmet situation with 280.5 m/s². Moreover, the helmet's EPS layer – a shock absorption layer – showed a clear crack in the area of impact after the experiment. Red arrows point on the crack in Fig. 43.

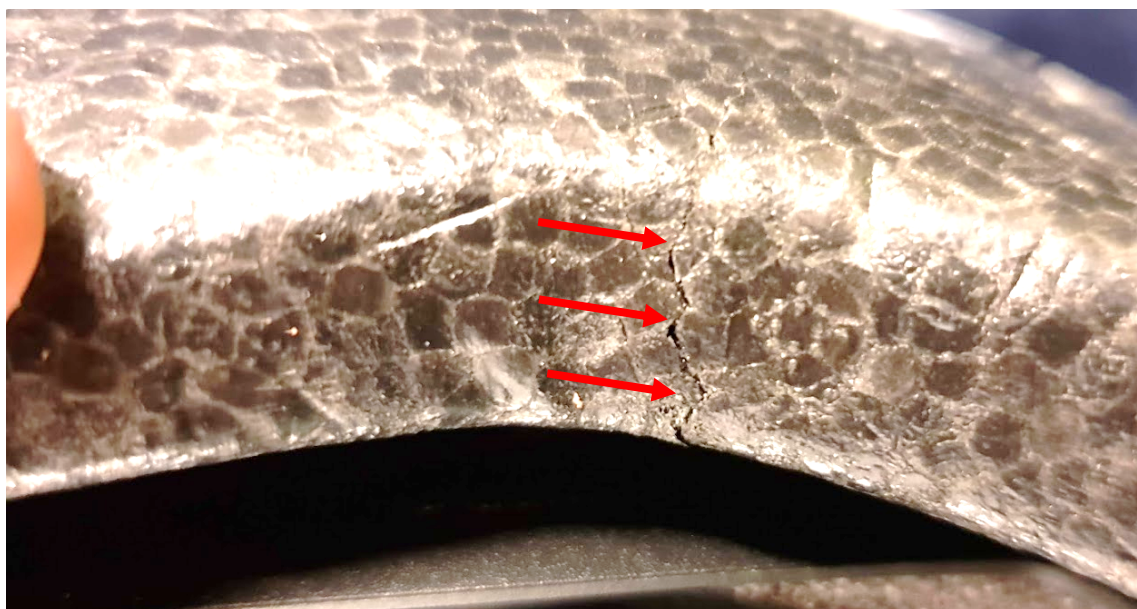


Fig. 43 Crack in the EPS of the helmet – visible from the side of impact

As a crack in the shock absorption liner occurred, it proved the helmets functionality in its base intention. On the other hand, it raises the question, if the presence of the helmet

generally raises the level of vulnerability for the transported child. In this context, it is surely worth to mention, that the presence of a helmet minimized the possibility of reporting a bicycle side fall without a head contact to the ground to an absolute minimum. In contrast, it was recognized in the helmeted scenario, that the limited neck flexibility was not enough to overcome the maximum of distance to the ground, produced by the combination and interaction of baby carrier arm rest, arm, shoulder and torso of the child. Even by a suboptimal constellation and interaction the head impact might be a reasonable outcome, even for the used dummies in the real and numerical test. This is stated also in the literature, especially regarding the treatment of children after similar cases [39,40]. Finally, the experiments without the helmet showed a value for the resultant head acceleration, which has to be considered as a presumable minimum of linear resultant head acceleration, when it comes to a comparable side fall scenario. This acceleration value might be raised to significant higher values, when it comes in fact to the presence of a head impact and not only to a rough deceleration of the head. This could be the case, when the geometry of the helmet helps to overcome the remaining gap between the child's head and the ground.

5.4 Chapter conclusions

The real-world experiments with an ATD helped to validate the numerical results. However, they underlined the differences between the HybridIII-3YO-dummies in virtual and real world. Especially the ability of lateral neck bending compared to a real neck of a human being. The dummies and models of the dummies, were initially intended for frontal impacts or sled tests, also connected injury criteria such as the Neck Injury Criterion (NIC) are mostly limited to phenomena of neck flexion and extension. Thus, it remains, that kinematics and acceleration values might be able to be mimicked by the use of these dummies and models. Their usage may lead to acceptable results under these conditions [96], especially for the evaluation of head accelerations as in this example and experiments. Nonetheless, several rough simplifications by using the MADYMO approach are leading to a specific uncertainty, which reduces the ability of proper assessment of the situation within the child's head. At first, this is the ellipsoidal representation of a complex geometry, which a rigid centre of gravity for this instance. As deformation and displacement of the cerebrum may take place, also the centre of gravity would change its relative position. Moreover, the interaction between the head and for example the ground or a vehicle's bonnet is a contact, which plays a central role

and is reduced within the MADYMO code to one single characteristic contact per pairing, following firstly the stiffness by loading and unloading curves for defining finally the peak force and secondly a hysteresis loop, which leads to a specific energy absorption; both important aspects, that might change through the change of geometry or instance-internal interaction already [14].

6 Creation of a Finite Element Head and Brain Model of a 2-year-old

“But we still haven’t unlocked the mystery of the three pounds of matter that sits between our ears.”

(Barack Obama, BRAIN Initiative inauguration, 2013)

6.1 Introduction

The numerical and physical experiments in the previous chapters used accelerometers, high-speed cameras, numerical simulations in different codes and full-scale drop tests in order to clarify motion patterns during impact situations. Even though these approaches delivered illustrative results each of them in their own sense, they were not able to overcome the visual barrier of the skull. Moreover, they all based in their assessment on a rigid, simplified head structure. This prevents the observer from having a deep understanding of motion and interaction of the engaged parts and instances with each other, which are crucial input and inevitable for an accurate injury assessment. Although dummies were completely or at least partially validated for the shown impact cases, the base for their validation can be found in the end in the medical imaging techniques of computed tomography (CT) and magnetic resonance imaging (MRI) and the evaluation of pathological cases. This form of evaluation implies already, that it is a comparison of the input variables such as fall conditions, velocity, angle etc. – which might be transmitted already incomplete or assumed – against pathological results. Particularly the view onto the injury causing event is missing, which forces to rely on experience, studies and empirical data. Since a few decades, the application of numerical models is seen as promising in the resort of connected research in order to overcome this issue. A group of models, which is significantly underrepresented is thereby the child model sector. Especially the physiological changes in the first years of living underlies in their presence and the current state for children even for the same age a wide spread. Several models try to cope this background by a scalable model, which bases on two averaged age states, for

example a 6-month-old infant and a 6-year-old child, but finally spans a line between them by increasing or decreasing scalable parameters. Even though the number of these models is raising, free availability of these models and their connectivity to regional averages of children is purely not given. It forms a demand, that is more and more in focus, particularly in sectors of automotive, where passive safety devices need to be created for specific user groups and act effectively for them.

Consequently, for the own purpose of assessing properly impact conditions and possible injury outcome in the context of this thesis, an original Finite Element Head and Brain Model¹ is presented and proposed for further usage. In this concern, it was necessary to gather data of a patient without pathology in form of DICOMs. The data needed to represent a possible average of a 2-year-old for the geographical region, where the model is about to be used and referred to, in this case the lower Silesian region of Wrocław in Poland. The proceeding of the data resulted then in an accurate geometrical (CAD) model, which was translated into a discrete (CAE) model for proceedings within the LS-DYNA code. A main aspect has to be seen in the envisaged calculability of the model in a timely manner by ensuring nonetheless a high level of detail in both, model and results. The term of “*in a timely manner*” has to be seen relatively, as current complex models are partially calculated over several days even on powerful clusters.

6.2 Choice of patient data

It is advised to start the choice of appropriate patient data by acquisition and statistical processing of data. According to this, the process needs to be directed to a specifically described or defined kind of envisaged patient or patient group. In terms of an envisaged biofidelic model. A base for such a catalogue are the craniometrics [116]. To give a hypothetical example aside the envisaged child model: this catalogue could describe the 50th percentile average male of the Caucasian race in the middle of his thirties and living in Eastern Europe, if it was the statistically described average main user of a MTB with a mounted baby carrier. A limitation to have access to such an appropriate data set can be seen in the circumstance, that medical imaging data is first of all due to personal data security not freely available and secondly created only due to the suspicion of a

¹ Herein presented Finite Element Head Model of a two-year-old child was worked out by the author within the project “aHEAD – The numerical system of multivariate head models to simulate the pathophysiology of brain injury”, co-funded by the National Centre for Research and Development of Poland under the grant number LIDER/8/0051/L-8/16/NCBR/2017.

pathological state of the patient, which makes the further and detailed medical investigation necessary. Particularly the latter makes the availability of CT-scans for infants and children very rare, as the imaging process induces radiation and becomes consequently to a last resort within patient treatment.

A preliminary catalogue of 12 anonymised data sets was provided on project request by the Dolnoslaski Szpital Specjalistyczny im. T. Marciniaka in Wrocław, Poland, which were hospital-internally chosen according to the main criteria of a regional average for a two-year-old male child without pathological finding. Consecutively, the anonymised data was analysed and reviewed by dr. Artur Kwiatkowski, Wojewódzki Szpital Specjalistyczny in Legnica, Oddział Neurochirurgiczny and dr. Konrad Kubicki, University Hospital of Wrocław, Department of Neurosurgery.

According to the initial craniometrical catalogue, one data set for the establishment of the envisaged Finite Element Head Model was chosen. As stated in their project-internal review, the preferred DICOM set included beside series with contrast also an angiographic series, which covers at least 2/3 of the head within the scan. This was seen as supportive for the recognition of vessels. Furthermore, the scans resolution is said to be fine detailed, also well described by a span of 1 mm only between the images. Also, a sagittal T1 series was included. Missing in this data set was the certainty of the absence or presence of a fontanelle due to missing clear visibility. The scans were limited to MRIs only – a CT was for none of the data sets included, which increases the level of difficultness for achieving all commonly implemented instances within a full Finite Element Head Model (FEHM).

6.3 Scope of the two-year-old FEHM

The aim behind the creation of the 2-year-old child FEHM is to simulate the pathophysiology of brain injury by creating the therefor necessary numerical system. Connected with the simulation of the pathophysiology is the detection of the respective pathomechanism behind. It is important to correlate so far only known pathophysiological outcome with identified loads to the brain, which would destruct specific brain structures. This detection is widely envisaged in this field of research, as it is promised to enhance injury prevention and treatment. Against the possibility for adult anthropomorphic, the success of a child model currently cannot be described by a wide model validation against real-world experiments, for example like the general used experimental results of Nahum

and Hardy, or other newly published post-mortem experiments [86,117,118]. For child models, the first milestone of success has to be seen in achieving and presenting a FEHM with all necessarily and functional instances to simulate the pathophysiology of brain injury due to mechanical load. Seeing it out of the view from current state-of-the-art head and brain models like SUFEHM, WSUHIM, KTH and UCDBTM, the implementation of non-linear material models is mandatory [52]. As a main contribution to the field, consequently a new quality of child head models has to be achieved by the presented approach. It shall not be stand for a single duplicate with an extended feature of a so far known model, but is intended to show a new insight into brain instance and tissue interaction. This makes for example also the detailed representation of gyri and sulci of the cerebrum necessary, which was exemplarily introduced to the league of state-of-the-art models by the YEAHM [119] model in 2017.

At this stage, it has to be described a catalogue, where instances are named, which are strictly necessary to overcome limitations or simplifications of current models. Consequently, a more accurate anthropomorphic has to be shown. The 2-year-old FEHM will show:

- the skull with changing thickness and respecting the layers of lamina interna, diploe and lamina externa
- the dura mater with its folds falx cerebri and tentorium cerebelli
- the pia mater
- the vascular system, especially with superior sagittal sinus, transversal sinus and bridging veins
- left and right hemispheres of the cerebrum including a white and grey matter segmentation
- the brain stem
- the cerebellum
- a separation of the Corpus Callosum (CC)
- the Liliequist membrane
- cerebrospinal fluid (CSF).

The calculation of the discrete (CAE) model is performed by using the solver of LS-DYNA.

6.4 Anatomical specialties of a child's head and brain

The beforehand presented catalogue concentrates on a list of main head and brain instances, which can be found namely in both elderly and young humans. What is partially differing in the geometry over the time of life, is in one example the volume ratio of white to grey matter of the cerebrum. Beside the ratio of white to grey matter, especially the existence of both matter and their connection is potentially important for head injury assessment and analysis. The mechanical properties such as Young's modulus or Poisson's ratio in terms of the values of both structures might be similar, the structure of white and grey matter differs significantly. White matter is recognized as inheriting in relation only a small number of cell bodies but a huge amount of long myelinated axons, connecting to a primarily cell body-rich grey matter. Hence, this interface of both structures is assumed to be highly influenced by their differing structural abilities to carry loads and could lead to characteristic injury patterns in the area of matter change. Moreover, and as above initially mentioned, the ratio of white to grey matter changes over the life span. It was stated, that the development of white matter starts in the brain stem and processes toward cerebellum and cerebrum, described by the direction from central to peripheral and from inferior to superior as well from posterior to anterior [120]. The authors of the European PIPER project chose for the ratio of white to grey matter in their model for a 3-year-old the value of 0.44 [85]. Regardless of this, it has to be respected, that this value might be an averaged value, which underlies a characteristic change in the first years of life as well due to the natural process of maturation. Maturation is said to lead to a decreasing grey matter volume. The general change of volume, either for white or for grey matter, as well as a disproportion of both matters to each other is strongly connected to diseases such as dementia or schizophrenia for mature brains. An optimal balance of white to grey matter on the other hand is believed to be supportive for a minimized energy consumption and maximized functional efficiency for healthy people [121].

Another specialty is described by the cranium, the human skull, a complex structure, which is formed out of the neurocranium and the viscerocranium. Together, they are surrounding the brain and forming as well the facial skeleton. Particularly the neurocranium undergoes significant changes in its bone structures. The neurocranium is formed out of the chondrocranium, the base of the skull and mainly membranous parts, which together are the cranial vault. This membranous cranial vault is composed by two outer layers of cortical bone, the lamina interna and lamina externa, filled on the inside

by the porous layer of the diploe. This composition is not valid for infants or very young children, as in their case the cranial vault is still unilaminar, but starts to develop the diploe gradually [122]. The composition of these structures can be seen in CT scans and is given below in Fig. 44 for a 2-year-old child and a 77-year-old woman. The process of forming out the diploe layer completely is said to be done up to the fourth year of life [122], while other research is stating the diploe already earlier. In a consequence, the diploe layer can be found also in some discrete (CAE) models of younger children [85]. The implementation of this porous structure can have influences to exemplarily flexibility and shock damping ability, hence to the mechanical behaviour of the skull instance during load.

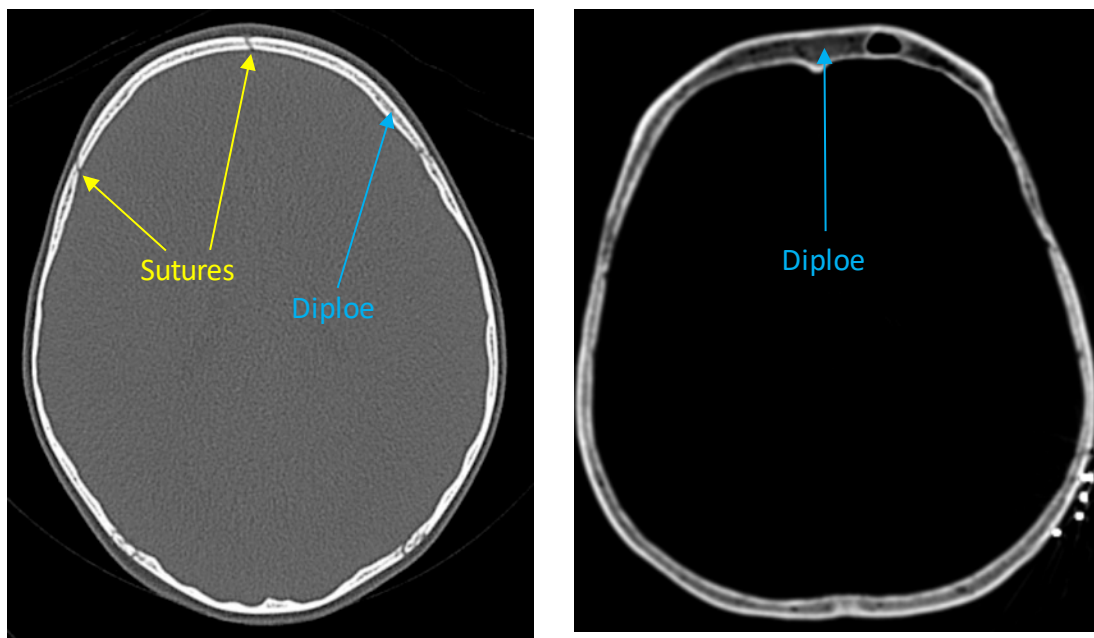


Fig. 44 CT of a 2-year-old child showing the sutures and portions of the diploe layer (left); CT with an established diploe layer of a 77-year-old woman (right)

The already establishing layer of the diploe can be seen in the child's CT scan in Fig. 44, even though it does not represent a permanent existing layer but rather appears portion wise due to the changing skull thickness. Similar to differences in the timely appearance of this layer, also general material information at a specific age are rare or cannot be simply transferred one-to-one. In a consequence, inter- and extrapolation of values based on real-world cases helped to estimate feasible values for child models. Cortical bone and porous bone was estimated in this context with a Young's modulus of 4 respectively 1 GPa [85],[77], while in the same elderly bone structures values of 10 to 12 GPa, respectively values of 0.6 to 1.1 GPa for the elderly porous bone are used [123]. Having

another look at Fig. 44, the thickness of the adult's cortical bone undergoes no significant changes. Oppositely, the overall skull thickness undergoes changes by the geometry and in a major sense by the changing thickness of the diploe layer. The portion wise appearance of the diploe layer in a young child's skull plays hence a specific role. Directly connected to the skull bones – also in a geometrical meaning – are the sutures and the fontanelles, which are showing as well changes over the life span. Fig. 45 gives a detailed view on the sutures and the fontanelle of a 2-year-old child and an adult skull.

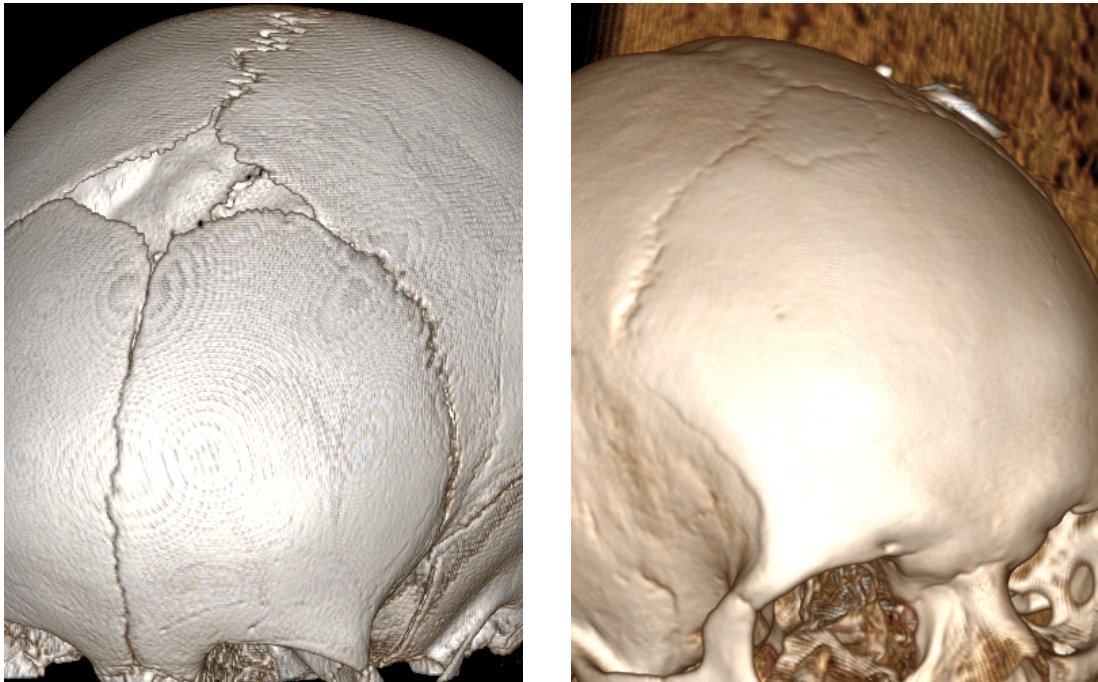


Fig. 45 Comparison of a child and adult CT with focus on the sutures and fontanelle

The sutures are acting as a fibrous joint in order to combine the different cranial bones with each other. Their flexible behaviour plays a significant role in the moment of giving birth, allowing a specific displacement and deformation of the whole skull. Nonetheless, the skull remains in this moment a complex assembly with the possibility to secure the brain. Over the next years of life, the sutures will change their material properties naturally and reach values close to the cranial bone, as it can be found in adult structures [77]. Giordano et al. used for their 3-year-old numerical model a Young's modulus of $E=8.1 \text{ MPa}$, a density $\rho=1.5 \text{ kg/dm}^3$ and the Poisson's ratio of 0.22 to describe the material characteristic of the sutures [85]. Although the sutures as a link change their material properties close to the one of cranial bone, geometrically the path of the sutures can be still recognized in CT of adults and elderly persons. This can be seen as well in Fig. 45.

It was reported, that sutures can change into a stiffer structure in extreme cases even relatively late within the mid-ages of humans [124].

Closely related to the sutures are the fontanelles, which are common gaps in the frontal and back side of the human head [122]. Fig. 45 showed the frontal fontanelle in the child's scan but without the visible membrane, as it is a CT-scan. It is a collagen-rich membrane, which fills out the fontanelle and closes over the first years due to calcification of the membrane itself and the common bone growing [125]. The fontanelles – similar to the case of sutures – or at least their original positions can be recognized also years after the closure of the skull. Again the circumstance of the fontanelle presence and its closure in terms of time and amount, as well as the change of its material properties close to the characteristics of cranial bone leads to an intense discussion of their implementation in FE models. For the case of the strict necessity of their implementation, underlying material properties may spread widely [126].

6.5 DICOM handling for the creation of a geometrical (CAD) model

Medical imaging data is provided and exchanged commonly as DICOM datasets, as a result of the medical investigation process by using computed tomography (CT) or magnetic resonance imaging (MRI). As the intended visualisation of tissues is different, the general physics behind CT and MRI are so as well. While CT bases on ionizing radiation and shows in its image the differing densities of materials, the MRI relies on a generated signal. One can describe each image of a MRI set as a kind of map, which visualizes the proton energy in the different tissue types. The response signal for this map is generated in this way, that randomly orientated protons in the scanned body part are excited by the MRI scanner. Then, the proton response after getting aligned in the bore of the scanner due to the magnetic field is measured. Furthermore, a repeating sequence of excitation and resonance of these protons is created. The latter by the radiofrequency pulses, which lead to a spinning of the protons in phase to each other.

The measured physical parameters thereby are two: On the first hand the relaxation of the protons after the pulse is removed and the protons are realigning with the magnetic field. The second parameter is the dephasing of the protons, which were forced into spinning by the radiofrequency pulses. In this context, it is the loss of resonance, which is measured. The first described phenomenon of realignment of the protons with the

magnetic field is the measured base for the T1 signal or T1-weighted image sets. If the protons are realigning faster, the signal is recognized as stronger and makes the tissue more visible in the MRI image. So called T2-weighted image sets are based on the T2-signal, which visualises the dephasing effect of the protons, so more precisely the speed of proton spin dephasing. The signal increases when the dephasing occurs slower. To use these two phenomena helps to visualise different types of tissue by their characteristic behaviour in these senses. Protons in fat are realigning quickly and show thereby a high energy. The strong T1 signal helps to identify a fat tissue. Consequently, weighting images toward T1 means to concentrate on fat in body tissue. Protons in water on the other hand, are dephasing considerably slower, which forms the base for T2-weighted images and the recognition of water on body tissues [127–129]. This knowledge can be used as well to distinguish in a timely manner T1- from T2-weighted images by concentrating on the cerebrospinal fluid (CSF). CSF is dark represented in T1-weighted images, but very bright visible in T2-weighted images, as CSF inherits no fat, but consists out of approx. 98–99% water and a smaller amount of protein and glucose [130]. Independent from T1- or T2-weighted images, bone cortex is containing no free protons and hence lacks in direct representation on MRI image sets for common repetition and echo times [127–129].

The above mentioned Repetition Time (TR) and Time to Echo (TE) are important parameters for the creation of T1- or T2-weighted images. TR describes in this concern the time between the pulse sequences at this one specific slice. TE as the second parameter defines the time from the start of the radiofrequency pulse up to the received echo of this sent signal [127–129]. The visual difference of T1- and T2-weighted images is given for the base of the envisaged 2-year-old child model in Fig. 46.

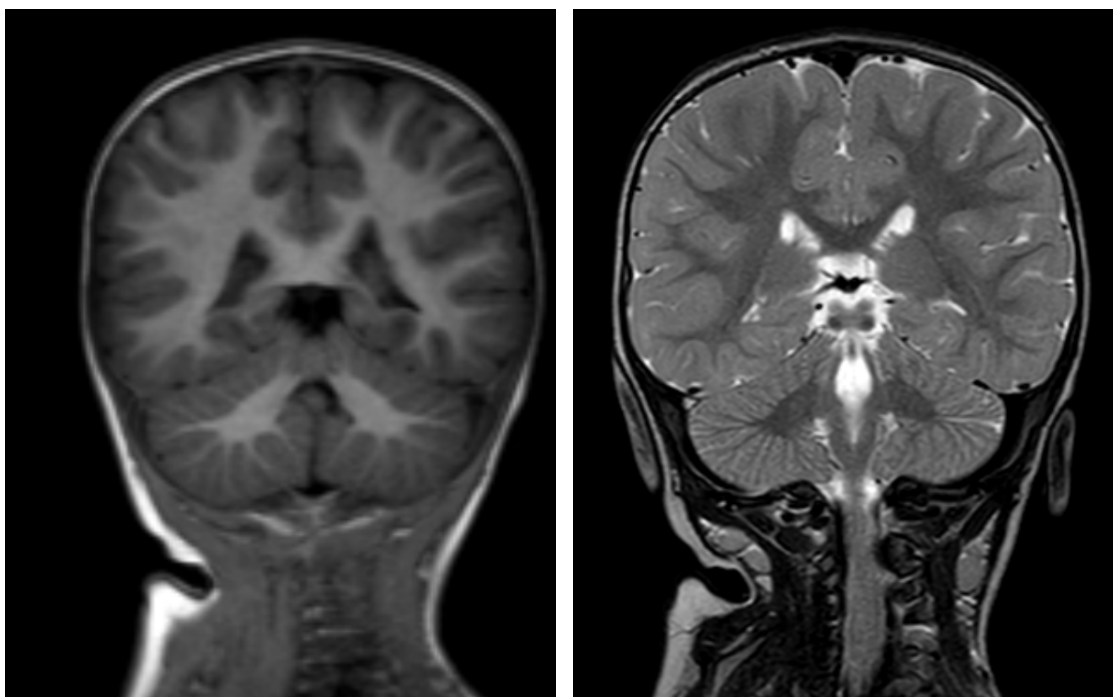


Fig. 46 T1-weighted (left) and T2-weighted (right) MRI of the 2-year-old child

Furthermore, common parameter values of TR and TE are given in Table 6, also the particularly used parameter values for the example shown in Fig. 46.

Table 6 Commonly used MRI T1- and T2- sequences and their approx. TR and TE times [128]

	TR [ms]	TE [ms]
T1 weighted (short TR and TE)	500	14
T2 weighted (long TR and TE)	4000	90
Example: 2YO T1W	7.1	3.2
Example: 2YO T2W	6041.1	100

Summarizing, producing T1- and T2-weighted images relies on a complex of decisions, which are in total influencing especially the visibility of specific structures due to their physical behavior during the MRI scan. Adjusting exemplarily TR and TE times or the additional usage of contrast during the scan can intensify a structure's visibility or lead close to its invisibility. Even though that per each MRI scan a bulk of scans and techniques is performed, it has to be respected, that each medical investigation is intended to prove the presence or absence of a specific pathological state. The creation of a global head model is regularly not intended as primary outcome of the CT- and MRI-based investigation, but exemplarily the verification of the absence of micro bleeding in a

patient after a head trauma. This circumstance might complicate the later workflow on the DICOMs for the brain model creation.

The work on generating geometrical models and data will be performed by direct work on the DICOM datasets. The dedicated open-source software *3D Slicer* enables in this concern to load and connect several different medical imaging sets at once. In a consecutive step, it is possible to compare information out of single pixels but for different loaded scans with each other. The possibility of this visualization and assessment enables the user to distinguish the numerous structures with a high level of certainty due to their characteristic behavior or visibility in T1- and T2-weighted images. Thus, it seems to be possible and particularly automatize the process of comparing location-related pixels of different scans with each other and categorizing these resulting voxels into separate instances. However, Miller stated, that also several years of intense research were not successful in establishing a generally accepted and doubtless working segmentation algorithm, which could fulfil the task based on MRI automatically. Consequently, still mainly manual methods are employed and preferred in practice [131].

By following an at least partially automatized approach of segmenting brain tissues, the integration of an atlas is a mandatory step. This kind of general map of occurrence for the specific brain structures has to be established beforehand. It shows finally the average occurrence for an instance for the group of patients, who were considered to be included in the data set for the atlas. Thus, this supportive element for the segmentation algorithm allows to correlate the selection with data, that is considered as reasonable or presumably true for the so far non-catalogued or segmented patient. It should be noted, that each of such an atlas with its own average is representing only the average for the patients, who were the base for this atlas. A bigger deviation from this average – it may be in terms of age, geographical origin, anatomical abnormalities etc. – may lead to a significant error in the result. It behaves similar in the preparation of the used DICOMs and the manual setup of input variables for each structure within the reading algorithm. As for the creation of MRIs the TE and TR times usually differ due to different assumed forms of injuries, also the choice of contrasts and greyscale values for each of the tissue types within the separated exemplarily T1-, T2-weighted or T2-FLAIR images underlies huge effort and higher experience, hence a high level of MRI interpretation competence. In a summary, the higher amount of work might be justified for the work on a bigger number of patients and their corresponding models. This reasonability is not given for a single model.

Consequently, establishing the presented child model follows the full manual approach. Threshold filters were applied only for the initial selection of a part complex. Fig. 47 shows here as an example the explained work steps for a mid-aged male patient. There, an initial selection of the grey matter via threshold filter includes also huge portion of the surrounding layers, particularly the skin. This circumstance forces to clean the initial selection manually – a gradual work, which has to be performed image by image. The higher effort reveals the general outer geometry of the cerebrum including the sophisticated structure of gyri and sulci in a more convenient detail level.

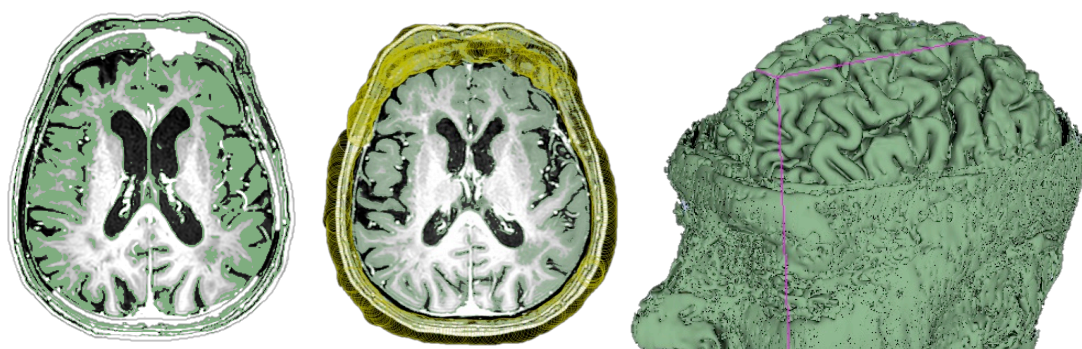
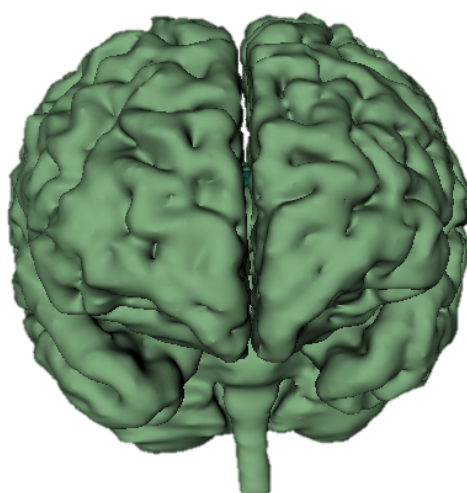


Fig. 47 Manual segmentation of grey matter by applying a threshold filter

The same approach has to be followed during the classification of connected but differing instances, especially regarding the white matter. Fig. 48 illustrates the resulting complex out of white and grey matter. With viewing with the MRI views in the bottom row of Fig. 48, the necessity gets clear to verify permanently in a manual way the selection results out of the sagittal, axial and coronal views as well as within different image sets such as T1, T2, T2-FLAIR, 3D-DRIVE etc. in order to keep the geometrical model accurate.



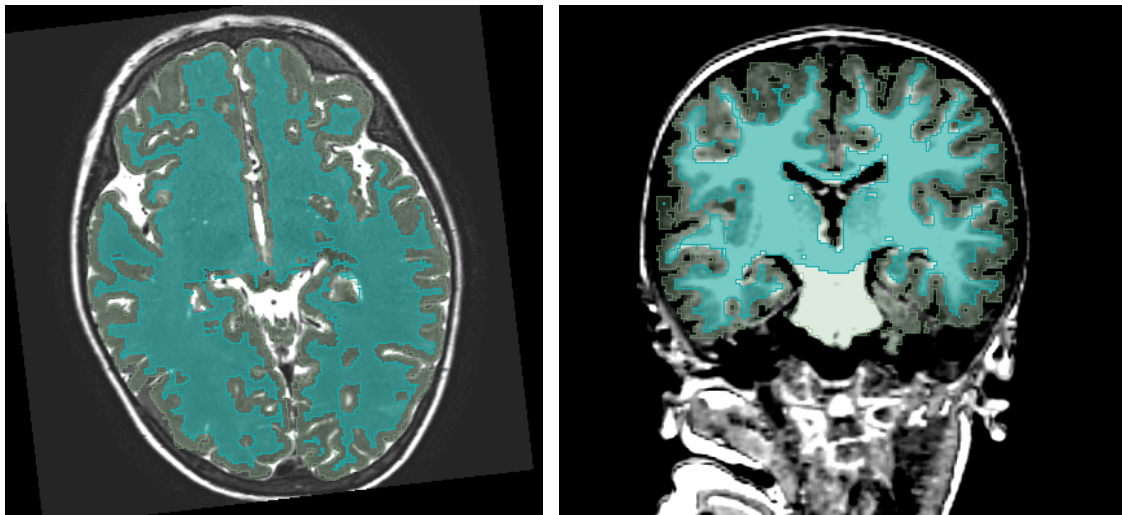


Fig. 48 An initial segmentation of the brain as a full complex (top) as a result of manual segmentation of white and grey matter in exemplarily T2-weighted 3D-drive axial scans (bottom, left) and T1-weighted coronal scans (bottom, right)

Comparing Fig. 48 with its views of the brain of a two-year-old and Fig. 47 with its visualizations of a mid-aged male adult, one can easily recognize the already widened structures of gyri and sulci for the adult. It points on the characteristically situation for a child's brain within its skull, which – in relation to the older patient – seems to be compressed and stuffed into the skull. Although this compressed state, it shall be noted, that the haptics of brain matter, which could be observed during surgery, is described as soft and often figuratively compared to a pudding [132]. The deformability of this structure, even though it is secured and free of a pathological state within the skull, leads to an important limitation of head models. The models are commonly created based on a real-world MRI. The permanently acting gravity during the process of an MRI-scan and according to this the position of the head of the patient in the MRI device leads to a natural deformation of the brain. As the brain finds increased support in accordance to the patient's laying position toward the meninges and the skull – barely surrounded by the CSF – the geometry is modified close to this area of support and contact in its natural shape. This may lead on the one hand to problems in distinguishing the separate brain instances, on the other hand to a general shape deviation. The circumstance might to be considered as one of the limitations of current MRI-based, high-detailed full body models and Finite Element Head Models which might represent by the initial position of the brain and the initial geometry of this brain a laying, but not a standing or sitting person, even though the model is configured to a standing or sitting anthropomorphic.

6.6 Original method to extract the skull geometry out of a MRI data set

It has been already stated, the DICOM data set for the presented child model does not contain a CT scan. It should be repeated, that none of the DICOM sets delivered from the hospital did so either. This sets another barrier in the creation of a head model, as regularly the base for the appropriate creation is a computed tomography. This technique is able to show differences in the materials' densities and hence is able to visualise bone. Bone does not contain free protons, which makes it invisible on conventional MRIs [127]. As the scans were also already performed and did not include it, it was not possible to have recourse on unconventional imaging techniques, for example the Black Bone MRI [133]. Nonetheless, the reconstruction of a proper fitting skull has priority in this task of model creation.

The recreation of the skull had to be based as well on the available data to avoid scaled, foreign model parts. It is thereby inevitable to have recourse on the given T1- and T2-variants. They enable to have a high-detailed view on structures according to the presence of fat or water in them. Skin layers or also thinner layers such as the dura mater can be recognized with a high level of certainty. Consulting with the neurosurgeons within the aHEAD-project and reviewing also the type of contact to the skull, the presence of these closely located structures makes it possible to define a corridor, in which mainly bone material would be present and visible on a CT-based DICOM. The borders toward the skin respectively to the dura mater are giving in a consecutive step information about the location of lamina externa and lamina interna. As this work has to be performed manually for each image of the scan and needs to be counterchecked by the other scans within the DICOM data set, the manual work effort is considerably high. A preliminary result of this work step is shown in Fig. 49.

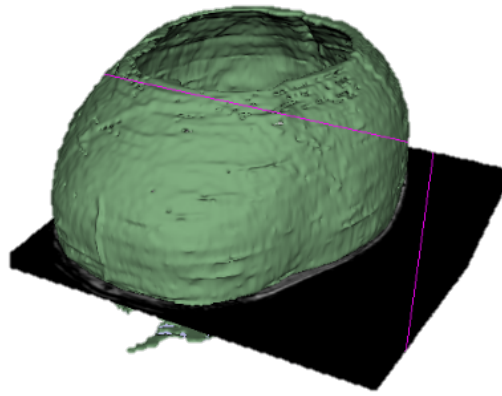


Fig. 49 Preliminary result of locating skull bone in a MRI

The method overall allows to generate in a first step a cage for the brain, which corresponds already to the geometry of the patient-specific brain and skull. It makes an iterative approach of refining the selection and consequently geometry inevitable, in order to gain results comparable to the detail-level of a CT-based skull-recreation (see Fig. 50). The advantage of this presented approach over morphing a foreign child skull to the geometry of the present brain model is given especially in the ability to follow the complexity of the brain geometry and keeping later a feasible distance between the different types of tissue. Moreover, the geometrical skull model is particularly not only following the structures of gyri and sulci, as in this case exemplarily layers of arachnoid with changing thickness would be simply neglected. This means, the morphed skull would tend to follow the pia mater due to the described uncertainty, but not the essentially important dura mater. But the approach involves the risk, that the skull thickness can be locally incorrect as it is basing on a manual and visual segmentation. A natural error has to be considered, as already contrast and intensity by the output via a computer screen are not able to show the full spectrum of the data behind the DICOM visualization, thus they are artificially reduced, as the manual work happens on the reduced output. An geometry adjustment has to be done in the end, which equals to an approximation based on experience and available empirical data. The disadvantage is significant, as the presented approach occupies several days of work, while a CT-based skull recreation could be performed in several minutes only. Nonetheless, it shows, that a preliminary skull model can be established out of a MRI data set and opens new approaches of model creation, which are not standing against the ethical maxim, to reduce medical action to the actual necessity of the medical investigation itself – without enhancing the medical treatment and investigation into a random data collection.

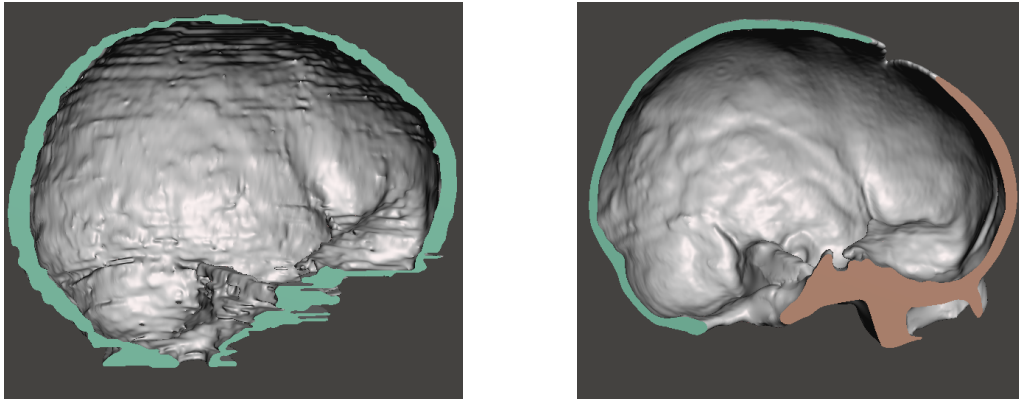


Fig. 50 The initial skull recreation by following the authors approach based on a MRI dataset (left) versus a conventional recreation based on a CT-scan (right), both shown in Meshmixer

The work step of the initial segmentation is followed consecutively by several iterations of correction, where a database of conventionally out of CT-scans created skulls for similar aged children can be helpful regarding the assessment.

In a consecutive step, the post-segmentation work has to be seen as extended by the manual implementation of so far also invisible features. Here, the face structure, sutures, fontanelle have to be named as examples. Fig. 51 shows the finalized skull geometry which includes already the entire facial skeleton and gives also an insight into the complexity of the achieved inner skull geometry as well as the accurate fitting situation of skull and brain in an assembly.

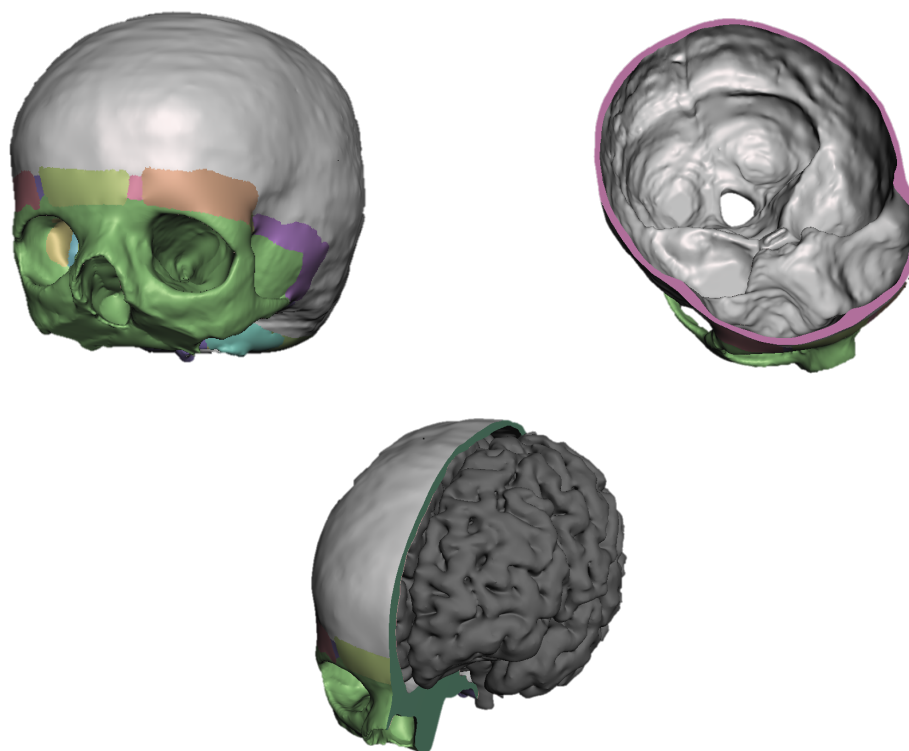


Fig. 51 The finalized skull geometry (top left) with its section view (top right). The combination of the geometrical models of brain and skull proves the applicability of the method (bottom)

The shown approach to generate a skull model out of an MRI provided finally a skull geometry, which is satisfying the demands of representing a pendant to the skull, surrounding the brain accurately in terms of geometry and overcoming thereby the lack of conventional data. The localization of the bone layers of lamina interna and externa might be corrected by a huge time effort and work force for consultation by medical doctors and neurosurgeons, but lacks in a certain amount of certainty. Another example has to be given in this context by the recognition of the diploe layer. Based on the MRI, it is impossible to declare a portion of the skull to this layer, as the skull contains no free protons and is not visible. The knowledge, that the layer of the lamina will show up with a rather constant thickness, see in this context again Fig. 44, the distance between both of these defined layers in the here achieved geometrical model will reveal the presence of the diploe layer – also in the discrete model later on. Implementing finally features such as the facial skeleton from another or even multiple patients points on a compromise, particularly an additional task.

Generally, that the model might not be able to keep up with the accuracy of a CT-scan-based model, degrades it in a specific manner to an advanced, but rather artistic solution

and furthermore underlines, that up from this stage the model has to be seen as a generic model, but not as a personalized model of a particular single patient. Nonetheless, this form of a generic or anonymized model ensures the ability to be combined with the neighbored instances in an acceptably accurate way, which has a top priority.

6.7 Translation of the CAD-data into a discrete (CAE) model

Establishing the geometrical models for the head and brain instances of the scope was connected to high effort in order to prepare an assembly, that was in the literature even described as an active tissue floating within a rigid cranium [134]. Especially by recapitulating the term of *floating* within the latter statement, it opens the view to a highly complex problematic regarding the translation of the geometrical data and composition into a discrete (CAE) model. Firstly, the beforehand created geometrical data of each appropriate instance needed to be translated from the standard of a stereolithography model (STL) into a solid CAD model, which can be done by using dedicated software as CATIA. In order to reduce the number of translations and hence also error, which is naturally occurring due to the process of translation, a workaround can be seen in a straight input into dedicated meshing software as Altair Hypermesh, which was used in this specific example. The software also enables the user to connect several crucial actions within the preparation steps of the discrete model. By loading a STL model and proceed surface based in the sector of meshing in the same software, working at a minimum of acting across several codes is achieved. Moreover, the permanent verification in terms of the element's quality is possible, which was done for all instances regarding the values of Jacobian, internal angles, element length, internal time increment, status of duplication and questionable connectivity.

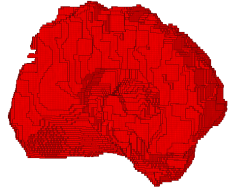
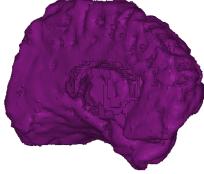
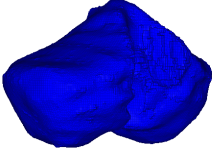
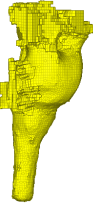
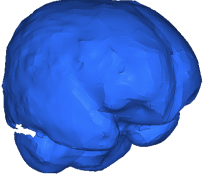
An intense focus was put on meshing the instances in a more advanced way than in commonly used Finite Element Head Models, where particularly geometrically complex parts such as the cortex were geometrically underrepresented in order to keep a hexahedral mesh. Also, the use of simpler meshing algorithms based on tetrahedral elements in order to keep a complex geometry but by risking to occur effects such as volumetric locking could be recognized mostly in currently available models. The latter, particularly for modelling soft, nearly incompressible materials such as the white and grey matter due to their high amount of water was more and more discussed [135]. The resulting artificial stiffening of tetrahedral elements can be at least limited by specific

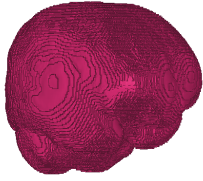
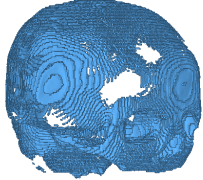
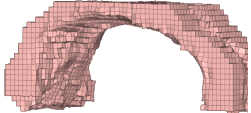
element formulation options in the later used LS-DYNA code, combined with an advised mesh convergence analysis. Mesh convergence is generally used as an assessment tool to find an adequate ratio between calculatory effort and element size, which is no more prone to significant changes in calculated stress by decreasing the element size, while the calculatory effort is kept in the same sense at a reasonable level. In a different approach to the described workarounds and the general demand of a mesh convergence, the decision was done moreover in this way, as the meshing toward a 100% hexahedral mesh for 3D instances was chosen and achieved, as these elements are not showing volumetric locking effects. The element size was optimized toward 1 mm, which takes recourse on the finest solution of the input for the geometrical data – the DICOMs slice step or resolution – while smaller hexahedral elements with a minimum Jacobian value of 0.3 – especially found at the most outer element layer – were used to keep the complexity of the input geometry within the discrete model. Basing on the instance of the skull – divided into its segmentations of lamina interna, lamina externa and diploe – as well as the complex of cerebrum, cerebellum and brainstem, it was possible to define the general space for the cerebrospinal fluid. The instance of the cerebrospinal fluid is thematically widely connected to a damper-like presence, told to be acting or securing the brain in moments of spontaneous mechanical load. Nonetheless, it still has to be seen as a rather described ideal or theory, while the actual true role of this literally two-millimeter-waterbed is not entirely clear, which might be as well connected to the wide spread of representations of CSF in the variety of Finite Element Head Models. A background needs to be seen in the problems arising out of the theoretical necessity of the clear and separate segmentation of both CSF and the neighboring structures of membranes. But the regular line up of an MRI examination is dependent and aligned to the assumed pathophysiology of the patient, which induces most often a lack of data for the creation of a generic model. This might be true already in terms of the resolution or slice thickness of the DICOM data set. Moreover, in the example of the Bridging Veins (BV), these might become only visible by the use of an appropriate technique such as the cerebral venous computed tomographic angiography (CTA), which represents a dedicated form of examination [136]. In a consequence, the composition of several visualization issues leads in most models and cases to simplification or combination of neighbored instances and their interaction, which might lead at least to benefits in terms of model calculation time and resources management. But nowadays increasing resources of calculation power enable to represent this initially mentioned *general space for the CSF* more accurately,

which inherits a problem of way higher complexity, when it comes to its presence and interaction. The CSF – seeing the border to the subarachnoid space – is in contact with the BVs. So far, CSF is mostly modelled only by solid finite elements and in terms of the assigned material properties by a low shear modulus [137]. The instance of CSF may include thereby likely also the pia mater, as this part of the meninges is covering the gyri and sulci and gets assessed in its results later just as the most outer node layer of the CSF. In newer approaches but basing on the modification of already existent FEHMs, a fluid-structure interaction (FSI) including arbitrary Lagrangian-Eulerian (ALE) formulation was used to represent CSF [138]. But still, it relies on a solid structure and a shell surface, which is locally considering moving or distorted mesh, but globally neglecting the subdural long-range flow of CSF. Closing the arch to the initially mentioned BVs, not only CSF might be modelled underrepresented, also the BVs are reduced in most of the models to 1D-elements, which are connecting in total only two nodes. In order to overcome this complex of underrepresentation and simplification, pia and dura mater as well as the bridging veins – whereas the dura and the BVs are connected to the superior sagittal sinus – all these instances were modelled separately by shell elements. The “*general space for the CSF*” in the presented child model was consequently filled by SPH. In this concern, also the implementation of the Liliequist membrane needs to be mentioned, which might be understood as an arachnoid membrane connecting dorsum sellae and the mammillary bodies [139] and influences already by its presence the possible flow of CSF.

All the implemented instances and their used general type of element are declared in Table 7.

Table 7 Description of the instances

Structure	Reference	Density (t/m ³)	Young's modulus or bulk modulus (MPa)	Other material parameters	Type & no. of FEs	Image of structure
White Matter—left/right hemisphere	Fernandes 2017 [52,119] - MAT_HYPER-ELASTIC	1.04	-	N = 0.49999 Mu1 = 0.0012 Alpha1 = 5.05007	hexa 233760/ 245830	
	GHBMC [74] MAT_VISCO-ELASTIC 1	1.06 e-9	Bulk modulus 2.19 e-3	G ₀ = 7.5 e-3 G ₁ = 1.5 e-3		
	THUMS MAT_VISCO-ELASTIC 2	1.00 e-9	Bulk modulus 2.16 e-3	G ₀ = 12.5 e-3 G ₁ = 6.125 e-3		
Grey matter—left/right hemisphere	Fernandes 2017 [52,119] - MAT_HYPER-ELASTIC	1.04 e-9	-	N = 0.49999	hexa 208498/ 201127	
	GHBMC [74] MAT_VISCO-ELASTIC 1	1.06 e-9	Bulk modulus 2.19 e-3	G ₀ = 6 e-3 G ₁ = 1.2 e-3		
	THUMS MAT_VISCO-ELASTIC 2	1.00 e-9	Bulk modulus 2.16e-3	G ₀ = 10 e-3 G ₁ = 5 e-3		
Cerebellum	Fernandes 2017 [52,119]	1.04 e-9	-	N = 0.49999 Mu1 = 0.0012 Alpha1 = 5.05007	hexa 128659	
Brainstem	Fernandes 2017 [52,119]	1.04 e-9	-	N = 0.49999 Mu1 = 0.0012 Alpha1 = 5.05007	hexa 20981	
Pia mater	LLC Elemance 2014; Ratajczak et al. 2019 [54,74]	1.13 e-9	31.5	v = 0.45000	shell 141831	
Dura mater (with falx cerebri and tentorium cerebelli)	LLC Elemance 2014; Ratajczak et al. 2019 [54,74]	1.13 e-9	31.5	v = 0.45000	tri shell 950 quad shell 25169	

Superior sagittal sinus and transversal sinus	LLC Elemance 2014; Ratajczak et al. 2019 [54,74]	1.04 e-9	28.2	v = 0.45000	tri shell 212 quad shell 9065	
Bridging veins	Delye et al. 2006; LLC Elemance 2014; Monea et al. 2014 [20,74,140]	1.13 e-9	30	0.48000	tri shell 410 quad shell 14291	
Lamina interna	Giordano and Kleiven 2016; Margulies 2000; Ratajczak et al. 2019 [54,77,85,141]	2.1e-9	4 e+3	0.25000	hexa 158553	
Diploe	Giordano and Kleiven 2016; Margulies 2000; Ratajczak et al. 2019 [54,77,85,141]	1.0 e-9	1 e+3	0.30000	hexa 121436	
Lamina externa	Giordano and Kleiven 2016; Margulies 2000; Ratajczak et al. 2019 [54,77,85,141]	2.1 e-9	4 e+3	0.25000	hexa 195357	
Cerebrospinal fluid (CSF)	DYNAmore GmbH 2018; Gomez-Gesteira et al. 2012 [142,143]	1 e-9	-	viscosity coefficient 7e-10	SPH 165289	
Corpus callosum	Fernandes 2017 [52,119]	1.04 e-9	Same as for WM	Same as for WM	hexa 6452	
Third ventricle complex	Fernandes 2017 [52,119]	1.04 e-9	Same as for WM	Same as for WM	hexa 762	
Liliequist membrane	Fernandes 2017 [52,119]	1.04 e-9	28.2	0.45000 0.45000	tri shell 56 quad shell 189	

The overview shows a limited number of differing element types. A focus was set especially on the calculability of the model. Exemplarily a major attribute of the model is the use of hexahedral elements for 3D elements without an exception. Investing a significant effort for meshing the complex geometry with hexahedral elements rewards with the avoidance of volume locking effects – consequently local stiffening – as it would have to be considered by using tetrahedral elements. Furthermore, preferably quadrilateral shell elements were used and – where possible or necessary – represented as fully-integrated elements in order to prevent from hourglassing.

The hourglassing effect can be found in non-physical deformation modes, which produce no stress and are occurring in shell elements with a single in-plane integration point as well as in solid elements with a single integration point. As the integration with more than one point is significantly more time-consuming during calculation, regularly the effect is tolerated but controlled over applying internal forces by the use of specific algorithms. As a drawback, the thereby occurring hourglass energy has finally to be seen as work, which is performed by the internally applied forces. Thus, this hourglass energy is now a part of the overall energy within the calculated system and needs to be considered as well. The dilemma has to be seen finally in finding to a decision: Should the model be created by using tetrahedral solid elements and triangular shells, which are not showing hourglassing effects, but tend significantly to element locking? Thus, the model might show locally recognizable stiffening effects. Alternatively, is a longer calculation time acceptable? Fully integrated solid and shell elements are not showing hourglass effects, but might be also less robust for large deformations [144]. Hence, a well-prepared mesh – especially for the cases of highly deformed soft material and tissue – is an inevitable demand, but shows more positive aspects for hexahedral solid elements and – if necessary – the use of fully integrated shell elements. The complete composition of the discrete (CAE) model in LS-DYNA with all translated and created instances is shown in Fig. 52.

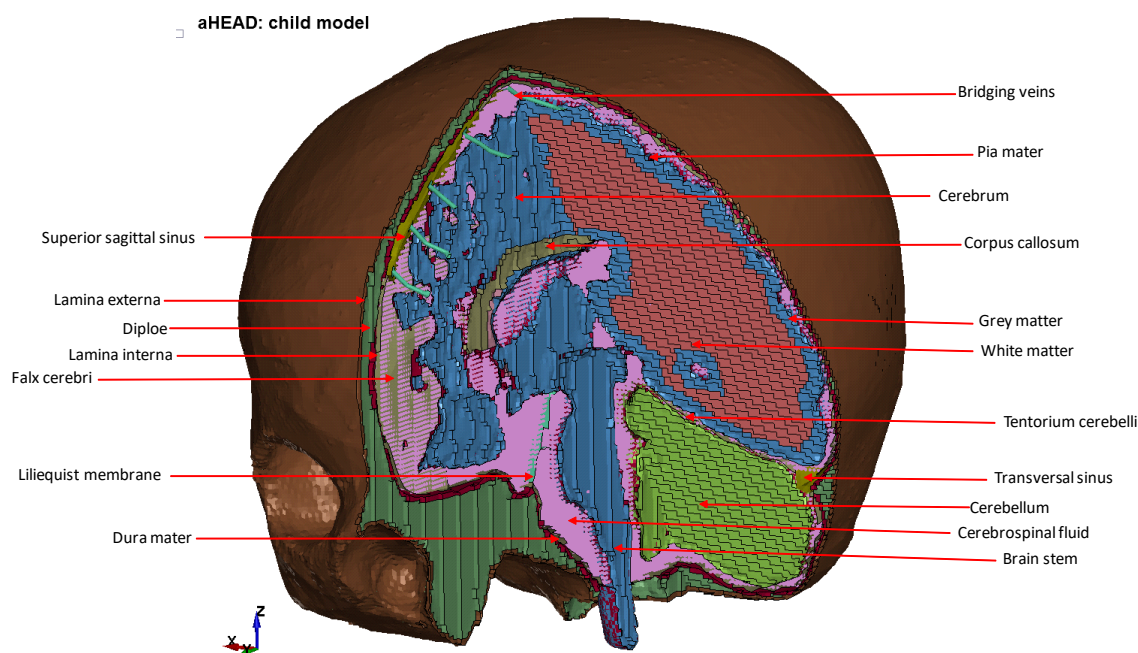


Fig. 52 Cut view and description of the implemented instances within the aHEAD 2-year-old child model

Beside the focus on the composition of the instances in terms of their mesh, also the choice of their assigned materials and interaction properties is of high importance. Table 7 showed for all instances also the used material card and the most important, describing material parameters. As the material properties are not based on own physical experiments, appropriate sources were given as well, which led majorly to the presented values.

All instances are actively interacting with their neighbors as regular contact algorithms were applied. In an example, the outer contact to the skull – regarding the instances' name definition it is meant the lamina externa – is realized by an automatic general contact, which bases on a bucket sort approach in order to make contact searching efficient. In a second step after detecting a contact, contact forces are calculated penalty-based. A penalty-based contact tends also not to excite mesh hourglassing by installing tangential interface springs for friction [145].

The interface between the skull – represented then by the lamina interna – and the dura mater includes a tied situation of the neighboring nodes of the two instances to mimic the adhesive character of this interaction, which is reported by neurosurgeons for the case of extraction. Furthermore, an additional general penalty-based contact is installed here in order to keep the dura in the according space.

Internally within the skull, contacts between the shell instances of dura, pia, sinuses, BVs and LM are handled by self-contact as a set of segments, similar to the principle of a deploying airbag. The same set of segments encloses and interacts with the CSF instance. In this context, different soft options were used according to soft issue modelling, which enables also to consider via the contact algorithm phenomena such as folding exemplarily during the action of high forces and significant deformations [145].

6.8 Re-calculating the side fall experiment by the use of the original FEHM child model

The full-scale experiment and its evaluation in Chapter 4 included both the HybridIII-3YO dummy from Humanetics and the HybridIII-3YO dummy out of the MADYMO 7.5 version. Finally, it needed to be stated, that aside the biofidelity and applicability of both solutions for a wide variety of automotive and kinematical research, the field of application for these dummy types is mainly in frontal impacts and sled tests. Although the models were reported to give acceptable results for side impact conditions [96] – even without a straight validation. The concern arised especially in regard of the neck structure, where discrepancies in the movement between virtual and physical dummy were recognized. Moreover, the neck-bending situation was found as presumably too stiff to mimic a real children's neck, which resulted in limited lateral bending during the fall to the ground. Nonetheless, the deceleration curves of the head correlated for the differing measurement techniques, but showed in a result for the head structure the behaviour of a rigid, single body with a constant centre of gravity. Regarding the complexity and deformability of both skull and brain, the simplified assumptions – as well as in terms of contacts and pairings – that were accepted by testing with these models in virtual and real space have to be seen critically [14]. Fig. 53 visualizes therefor the idea behind the recalculation of the experimental test, but by including the beforehand presented original FEHM of a 2-year-old. The case in chapter 4 showed a side fall, whereas the child was seated in the baby carrier. Even though the influence of the stiff neck in combination with the interaction of arm and shoulder with baby carrier and ground led to the absence of a direct cranial impact. The recalculation will concentrate here on the equivalent side fall situation, but with an impact under the premise of the absence of any pre-impact velocity reduction.

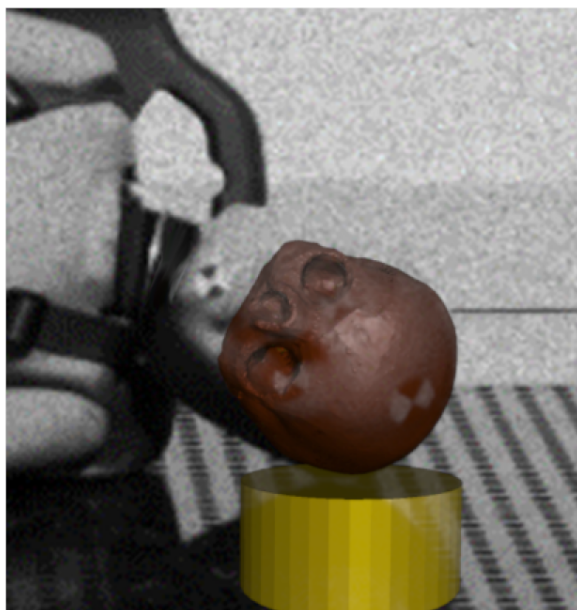


Fig. 53 Simulative case of a direct head impact to the ground with the presented aHEAD child model

Therefore, the head model is set up in this way, that the skull will impact to the rigid floor with a resultant linear velocity of 5.01 m/s in a comparable position regarding to the full-scale experiment. The impact velocity can be seen in this scenario as the maximum value, which can be expected out of the dropping height to the ground. It includes the assumption, that no major impact velocity lowering interaction to the ground of shoulders, the arms or even the baby carrier (leg cover or backrest) would be recognized. Out of a different point of view, the value also correlates with a wide range of simulations out of chapter 3, where the child's head impacted to the bonnet during a crash scenario with the same or a comparable velocity. It shows moreover, that a simple side fall already should be regarded as very comparable and comparably severe as an impact to a vehicle in traffic accidents. The presented in this chapter calculation was running for 67 hours to show 27 ms of calculated simulation time. Thereby, mass scaling was applied, which led to a mass increase of 5.57 %.

Fig. 54 visualizes the general motion of skull and brain for the times of $t = 0$ to 10 ms after the start of the simulation.

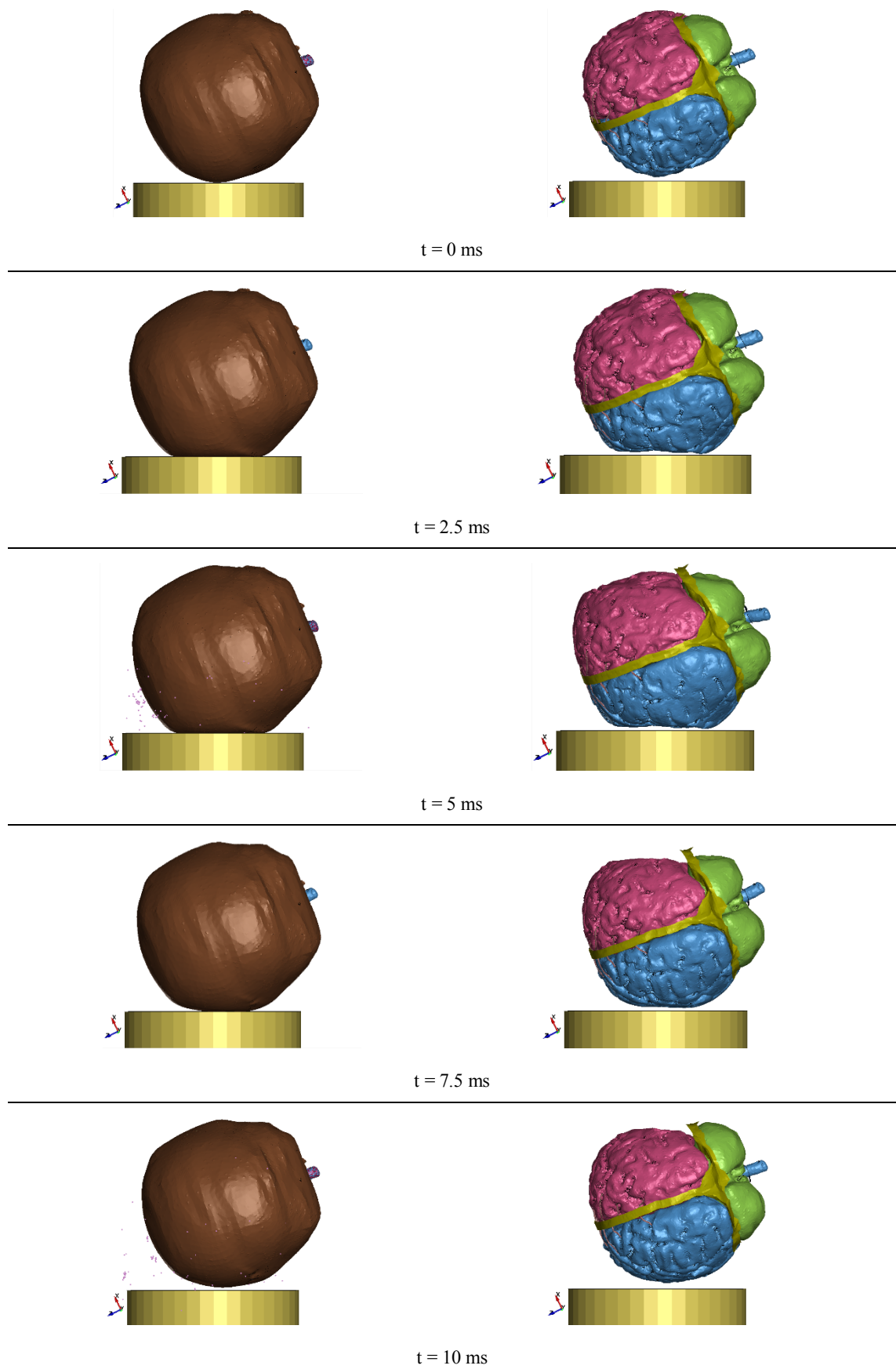


Fig. 54 Overview of skull and brain motion during the impact for $t = 0$ to 10 ms after the start of the simulation

In this figure, it can be recognized, how the skull impacts the rigid ground. On the first view, the skull adapts to the flat surface of the anvil underneath, whereas the skull tends to warp to the inside. This forces this warped shape even toward the cerebrum, as it can be seen for the time $t = 2.5$ ms. It points again on the characteristically bulked and compressed geometrical situation of a young's child brain inside the skull. At the same time, the so far easily recognizable structures of gyri and sulci seem to disappear, as the brain's state of being pressed onto the dura and the underneath located, way stiffer lamina interna of the skull arises. On the opposite side, the cerebrum is still in motion due to inertia. In a result, also on the opposite side of the impact a warping appears and follows intense stress states – strongly connected to the coup-contrecoup-phenomenon. Comparing the visualisations around the time of $t = 5$ ms, it can be noted, that the skull – after decelerating the whole head model due to its partial elasticity – already starts with its back motion. Moreover, 1st and 3rd principal stresses of the impacted area of the skull indicating a slight stress state beyond the elasticity borders, thus a more severe injury of the skull might be already in range. The majority of the intracranial instances are still before this point and still being decelerated. Fig. 55 shows therefore the resultant acceleration curve for a hexahedral element of the corpus callosum.

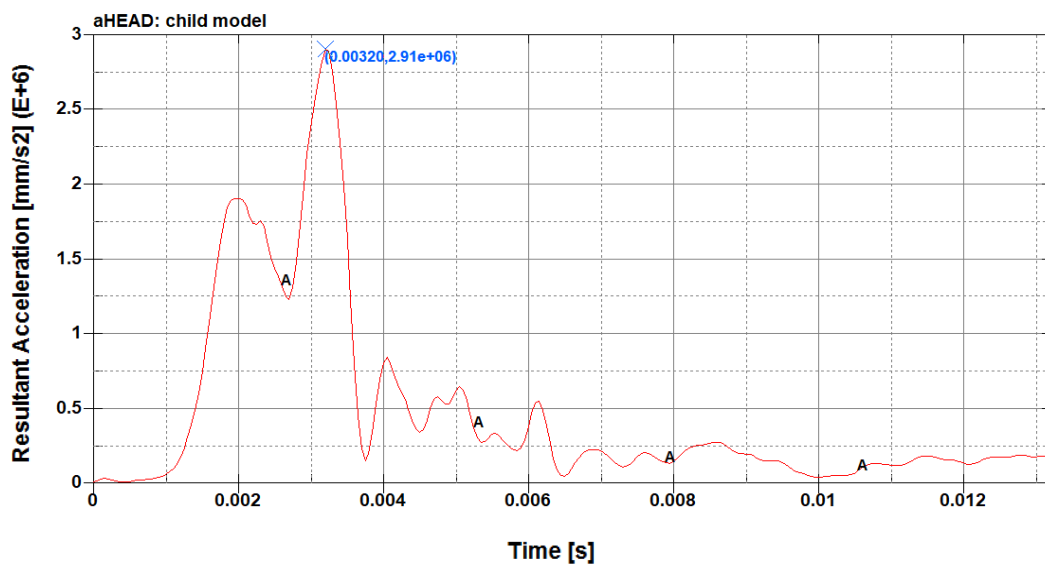


Fig. 55 Resultant acceleration of an element of the corpus callosum

The first significant deceleration of this element happens up to $t = 2$ ms, when the skull impacts and deforms onto the ground. The corpus callosum is located central in the brain structure, connecting both hemispheres. The element is still in significant motion due to inertia, before it gets as well into the state of being compressed maximally, in this case at

approx. $t = 3.2$ ms. Seeing Fig. 55 and taking recourse on the visualisations, the beforehand described circumstance points out on two important assumptions before the head model was created. Firstly, the head should not be seen in a complex head motion assessment only as a single instance with a single centre of gravity. As there are at least two significant peaks in the deceleration curve – here: the initial slowdown of the skull and finally the deceleration of the brain. Thus, deceleration behaviour will be locally different. This leads to the second assumption, that the particular affected instance of the brain receives hence also different support by its neighbours. Consequently, injury patterns might be given locally already, while the popularly used rigid dummy models and the commonly out of them calculated HIC-value might not point on this pattern clearly. It represents in the end only the resultant translational acceleration. In this scenario, a peak translational acceleration of 296 g was calculated for the single, central located hexahedral element of the corpus callosum. The value thereby corresponds to the results of an experiment out of the literature, where unhelmeted head impacts for a HybridIII-3YO-ATD in bicycle side falls were measured. In their experiments, the head impact had to occur firstly, before or without the interference of the baby carriers back rest [39]. Within these experiments, the measured mean of head acceleration covered the range of 2417 to 2931 m/s^2 , leading to calculated mean HIC(15) values between 709 and 1041 for the different used baby carrier types. It shall be noted, that the authors of the experiments pointed on two studies in their article, where most of the fatal head injuries were connected to a HIC value between 500 and 2500, moreover the HIC(15)-value of 700 seemed for them to be an equivalent to the risk for a mid-sized adult male [39]. Generally – and beside all discussion about the necessity of downscaling values for children – HIC(36) = 1000 is seen as a threshold for severe but not life-threatening head injury [51]. The meaningfulness of the HIC-value is frequently discussed, as it cannot be considered globally for all impact conditions, regardless of impact direction and region. This gets also visible by regarding the pure peak translational acceleration value here in this example: A 50% probability of a critical AIS 5 head injury (according to the Abbreviated Injury Scale) could be categorized for the here presented case [71].

Another situation of this beforehand mentioned load support of instances by their neighbouring instances is shown in Fig. 56, where the falx cerebri spans between both hemispheres at $t = 5$ ms. Clearly visible, the structures of gyri and sulci are flattened in this moment, while the falx cerebri supports also the right hemisphere.

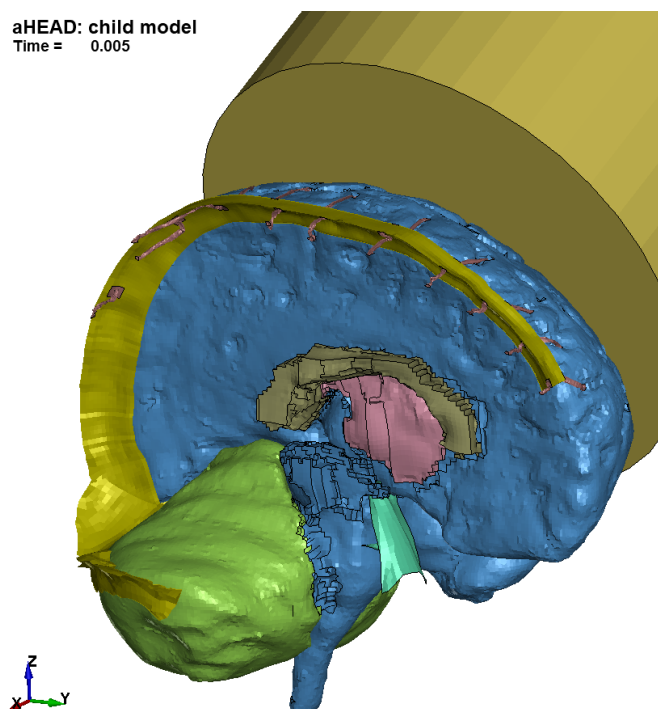


Fig. 56 Interaction of the falx cerebri with both hemispheres at $t = 5$ ms after the impact

The falx cerebri is in this context not the only instance, which is keeping the hemispheres in their natural position. Superior sagittal sinus and the bridging veins, which are connecting all the involved instances as a valveless blood channel system [146], are carrying loads additionally. Especially in the parietal region, the SSS is compressed by the approaching right hemisphere, which leads in this example to a significant pressure rise of the full system out of SSS, BVs and transversal sinus. An initial pressure value of 12 mm Hg or 1.6 kPa respectively was applied here to the model, representing a value for medium to large (intracranial) veins [134]. It has to be mentioned, that the real value would underlie permanent changes due to the blood circulation. Thus, the specification of the value should be understood as an initial but moment-specific value for the situation of the impact, even though it might be a smaller or higher value depending on the heartbeat. In the simulation the value was rising to a level of approx. 3 kPa. Beside the locally compressed and hence in total pressurized complex of transversal sinus, SSS and the attached BVs due to the laid-up hemisphere, especially the BVs are undergoing another significant motion and deformation. The here implemented 10 pairs of BVs are connecting each of the hemispheres with the SSS by bridging the subdural space and are in the centre of focus regarding the common post-impact injury of subdural hematoma (SDH). SDH as a potentially life-threatening injury describes a tearing or rupture of such

a BV after being subjected to shearing force, which appears due to a relative motion of brain and skull (see Fig. 57) [45,52,55].

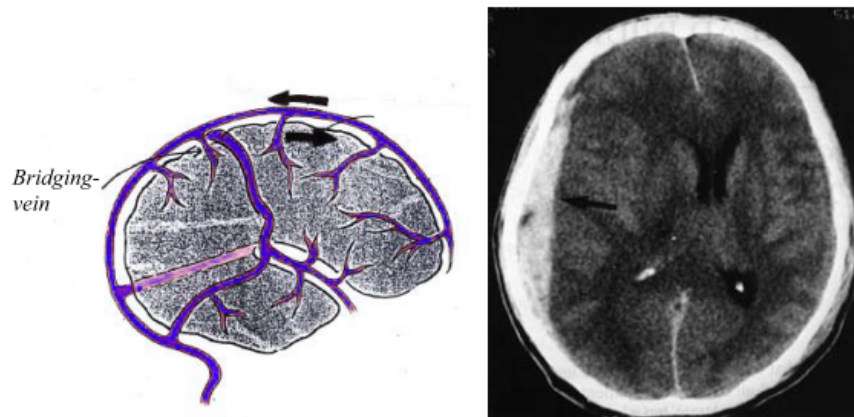


Fig. 57: Injury mechanism for Subdural Haematoma (left) and related CT (right), [55]

Literature states thereby shear force as a major criterion to provoke this secondary injury of rupture close to the connection to the SSS. Closely connected to this are the approaching angle of the BV to the SSS and the partially reported necking of the BV. Moreover, especially the angulation is changing over lifetime, also due to the volume loss of the brain by 5% per decade, starting approx. at a lifetime of 40 years. Surgeons also mind in this context of the final rupture the slight cornering of a BV at the border to the subarachnoidal space – located around 10 mm aside the SSS – where this structure seems to be as well prone to the injury pattern of SDH [147]. As the direction of force is this simulation is different – and especially BVs for young brains are less vertically angled but follow rather the lamina interna and dura mater – the example shall concentrate on the significant tension and twisting of the BVs, visible in the following Fig. 58. Nonetheless, the BVs of children were reported during autopsy as very fragile [148]. It was stated furthermore, that the BVs were easily able to be disrupted not only by applying excessive stretching force during manipulation, but also under the force of gravity [148].

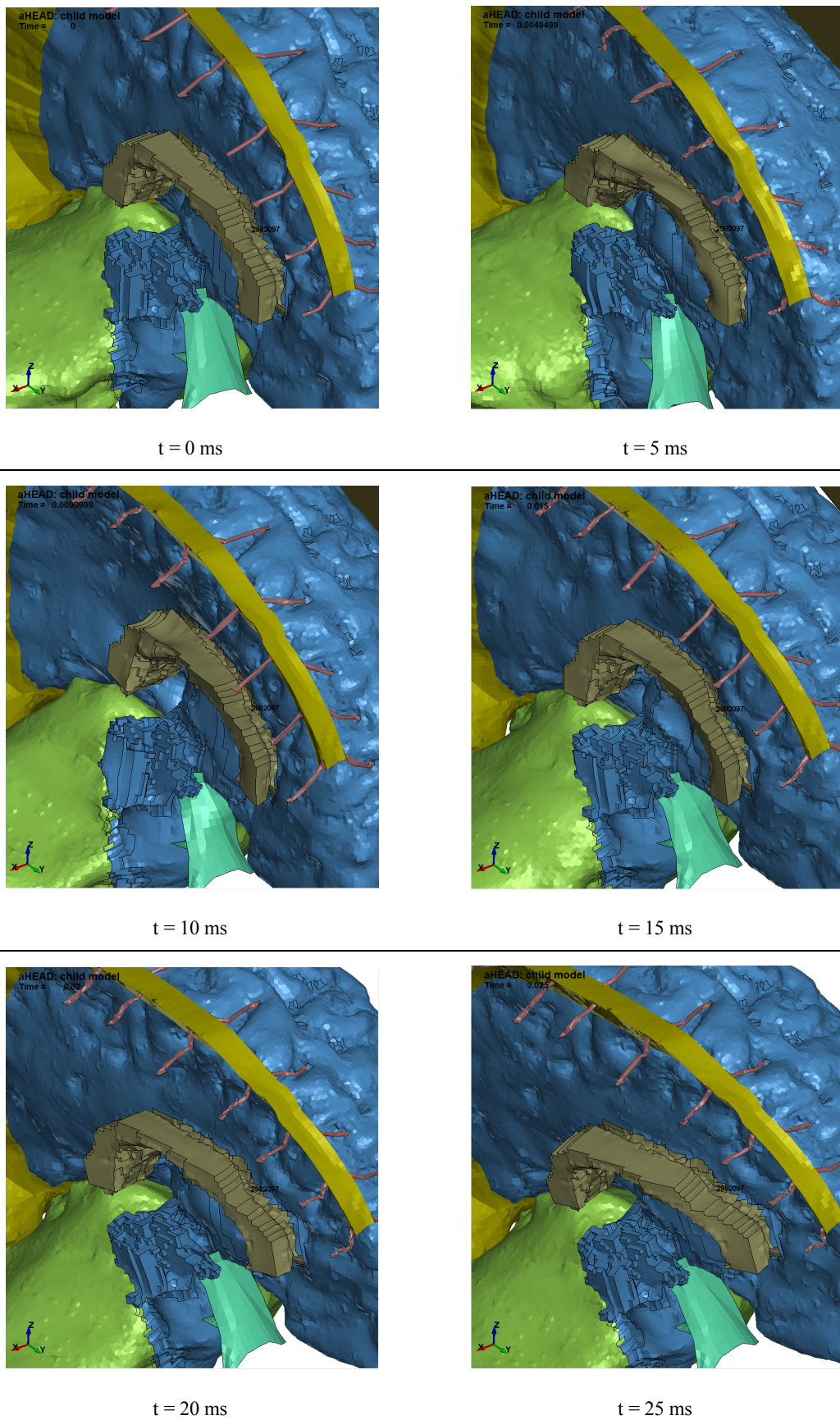
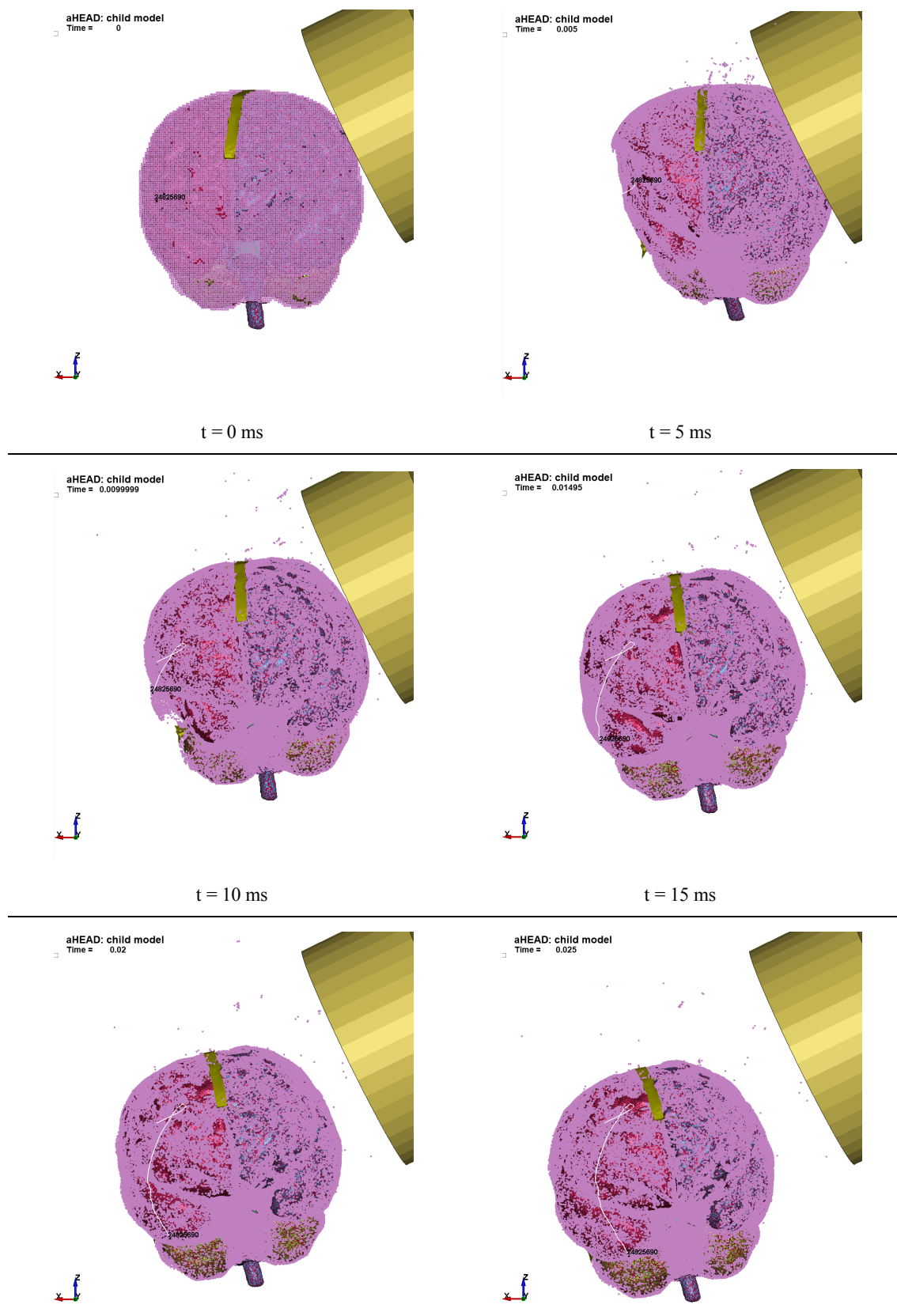


Fig. 58 Tension and twisting of the Bridging Veins, deformation of the corpus callosum

As in current state-of-the-art Head and brain models the BVs are still modelled idealistically by the use of 1D-elements, the representation by shell tubes enables to recognize the complex motion and shows over time their change between the states of being tensioned, being folded or twisted and restoring their initial shape. Tearing the connection area to the SSS on their movement away is as well a significant behaviour that can be recognized. The assessment of the BVs' tension in the connection area to the SSS, which naturally includes at least a minor shear component due to the angulation, increases already in this example the importance of the visualisation of this mechanism. It underlines, that the occurrence of this phenomenon arises also in cases aside from whiplash effects, which would be commonly found in sled tests or rear-end vehicle crashes. The angle in both impact and BV angulation plays thereby a role. Furthermore, the slightly stiffer cornering of the BVs at the border to the subarachnoidal space might be prone as well for this pattern and was so far not able to be assessed by oversimplified 1D-elements. 1D elements were so far able to show a general approach of BVs in terms of their location, but connected regularly to the neighbouring instances by node-to-node-connection or node sharing in one node per side only. This inherits, that calculatory results can be assessed separately from each side only. The question about actual motion and stress- or strain-states in the point of connection remains open. This is particularly true for the mentioned connection area to the SSS, described geometrically important by the necking and approaching angle [140,149]. Implemented as a 1D element even without changing section, these specialties and information were obsolete for models on the market so far, hence where a major contribution to further research is seen in this model. The BVs itself – so far mainly represented as 1D elements – were hardly to implement and include in terms of interactions and contacts with all their surroundings. One of the major surrounding instances is the cerebrospinal fluid, which is characterised as a composition by approx. 99% water, some glucose and some proteins. Modelled among the several available head and brain models numerically mainly by tetrahedral elements, which are filling up the gap between dura and pia, the motion of these elements is significantly restrained or suppressed. The use of SPH within the presented model allows respecting the flow of the water-like structure, which was particularly recognized in bigger cavities exemplarily close to the Liliequist membrane along the brainstem and medula or in temporarily larger cavities on the opposite side of the cerebrum's impact region. Especially regarding the latter, Fig. 59 shows the trace of a SPH particle over the simulation. The Liliequist membrane seems to act in this regard similar as a shield or

snowplow in order to protect the brainstem in this area from high-velocity backflow or wave phenomena, as it reduced appropriate effects by its implementation to the model significantly.



t = 20 ms

t = 25 ms

Fig. 59 Trace of a SPH particle representing CSF

Surprisingly, the flow – or in general: a clearly recognizable velocity of CSF SPH-particles – was not found in this amount within the lateral ventricles, which can be seen in the qualitative velocity plot in Fig. 60.

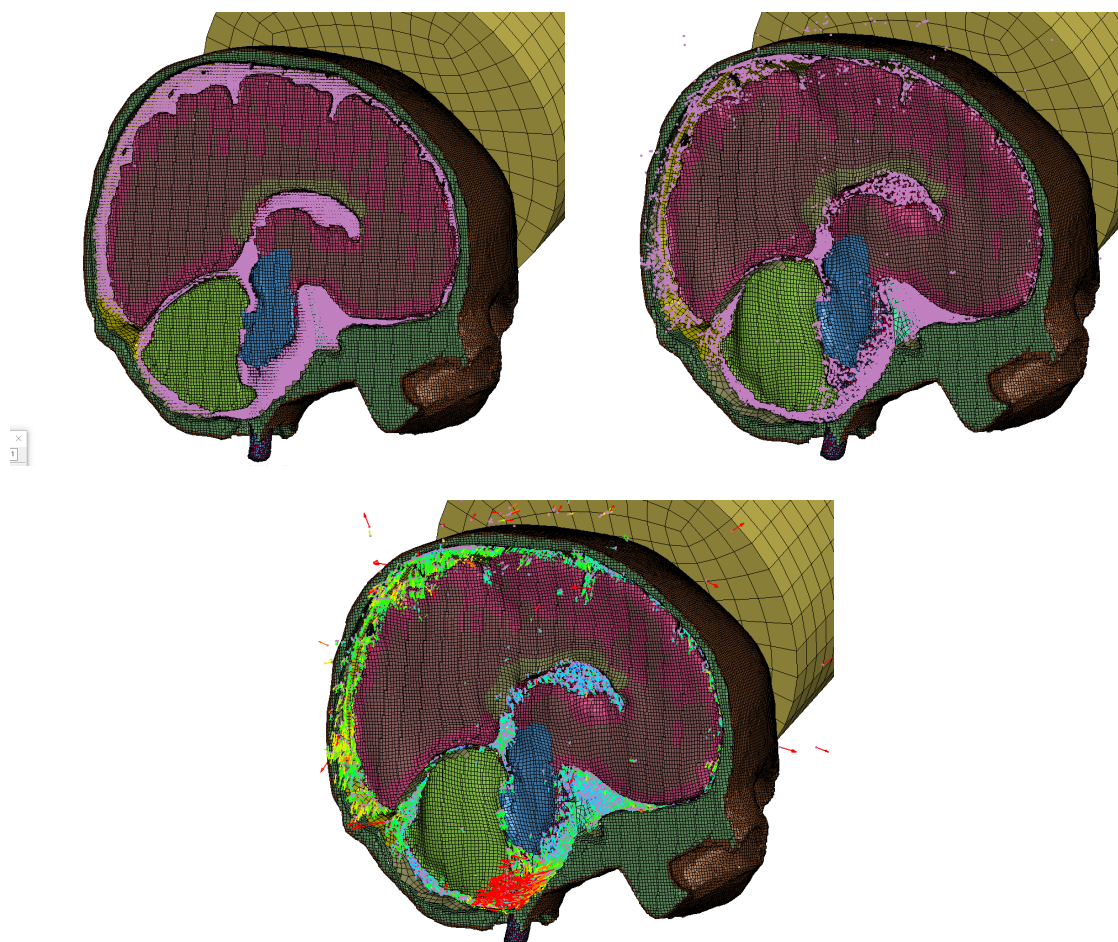
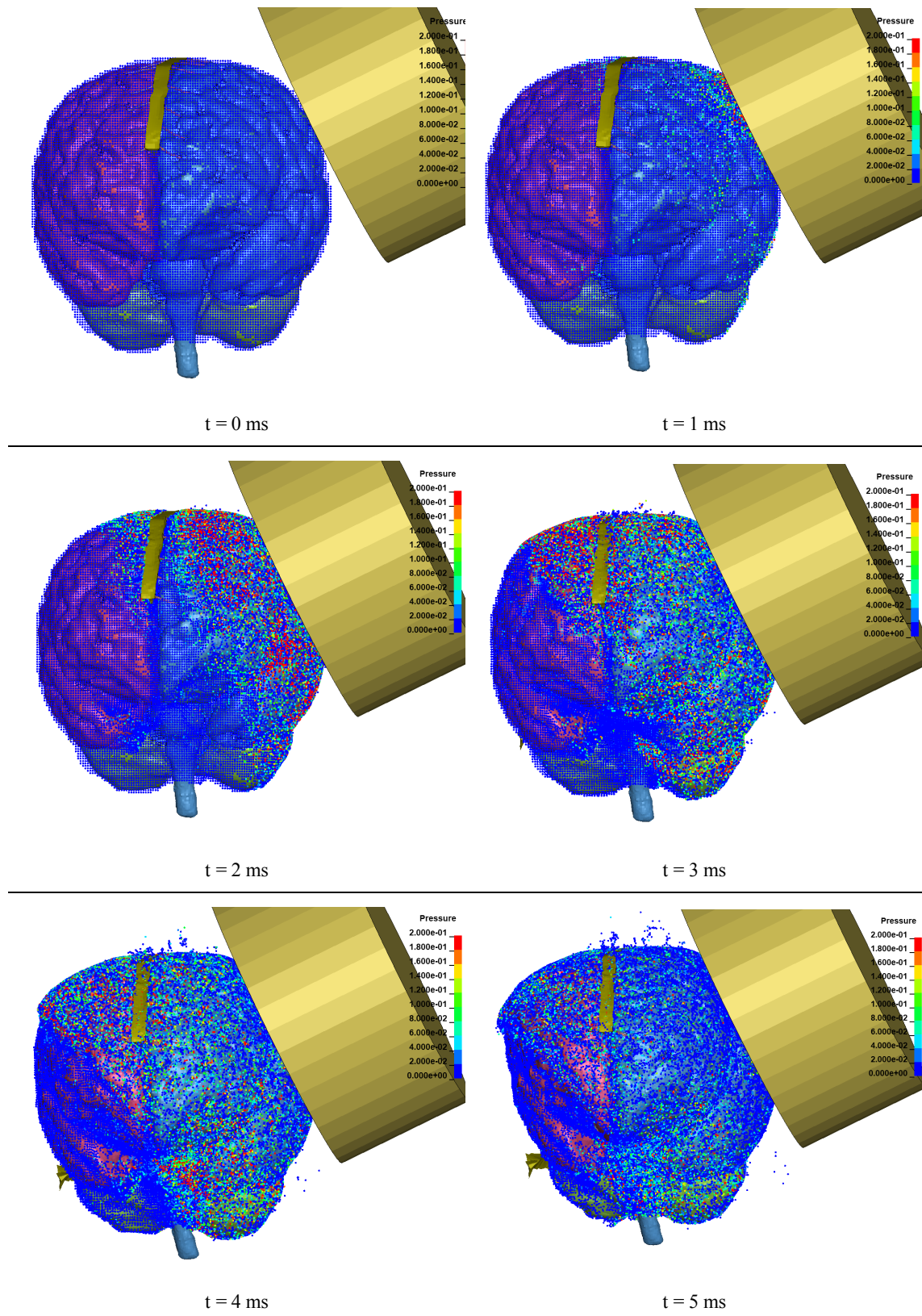


Fig. 60 Cut-view to visualize CSF motion before and during the impact (top) as well a qualitative velocity plot for the CSF (bottom)

Fig. 60 shows for the plane of the cut the arising wave of the CSF after the impact, which propagates toward the opposite side of the skull. A significant higher stream velocity is generated along the dura mater. Thus, CSF seems to play a supportive role inside the lateral ventricles due to its incompressibility as a liquid while being rather volatile on the outside of the brain. The wave propagation over the pia mater of the brain is shown in Fig. 61. Clearly visible, an initially arised pressure value hitting the visual threshold of 200 kPa starts around the area of the direct cranial impact at around 1 ms after the simulations' start.



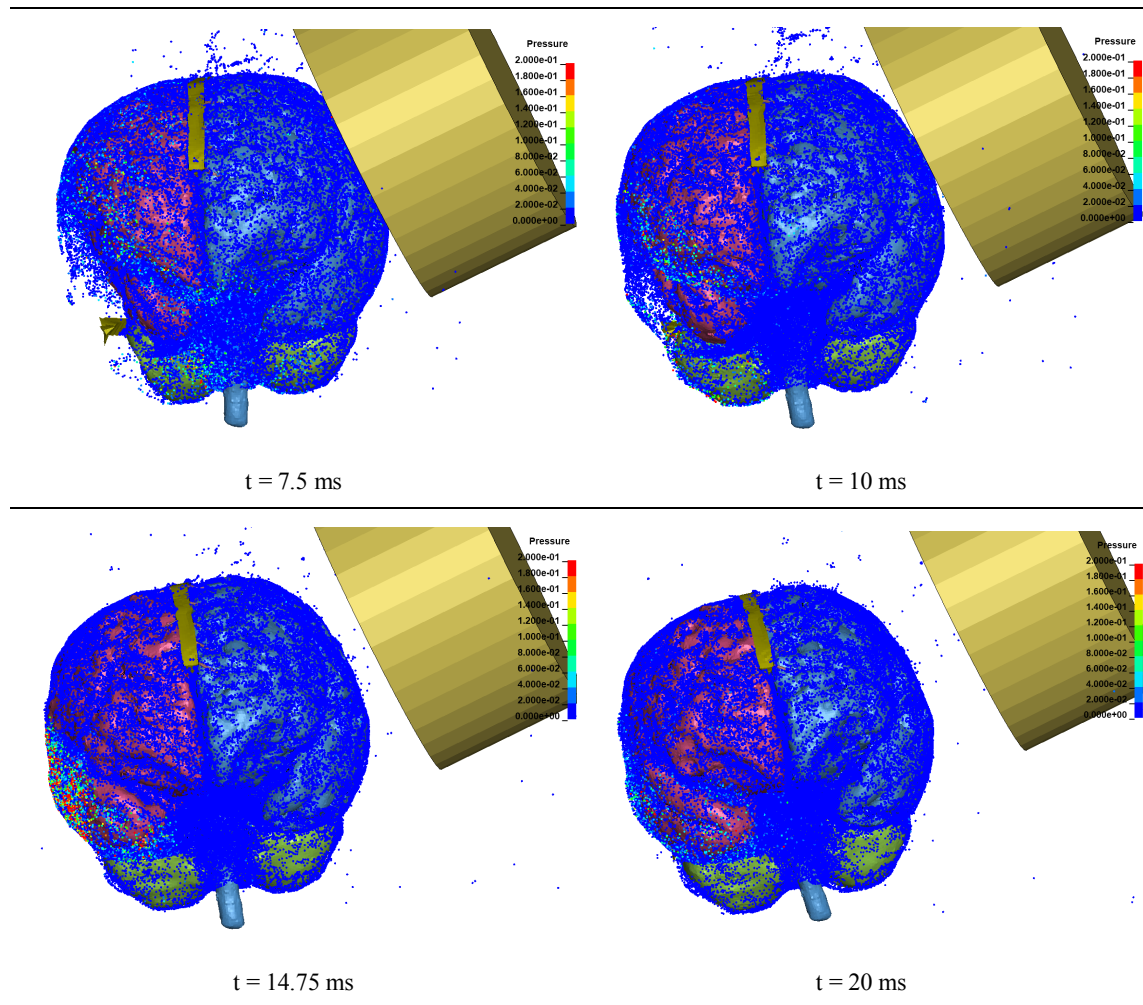
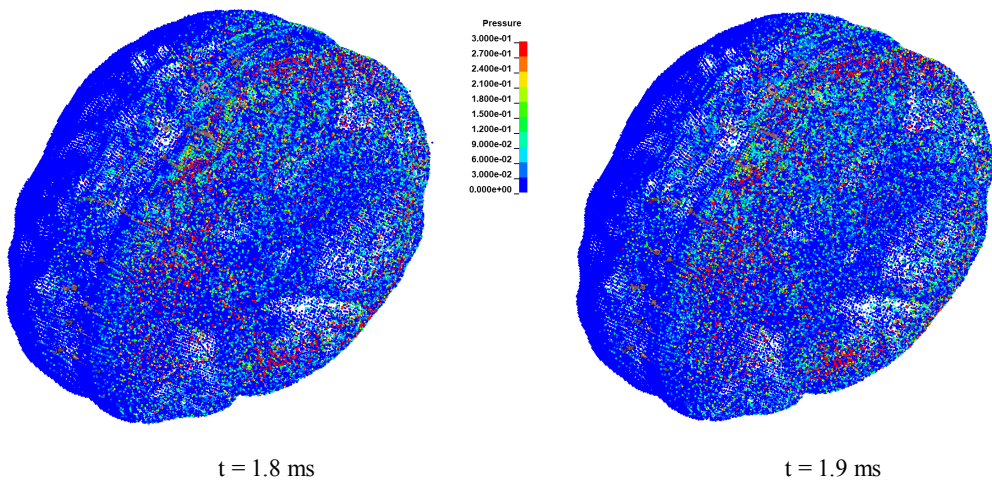
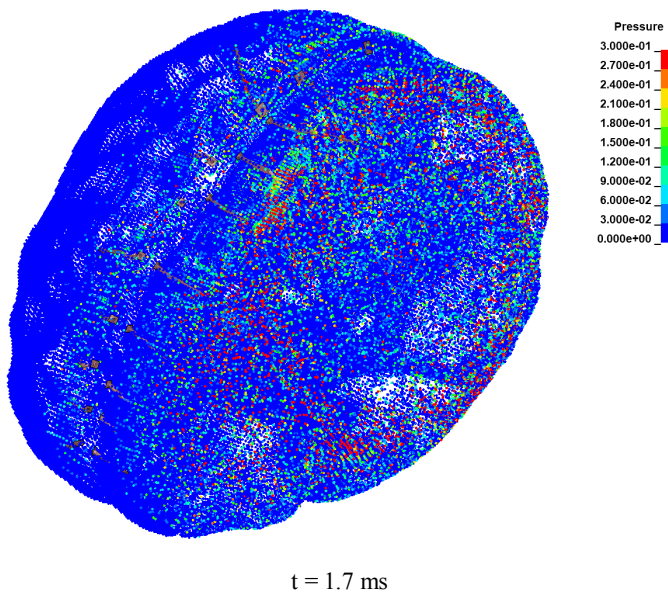
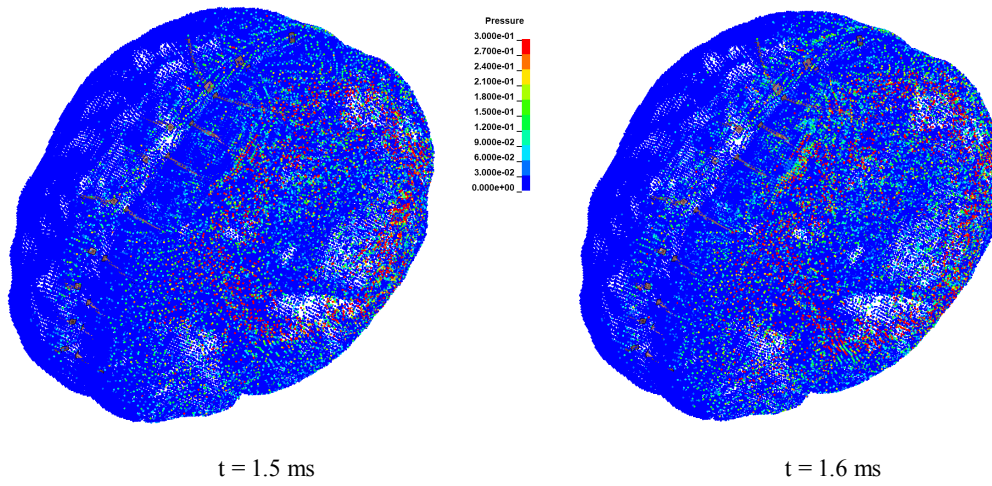


Fig. 61 Wave propagation showing CSF pressure in a scale from 0 to 200 kPa

The wave propagates also after passing SSS and falx cerebri. The presence and the elasticity of these instances can be recognised also by the change of the appearance of the wave, which seems to proceed now wider and also backwards, as a result of the first reflections of the impact wave visible from $t = 3$ ms. Furthermore, the coup-contrecoup-effect should be noted, which gets visualised by the rising pressure level at $t = 14.75$ ms on the opposite side of the initial impact.

In a more detailed view on the happenings for $t = 1.5 \dots 2.1$ ms after the simulations' start, Fig. 62 gives a visual overview. A special focus shall be set onto $t = 1.7$ ms in this sequence, where even the shape of the Bridging Veins gets visible within the pressure value plots.



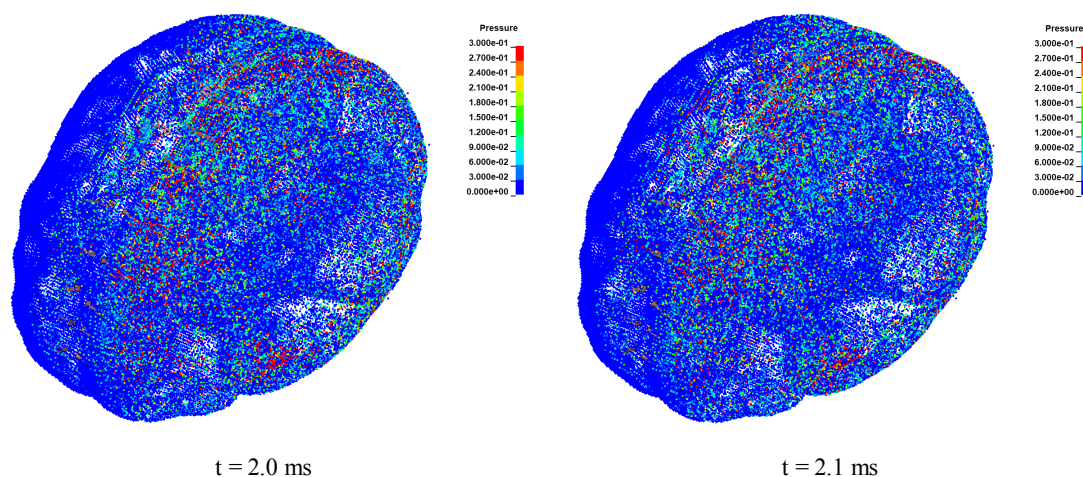


Fig. 62 Interaction of CSF with the SSS and BVs via pressure, scale 0 to 300 kPa

The upper scale limit of 300 kPa is not chosen randomly, as *Deck and Willinger* recommended this value as a tolerance level in CSF regarding the injury of SDH [150]. It should be discussed more in detail, in which time width a pressure corridor has to appear for a young patient of this age in order to provoke the secondary injury of SDH as an outcome. The appearance of the described pressure values points on the vulnerability of the seated child during this *simple* side fall case.

6.9 Chapter conclusions

The chapter pointed in a first thought on the gap of information between simplified models and their simulative outcome. Even though simplified models and their simulative results can widely match with experimental and empirical data, they cannot overcome the lack of information of in-detail motion or mechanism behind injury occurrence.

Basing on the so far central example of a baby carrier transported child involved in an impact scenario, a preliminary, but original finite element head and brain model of a two-year-old was presented and described in this chapter. The model bases on patient-specific medical imaging data and avoids having recourse on scaled or morphed models of even different patients or subjects. Moreover, it uses a fully hexahedral mesh for 3D-instances – showing geometrically highly complex details as gyri and sulci – and it implements SPH for the representation of the CSF. By the higher detailed level, a contribution to current related research is done.

The results of the simulation were covered by experimental data out of the literature and pointed on the severity of a simple side fall accident, when it comes to an unhelmeted,

direct cranial impact. Principal skull stress, resultant translational acceleration, HIC(36) and CSF pressure were pointing on the vulnerability of the child in this scenario. Moreover, it was possible to show significant brain motion and identify the occurrence of the coup-contrecoup-phenomenon.

The mentioned results and phenomena are not exclusive. The presented model is envisaged to increase numerical researchability of BVs and their geometrical vulnerability in the complexity of brain motion. Moreover, also exemplarily injury-related relative motion between cerebellum and brainstem is investigable in detail. Thus, the presented FEHM helps to research in terms of injury mechanism and to reveal injury pattern beside the common and generally accepted head injury predictors.

7 Challenging the vulnerability of the child's head during impacts by implementing an additional passive safety device to the baby carrier

“The result might be different in falls from moving bicycles. [...] On the other hand, a high-back seat lowered the head impact while wearing a helmet without exception. For that reason, it is important to use both a helmet and high-back seat simultaneously.”

Miyamoto & Inoue, 2010 [39]

7.1 Introduction

When it comes to the discussion and research about falls or impacts connected to VRU in traffic environment, a significant amount of words is used in contrary ways. The common ground for the variety of formulation and naming is finally the consent, that the vulnerability of a road user in a defined scenario is the centre of interest. In the highlighted crash situations, the seated child's overall situation is mainly dependent on a properly mounted baby carrier with a sufficient geometry and properly fitted harness system. Against the initial assumption, the baby carrier acts or *could then act* partially as a passive safety device with crashworthiness. It would overcome its poor crashworthiness by serving in a more complex way than simply representing a seat and defined position on the bicycle. The definition of the seating position and to keep the seated child in this position is a major demand. Especially the chapters 3 and 4 showed the importance for the child of being driven but within a defined geometrical space, as a specific motion and hence the impact conditions could be controlled by it. Especially by recapitulating the influence of the height of the impacting vehicle. It led to the conclusion, that a specific corridor regarding the height of the impacting vehicle's BLE increased the possibility, that at least no head contact to the bonnet could be observed. Nonetheless, the possibility for a head impact to the ground remains. Moreover, chapter 3 to 5 pointed also on the

importance of a properly sized armrest and backrest structure, which might act in favor of the child regarding the lateral head impact to the ground. In a short summary, multiple lateral head impacts have to be considered, especially when an impact to a vehicle is followed by a fall to the ground (see Fig. 63).

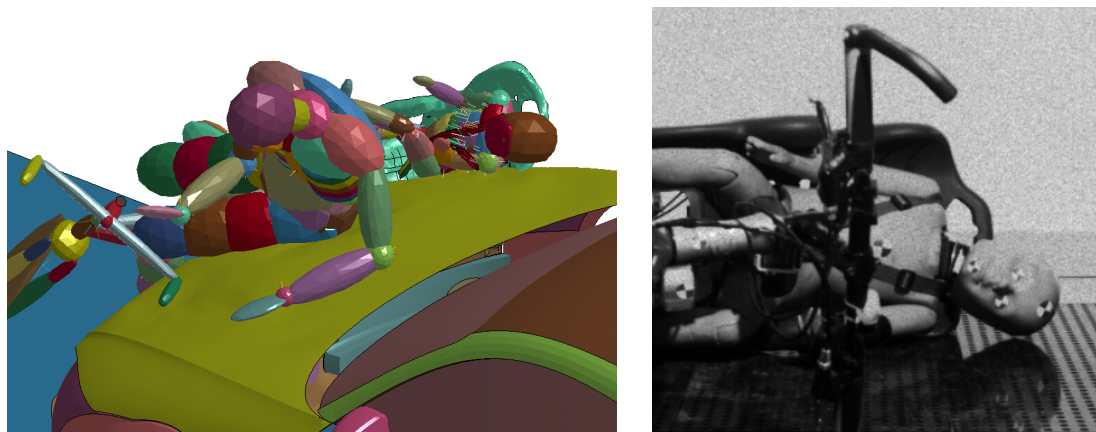


Fig. 63 Common lateral head impacts for crashes against a vehicle and the ground

Possibilities to encounter or to lower the severity of those lateral head impacts are given, exemplarily wearing a helmet, which seems to remain the top priority advice. It should be recapitulated, that also the baby carrier itself was recognized as acting similar, particularly by the presence of the sufficient long backrest [39]. Nonetheless, the high or engaging geometry – especially a head rest with side support, which is standard in infant and child seats for in-car usage – is not standard for bicycle child carriers. Simply, as wind resistance would rise and occurring side forces are small during the bicycle ride. Consequently, an excessive technical improvement of the structure and system of a bicycle baby carrier would be contra productive in several aspects. It starts with the so far exceptional good cost-benefit ratio of these seats, which would make the “simple but working and environmentally friendly” manner of the solution obsolete. Moreover, significantly risen weight could increase the risk of flipping the bicycle and clearly reduces maneuverability. Nonetheless, the presence of several head impacts – at least in a higher possibility – overwhelms the impact handling capabilities of a bicycle helmet. Chapter 4 showed the cracking of the helmet after one single impact to the ground after a simple side fall. In the case, that a first impact occurs against a vehicle's bonnet, the helmet might be significantly reduced in its protective manner for the consecutive fall to the ground. Thus, the installation of a light head-restraint and support structure to the baby carrier's geometry might enable to have recourse on several advantages, which are mainly described by an improved control over movability of head and neck during the

impact scenario. This restrictor and restraint would support also in terms of insufficient muscular abilities of young children. In the moment of impact, the side impact behavior would be positively influenced due to shock absorption properties, regardless of the presence of a safety helmet. To this complex related, a systematical solution of an attachable, additional shock absorption element is shown in Fig. 64.

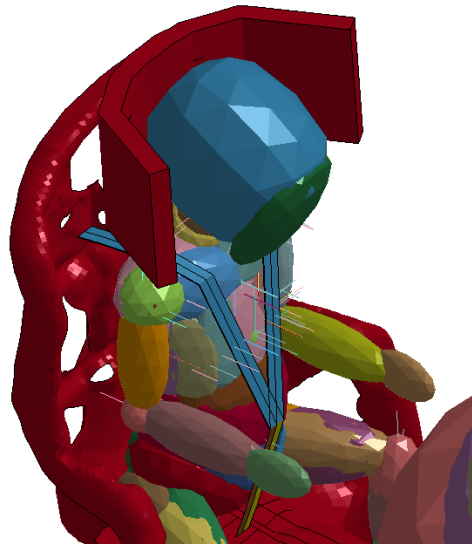


Fig. 64 U-band: an attachable, additional shock absorption element, represented in the discrete (CAE) model

An adjusted and preformed geometry is intended in order to fit the head as well a possible also to a worn helmet. Furthermore, it would enable to control head, neck and particularly shoulder movement during the impact. However, an important demand has to be seen as well in the applied material regarding the shock absorption layer, which has to be able to handle more than one major impact only. In the following, a major focus shall be set on a substitution of the commonly used EPS for shock absorption layers, which does not fit the idea of a sustainable component for an eco-friendly mean of transport, aside the missing property of handling multiple impacts without losing its structural integrity.

7.2 Agglomerated cork as a sustainable substitution for EPS

Nowadays, including preferably natural materials or substituting the pure synthetic materials by natural materials in so far generally accepted products and solutions is a raising demand on the market. Cork appeared as one of the top choices for a substitutional natural material and is in favour regarding consumer awareness and current “go green”

tendencies by showing up with wide applicability in a variety of products. Moreover, also as a natural product the increased recyclability for the end of the product's lifecycle is given, making the natural, improvable and property-tailorable material an interesting choice for manufacturers. While the used material is often simply named cork, is in fact a cork agglomerate, a combination of cork grains. In its base, cork is a side product from the cork stopper production process, which found its way into mechanical, thermal and acoustic product areas. Naming flooring panels, facades for houses, general outdoor applications and even aerospace [151], the wide difference in temperature conditions gets obvious and demands also to concern and question the material's performance within this range. Having a closer look on passive safety devices for the human head, cork was applied already in World War I and early Formula 1 helmets, but lost its spot to EPS due to the synthetic solution's brilliant cost-benefit-ratio and having a significant lower density. Cork is sustainable and comes as the harvested bark from the oak *Quercus suber L.*, whereas the harvesting takes place approx. every 9 years. By the process of harvesting, the oak as a tree is not harmed, as it renews its outer bark naturally over its regular life span of approx. 150 to 200 years [152]. It is mandatory, that the initial or first harvesting takes place up from the trees age of around 25 years, when the diameter covers already 20 to 25 cm [99,153]. Recognizing Portugal as one of the largest manufacturers of cork material and products worldwide, *Quercus suber L.* finds also its natural home in the Mediterranean area. Cork is a light material, showing the admired honeycomb structural pattern of its closed cells naturally. In this context, the low density and weight is achieved as the cells are enclosing more gas than showing solid volume, which fractions approx. 15% of the total volume only [52], [154]. The density of agglomerated cork covers regularly the range of 130 to 250 kg/m³, respecting that cork agglomerates properties are dependent and controlled mainly over its density and chemical composition [155]. The cell walls of the cork thereby contain in a majority suberin (35 – 45 weight %) as well as lignin (17 – 27 weight %), polysaccharides (13 – 23 weight %) and extractives (10 – 20 weight %) [156–159]. The chemical composition is reported to have a significant influence when it comes to compression properties, where lignin plays a bigger role for the resistance under compression and suberin contributes to elasticity and relaxation abilities [160], [161].

As initially mentioned, the material cork has been researched with growing interest due to its wider applicability for longer time already. Clearly impact-related research with intense dedication to the mechanical behaviour can be found mainly within the last

decade. Especially with a focus on cork's ability to be property-tailored, micro-agglomerated cork material has been promoted in several results and findings as a benefit and in its presence as an improving circumstance regarding crashworthiness or energy absorption [162–165]. Nevertheless, the try to substitute a material is naturally connected with the comparison to the substituted material itself and also initially to their combination within the application. So also Coelho et al., who presented research about mixed specimen out of expanded polystyrene (EPS) and agglomerated cork material under multi-impacts, while Kottner et al. concentrated on single impacts by comparing the results to full synthetic specimen [162], [165]. In a multi-impact focused work, Jardin et. al pointed on the outstanding properties of cork and related to this to the benefits of cork for the application. They presented a comparison of agglomerated and expanded cork to expanded polystyrene (EPS) and expanded polypropylene (EPP) [163]. Further multi-impact studies regarding agglomerated cork's mechanical behaviour were presented by Sanchez-Saez et al., Coelho et al. and Fernandes et al., whereas the latter showed studies under increased impact energy levels [162], [164], [166]. Especially in terms of the mechanical properties' dependency of cork in agglomerated and expanded representation on grain size, binder and the consequent density, Jardin et al. and Santos et al. enriched the literature [163], [167]. The overall research, which can be found in the literature, is hence contributed to consequently also appearing applications, for example in frontal impact absorbers for vehicles or the usage in side-impact accidents [168], [169]. The focus of several of the presented studies was set clearly on the comparability of a property-tailored, natural material to the performance of the so far widely used synthetic reference – the EPS. EPS in passive safety devices, especially within the automotive sector or simply as a helmet, is forced over its lifetime to act in a wide range of temperatures. Thus, substituting EPS by cork, the natural substitute would be have to perform under the same conditions. The influence of extremely high or low temperature on the mechanical behaviour and hence performance level of cork was so far not covered by a specific study. A few information exist, as for example results were presented regarding the temperature influence to the crashworthiness were given for a range of 21 to 50°C and for impact energies from 120 to 850 J [170], as well as the chemical stability was described for temperatures from 150 to 500°C [33]. Having recourse on the initial idea to add a passive safety device made out of the natural material of cork to the bicycle baby carrier, it gets clear, that it means a wider temperature range than the mentioned range between 21 and 50°C. Moreover, it would have to act predictably and offer stable

performance at sub-zero temperatures for an application in wintertime as well as in high temperatures after being heated up in the intense summer sun. Thus, it is necessary to describe corks behaviour by experimental test for these conditions, but as well to have a closer look on cork's structure, which is directly connected to its general mechanical properties.

In addition to the experimental tests, which are intended to reveal the mechanical performance of the substitute, also side aspects have to be considered. Especially the “greener” market nowadays plays an important role. It might be already accepted, that a natural material or alternative to synthetics may be close, but is actually not reaching in all aspects the synthetic's level of performance. Also the action of applying principles and natural forms can be of high importance in this context. The material cork thereby serves in both of these major aspects, as it shows naturally a honeycomb structure, even though this honeycomb is in terms of geometry not perfectly shaped. Fig. 65 gives a magnified view on this structure. Cork is known for its properties for centuries already, but found its application so far mainly as bottle stoppers or in architecture and interior design floor as panels due to being a hypoallergenic material.

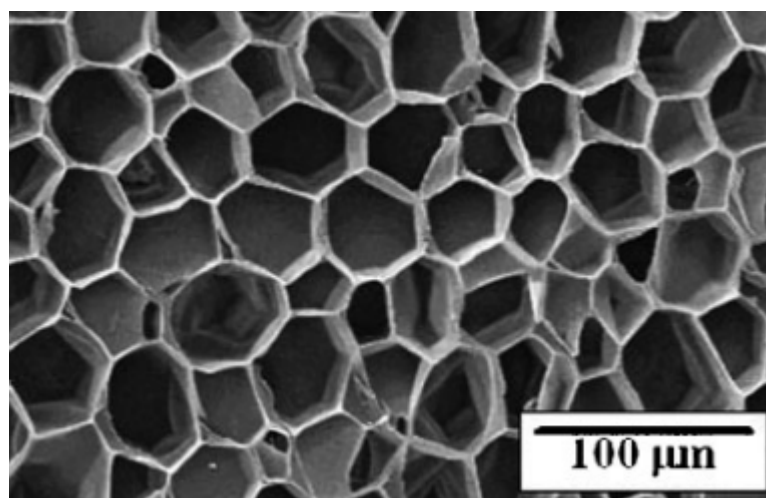


Fig. 65 Cork's structure [158]

In its rather newer form as agglomerated cork, where cork grains are combined in a user-defined grain size with a commonly synthetic binder – mostly binders are based on polyurethane (PU) – its material properties are highly adjustable. Even though the synthetic binder is still a drawback regarding sustainability, agglomerated cork is seen as competitive with EPS [52,170]. This is underlined by a view on the descriptive stress-strain-curve in Fig. 66.

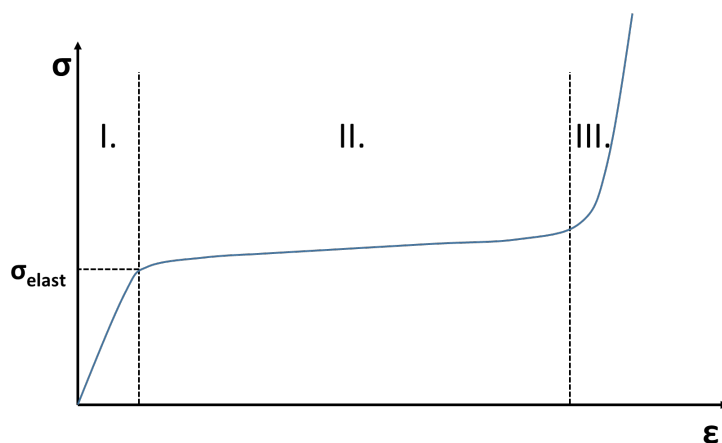


Fig. 66 Exemplary stress-strain-curve for cork material and uniaxial compression

The curve might be recognized as comparable to a curve for EPS-material, even though it differs fundamentally in one property. The graph is parted into three stages, where the first (I) stage shows a practically linear behaviour in the range of very small strains, mainly due to the elastic bending of the cork's cell walls. The for energy absorption layers important second stage (II) adjoins, where a nearly constant but only slightly increasing stress level is recognized over a large range of strain. This plateau is connected to the progressive cell collapse, which happens within the cork's structure. But moreover, this plateau is connected to viscoelastic buckling of the cell walls, which makes the material interesting for multi-impact conditions. The viscoelastic properties are giving the cork material the ability to recover to its initial shape – of course for cells which remain within this corridor of the second stage – up to 95%. This recovering happens immediately after the impact [52,171]. The second stage changes into the third stage (III) with a steep increasing stress value for only a small increase of strain. This is connected to plastic and viscoplastic yielding effects as well as brittle crushing of the cell walls. It comes finally to a total cell collapse by densification.

Recapitulating the above mention fundamental difference in both material's behaviour, both EPS and cork show lowered energy absorption capabilities after a critical impact with high strains. Unlike EPS, cork is nevertheless able to recover its initial shape after a moderate impact and shows up with a process of recovery, which enables to use the material for multi-impact situations and applications in enhanced passive safety devices.

Several research proved in this context, that the described behaviour was independently recognizable even up to high initial strain rates during quasi-static and dynamic drop tower tests [153,172]. A general demand for handling materials in impact applications –

thus, exemplarily also for passive safety gear – is to know the materials behavior up to an initial strain rate of 300 s^{-1} . EPS loses its strain rate independency already at 233 s^{-1} , which marks cork as a rather predictable material with higher values [52,153]. Nonetheless, EPS with its so far appreciated cost-benefit-ratio shines with a low density of around 90 kg/m^3 – and in the example of a motorcycle safety helmet with a common thickness of 40 mm. On the other side, cork would be characterised by a higher density of around 120 to 250 kg/m^3 , leading to a higher mass of the passive safety device. A combination of 216 kg/m^3 cork and a thickness of 35 mm was reported as being promising [52]. In a different aspect, the higher mass of the passive safety device then should be considered regarding the increased initial moment during the impact itself, which acts on skull and brain, under the premise that such a cork helmet would be worn [170]. Nonetheless, as the envisaged passive safety device is apart from the bicycle helmet, this aspect might be seen here as a side information with a lower priority.

7.3 Experimental tests

Particularly cork agglomerates were described as a promising material for impact applications due to their crashworthiness capabilities [163]. Connected experimental tests were intended to research this material regarding its shock absorption behaviour and to compare cork to the commonly applied EPS under room temperature. Cork (micro-) agglomerate with a density of 216 kg/m^3 was seen in a result as a promising material configuration in order to substitute EPS. The temperature needs to be seen in this context as an important value, which is already of higher importance during the manufacturing of cork agglomerates. Strictly seen, cork agglomerates are a side product made out of cork scrap. But the usage reduces wasting in the cork industry and has to be seen on the plus-side [173]. As already explained above, cork agglomerates are consisting of cork granules and PU thermosetting resins. Therefore, the milled cork granules need to be first of all cleaned and dried, before the mixture is prepared by agglutination. This means particularly a combination by applying pressure, heat and a binder. The granules have to match thereby a user-defined size and density. The prepared mixture is brought then into a mould, where it gets pressed and heated up, reaching temperatures of around 110 to 150°C . Research showed, that the amount of the used binder, which influences also the density of the agglomerate, follows also a change in the mechanical response during compression tests [167]. On this overall background, the here envisaged experimental tests are intended to take place for a wider range of temperatures, which potentially also

might affect the binder's integrity and be observable, while the specimen's material composition in this experiment shall be comparable to available research. The finally used compositions are shown in Table 8.

Table 8 Used cork materials in this experiment and the temperatures during the tests, based on author's publication [174]

Cork type	Section	Cork type Density [kg/m ³] Grain size [mm]	Temperature [°C]
AC168		Micro-agglomerated 168 1-5	-30; -15, 0, 100
AC199A		Micro-agglomerated 199 0.5-2	-30; -15, 0, 24, 100
AC199B		Micro-agglomerated 199 0.5-1	-30; -15, 0, 100
AC216		Micro-agglomerated 216 2-4	-30; -15, 0, 24, 100
EC159		Expanded 159 4-10	-30; -15, 0, 24, 100

One exception from the so far described cork compositions is the Expanded Cork (EC) in the list above, which is called also black cork agglomerate. It is produced by agglutinating virgin cork granules, obtained from the oak tree branches by pruning. These particles show a high extractive concentration, which is used later as a natural adhesive.

Beforehand, the granules will be pressurized in autoclaves reaching temperatures of around 300 to 370°C under approx. 40 kPa of pressure. This process follows the expansion of the granules, which releases suberin, the granules' natural resin. In the end, this enables the agglomeration without using additives such as adhesives. Even though the strength of suberin is significant lower than by using a PU-based binder, which gets recognizable in impact conditions, EC shall be tested as a more sustainable representative of cork agglomerates [163,166,170].

All specimens were conditioned regarding their temperature in a furnace. The furnace was therefore equipped with a heater, which enabled to set up temperatures up to 100°C. In order to reach the sub-zero temperatures, a nitrogen cooling connector was also installed to the furnace. Induced circulation enabled to keep the specific temperature within the chamber for the test. Only during the tests at room temperature, the chamber door was opened and the heating/cooling-devices were deactivated. The specimens' temperature was moreover supervised by the device's temperature sensors. Moreover by a control specimen inside the chamber with a K-type thermocouple. The thermocouple was placed into the core of this separate specimen.

An Instron Dynatup 9250HV drop tower with instruments was used for the dynamic impact tests, whereas the initial impact velocity was set up to 9.2 m/s. Corresponding to the specimen's measurements of 50 mm x 50 mm for the section and a height of 60 mm, the impacting flat tup had a radius of 50 mm. The mass was set up to 11.2 kg. The impact was recorded in two ways: by a load cell with a sample rate of 204.8 kHz and visually by the use of a high-speed camera Phantom V12 at a frame rate of 10000 fps. The exposure time was set to 40 µs during sub-zero temperature testing, on any other cases to 50 µs. Analysing the video recordings with the dedicated software TEMA Motion enabled to create displacement-time data sets for beforehand installed high-contrast markers, which were located on the drop tower's impactor and anvil. The correlation of both measuring techniques with their differing sample rates was realized afterwards by using the software National Instruments LabVIEW 2013.

The following Fig. 67 visualizes the process of compression for cork specimens with the densities of 199 kg/m³ and 216 kg/m³ at the temperatures of -30°C and 100°C and an initial impact energy level of 500 J. The specimens were impacted central by the flat impactor. The highest displacement was recognized for the shown specimens at a time around 7.5 to 8 ms after the initial full contact to the impactor.

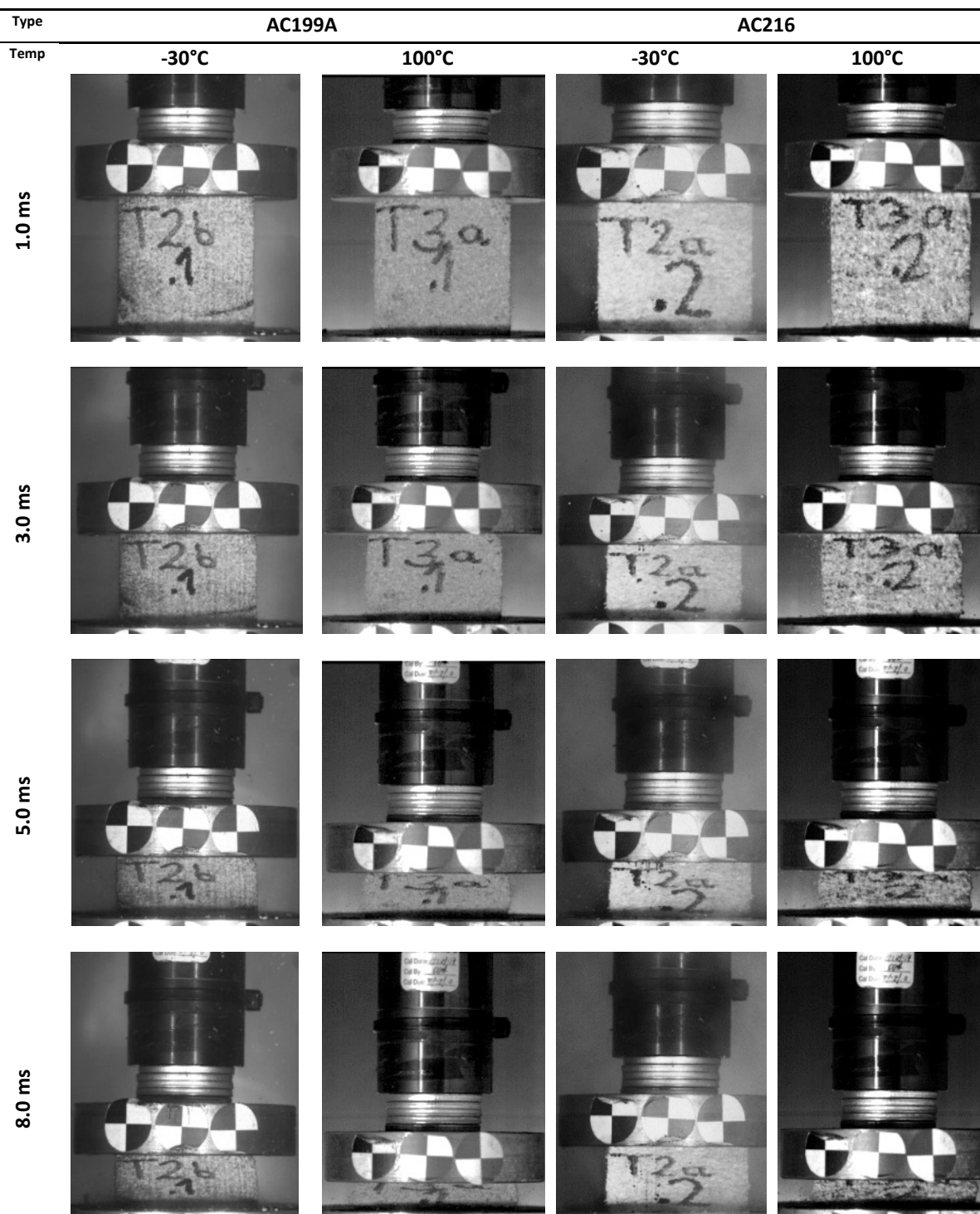


Fig. 67 Process of compression for two types of cork material (AC199A, AC216) at the temperatures of -30°C and 100°C, each under 500 J initial impact energy, based on author's publication [174]

The samples underwent thereby large uniaxial strain according to the beforehand described collapsing and buckling of the cell walls. Also recognizable by the form of deformation is cork's general Poisson's ratio of around 0 to 0.15 [163]. With a more temperature dedicated focus on the shown sequence, the overall temperature difference

of 130°C follows changes in the compression response. Each of the composition is less stiff under the temperature of 100°C, leading to a higher displacement of the specimen. Characteristically, cracks were recognized in nearly every specimen after the test at this highest tested temperature. After the test, the specimen remained with a deformation, which shows in the projected view the shape of a barrel. It was accompanied with the observation during the compression tests, that the specimens' walls or parts of it were at least partially separated, forming finally this barrel-kind perception. This is shown in Fig. 68 a) and b), in its tendency also in Fig. 68 c). The effect did not occur for the here shown tests at -30°C. A general exclusion from this “barrel effect” is the EC. The background needs to be seen in the missing additional adhesive for the composition of black cork agglomerates, whereas the adhesive capabilities of the suberin as binder are lost under the high energy impact.

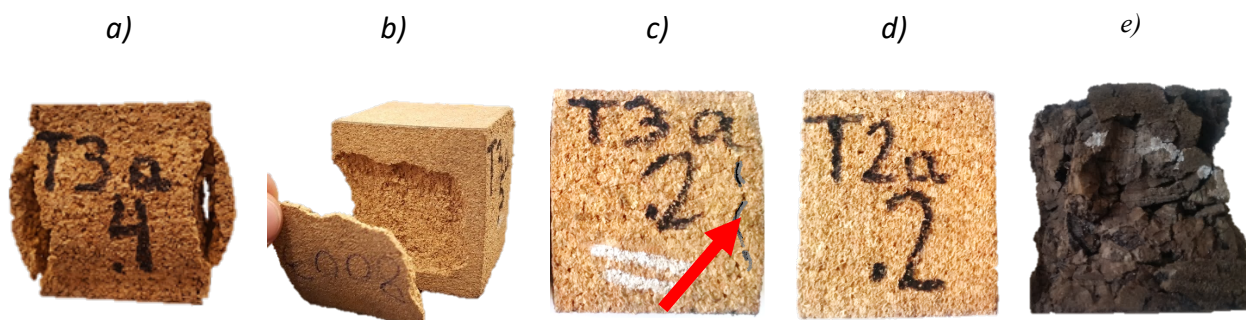


Fig. 68 The cork specimen after a single 500 J impact, based on author's publication [174]:
at 100°C: a) AC168, b) AC199B, c) AC216 (crack marked);
at -30°C: d) AC216, e) EC159

The expanded or black cork EC159 was in this test scenario not able to withstand the 500J impact. In a consequence, the energy was decreased in the further tests to a significant lower value, which was intended to enable findings about the material's crashworthiness. Particularly for compositions of agglomerated cork a deflection threshold of 38 mm was introduced, as the micro-agglomerated cork specimens were able to withstand the impact up to this deflection in all cases. The introduction is intended for better comparability of the results. Exceeding this deflection threshold – but particularly the value of 45 mm – meant an interaction with the bumpers of the drop tower, which were installed in order to prevent the test stand and its sensors from damage. The interaction with the bumpers could be seen clearly by analysing the recorded data of the EC159 specimens. Generally, during the test, the crushing force of the specimen equalled around 20 to 40 % of the agglomerated cork's crushing force. With passing the 45 mm deflection mark, the value

increased significantly. Thus, energy absorption took place by the test stand’s bumpers. It points at this moment already on the missing integrity of the specimen. Consequently, data was cut accordingly and no more taken into consideration.

The analysis of the gathered data led to three main findings, which shall be presented in the following.

Strongly connected to the beforehand focused temperature is **Finding 1**. The temperature of the application influences significantly the crashworthiness of the here tested cork material. Fig. 69 shows for the tested materials of AC168, AC199A, AC199B, AC216 and EC159 the absorbed energy at the deflection threshold of 38 mm for the tested temperatures between -30°C and 100°C [174].

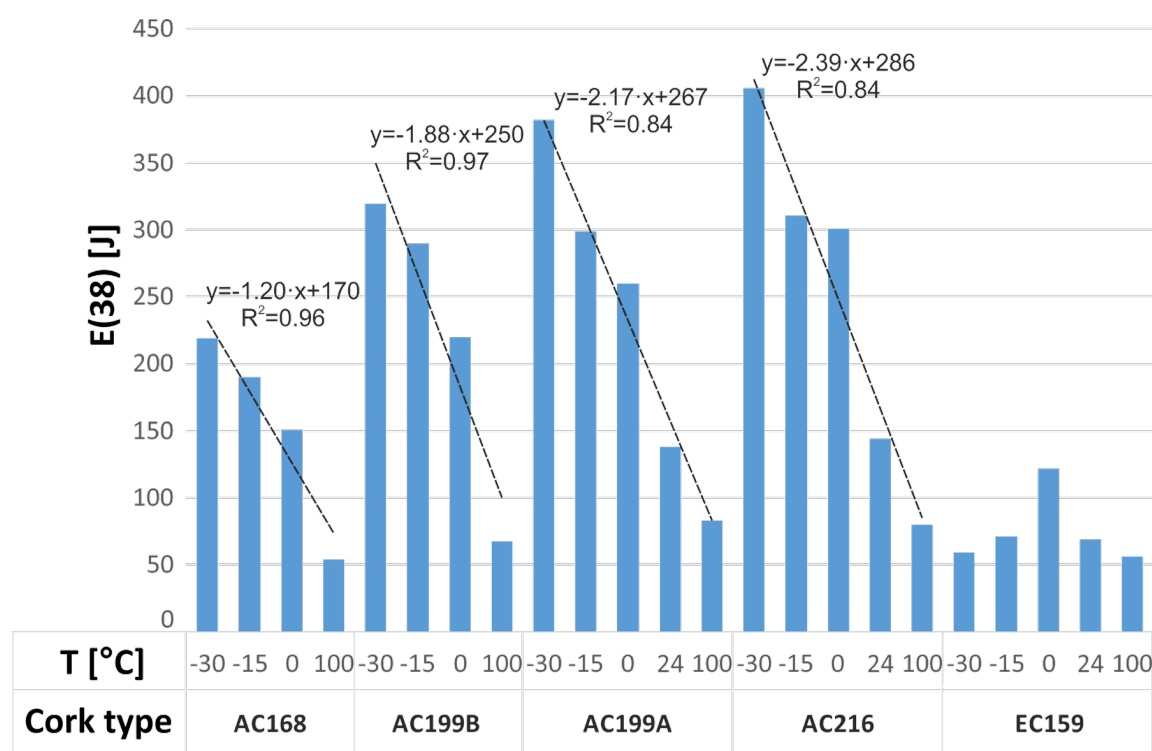


Fig. 69 Temperature influence on the absorbed energy, shown for a 500 J impact at a deflection of 38 mm, based on author’s publication [174]

Due to the decreasing stiffness of the specimen by rising temperature, the absorbed energy drops to less than a quarter for the highest tested temperature. The only linear trendline supports in terms of readability. Furthermore, the increasing density of the agglomerates changed the inclination of this trendline, underlining, that a denser material increases the effect of loss of absorption capabilities over raising the application temperature. Mentioning only aside, the EC was not able to withstand the impact and hence did not give more interpretable data or trends in this concern – the specimen was already

destroyed. Finding 1, with regard on the intention to use cork as a substitutional material in passive safety devices, points on the importance on the absorption layer's thickness in the specific application and its intended temperature range of application. The influence of temperature to the absorbed energy was seen here to be linear, which would enable manufacturers to estimate suiting measurements and compositions based on this data set.

Finding 2 concentrates on the two cork agglomerates AC199A and AC199B, which are characterized by the same density, but were produced with a different grain size. Fig. 70 shows the influence of the grain size, by presenting the ratio of absorbed energy for both cork agglomerated in dependency of the specimen's deflection at the various tested temperatures [174].

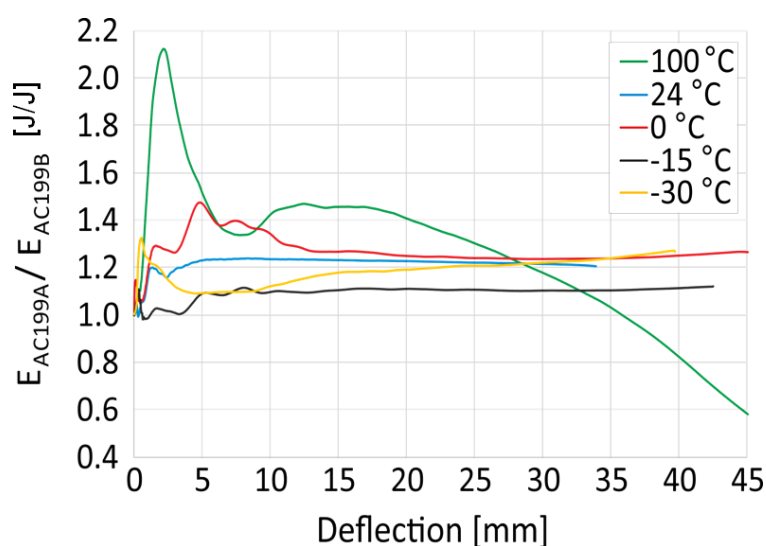


Fig. 70 The grain size's influence on ratio of energy absorbed by AC199A and AC199B in dependency of the specimen's deflection under the tested temperatures, based on author's publication [174]

Although the experiment led to the convincement, that the crashworthiness is influenced by the cork's grain size, the explanation is connected as well to binder, impact energy and temperature. It can be recognized by having another view on the visualization of the cork sections, which was given in Table 8, that the amount of PU-based binder in the AC199B samples was higher than in AC199A, as AC199A had a bigger grain size. Furthermore, thermal effects due to the viscoelastic and viscoplastic behaviour of cork were recognized during the 500 J impact. In this context it need to be underlined, that the cork grain itself is a very good heat insulator characterised by a small heat capacity, especially compared to the PU-based binder [159], while compressing the air within the cork cells is an adiabatic process [170]. The adhesive behaviour of the binder was lowered comparing to the lower temperatures by holding the specimens at 100°C. It led also to a higher viscosity

of the binder. Similar under the event of compression, the cork grain acts as a small heat capacitor and heats the binder around. In a consequence, the viscosity increases and adhesive capabilities decrease for a short time. Moreover, this leads to a grain separation, at least in the microstructure. By this structural damage the energy absorption capabilities of AC199B are as well decreased in relation to AC199A, which gets visible in Fig. 70 for deflections up to approx. 60% or 35 mm. After this value of 35 mm deflection, the ratio of absorbed energy for AC199A vs AC199B decreases more and is valued below 1 Joule/Joule. There, the larger granules are showing up to be more brittle and fracturing under the high compression, being hence more prone to this effect than the smaller granules of AC199B. Separate inspections of the larger grains of AC199A after the experiments itself showed micro-fractures in the inside of the grains. [174]

With **Finding 3**, a focus on the force-deflection curves under the influence of the application temperature shall be set. Fig. 71 presents therefor the according graphs for the 500 J impact by considering the AC199A cork material [174].

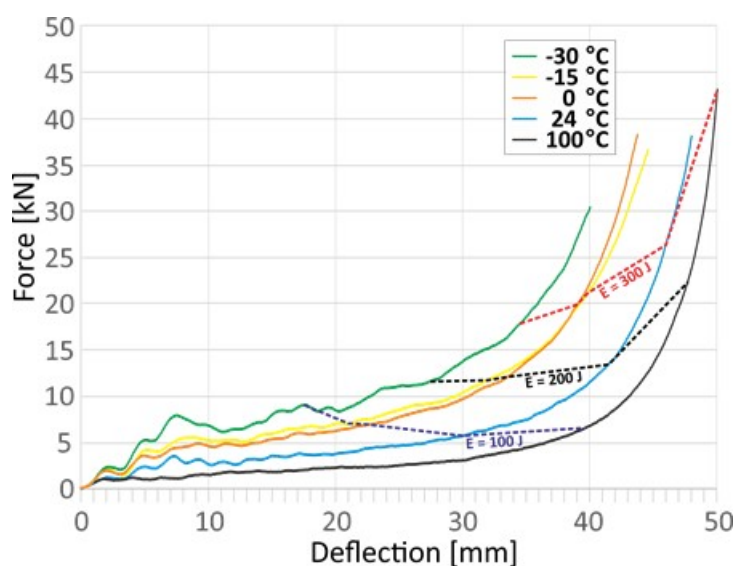


Fig. 71 Cork AC199A force-deflection curves for the tested temperatures with the marked absorbed energy levels, based on author's publication [174]

Fig. 71 presents for the curves as well the absorbed energy levels of 100, 200 and 300 J, showing in total an inversely proportional force level to the temperature. While the 100J-level nearly forms a horizontal plateau, the level-curve for 300 J rises with exponential character. Hence, the influence on absorption capabilities is higher by temperature changes for low-energy-impacts. Giving an example of an absorption liner, which was intended to absorb 100 J: It would be necessary to design this layer by 17 mm in thickness for -30°C, while the same layer should measure 39 mm in thickness for an application

temperature of 100°C. The same example but for an energy level of 300 J would demand a layer thickness of 35 mm for -30°C, 50 mm for 100°C respectively. It can be stated, that for low-energy-impacts the maximum force has to decrease by having recourse on a greater product thickness, while for high-energy-impacts maximum force and displacement will be of increasing nature. The importance of the finding has to be seen for the proper dimensioning of absorption liners for low-energy-impacts with a wide temperature range [174].

7.4 Material modelling

Cork with a density of 216 kg/m³ was described as a promising choice for substituting EPS in passive safety devices [163]. Consecutive own experimental tests at the institution were carried out and supported this statement, as described in the previous chapter. In order to proceed with a simulation-based design approach of the envisaged additional passive safety device for the baby carrier, the gathered experimental data shall be implemented in a material model. Generally, material models for cork with a density of 216 kg/m³ are established and described in the literature [52]. Even though availability might be given, applicability has to be seen critically, when for example the own used grain size is different, or the binder in its constellation is not entirely clear or also the initial impact energy level is differing. Another aspect is the used solver code: material cards are partially different or missing at all from code to code. In this situation, the argument for creating a specific, case-tailored material model is given, especially when own experimental data is present. In the following, the usage of the experimental data is shown, in order to create a cork material model for implementing the additional passive safety device in the single-impact side fall case, which was focused in the chapters 4 and 5.

The model creation is based on the force-displacement-curve, which was gathered by using the Dynatup drop tower and the high-speed camera Phantom V12 during an approx. 110 J initial impact test – dynamic compression respectively – at room temperature (24°C). The graph is shown in Fig. 72 in its raw data.

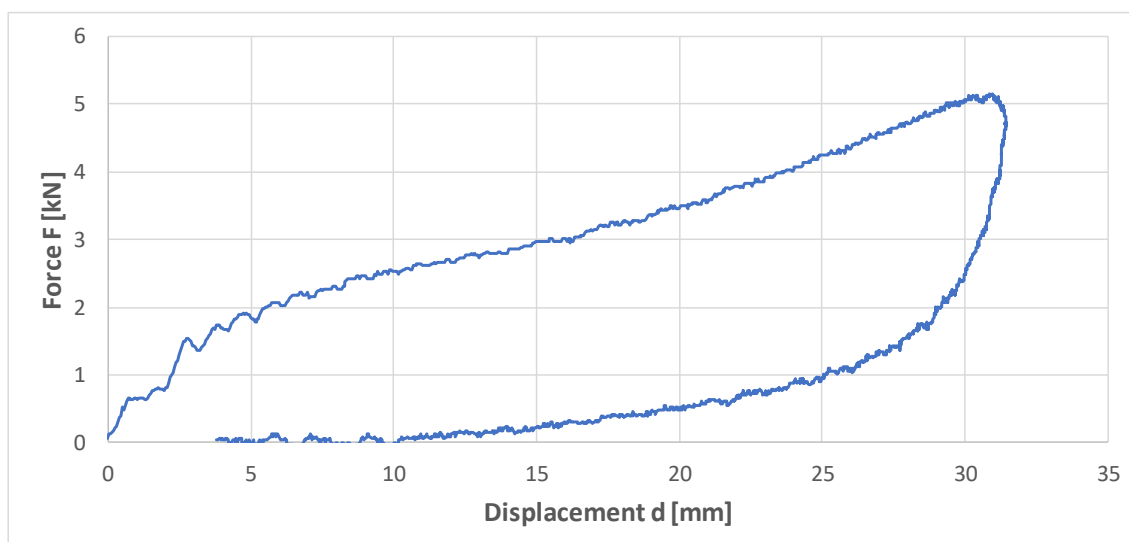


Fig. 72 Force-displacement-curve of AC216 during an approx. 110 J impact at room temperature

The usage of force-displacement or stress-strain data out of tensile and compression tests is common practice in numerical approaches and done mostly in tabular form. The input data set is preferably a non-oscillating data curve for simplified material models such as MAT181 in LS-DYNA, which is internally filtered and reproduced by a polynomial for loading and unloading. The material card was introduced 2002 with LS-DYNA v970 and is since then widely used for representing rubber and foam models. In contrary to regular material models, the complex and highly time-consuming effort of identifying material parameters can be omitted, as MAT_SIMPLIFIED_RUBBER (MAT181) is reproducing the uniaxial tension and compression test data. Its Ogden's functional behind the material card depends on principal stretch ratios, while principal strain is following from the principal stretch ratio. The data is evaluated internally, but directly from the basing engineering stress-strain or force-displacement data. A closer explanation of the material formulation is given in [175,176]. Clearly, a limitation of the applicability of MAT181 for cork needs to be seen in rubber incompressibility and the missing or limited damage model. Recapitulating, cork shows during its loading plateau mainly elastic cell wall buckling, but with increasing plastic and viscoplastic yielding effects up to the final total cell collapse – the densification. Nonetheless, the possibility to have recourse on a hyperelastic material model which allows to respect even these beginning effects during the 110 J impact test by a hysteresis and a Poisson's ratio close to 0, the possibility to model the single impact is given here and has priority. Fig. 73 shows the base for this approach of modelling, the numerical representation of the drop tower test, where a

specimen with the same measurements is placed on anvil and will be compressed according to mass and impact velocity of the real impactor.

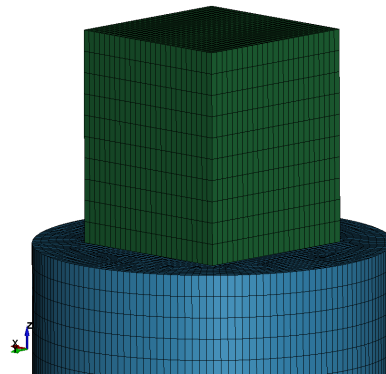


Fig. 73 Numerical model for the implementation of the cork material model

The simulation was performed for 25 ms in total. In Fig. 74 the displacement-time-curves of experiment and simulation are compared.

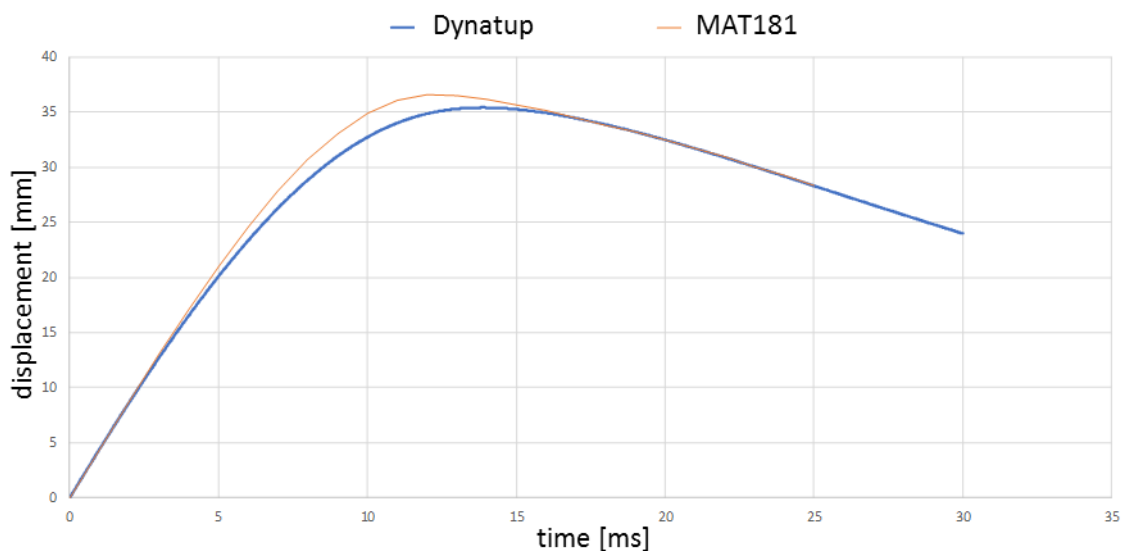


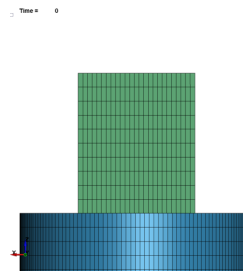
Fig. 74 Displacement-time curve of experimental and numerical test data

It is visible, that the initial data set of the physical impact test offered a longer time range, while the material model was calculated and plotted only for 25 ms. In this concern it has to be noted, that the specimen was not fixed to the anvil or to the impactor. In the back motion of the impactor, it comes to the loosening between all the instances, which can be seen in Fig. 75.

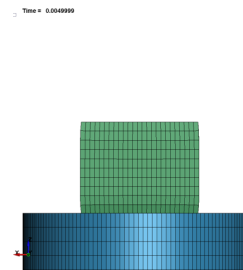


Fig. 75 Bounce of the cork specimen at $t = 34$ ms

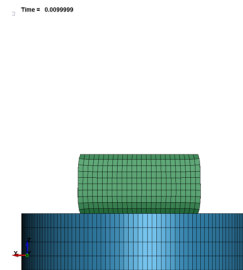
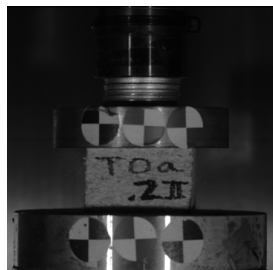
Having recourse on Fig. 74, it gets clear that the displacement-time-curve of the experiment is connected to the impactor motion and is able to show the corks behaviour only up to the moment of their loosening, which occurred around 25 ms, respectively on both sides of the specimen 27 ms after the impact. In order to fit the behaviour after the maximum of displacement, the parameters of HU and SHAPE were used additionally within the material card. Both are used frequently to mimic a quasi-damage of the material by adjusting the relaxation, meaning to fit the recovery to the objects initial shape. The sequence in Fig. 76 gives an overview on the cork materials behaviour in terms of displacement for both the experimental tests and the numerical representation in LS-DYNA by material card MAT181.



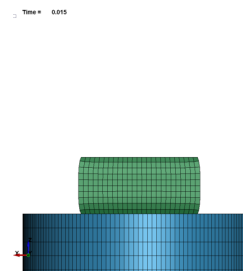
t = 0 ms



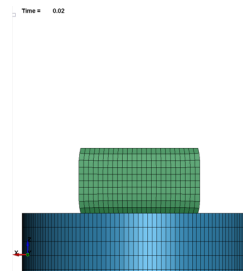
t = 5 ms



t = 10 ms



t = 15 ms



t = 20 ms

Fig. 76 Sequence of compression for the real experiment and the numerical model using MAT181

7.5 Numerical simulation: considering the U-band as a passive safety device

The beforehand presented pragmatic implementation of corks behaviour into a material model using MAT181 allows in a consecutive step to simulate the envisaged additional passive safety device during its single impact to the ground. In this scenario it is intended to protect the child's head by lowering the severity of the impact for the head and brain structure. The solution, which was named *U-band*, was coupled therefore with the structure of the baby carrier and also with the aHEAD 2-year-old Finite Element Head Model out of chapter 5. It is intended to state about the crashworthiness and hence about the influence of the cork material shock absorption layer. Following this idea, the situation is again adjusted to the bicycle side fall, which was topic in chapter 4. In order to make the calculatory results the most comparable, the simulation was calculated in a control simulation once again, where only the shock absorption cork layer was excluded. The results will be shown at the specific positions.

Fig. 77 shows the sequence of the case with the shock absorber for the times $t = 0 \dots 30$ ms in 5 ms-steps, where the initial resultant linear velocity of 5.01 m/s was applied to all instances except the rigid and fixed ground. Consequently, a major head impact will be recognized. Its visualization let assume, that the inner brain structure will have the need to handle the majority of the impact energy between 5 and 10 ms, as the step at 10 ms shows a significant deflection of the cerebrum from its natural geometrical situation, especially on the opposite side of the impact. In the same moment, the left hemisphere is compressed toward the structures of pia, dura and lamina interna. Within the next 5 ms, the full head structure will initiate already the back motion from this impact to the U-band and ground, while it will take approx. additional 15 ms more, until cerebrum and cerebellum are regaining their initial situation within the skull. In this time range, again clearly the coup-contrecoup-phenomenon is recognizable. Furthermore, similar to the simulation in 6.8, a flow of cerebrospinal fluid toward the opposite side of the impact is visible.

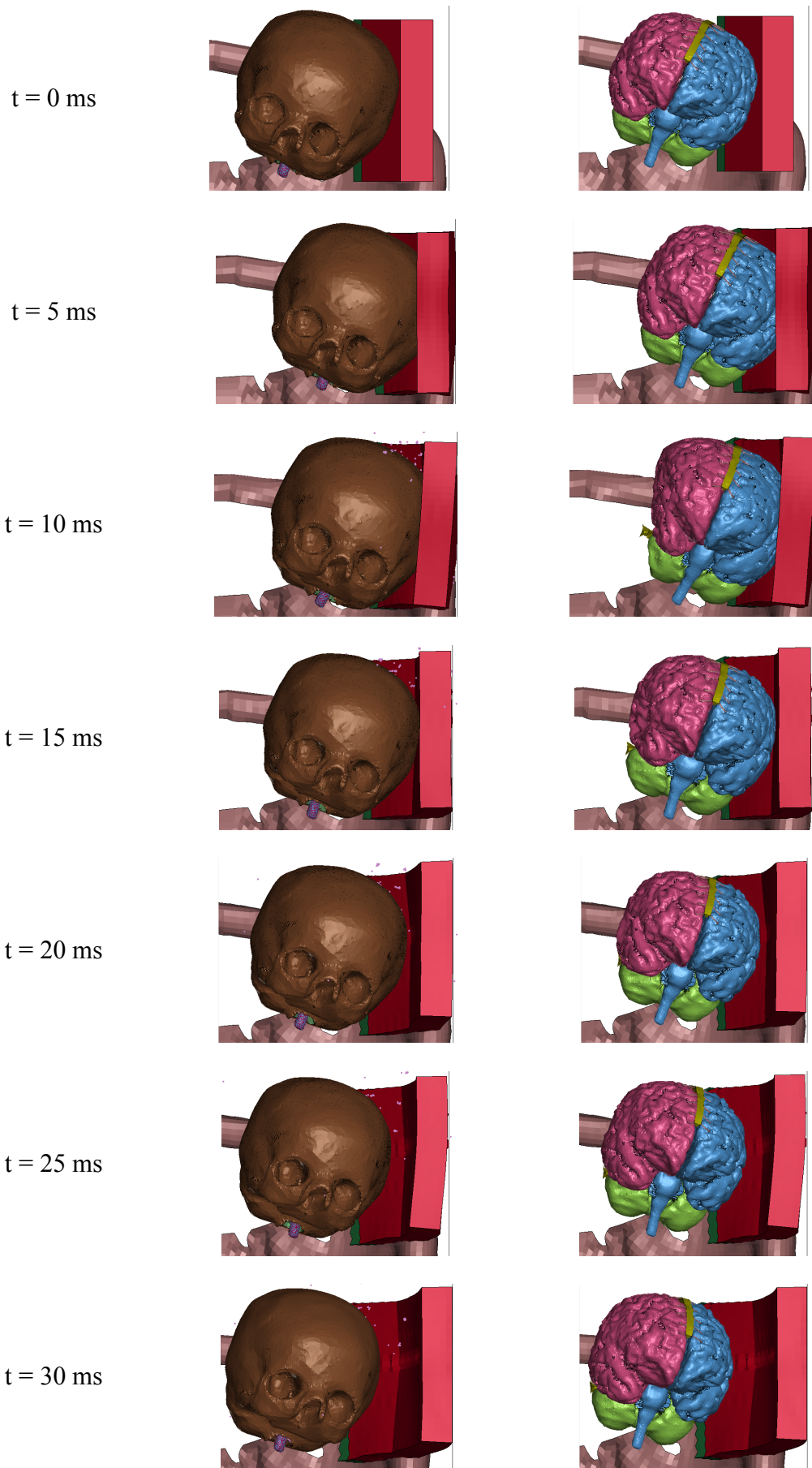


Fig. 77 Sequence of the side fall situation with included U-band

As the general motion is comparable to the simulation, where no shock absorption layer was installed, the question arises about the necessity of the passive safety device. So far, significant displacement is visible again, as well as the coup-contrecoup-phenomenon, which in total would be generally envisaged to be eliminated or significantly reduced.

The following graph in Fig. 79 shows the resultant acceleration over time for variants of included and excluded shock absorption layer, but for the same hexahedral solid element nr. 2610789, which is located in the corpus callosum.

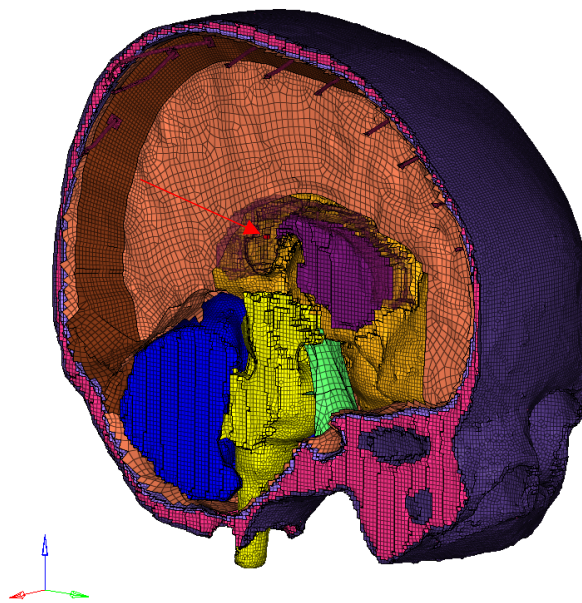


Fig. 78 Solid hexahedral element #2610789 in the corpus callosum used for acceleration assessment

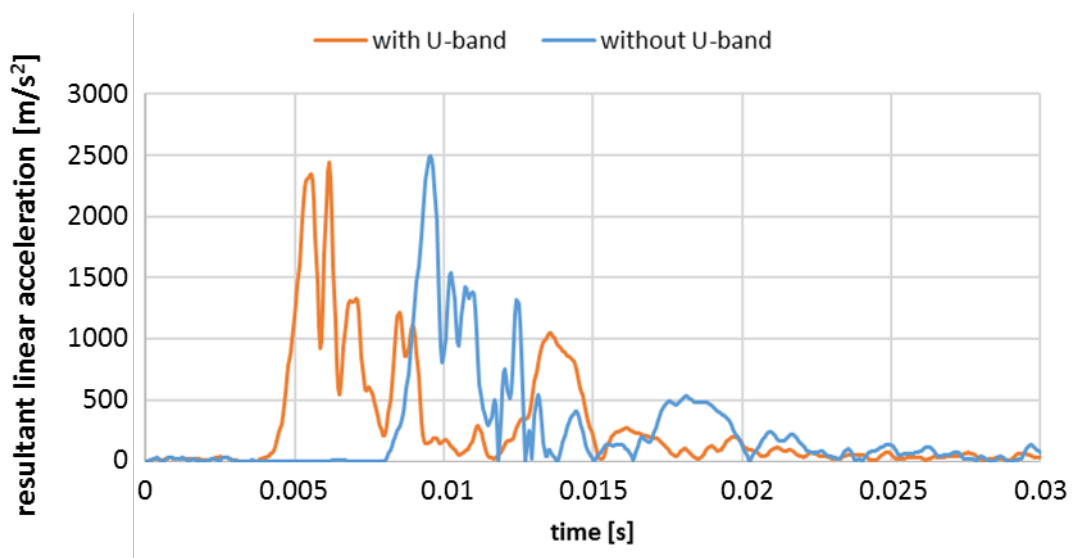


Fig. 79 Resultant acceleration time graph for the hexahedral element #2610789 in the corpus callosum

Interestingly, the peak resultant acceleration value is comparable and lowered only by approx. 20 m/s^2 for the situation with the cork layer. It needs to be noted, that the two graphs are timely shifted, as the head model without U-band travels longer before it comes to the direct impact to the ground. The curves are in their behaviour comparable and show generally a limited effect of the shock absorption layer for the inner brain structure of the corpus callosum regarding the shock absorption. This might be even independent from the hypothetically applied material of the shock absorption layer. The mechanical passing of the impact's shock wave may play thereby also a role. Nonetheless, it needs to be mentioned, that the peak acceleration value occurs not on the same curve peak. While the maximum for the simulation without U-band occurs on the first significant peak at around 9.6 ms with 2460 m/s^2 , the maximum with U-band occurs now at the second peak, while this peak appears higher, whereas the value of 1510 m/s^2 at 10.2 ms changed to a value of 2440 m/s^2 at 6.15 ms . The same effect can be recognized several times over the shown sequence and time range. It can be recognized, that by considering the cork layer in the application, the general curve values are lowered by approx. 50 to 70 m/s^2 .

The graph in its progression points generally on three stages, which the hexahedral element of the corpus callosum as a deformable instance within the skull is facing during the scenario. It starts generally with the deceleration of the skull, which leads to a significant raise in the deceleration. Consecutively in the second stage, the corpus callosum as the hemisphere connecting instance is still showing motion due to inertia but being increasingly pressed into a state of compulsion. While the impact sided hemisphere is compressed into the lamina interna, the opposite located hemisphere is still moving due to inertia. In this moment – this was also shown in the earlier side fall case in Fig. 56 – the falx cerebri acts supportive by carrying load. This limits the load on the corpus callosum, but particularly in dependency of the force direction. In this context it should be here noted, that the case in chapter 6.8 showed a differing impact angle to the skull. Regarding the force direction and impact position, it underlines regarding the translational acceleration peaks of 295 g in chapter 6.8 versus the 250 g in this example the supportive character, but impact direction dependent character of the falx cerebri. Elastic behaviour repeats the happenings during the second stage in the back motion but forms thereby the third stage. This third stage can be recognized in terms of the applied U-band for the times approx. between 11.6 and 15 ms .

The observation of this behaviour for a hexahedral element in the corpus callosum shows the importance to consider the presence of a movable and deformable brain in the

assessment of a head, when involving the case of acceleration-deceleration behaviour, even apart from an impact. In contrary, giving the an example of the assessment of passive safety gear, the procedure relies in practice not on a moving centre of gravity or mass for a head, especially when it comes to the calculation of HIC. This might lead to some discrepancies in the understanding of a helmet or the here presented cork layer as passive safety device, especially in its performance capabilities. Fur the explanation and further assessment, also a control group of 11 elements of the diploe layer was chosen (see Fig. 80). It will be used supportive for the result interpretation at the specific points.

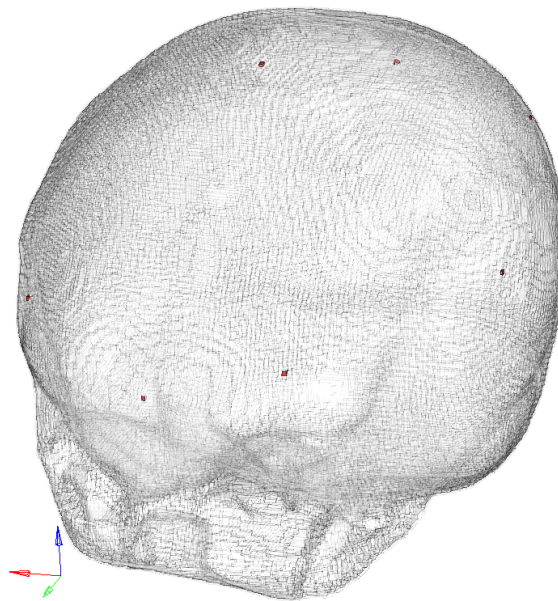


Fig. 80 Choice of 11 hexahedral solid elements (red colour) of the diploe layer for acceleration assessment

A shock absorption layer in bicycle helmets is in its thickness location-specific different, but mainly measured below 30 mm. Generally, the shock absorption layer acts in the same way as the deformation or crash zone in vehicles. Characterized by crash boxes as well as the general front-structure, it is intended by these structures to simply waste energy by huge, but directed deformation and self-destruction. Even though a helmet shock absorption layer is intended to use the same principle, the geometrical space for this is reduced to a minimum. Considering the extreme case of a missing shock absorption layer, thus the absence of a helmet, the function of energy wasting by deformation will be fulfilled by the skull itself, leading to significant visible deformation of the skull beyond elastic borders, which are shown in combination with the occurring 1st and 3rd principal stresses in Fig. 81.

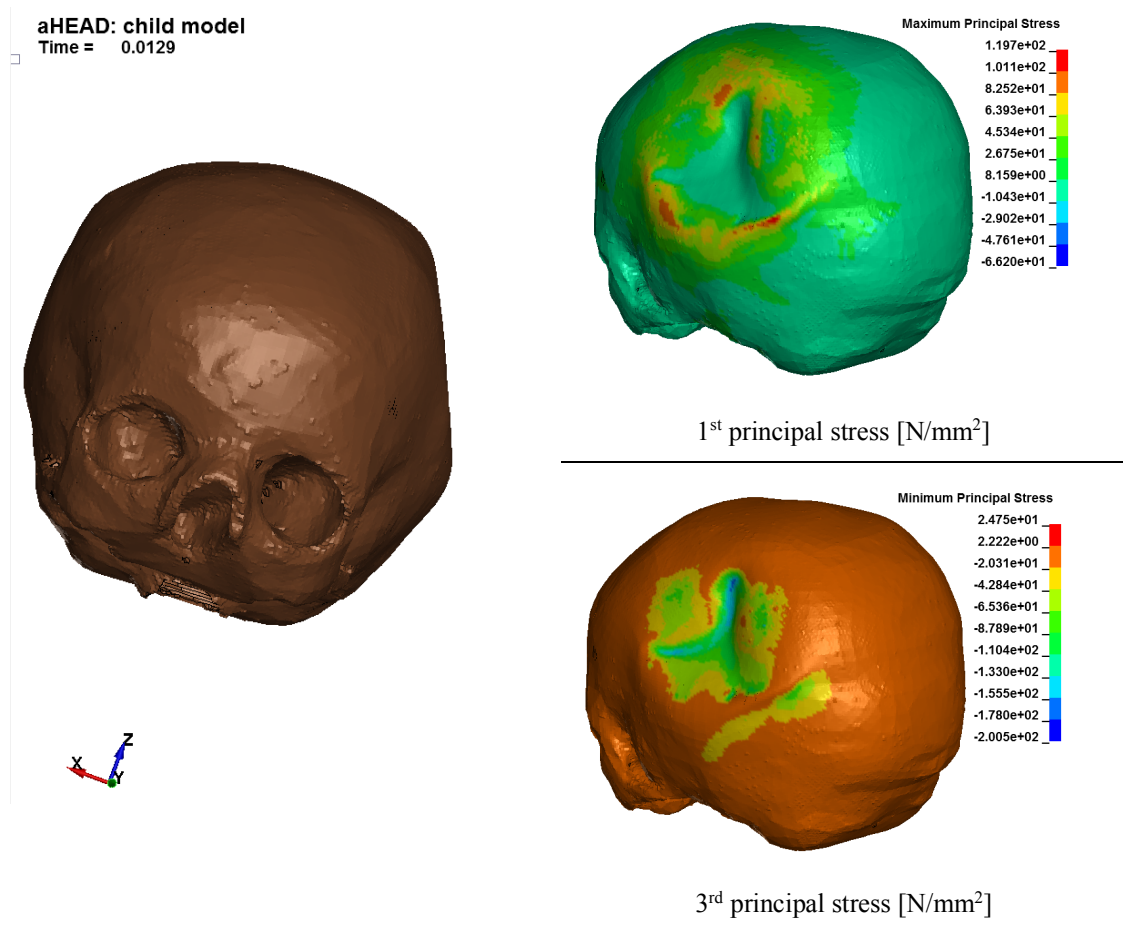


Fig. 81 Visualisation of the skull deformation without the U-band and 1st and 3rd principal stresses

The resultant acceleration graph (see Fig. 82) for the rigid body of the diploe thereby shows a peak at slightly over 227 g and reveals a calculated HIC(36) value of 1222.

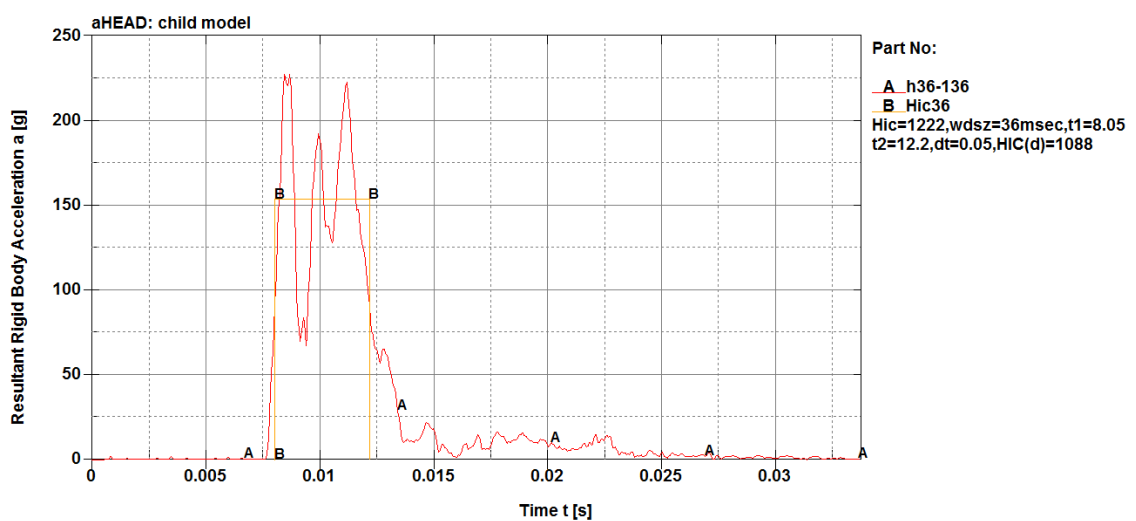


Fig. 82 Resultant translational acceleration of the diploe layer and HIC without applied cork layer

It should be taken carefully, that the HIC here is not completely comparable and in line to the definition of the HIC, as the diploe's centre of gravity or mass might be close to the head's centre of gravity or mass, but might be a different geometrical point. Including the cork layer in the simulation follows a decrease of the diploe's resultant rigid body acceleration peak by more than 50 g. Moreover, the HIC value dropped to 810, while the time interval elongated by approx. a millisecond, which is shown as well in Fig. 83.

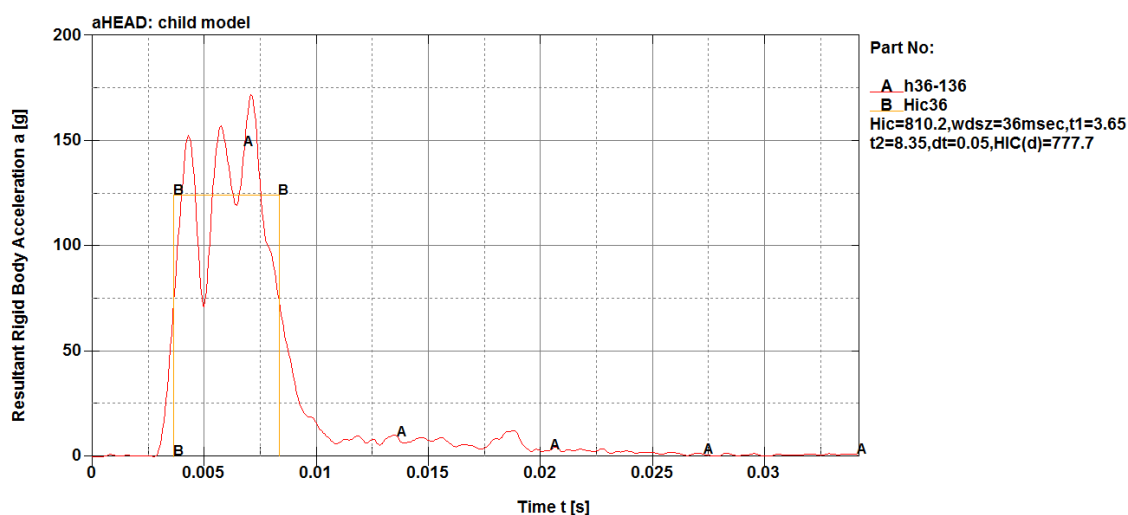


Fig. 83 Resultant translational acceleration of the diploe layer and HIC with applied cork layer

The actual measured effect of lowered HIC and acceleration values during the performance assessment shows to be connected straight to the assumption of a non- movable centre of gravity or mass of the head form and as well to the effect or spreading the impact force to a wider area or section. This is underlined by a view on Fig. 84, which shows a significant lowered deformation of the skull, following as well a less severe deformation pattern of the skull structure within the impacted area. In this respect, the U-band provides with very comparable capabilities as a safety helmet, which was for example also used for comparison purpose in the experiments in the literature, especially regarding the calculated HIC value [39].

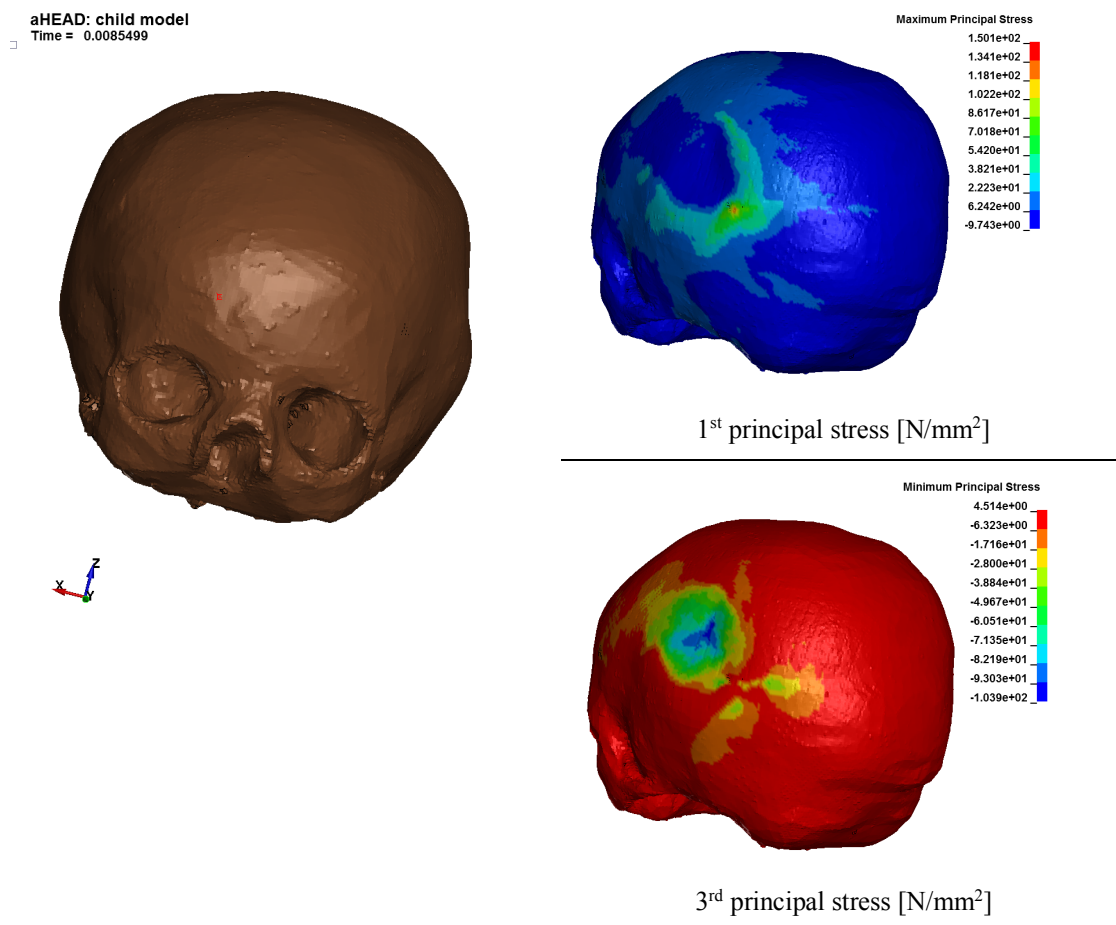


Fig. 84 Visualisation of the skull deformation with the U-band and 1st and 3rd principal stresses

By spreading the occurring impact forces to a wider area, deflection took mainly place in the absorption liner, which is regarding the calculated HIC value also considered in lowering the risk of skull fracture. The acting acceleration on the rigid body of the diploe was lowered thereby by approx. 23%. Moreover, the cork specimen tested within the experiments of chapter 7.3 were capable to handle the 110 J impact entirely, which would allow the presented U-band even to handle theoretically a consecutive impact in the same scenario at the same position.

7.6 Chapter conclusions

Particularly cork with a density of 216 kg/m³ was described in the literature as a material tailorable in its mechanical properties and also as a promising choice for substituting the synthetic material of EPS in helmets as passive safety devices [163]. Own experiments under high impact energies and extreme low and high temperatures with a selection of cork agglomerates enabled to state, that:

1. Cork material's capability of energy absorption during an impact is mainly dependent on its material density and the temperature of application. With a rising density of the specimen, the temperature's influence to the energy absorption rises as well.
2. The results from the previous research presented by Ptak et al. in 2017 were able to be confirmed [170]. With choosing the grain size, the amount of glue or binder for the cork agglomerate is influenced as well. By this, the amount of glue influences regarding the drop of registered reaction force, which is particularly visible for the cork samples at a temperature of 100°C. A significant influence to the overall absorbed impact energy was recognized.
3. The performance of the cork agglomerates is affected by the temperature significantly, especially for high-energy impacts.

Moreover, the experimental data was used to establish numerical simulations of

- 1) the material AC216 for the first impact in order to implement it into the simulation of
- 2) the proposed technical solution of the U-band.

The simulation of the cork material was realized by using the material card MAT_SIMPLIFIED_RUBBER (MAT181) in LS-DYNA, as it offers generally to have recourse on experimental data out of uniaxial tension and compression tests. It helps to omit the complex and highly time-consuming effort of identifying material parameters. The less complex case of the single drop and cushioning situation within this side fall scenario was able to be modelled accurately.

Consecutively, the U-band was coupled with the structure of the baby carrier and also with the aHEAD 2-year-old Finite Element Head Model out of chapter 5. The simulation of the U-band as passive safety device showed a significant lowering potential regarding the resultant translational skull acceleration and skull deformation. Consequently, the solution is promising in reducing the severity of crashes for the seated child's head. Moreover, the U-band was recognized as being comparable to a bicycle helmet in the crash and absorption characteristics. The solution overcomes thereby also the restriction of securing in a single impact only, as the cork agglomerate is able to handle multiple impacts of the concerned impact energy level.

8 Final conclusions and future related work

Finally, the main conclusions, which were obtained by this work, shall be presented within this chapter. Furthermore, ideas for future and related research are proposed.

8.1 Final conclusions

The bicycle has been promoted as a clean, cheap and healthy means of transport in urban areas, excelling even the public transport by an increased flexibility in personally preferred travel path and time. This flexibility and freedom with health-oriented side effects is promoted mainly toward the direct user, the bicyclist. Moreover, a slightly overseen group of vulnerable road users is also included in this movement: children, which are transported in dedicated baby carriers.

Commonly, the idealistic visualisation of the unharmed, flexible and environmentally friendly life of a bicyclist is used for promotion. On the opposite side, conflict situations in the traffic are daily business due to the different means of transport with their various characteristics. In addition, this happens especially on limited, shared space in cities. In the worst cases of impacts of bicyclists against other vehicles, particularly the vulnerability of this group gets visible due to their missing cage. Thereby, related kinematics and injury biomechanics were well described within the literature. Research covered intensively related aspects for both pedestrians and bicyclists as familiar representatives of VRUs. Oppositely, bicycle transported children were so far rather passively recognized and indirectly addressed, for example by referring them in user instructions for baby carriers or consumer tests of these items. Another source of information was found so far on the other time mark – after the impact and with the presence of an injury – by emergency departments or hospital admissions. However, the post-impact kinematics and hence also the injury mechanisms leading to the recognized injury outcome, remained in a clear form widely undescribed for this special form of traffic participant.

Consequently, for **chapter 3** the main motivation was to assess the vulnerability of these children by setting up an original numerical model and approach to simulate related vehicle impacts. The crashworthiness of bicycle baby carriers figured out to be low. In fact, the bicycle baby carrier was recognized during these simulations primarily as an additional seat on a bicycle, while the seat was not able to act as a passive safety device. This is particularly true for lateral vehicle impacts, where the seat's geometry is insufficient to protect the child in a significant way from the impacting and penetrating vehicle. Oppositely, by using the harness and connecting child and bicycle with baby carrier mechanically, the significant to pedestrians and bicyclists differing crash kinematics were able to be recognized and to be described. Underlining the literature consensus to wear additional safety gear such as a helmet, the head was – among others but with a special concern – in the simulations recognized as a mainly affected body part. It was stated as a central conclusion, that the post-impact kinematics of a child model in the bicycle baby carrier correlated neither with the kinematics of an impacted pedestrian nor with these of an impacted bicyclist. Bicycle baby carrier transported children form due to their specific seating situation a separate, third group.

As chapter 3 focused in the simulation on one specific vehicle front-end geometry only, the influence of the height of the BLE to the WAD of the child was a main interest in **chapter 4**. Finally, the formula for estimating the child's WAD in dependency of the vehicle BLE and initial vehicle impact velocity was presented. The calculation is three-parted, as the raising BLE provoked for the complex of child and bicycle a switch from a somersault-like move over the bonnet into a clear frontal projection. Generally, the height of the BLE figured out to be the variable of higher importance for the experiment and hence the estimation of the child's WAD. For a specific corridor of the BLE, no head impact to the bonnet was recognized. Nonetheless, the absence of the head impact to the bonnet or front-end did not stand for a safer impact constellation or a vehicle design recommendation. It has to be noted, that the possibility of a (consecutive) head impact to the ground remained.

Thereby – and shown by the full-scale experiments involving a 3-year-old ATD in **chapter 5** – the vertical head impact velocity for this colloquially “simple side fall” was comparable to numerous numerical simulations involving an impacting vehicle. It pointed on the potential of severity of these direct cranial impacts, which can occur in connection with the usage of bicycle baby carriers and the presence of unintended fall or impact situations. What was hidden so far mostly in the experimental and numerical tests,

was the deeper view into the motion of the head, particularly the deformability of the skull and its internal structure represented by the brain. The experiments made the limitation visible, which is naturally taken by using a rigid head structure with a constant CoG for injury assessment via ATDs or MADYMO dummies. Even though the approaches are validated and supported by empirical data. Basically, only the acceleration of a rigid body over time for the assessment remains for the brain as a system, while the real structure of head and brain is highly non-linearly characterized and inherits an intensive complex interacting and deformable structure.

To overcome this restriction in appropriately reflecting the biomechanical response of the brain to an impact, **chapter 6** described the creation of the Finite Element Head Model of a two-year-old with an advanced structure and material characterisation compared to models, which are currently found in the literature. The model was in its initial version presented and described in this doctoral dissertation. By using special chosen, patient-specific medical imaging data, it was avoided to base the model on scaled adult anthropomorphic. Furthermore, a focus was set on realising a fully hexahedral mesh for 3D-instances, whereas highly complex geometrical details as the gyri and sulci were integrated as well. The space for CSF was filled by applying smoothed-particle hydrodynamics, which allows revealing the complex motion of the CSF even during impact conditions. However, as it was already revealed by the literature review, also the work in chapter 6 had to face the non-availability of robust data over the entirety of population for a common, conservative validation of a generic model. The original FEHM of a two-year-old in chapter 6 enriches the state-of-the-art with its implemented and shown features. It proposes in this context a different approach of comparability to real-world accident data but also to other current paediatric models by revealing the entirety of its material and structural data. In a special concern to the so far highlighted side fall of a child seated in a bicycle baby carrier, the potential severity of the fall for the child's head was pointed out once again.

Chapter 7 focused with the presentation of an additional, attachable passive safety device for bicycle baby carriers consequently on the issue of the head's vulnerability due to a direct-cranial impact, which might occur in vehicle collisions more than once. Regularly, personal passive safety gear such as a helmet finds its shock-absorption layer made out of EPS. The proposed passive safety device *U-band* in opposite bases on the application of the sustainable material of agglomerated cork with a density of 216 kg/m^3 . In order to describe the cork material in its mechanical properties, own experiments under high

impact energies and extremely low and extremely high temperatures were carried out. In the findings, it was stated about cork material energy absorption capabilities in significant dependency of the density and temperature of application. Moreover, the used grain size and hence the amount of synthetic binder were identified under high temperatures as influencing the level of absorbed impact energy. The results showed, that the performance of the cork agglomerates under high-energy impacts is significantly influenced by the temperature. Overall, the experimental results were used to establish a material model of the chosen agglomerated cork with a density of 216 kg/m^3 in LS-DYNA. In a consecutive step, the numerical models of bicycle baby carrier, proposed U-band with implemented cork material model and the aHEAD 2-year-old FEHM were coupled with each other. It enabled simulating the case of the side fall accurately and particularly to visualize and assess the head and brain's response to the ground impact. The implementation of the U-band revealed a significant lowering of the resultant translational head acceleration and hence also skull deformation. A benefit, which is commonly achieved by a helmet as a passive safety device. Moreover, the U-band excels the helmet by the application of agglomerated cork as a shock absorption layer, as it overcomes the restriction of handling a single, major impact only, limiting the child's injuries in multi-impact scenarios.

This doctoral dissertation concentrated on bicycle-transported children regarding their vulnerability and hence their injury biomechanics in impact scenarios. It contributed to the state of the art by:

- 1) establishing an original description of the seated child kinematics and biomechanics during and shortly after (vehicle) impacts,
- 2) giving an insight into the biomechanics and mechanisms behind a head and brain injury by the novel, advanced Finite Element Head Model of a two-year-old,
- 3) evaluating and proposing the implementation of the additional passive safety device into the bicycle baby carrier.

Overall, the author of this doctoral dissertation forms the final conclusion:

“The post-impact kinematics of a child model, which is seated in a bicycle baby carrier is neither represented by pedestrian’s nor bicyclist’s kinematics. They form a separate, third group.”

8.2 Future research

The results presented in this doctoral dissertation are not closing the related topics. Beside the general ambition to enhance or enrich the current research, presented results are naturally also envisaged and hoped to motivate further related work.

The chapters 3 and 4 helped to describe kinematics and to gain also a closer view on the influence out of the specific constellation of bicycle with baby carrier and a variety of vehicle front-end shapes. Seeing the popularity of front-mounted baby carriers on bicycles or trailers for even two children, these cases might not be reflected entirely by research in the current literature. The same has to be mentioned concerning vehicle front-ends, which can be different from the presented here. In this context, also various and partially contradicting definitions of vehicle front-end shapes enrich the problem, which points to the lack of a generally accepted definition. Establishing a consensus in vehicle shape definition and including also newer front-end shapes and designs would help in a wider sense. By renewing simulations and experiments by the variety of shapes, results over literature will be more comparable and would give an insight, if newer front-ends helped to improve crash characteristics for children in bicycle baby carriers.

The most of the potential for future work has to be seen in the head model, as a validated model could help to investigate the so far available data deeper and reveal crucial information regarding the injury mechanisms behind the related injuries. Unfortunately, it is rather unlikely, that robust data for young children over the entirety of the population will occur in a timely manner. Moreover, there is currently no clear consensus about the approach of a quasi-validation, which might be found even partially in tests of actual or substitutional material. A common benchmark for the available paediatric head models is missing, but could help to establish a link for clear comparison. This would significantly enhance the robustness of these models. This points especially regarding the rigorous comparison to real-world accident data as well as toward substitutional material tests, for example of porcine.

Bibliography

1. Fisher, A.J.; Hall, R.R. The influence of car frontal design on pedestrian accident trauma. *Accid. Anal. Prev.* **1972**, *4*, 47–58, doi:10.1016/0001-4575(72)90057-7.
2. Scholten, A.C.; Polinder, S.; Panneman, M.J.M.; Van Beeck, E.F.; Haagsma, J.A. Incidence and costs of bicycle-related traumatic brain injuries in the Netherlands. *Accid. Anal. Prev.* **2015**, *81*, 51–60, doi:10.1016/j.aap.2015.04.022.
3. Murray, J.; Ryan-Krause, P. Bicycle Attachments for Children: Bicycle Seats, Trail-a-bikes, and Trailers. *J. Pediatr. Heal. Care* **2009**, *23*, 62–65, doi:10.1016/j.pedhc.2008.10.003.
4. Ptak, M. Method to assess and enhance vulnerable road user safety during impact loading. *Appl. Sci.* **2019**, *9*, 1000, doi:10.3390/app9051000.
5. ETSC *Revision of the regulation on protection of pedestrians and other vulnerable road users*; 2009;
6. European Parliament and Council Regulation (EC) no 78/2009 of The European Parliament and of the Council. *Off. J. Eur. Union* **2009**, 2008.
7. SWOV Fact sheet Vulnerable road users. **2012**, 1–5.
8. Powell, E.; Tanz, R. Tykes and Bikes, Injuries associated with bicycle-towed child trailers and bicycles-mounted child seats. *Arch Pediatr Adolesc Med* **2000**, *154*.
9. Austroads *The Australian National Cycling Strategy 2011–2016: Gearing up for active and sustainable communities*; Austroads: Sydney, Australia, 2010; ISBN 9781921709296.
10. Oxley, J.; O’Hern, S.; Raftery, S.; Woolley, J. How safe are children when transported by bicycle? *Traffic Inj. Prev.* **2016**, *17*, 163–167, doi:10.1080/15389588.2016.1199866.
11. Ptak, M.; Wilhelm, J.; Sawicki, M.; Rusiński, E. CHILD SAFETY ON VARIOUS BICYCLE-MOUNTED SEATS DURING VEHICLE IMPACT. *Transport* **2019**, *34*, 1–8, doi:10.3846/transport.2019.9083.
12. Ptak, M.; Wilhelm, J.; Saunders, N. Safety analysis of a bicycle-mounted child seat. *IEEE 2018 XI Int. Sci. Conf. Automot. Saf.* **2018**, 1–6, doi:10.1109/AUTOSAFE.2018.8373316.
13. Raftery, S.J.; Oxley, J.; Thompson, J.; Wundersitz, L.N.; (CASR), U. of A.C. for A.S.R. *Transportation of children with bicycle seats, trailers, and other carriers: considerations for safety*; 2016;
14. Simms, C.; Wood, D. *Pedestrian and cyclist impact*; Solid Mechanics and Its Applications; Springer Netherlands: Dordrecht, 2009; Vol. 166; ISBN 9789048127429.
15. King, A.I. *The Biomechanics of Impact Injury*; 2018; ISBN 978-3-319-49790-7.
16. Fanta, O.; Bouček, J.; Hadraba, D.; Jelen, K. Influence of the front part of the vehicle and cyclist’s sitting position on the severity of head injury in side collision. *Acta Bioeng. Biomech.* **2013**, *15*, 105–112, doi:10.5277/abb130113.

17. Carter, E.L.; Neal-Sturgess, C.E. MADYMO Reconstruction of a Real-World Collision between a Vehicle and Cyclist. *Int. J. Crashworthiness* **2009**, *14*, 379–390, doi:10.1080/13588260902823999.
18. Nie, J.; Yang, J. A study of bicyclist kinematics and injuries based on reconstruction of passenger car-bicycle accident in China. *Accid. Anal. Prev.* **2014**, *71*, 50–59, doi:10.1016/j.aap.2014.04.021.
19. Cesari, D.; Cavallero, C.; Farisse, J.; Bomnoit, J. EFFECTS OF CRASH CONDITIONS ON PEDESTRIAN LEG KINEMATICS AND INJURIES BASED ON CADAVER AND DUMMY TESTS. In Proceedings of the Proceedings, Annual Conference - American Association for Automotive Medicine; Washington D.C., 1985; pp. 275–285.
20. Monea, A.G.; Van der Perre, G.; Baeck, K.; Delye, H.; Verschueren, P.; Forausebergher, E.; Van Lierde, C.; Verpoest, I.; Vander Sloten, J.; Goffin, J.; et al. The relation between mechanical impact parameters and most frequent bicycle related head injuries. *J. Mech. Behav. Biomed. Mater.* **2014**, *33*, 3–15, doi:10.1016/j.jmbbm.2013.06.011.
21. IMPROVER Impact on road safety due to the increasing of sports utility and multipurpose vehicles. **2006**.
22. Ptak, M. Pedestrian safety: A new method to assess pedestrian kinematics. *Transport* **2019**, *34*, 41–51, doi:10.3846/transport.2019.7081.
23. Simms, C.K.; Wood, D.P. Pedestrian Risk from Cars and Sport Utility Vehicles - A Comparative Analytical Study. *Proc. Inst. Mech. Eng. Part D J. Automob. Eng.* **2006**, *220*, 1085–1100, doi:10.1243/09544070JAUTO319.
24. King, A.I.; King, A.I. Car-Pedestrian Impact. In *The Biomechanics of Impact Injury*; Springer International Publishing: Cham, 2018; pp. 569–595.
25. Ptak, M. *Assessment of the influence of vehicle front-end construction elements on vulnerable road users safety enhancement. (in Polish) - PhD Thesis: 7/2012*; Wroclaw University of Science and Technology, Wroclaw, 2012;
26. Li, G.; Wang, F.; Otte, D.; Cai, Z.; Simms, C. Have pedestrian subsystem tests improved passenger car front shape? *Accid. Anal. Prev.* **2018**, *115*, 143–150, doi:10.1016/j.aap.2018.03.014.
27. Han, Y.; Li, Q.; He, W.; Wan, F.; Wang, B.; Mizuno, K. Analysis of Vulnerable Road User Kinematics Before/During/After Vehicle Collisions Based on Video. *IRC-17-26 IRCOBI Conf. 2017* **2017**, 151–165.
28. Euro-NCAP EUROPEAN NEW CAR ASSESSMENT PROGRAMME (Euro NCAP) FRONTAL IMPACT. **2013**, 52.
29. Zander, O.; Gehring, D.; Lesmann, P. Improved safety of bicyclists in the event of a collision with motor vehicles and during single accidents. *23rd ESV Conf. Proc.* **2013**, 1–11.
30. Schijndel, M. Van; Hair, S. De; Rodarius, C.; Fredriksson, R. Cyclist kinematics in car impacts reconstructed in simulations and full scale testing with polar dummy. *Proc. ...* **2012**, 800–812.
31. Roudsari, B.S.; Mock, C.N.; Kaufman, R.; Grossman, D.; Henary, B.Y.; Crandall, J. Pedestrian

- crashes: Higher injury severity and mortality rate for light truck vehicles compared with passenger vehicles. *Inj. Prev.* **2004**, *10*, 154–158, doi:10.1136/ip.2003.003814.
32. Henary, B.Y.; Crandall, J.; Bhalla, K.; Mock, C.N.; Roudsari, B.S. Child and adult pedestrian impact: the influence of vehicle type on injury severity. *Annu. Proc. Assoc. Adv. Automot. Med.* **2003**, *47*, 105–26.
33. Otte, D. Severity and Mechanism of Head Impacts in Car to Pedestrian Accidents. In Proceedings of the Proceedings of the International Research Council on Biomechanics of Injury (IRCOBI) Conference; 1999; pp. 329–341.
34. Supreme Audit Office in Poland Cyclist and pedestrian safety. *KIN.410.008.00.2015* **2016**.
35. Küster Fabian A European Roadmap for cycling – ECF proposal. *Eur. Cyclists' Fed.* **2015**.
36. Tanz, R.R.; Christoffel, K.K. Tykes on bikes: Injuries associated with bicycle-mounted child seats. *Pediatr. Emerg. Care* **1991**, *7*, 297–301, doi:10.1097/00006565-199110000-00010.
37. European Committee for Standardization *DIN EN 14344: Child seats for cycles - Safety requirements and test methods*; Brussels, 2004;
38. Milne, G.; Deck, C.; Bourdet, N.; Alline, Q.; Gallego, A.; A.P., C.; Willinger, R. Assessment of Bicyclist Head Injury Risk under Tangential Impact Conditions. *IRC-13-90 IRCOBI Conf. 2013* **2013**, *33*, 735–746.
39. Miyamoto, S.; Inoue, S. Reality and risk of contact-type head injuries related to bicycle-mounted child seats. *J. Safety Res.* **2010**, *41*, 501–505, doi:10.1016/j.jsr.2010.10.004.
40. Kishibe, S.; Miyazaki, Y.; Nomura, O.; Takei, H.; Hagiwara, Y.; Kitamura, K.; Nishida, Y.; Yamanaka, T. PA 04-3-0464 Fall injury in infants while the patient is operating a bicycle. In Proceedings of the Injury Prevention; 2018; Vol. 24, p. A8.3-A9.
41. Kroeyer, H.R.G. The relation between speed environment, age and injury outcome for bicyclists struck by a motorized vehicle - A comparison with pedestrians. *Accid. Anal. Prev.* **2015**, *76*, 57–63, doi:10.1016/j.aap.2014.12.023.
42. Lindman, M.; Jonsson, S.; Jakobsson, L.; Karlsson, T.; Gustafson, D.; Fredriksson, A. Cyclists interacting with passenger cars; a study of real world crashes. *Int. Res. Counc. Biomech. Inj.* **2015**, 1–12.
43. Bundesministerium für Verkehr und digitale Infrastruktur Halbzeitbilanz des Verkehrssicherheitsprogramms 2011-2020. **2015**.
44. Fernandes, F.A.O.; Alves de Sousa, R.J.; Ptak, M. Finite element head modelling and head injury predictors. In *SpringerBriefs in Applied Sciences and Technology*; 2018; pp. 1–23.
45. Ratajczak, M.; Szaśiadek, M.; Będziński, R. An analysis of the effect of impact loading on the destruction of vascular structures in the brain. *Acta Bioeng. Biomech.* **2016**, *18*, 21–31, doi:10.5277/ABB-00552-2016-02.
46. van Baar, G.J.C.; Ruslin, M.; van Eijnatten, M.; Sándor, G.K.; Forouzanfar, T.; Wolff, J. 3D

- assessment of damaged bicycle helmets and corresponding craniomaxillo-mandibular skull injuries: a feasibility study. *Injury* **2017**, doi:10.1016/j.injury.2017.09.031.
47. Skjerven-Martinsen, M.; Naess, P.A.; Hansen, T.B.; Rognum, T.O.; Lereim, I.; Stray-Pedersen, A. In-depth evaluation of real-world car collisions: Fatal and severe injuries in children are predominantly caused by restraint errors and unstrapped cargo. *Traffic Inj. Prev.* **2011**, *12*, 491–499, doi:10.1080/15389588.2011.596868.
48. Bandak, F.A. Biomechanics of impact traumatic brain injury. In *Crashworthiness of Transportation Systems: Structural Impact and Occupant Protection*; Springer Science & Business Media, 1997; pp. 53–93 ISBN 978-94-010-6447-7.
49. Fernandes, F.A.O.; Sousa, R.J.A. De Motorcycle helmets — A state of the art review. *Accid. Anal. Prev.* **2013**, *56*, 1–21, doi:10.1016/j.aap.2013.03.011.
50. United Nations *ECE Regulation 22.05, 2002. Uniform provision concerning the approval of protective helmets and their visors for driver and passengers of motor cycles and mopeds*; 2002;
51. Shuaeib, F.M.; Hamouda, A.M.S.; Radin Umar, R.S.; Hamdan, M.M.; Hashmi, M.S.J. Motorcycle helmet - Part I. Biomechanics and computational issues. *J. Mater. Process. Technol.* **2002**, *123*, 406–421, doi:10.1016/S0924-0136(02)00048-1.
52. Fernandes, F.A.O. *Análise Biomecânica de impactos com capacetes: novos materiais e geometrias*, Biomechanical analysis of helmeted head impacts: novel materials and geometries, Universidade de Aveiro, 2017.
53. Yoganandan, N.; Sances, A.; Pintar, F.A.; Walsh, P.R.; Ewing, C.L.; Thomas, D.J.; Snyder, R.G.; Reinartz, J.; Droese, K. Biomechanical tolerance of the cranium. In *Proceedings of the SAE Technical Papers*; 1994; Vol. 103, pp. 184–189.
54. Ratajczak, M.; Ptak, M.; Chybowski, L.; Gawdzińska, K.; Będziński, R. Material and Structural Modeling Aspects of Brain Tissue Deformation under Dynamic Loads. *Materials (Basel)*. **2019**, *12*, 271, doi:10.3390/ma12020271.
55. Kleiven, S. Finite Element Modeling of the Human Head. *Med. Biol. ...* **2002**, *12*, 14–21.
56. Ptak, M.; Wilhelm, J.; Klimas, O.; Reclik, G. Numerical Simulation of a Motorcycle to Road Barrier Impact. *Springer Nat. Switz.* **2019**, 1–9, doi:10.1007/978-3-030-04975-1_65.
57. Fernandes, F.; Alves de Sousa, R.; Ptak, M.; Migueis, G. Helmet Design Based on the Optimization of Biocomposite Energy-Absorbing Liners under Multi-Impact Loading. *Appl. Sci.* **2019**, *9*, 735, doi:10.3390/app9040735.
58. Migueis, G.F.J.; Fernandes, F.A.O.; Ptak, M.; Ratajczak, M.; Alves de Sousa, R.J. Detection of bridging veins rupture and subdural haematoma onset using a finite element head model. *Clin. Biomech.* **2019**, *63*, 104–111, doi:10.1016/j.clinbiomech.2019.02.010.
59. Miller, K.; Wittek, A.; Joldes, G. Biomechanics of the brain for computer-integrated surgery. *Acta Bioeng. Biomech.* **2010**, *12*, 25–37, doi:10.1007/978-1-4419-9997-9.

60. Fernandes, A.O.; Sousa, R.J.A. De Head injury predictors in sports trauma – A state-of-the-art review. **2015**, *229*, 592–608, doi:10.1177/0954411915592906.
61. Fernandes, F.A.O.; Alves de Sousa, R.J.; Ptak, M.; de Sousa, R.J.A.; Ptak, M. *Head Injury Simulation in Road Traffic Accidents*; SpringerBriefs in Applied Sciences and Technology; 1st ed.; Springer International Publishing: Cham, 2018; ISBN 978-3-319-89925-1.
62. Yao, J.F.; Yang, J.K.; Fredriksson, R. Reconstruction of head-to-hood impact in an automobile-to-child-pedestrian collision. *Int. J. Crashworthiness* **2006**, *11*, 387–395, doi:10.1533/ijcr.2005.0118.
63. Klinich, K.D.; Saul, R.A.; Auguste, G.; Backaitis, S.; Klienberger, M. *Techniques for developing child dummy protection reference values*; National Highway Traffic Safety Administration: Washington, DC, USA, 1996;
64. Burdi, A.R.; Huelke, D.F.; Snyder, R.G.; Lowrey, G.H. Infants and children in the adult world of automobile safety design: Pediatric and anatomical considerations for design of child restraints. *J. Biomech.* **1969**, *2*, 267–280, doi:10.1016/0021-9290(69)90083-9.
65. McNally, D.S.; Rosenberg, N.M. MADYMO simulation of children in cycle accidents: A novel approach in risk assessment. *Accid. Anal. Prev.* **2013**, *59*, 469–478, doi:10.1016/j.aap.2013.07.022.
66. Stiles, J.; Jernigan, T.L. The basics of brain development. *Neuropsychol. Rev.* **2010**, *20*, 327–348, doi:10.1007/s11065-010-9148-4.
67. Meyer, F.; Deck, C.; Willinger, R.; Meyer, P. Development of a 3-year-old child head–neck finite element model and derivation of novel head injury criterion. *Int. J. Crashworthiness* **2014**, *19*, 233–243, doi:10.1080/13588265.2013.815018.
68. D. Muñoz, A. Mansilla, F.L.-V.R.M. a Study of Current Neck Injury Criteria Used for Whiplash Analysis. Proposal of a New Criterion Involving Upper and Lower Neck Load Cells. *Proc. 19th Exp. Saf. Veh. Conf.* **2005**, 1–14.
69. Boström, O.; MY, S.; Aldman, B.; HA, H.; Haland, Y.; Lovsund, P.; Seeman, T.; Suneson, A.; Saljo, A.; Ortengren, T. A new neck injury criterion candidate -- Based on injury findings in the cervical spinal ganglia after experimental neck extension trauma. *Proc. 1996 Int. IRCOBI Conf. Biomech. Impact, Sept. 11-13, 1996, Dublin, Irel.* **1996**, 123–126.
70. Schmitt, K.-U.; Muser, M.H.; Niederer, P. a New Neck Injury Criterion Candidate for Rear-End Collisions Taking Into Account Shear Forces and Bending Moments. *Technology* **2000**, 1–9.
71. Haasper, C.; Junge, M.; Ernstberger, A.; Brehme, H.; Hannawald, L.; Langer, C.; Nehmzow, J.; Otte, D.; Sander, U.; Krettek, C.; et al. Die Abbreviated Injury Scale (AIS): Potenzial und probleme bei der anwendung. *Unfallchirurg* **2010**, *113*, 366–372, doi:10.1007/s00113-010-1778-8.
72. National Highway Traffic Safety Administration Federal Motor Vehicle Safety Standard 208. **2018**.
73. Yoganandan, N.; Yoganandan, N.; Nahum, A.M. *Accidental injury: Biomechanics and prevention*; 2015; ISBN 9781493917327.
74. LLC Elemance Global Human Body Models Consortium. *User Man. M50 Occupant Version 4.2*

LS-DYNA 2014.

75. Crandall, J.R.; Myers, B.S.; Meaney, D.F.; Zeller Schmidtke, S. *Pediatric Injury Biomechanics*; Springer New York: New York, United States, 2013; ISBN 978-1-4614-4153-3.
76. Prange, M.T.; Kiralyfalvi, G.; Margulies, S.S. Pediatric rotational inertial brain injury: The relative influence of brain size and mechanical properties. In *Proceedings of the Stapp Car Crash Conference Proceedings*; 1999; Vol. P-350, pp. 333–341.
77. Margulies, S.S. Infant Skull and Suture Properties: Measurements and Implications for Mechanisms of Pediatric Brain Injury. *J. Biomech. Eng.* **2000**, *122*, 364, doi:10.1115/1.1287160.
78. Coats, B.; Margulies, S.S.; Ji, S. Parametric study of head impact in the infant. *Stapp Car Crash J.* **2007**, *51*, 1–15.
79. Klinich, K.D.; Hulbert, G.M.; Schneider, L.W. Estimating Infant Head Injury Criteria and Impact Response Using Crash Reconstruction and Finite Element Modeling. In *Proceedings of the SAE Technical Papers*; 2002; Vol. 2002–Novem, pp. 165–94.
80. Roth, S.; Raul, J.-S.; Ludes, B.; Willinger, R. Finite element analysis of impact and shaking inflicted to a child. *Int. J. Legal Med.* **2007**, *121*, 223–8, doi:10.1007/s00414-006-0129-3.
81. Roth, S.; Vappou, J.; Raul, J.-S.; Willinger, R. Child head injury criteria investigation through numerical simulation of real world trauma. *Comput. Methods Programs Biomed.* **2009**, *93*, 32–45, doi:10.1016/j.cmpb.2008.08.001.
82. Untaroiu, C.D. A Finite Element Model of a 6-Year-Old Child for Simulating Pedestrian Impacts. **2016**, doi:10.1080/15389588.2015.1073073.
83. Ito, K.; Tokuyama, M.; Miyazaki, H.; Hayashi, S.; Kitagawa, Y.; Yasuki, T. DEVELOPMENT OF CHILD FINITE ELEMENT (FE) MODELS AND VEHICLE-TO-PEDESTRIAN COLLISION SIMULATIONS. *Proc. 25th Tech. Conf. Enhanc. Saf. Veh. (ESV), June 5-8 2017, Detroit, MI* **2017**, 1–17.
84. Beillas, P.; Giordano, C.; Alvarez, V.; Li, X.; Ying, X.; Chevalier, M.; Kirscht, S.; Kleiven, S.; Beillas, P.; Giordano, C.; et al. Development and performance of the PIPER scalable child human body models, HAL Id : hal-01720414. In *Proceedings of the 14th International Conference on the Protection of Children in Cars, Munich, Germany*; 2016; p. 19.
85. Giordano, C.; Kleiven, S. Development of a 3-Year-Old Child FE Head Model, Continuously Scalable from 1.5- to 6-Year-Old. *IRCOBI Conf.* **2016**, 288–302.
86. Nahum, A.M.; Smith, R.; Ward, C.C. Intracranial Pressure Dynamics During Head Impact. *SAE Tech. Pap. Ser.* **2010**, *1*, doi:10.4271/770922.
87. Hardy, W.N. Response to the Human Cadaver Head to Impact. **2007**.
88. Ptak, M. Pedestrian safety: a new method to assess pedestrian kinematics. *Transport* **2018**, *33*, (in print).
89. Ptak, M.; Rusiński, E.; Karliński, J.; Dragan, S. Evaluation of kinematics of SUV to pedestrian

- impact—Lower leg impactor and dummy approach. *Arch. Civ. Mech. Eng.* **2012**, *12*, 68–73, doi:10.1016/j.acme.2012.03.016.
90. Ptak, M.; Karliński, J. Pedestrian passive safety during the SUV impact: regulations vs. reality. *2012 IRCOBI Conf. Dublin, Irel.* **2012**, 103–113.
91. Ptak, M.; Rusiński, E.; Wnuk, M.; Wilhelm, J.; Więckowski, J. *Numerical simulation using finite element method and multibody pedestrian dummy - report no. 142/2016*; Wrocław, 2016;
92. Zander, O.; Gehring, D.; Leßmann, P. Improved safety of bicyclists in the event of a collision with motor vehicles and during single accidents. *23rd ESV Conf. Proc.* **2013**, 1–11.
93. Treaty, E.C.; Treaty, E. No 631/2009 Official Journal of the European Union L195/1. *Regulation* **2009**.
94. Liers, H. Extension of the Euro NCAP effectiveness study with a focus on MAIS3+ injured pedestrians. *TU Dresden* **2010**.
95. Cambridge University Engineering Department Materials data book. *Mater. Courses* **2003**, 1–41, doi:10.1016/0261-3069(88)90026-X.
96. Madymo TASS Release Notes Manual, Release 7.5. **2013**.
97. Yi, Q.; Chien, S.; Li, L.; Niu, W.; Chen, Y.; Good, D.; Chen, C.-C.; Sherony, R. Development of test scenarios and bicyclist surrogate for the evaluation of bicyclist automatic emergency braking systems. *J. Intell. Connect. Veh.* **2018**, doi:10.1108/JICV-02-2018-0005.
98. Ptak, M.; Konarzewski, K. Numerical Technologies for Vulnerable Road User Safety Enhancement. In *New Contributions in Information Systems and Technologies*; 2015; Vol. 354, pp. 355–364 ISBN 9783319165271.
99. Wilhelm, J.; Ptak, M.; Rusiński, E. Simulated depiction of head and brain injuries in the context of cellularbased materials in passive safety devices. **2017**, *50*, 98–104, doi:10.17402/222.
100. EEVC Q-dummies Report. **2008**, 51.
101. TNO Human Body Models Manual Releas 7.6. **2015**, 122.
102. Jurecki, R.; Stańczyk, T.; Jaśkiewicz, M. Driver's reaction time in a simulated, complex road incident. *Transport* **2017**, *32*, 44–54, doi:10.3846/16484142.2014.913535.
103. Crocetta, G.; Piantini, S.; Pierini, M.; Simms, C. The influence of vehicle front-end design on pedestrian ground impact. *Accid. Anal. Prev.* **2015**, *79*, 56–69, doi:10.1016/j.aap.2015.03.009.
104. Bourdet, N.; Deck, C.; Serre, T.; Perrin, C.; Llari, M.; Willinger, R. In-depth real-world bicycle accident reconstructions. *Int. J. Crashworthiness* **2014**, *19*, 222–232, doi:10.1080/13588265.2013.805293.
105. Mazurkiewicz, L.; Baranowski, P.; Karimi, H.R.; Damaziak, K.; Malachowski, J.; Muszynski, A.; Muszynski, A.; Robbersmyr, K.G.; Vangi, D. Improved child-resistant system for better side impact protection. *Int. J. Adv. Manuf. Technol.* **2018**, *97*, 3925–3935, doi:10.1007/s00170-018-2236-y.

106. Jamroziak, K.; Bocian, M.; Kulisiewicz, M. Identification of a Subsystem Located in The Complex Dynamical Systems Subjected to Random Loads. *J. Comput. Nonlinear Dyn.* **2016**, *12*, 14501, doi:10.1115/1.4034274.
107. Fernandes, F.A.O.; Sousa, R.J.A. De; Ptak, M. A damage model for the simulation of crack initiation and propagation in automotive windshield laminated glass structures. *Int. J. Crashworthiness* **2020**, *0*, 1–9, doi:10.1080/13588265.2020.1727077.
108. Hernandez, F.; Wu, L.C.; Yip, M.C.; Laksari, K.; Hoffman, A.R.; Lopez, J.R.; Grant, G.A.; Kleiven, S.; Camarillo, D.B. Six Degree-of-Freedom Measurements of Human Mild Traumatic Brain Injury. *Ann. Biomed. Eng.* **2015**, *43*, 1918–1934, doi:10.1007/s10439-014-1212-4.
109. Allgemeiner Deutscher Automobil-Club (ADAC) ADAC-Test zum Kindertransport auf Fahrrädern Available online: https://tp-online.de/leben/auto/ratgeber/adac-test-zum-kindertransport-auf-fahrraedern_bid-11565323 (accessed on Jul 13, 2018).
110. Baranowski, P.; Damaziak, K.; Malachowski, J.; Mazurkiewicz, L.; Muszyński, A. A child seat numerical model validation in the static and dynamic work conditions. *Arch. Civ. Mech. Eng.* **2014**, doi:10.1016/j.acme.2014.07.001.
111. Mercedes-Benz CLA and GLE, picture Available online: <https://images.app.goo.gl/JEFXnMaHjkFcvgzU7> (accessed on Jan 21, 2020).
112. Otte, D. A review of different kinematic forms in two-wheel- accidents-their influence on effectiveness of protective measures. In Proceedings of the SAE Technical Papers; 1980; pp. 561–605.
113. Otte, D. Wrap Around Distance WAD of Pedestrian and Bicyclists and Relevance as Influence Parameter for Head Injuries. *SAE Tech. Pap. 2015-01-1461* **2015**, doi:10.4271/2015-01-1461.
114. TASS Design, Simulation and Virtual Testing - Model Manual, Version 7.5. *MADYMO Util. Man.* **2013**, 5–7.
115. Humanetics Innovative Solutions Hybrid III 3 Year Old Child | Humanetics ATD Available online: <http://www.humaneticsatd.com/crash-test-dummies/children/hiii-3yo>.
116. Kubicki, K. Kraniometria, Multimedia presentation, 19.01.2018, aHEAD project, <http://www.aheadproject.org> 2018.
117. Alshareef, A.; Giudice, J.S.; Forman, J.; Shedd, D.F.; Reynier, K.A.; Wu, T.; Sochor, S.; Sochor, M.R.; Salzar, R.S.; Panzer, M.B. Biomechanics of the Human Brain During Dynamic Rotation of the Head. *J. Neurotrauma* **2020**, 1–34, doi:10.1089/neu.2019.6847.
118. Horgan, T.J.; Gilchrist, M.D. Influence of FE model variability in predicting brain motion and intracranial pressure changes in head impact simulations. *Int. J. Crashworthiness* **2004**, *9*, 401–418, doi:10.1533/ijcr.2004.0299.
119. Fernandes, F.A.O.; Tchepele, D.; Alves de Sousa, R.J.; Ptak, M.; de Sousa, R.J.A.; Ptak, M. Development and validation of a new finite element human head model - Yet another head model (YEAHM). *Eng. Comput. (Swansea, Wales)* **2018**, *35*, 477–496, doi:10.1108/EC-09-2016-0321.

120. Barkovich, A.J.; Kjos, B.O.; Jackson Jr, D.E.; Norman, D.; Jackson, D.E.; Norman, D.; Jackson Jr, D.E.; Norman, D. Normal maturation of the neonatal and infant brain: MR imaging at 1.5 T. *Radiology* **1988**, *166*, 173–180, doi:10.1148/radiology.166.1.3336675.
121. Lui, S.; Ouyang, L.; Deng, W.; Yang, H.; Tang, H.; Jiang, L.; Huang, X.; Song, B.; Zhou, X.; Maclean, S.; et al. Global gray/white matter ratio and gray matter volume reflect abnormal aging neurodevelopment in treatment naive schizophrenics. *Proc. 14th Sci. Meet. Int. Soc. Magn. Reson. Med.* **2006**, *14*, 2078.
122. Jin, S.W.; Sim, K.B.; Kim, S.D. Development and growth of the normal cranial vault: An embryologic review. *J. Korean Neurosurg. Soc.* **2016**, *59*, 192–196, doi:10.3340/jkns.2016.59.3.192.
123. Schoell, S.L.; Weaver, A.A.; Urban, J.E.; Jones, D.A.; Stitzel, J.D.; Hwang, E.; Reed, M.P.; Rupp, J.D.; Hu, J. Development and Validation of an Older Occupant Finite Element Model of a Mid-Sized Male for Investigation of Age-related Injury Risk. *Stapp Car Crash J.* **2015**, *59*, 359–83.
124. Khandare, S. V; Bhise, S.; Shinde, A.B. Age estimation from cranial sutures – a Postmortem study. *Int. J. Healthc. Biomed. Res.* **2015**, 3–192.
125. Junqueira, L.C.; Carneiro, J. *Histologie: Lehrbuch der Cytologie, Histologie und mikroskopischen Anatomie des Menschen*; Springer-Verlag, 2013; ISBN 9783662219966.
126. Khalid, A.G.A.; Jones, M.D.; Prabhu, R.; Whittington, W.; Bakhtarydavijani, H.; Theobald, P.S. Development of a Paediatric Head Model for the Computational Analysis of Head Impact Interactions. **2017**, *4*, 62822.
127. RADIOLOGY masterclass MRI interpretation Available online: https://www.radiologymasterclass.co.uk/tutorials/mri/mri_signal#top_6th_img (accessed on Jun 12, 2018).
128. Preston, D.C. Magnetic Resonance Imaging (MRI) of the Brain and Spine: Basics Available online: http://casemed.case.edu/clerkships/neurology/Web_Neurorad/MRI_Basics.htm (accessed on Jun 12, 2018).
129. Lee, J.K.T. *Computed Body Tomography with MRI Correlation*; Lippincott Williams & Wilkins, 2006; ISBN 9780781745260.
130. Bloomfield I, G.; Johnston I, H.; Bilston L, E. Effects of Proteins, Blood Cells and Glucose on the Viscosity of Cerebrospinal Fluid. *Pediatr Neurosurg* **1998**, *28*, 246–251, doi:10.1159/000028659.
131. Miller, K. *Biomechanics of the Brain*; Miller, K., Ed.; Biological and Medical Physics, Biomedical Engineering; Springer Science & Business Media: New York, NY, 2011; ISBN 1441999973.
132. Boron, W.; Boulpaep, E. *Medical Physiology 3rd Edition*; Elsevier, 2016; ISBN 9781455743773.
133. Eley, K.A.; Watt-Smith, S.R.; Golding, S.J. “Black bone” MRI: A potential alternative to CT when imaging the head and neck: Report of eight clinical cases and review of the Oxford experience. *Br. J. Radiol.* **2012**, *85*, 1457–1464, doi:10.1259/bjr/16830245.

134. Miller, K. *Biomechanics of the brain*; Springer New York: New York, United States, 2011; ISBN 978-1-4419-9996-2.
135. Miller, K.; Chinzei, K. Mechanical properties of brain tissue in tension. *J. Biomech.* **2002**, *35*, 483–490, doi:10.1016/S0021-9290(01)00234-2.
136. Brockmann, C.; Kunze, S.; Scharf, J. Computed tomographic angiography of the superior sagittal sinus and bridging veins. **2011**, 129–134, doi:10.1007/s00276-010-0714-5.
137. Wittek, A.; Joldes, G.; Nielsen, P.M.F.; Doyle, B.J.; Miller, K. Computational biomechanics for medicine: From algorithms to models and applications. *Comput. Biomech. Med. From Algorithms to Model. Appl.* **2017**, 1–173, doi:10.1007/978-3-319-54481-6.
138. Zhou, Z. Evaluation of Fluid-Structure Interaction and Biofidelity of Finite Element Head Models, Royal Institute of Technology (KTH), 2019.
139. Dias, D.A.; Castro, F.L.O.; Yared, J.H.; Lucas Júnior, A.; Ferreira Filho, L.A.; Ferreira, N.F.P.D. Liliequist membrane: Radiological evaluation, clinical and therapeutic implications. *Radiol. Bras.* **2014**, *47*, 182–185, doi:10.1590/0100-3984.2013.1809.
140. Delye, H.; Goffin, J.; Verschuere, P.; Vander Sloten, J.; Van der Perre, G.; Alaerts, H.; Verpoest, I.; Berckmans, D. Biomechanical properties of the superior sagittal sinus-bridging vein complex. *Stapp Car Crash J.* **2006**, 625–36, doi:10.4271/2006-22-0024.
141. Ratajczak, M. Analysis of biomechanical parameter changes in brain tissues due to dynamic loads, Wrocław University of Science and Technology, Poland, 2018.
142. Gomez-Gesteira, M.; Crespo, A.J.C.; Rogers, B.D.; Dalrymple, R.A.; Dominguez, J.M.; Barreiro, A. SPHysics - development of a free-surface fluid solver - Part 2: Efficiency and test cases. *Comput. Geosci.* **2012**, *48*, 300–307, doi:10.1016/j.cageo.2012.02.028.
143. DYNAmore GmbH LS-DYNA Examples, Wave-Structure Interaction Available online: <https://www.dynaexamples.com/sph/intermediate-examples/wavestructure>.
144. Livermore Software Technology Corporation Hourglass (HG) Modes Hourglassing Avoiding or Minimizing Hourglass Modes. **2012**, 1–7.
145. Livermore Software Technology Corporation (LSTC) Contact in LS-DYNA - Practical Guidelines. **2012**.
146. Roos, K.L. Acute Bacterial Infections of the Central Nervous System. *Neurol. Gen. Med.* **2008**, 769–787, doi:10.1016/B978-044306707-5.50043-2.
147. Raimondi, A.J. *Pediatric Neurosurgery: Theoretical Principles. Art of Surgical Techniques*; 1st ed.; Springer-Verlag New York, 1987; ISBN 978-1-4757-4202-2.
148. Cheshire, E.C.; Malcomson, R.D.G.; Sun, P.; Mirkes, E.M.; Amoroso, J.M.; Ruttly, G.N. A systematic autopsy survey of human infant bridging veins. *Int. J. Legal Med.* **2018**, *132*, 449–461, doi:10.1007/s00414-017-1714-3.
149. Famaey, N.; Ying Cui, Z.; Umuhire Musigazi, G.; Ivens, J.; Depreitere, B.; Verbeken, E.; Vander

- Sloten, J. Structural and mechanical characterisation of bridging veins: A review. *J. Mech. Behav. Biomed. Mater.* **2015**, *41*, 222–240, doi:10.1016/j.jmbbm.2014.06.009.
150. Deck, C.; Willinger, R. Head injury prediction tool for predictive systems optimization. *7th Eur. LS-DYNA Conf.* **2008**, 14–15.
151. Silva, J.M.; Devezas, T.C.; Silva, A.; Gil, L.; Nunes, C.; Franco, N. Exploring the Use of Cork Based Composites for Aerospace Applications. *Mater. Sci. Forum* **2010**, *636–637*, 260–265, doi:10.4028/www.scientific.net/MSF.636-637.260.
152. Tchepel, D.; Fernandes, F.A.O.; Anjos, O.; Alves de Sousa, R. Mechanical Properties of Natural Cellular Materials. In *Reference Module in Materials Science and Materials Engineering*; Elsevier, 2016 ISBN 9780128035818.
153. de Sousa, R. a.; Goncalves, D.; Coelho, R.; Teixeira-Dias, F.; Alves De Sousa, R.J.; Gonçalves, D.; Coelho, R.; Teixeira-Dias, F. Assessing the effectiveness of a natural cellular material used as safety padding material in motorcycle helmets. *Simulation* **2012**, *88*, 580–591, doi:10.1177/0037549711414735.
154. Sousa-Martins, J.; Kakogiannis, D.; Coghe, F.; Reymen, B.; Teixeira-Dias, F. Response of cork compounds subjected to impulsive blast loads. *Eur. Phys. J. Spec. Top.* **2012**, *206*, 61–70, doi:10.1140/epjst/e2012-01587-1.
155. Anjos, O.; Rodrigues, C.; Morais, J.; Pereira, H. Effect of density on the compression behaviour of cork. *Mater. Des.* **2014**, *53*, 1089–1096, doi:10.1016/j.matdes.2013.07.038.
156. Aroso, I.M.; Fernandes, E.M.; Pires, R.A.; Mano, J.F.; Reis, R.L. Cork extractives exhibit thermo-oxidative protection properties in polypropylene–cork composites and as direct additives for polypropylene. *Polym. Degrad. Stab.* **2015**, *116*, 45–52, doi:10.1016/J.POLYMDEGRADSTAB.2015.03.006.
157. Pinto, P.C.R.O.; Sousa, A.F.; Silvestre, A.J.D.; Neto, C.P.; Gandini, A.; Eckerman, C.; Holmbom, B. Quercus suber and Betula pendula outer barks as renewable sources of oleochemicals: A comparative study. *Ind. Crops Prod.* **2009**, *29*, 126–132, doi:10.1016/J.INDCROP.2008.04.015.
158. Silva, S.P.; Sabino, M. a.; Fernandes, E.M.; Correlo, V.M.; Boesel, L.F.; Reis, R.L. Cork: properties, capabilities and applications. *Int. Mater. Rev.* **2005**, *50*, 256–256, doi:10.1179/174328005X41168.
159. Pereira, H. Chemical composition and variability of cork from Quercus suber L. *Wood Sci. Technol.* **1988**, *22*, 211–218, doi:10.1007/BF00386015.
160. Oliveira, V.; Rosa, M.E.; Pereira, H. Variability of the compression properties of cork. *Wood Sci. Technol.* **2014**, *48*, 937–948, doi:10.1007/s00226-014-0651-2.
161. Pereira, H. Variability of the Chemical Composition of Cork. *BioResources* **2013**, *8*, 2246–2256, doi:10.15376/biores.8.2.2246-2256.
162. Coelho, R.M.; Alves de Sousa, R.J.; Fernandes, F.A.O.; Teixeira-Dias, F. New composite liners for energy absorption purposes. *Mater. Des.* **2013**, *43*, 384–392, doi:10.1016/j.matdes.2012.07.020.

163. Jardin, R.T.; Fernandes, F.A.O.; Pereira, A.B.; Alves de Sousa, R.J. Static and dynamic mechanical response of different cork agglomerates. *Mater. Des.* **2015**, *68*, 121–126, doi:10.1016/j.matdes.2014.12.016.
164. Sanchez-Saez, S.; Barbero, E.; Garcia-Castillo, S.K.K.; Ivañez, I.; Cirne, J. Experimental response of agglomerated cork under multi-impact loads. *Mater. Lett.* **2015**, *160*, 327–330, doi:10.1016/j.matlet.2015.08.012.
165. Kottner, R.; Hynek, R.; Mandys, T.; Bartošek, J. Material property determination of the lining layers of a versatile helmet. *MATEC Web Conf.* **2018**, *157*, 6005, doi:10.1051/mateconf/201815706005.
166. Fernandes, F.A.O.; Jardin, R.T.; Pereira, A.B.; Alves de Sousa, R.J. Comparing the mechanical performance of synthetic and natural cellular materials. *Mater. Des.* **2015**, *82*, 335–341, doi:10.1016/j.matdes.2015.06.004.
167. Santos, P.T.; Pinto, S.; Marques, P.A.A.P.; Pereira, A.B.; Alves de Sousa, R.J. Agglomerated cork: A way to tailor its mechanical properties. *Compos. Struct.* **2017**, *178*, 277–287, doi:10.1016/j.compstruct.2017.07.035.
168. Costas, M.; Díaz, J.; Romera, L.E.; Hernández, S.; Tielas, a. Static and dynamic axial crushing analysis of car frontal impact hybrid absorbers. *Int. J. Impact Eng.* **2013**, *62*, 166–181, doi:10.1016/j.ijimpeng.2013.06.011.
169. Tay, Y.Y.; Lim, C.S.; Lankarani, H.M. A finite element analysis of high-energy absorption cellular materials in enhancing passive safety of road vehicles in side-impact accidents. *Int. J. Crashworthiness* **2014**, *19*, 288–300, doi:10.1080/13588265.2014.893789.
170. Ptak, M.; Kaczynski, P.; Fernandes, F.A.O.; de Sousa, R.J.A. Assessing impact velocity and temperature effects on crashworthiness properties of cork material. *Int. J. Impact Eng.* **2017**, *106*, 238–248, doi:10.1016/j.ijimpeng.2017.04.014.
171. Gibson, L.J.; Easterling, K.E.; Ashby, M.F. The Structure and Mechanics of Cork. *Proc. R. Soc. Lond. A. Math. Phys. Sci.* **1981**, *377*, 99–117.
172. Gameiro, C.P.; Cirne, J. Dynamic axial crushing of short to long circular aluminium tubes with agglomerate cork filler. *Int. J. Mech. Sci.* **2007**, *49*, 1029–1037, doi:10.1016/j.ijmecsci.2007.01.004.
173. Fernandes, F.A.O.; Tavares, J.P.; Alves de Sousa, R.J.; Pereira, A.B.; Esteves, J.L. Manufacturing and testing composites based on natural materials. *Procedia Manuf.* **2017**, *13*, 227–234, doi:10.1016/j.promfg.2017.09.055.
174. Kaczynski, P.; Ptak, M.; Wilhelm, J.; Fernandes, F.A.O.; de Sousa, R.J.A. High-energy impact testing of agglomerated cork at extremely low and high temperatures. *Int. J. Impact Eng.* **2019**, *126*, doi:10.1016/j.ijimpeng.2018.12.001.
175. Bois, P.A. Du A simplified approach to the simulation of rubber-like materials under dynamic loading - Implementation of MAT _ 181 in LS-DYNA. In Proceedings of the 4th European LS-

- DYNA Users Conference; 2003; pp. 31–46.
176. Kolling, S.; Bois, P.A. Du; Benson, D.J. A Simplified Rubber Model with Damage. *4. LS-DYNA Anwenderforum, Bamb. 2005* **2005**.

Statement of authorship

I hereby certify, that this thesis has been composed by myself and describes my own work, unless otherwise acknowledged in the text. All references and verbatim extracts have been quoted and all sources of information have been specifically acknowledged. It has not been accepted in any previous application for a degree.

Wrocław, _____

Place, Date

Signature